Geochemistry of dolerites from the Parana flood basalt province, southern Brazil

Thesis

Geochemistry of dolerites from the Parana flood basalt province, southern Brazil

UNRESTRICTE

A thesis presented for the degree of

Doctor of Philosophy

by

MARCEL REGELOUS

B. A. (Hons.) *Oxon.* 1989

Department of Earth Sciences,

The Open University.

April 1993

"...the organization and presentation of the material is excellent."
International Journal for Numerical and Analytical Methods in Geomechanics

"... the book is a most worthwhile volume. All structural geologists, petroleum geologists and engineering geologists should make themselves aware of the concepts treated in this book. It will become a standard library reference source. "
S.F. Cox
Earth-Science Reviews

"...its main strength is the depth of insight it shows." *Nature*

'A delight to read, full of intriguing speculation as well as facts'

– Kenneth B. Wilson in the *Methodist Recorder*

"That rarest of scholarly achievements—a book so sensible, so searching, and so patently necessary as to make one wonder why it hadn't been written many times and many years ago."—Earl Rovit in *American Scholar*

'Horrifying, fascinating!'—*Punch.*

"A most engaging book...It is comprehensive, acute, tightly written, solidly documented, a delight to hold and to read."—Lynn Marshall in *Journal of American History*

'He is a born raconteur' – *Daily Mail*

'His pages are enlivened with a gleaming humour which enhances the book's overwhelming attraction. A triumph!' – *Daily Telegraph*

'Few volumes so slender contain so much wit, point, and originality of thought and expression. The book is a delight. No one with a speech to make who has exhausted his own stores of wit and wisdom should neglect this glittering hoard.'
Richard Ollard, *British Book News*

"A superb volume... every serious earth scientist will have to possess his or her own copy."
EOS

Acknowledgements

I would like to thank my supervisors Chris Hawkesworth and Nick Rogers for their help throughout this research, and for their comments on earlier versions of this thesis which much improved the text. Marta Mantovani of the Instituto Astronomico e Geofisico, Sao Paulo University provided the support in Brazil without which this project would not have been possible. Dentinho, Nick, Cherry and Dave are thanked for their company in the field, Goonie Marsh for the lift from Windhoek to Cape Town, and the Erlank family for their hospitality during my stay in Cape Town.

Kay Chambers prepared the thin sections and Andy Tindle and Dentinho helped with the operation of the microprobe. Steve Wyatt and Keith Parish of the Oxford XRF lab., and John Watson and Pete Webb at the Open University provided the major and trace element analyses. Nick Rogers supplied the INAA data, and Simon Kelley and Simon Turner are thanked for their help in the Ar—Ar lab., and for useful comments on early versions of Chapter 4. Mabsie, Peter, Yiming, Frank and others in the Radiogenic Isotope Lab. are thanked for their help and company. Dan McKenzie kindly sent me a copy of the program used to calculate melt volumes and compositions in Chapter 5, and Kerry Gallagher adapted it to run on a Macintosh.

Thanks to Phil G., Tim B., and Anthony for company and entertainment in T19. Phil W., Geoff, Steve R., Mark S., and the occasional visitor to 10 Orne Gardens (especially Alex, May and Justine) are thanked for the odd bowl of cornflakes, and for allowing me to do their washing up. Many others at the O. U. have helped to make my time in Milton Keynes bearable, in particular Jason, Andy M. and John B. for caving trips to Yorkshire; Kay and the other members of the hockey team; Beto, Phil B., Bill, Jon D., Brandon, Steph and the rest of the footie boys; Maria, Ben, Terre, Fran and Christian for Latin American evenings; Helen for crossword answers and trips to Whipsnade; Mark G., Fran, Ben and Tim B. for tennis; Alex for lifts, and the holiday in Dorset; Shaggers and Simon T. for homebrew; Penny, Theresa, Ashley, Bill, Rob and the Vicarage crowd for excellent parties; all these and many others, particularly Sam, Kate, Russell, Carl, Barbara, Jugs and Fiona for their company in the Cellar or at the Vaults.

Abstract

The Cretaceous Parana-Etendeka flood basalt magmatism of South America and Africa was accompanied by intense intrusive activity. This study examines the geochemistry and petrogenesis of dykes from two regions of southern Brazil.

Dykes from the Ponta Grossa region of Parana State fed the basalt lava flows of the northern Parana. The dolerites underwent extensive crystal fractionation at pressures of less than about 5kb, but do not represent parental magmas to the associated rhyolites. The dolerites have received a contribution from a LREE enriched source with time-integrated high Rb/Sr relative to the bulk earth, and yield model Nd and $^{207}Pb/^{206}Pb$ ages which are similar to ages obtained from the basement rocks of southern Brazil. This suggests that the distinctive trace element and isotope signature of these dolerites was derived from a source in the subcontinental mantle.

The dolerites of Sao Paulo State are divisible into three magma types, which cannot be related either to one another, or to the flood basalts to the west by any simple petrogenetic process. The geochemical variation within dolerites of the Paraiba and Ubatuba magma types was controlled by assimilation fractional crystallisation and magma mixing processes at shallow levels in the crust. In contrast, the basanites of the Sao Sebastiao magma type underwent limited crystal fractionation of olivine and clinopyroxene at pressures of >4 kb. Much of the geochemical variation within this group of rocks is related to variations in the degree of partial melting (estimated to be 0.1—5%) of a spinel bearing source. The Sao Sebastiao basanites have very similar trace element and isotope compositions to Recent basanites erupted on the South Atlantic island of Tristan da Cunha, and are interpreted as the expression of the Tristan plume at 80 Ma.

Selected whole rock samples and mineral separates have been dated by the laser ablation Ar—Ar technique. The Ponta Grossa dolerites yield isochron ages of 130.5±2.9—134.1±1.3 Ma. The Paraiba and Ubatuba magma types were intruded at between 129.4±0.6 and 135.8±1.1 Ma. A biotite separate from a sample of the Sao Sebastiao magma type yielded a much younger age of 80.1±0.4 Ma, which suggests that these may be related to the alkalic intrusive complexes of Sao Paulo State.

These ages imply that the Parana magmatism occurred within about 3 Ma at 131—134 Ma, although there is evidence that plagioclase alteration may be responsible for some of the apparent age range. The data suggest that the flood basalt magmatism occurred contemporaneously with continental rifting in the South Atlantic, and are consistent with a model in which the Parana-Etendeka flood basalts represent decompression melts generated during continental rifting above the abnormally hot mantle associated with the Tristan da Cunha mantle plume. This model can also account for the observed volume of magma. A comparison of the major element compositions of flood basalts from various CFB provinces with the predicted composition of decompression melts, suggests that many of these basalts have inherited a distinctive major element signature from the subcontinental lithospheric mantle.

HIGHER DEGREES OFFICE

LIBRARY AUTHORISATION FORM

Please return this form to the Higher Degrees Office with the bound library copies of your thesis. All students should complete Part 1. Part 2 applies only to PhD students.

Student: MARCEL REGELOUS PI: M7063353

Degree: PhD

Thesis title: GEOCHEMISTRY OF DOLERITES FROM THE PARANA FLOOD BASALT PROVINCE, S. BRAZIL

Part 1 Open University Library Authorisation (to be completed by all students)

I confirm that I am willing for my thesis to be made available to readers by the Open University Library, and that it may be photocopied, subject to the discretion of the Librarian.

Signed: _____ Date: 12th Oct. 1993

Part 2 British Library Authorisation (to be completed by PhD students only)

If you want a copy of your PhD thesis to be held by the British Library, you must sign a British Doctoral Thesis Agreement Form. You should return it to the Higher Degrees Office with this form and your bound thesis. *You are also required to supply a third, unbound copy of your thesis.* The British Library will use this to make their microfilm copy; it will not be returned. Information on the presentation of the thesis is given in the Agreement Form.

If your thesis is part of a collaborative group project, you will need to obtain the signatures of others involved for the Agreement Form.

The University has agreed that the lodging of your thesis with the British Library should be voluntary. Please tick either (a) or (b) below to indicate your intentions.

(a) ☐ I am willing for the Open University to supply the British Library with a copy of my thesis. A signed Agreement Form and 3 copies of my thesis are attached (two bound as specified in Section 9.4 of the Research Degree Handbook and the third unbound).

(b) ☑ I do not wish the Open University to supply a copy of my thesis to the British Library.

Signed: _____ Date: 12th Oct. '93

Contents

Chapter 1 1

Introduction; the Parana-Etendeka flood basalt province 1

1.1 Physical characteristics of flood basalt magmatism 1

1.2 Geochemical characteristics of CFB magmatism 3

1.2.1 The major element geochemistry of CFB 3

1.2.2 Trace element and isotope geochemistry, and the nature of the mantle source 5

1.3 Geodynamic origins of CFB magmatism 6

1.4 The Parana-Etendeka CFB province 8

1.4.1 Regional geology of southeastern Brazil 8

1.4.2 Flood basalt magmatism in the South Atlantic 11

1.4.3 Geochemistry and stratigraphy of the flood basalts 16

1.4.3.1 Classification of magma types 16

1.4.3.2 Geochemical stratigraphy of the Parana basalts 18

1.4.3.3 Geochemical stratigraphy of the Parana rhyolites 22

1.4.4 Geochemical stratigraphy of the Etendeka lavas 23

1.4.5 Intrusive rocks of the Parana-Etendeka province 24

1.5 Aims of study, and structure of this thesis 26

Chapter 2 28

Geochemistry and petrogenesis of the Ponta Grossa dolerites 28

2.1 Introduction 28

2.2 Petrography and mineral chemistry 30

2.2.1 Pyroxene geothermometry 33

2.3 Whole-rock major element geochemistry 34

2.4 Trace element geochemistry 39

2.5 The role of weathering and subsolidus alteration 40

2.6 The role of fractional crystallisation 42

2.6.1 Major element modelling 42

2.6.1 Trace element modelling 44

2.7 Relationship of the intrusive rocks to the basaltic lavas of the northern Parana 50

2.8 Relationship of the more evolved intrusive rocks to the rhyolitic lavas of the northern Parana 54

2.9 Isotope geochemistry of the Ponta Grossa dolerites 56

2.9.1 Sr and Nd isotope geochemistry 56

2.9.2 Pb isotope geochemistry 59

2.9.3 Age significance of the Pb isotope data 61

2.9.4 Pb isotope evolution 62

2.9.5 Sr and Nd isotope evolution 63

2.10 Conclusions 65

Chapter 3 68
Geochemistry of dolerites from Sao Paulo State 68
3.1 Introduction 68
3.2 The dolerites of the Paraiba magma type 70
3.2.1 Introduction 70
3.2.2 Petrography and mineral chemistry 71
3.2.3 Major element whole rock geochemistry 72
3.2.4 Trace element geochemistry 74
3.2.5 Sr and Nd isotope geochemistry 77
3.2.6 Geochemical constraints on the contamination process 79
3.2.6.1 Major element constraints 79
3.2.6.2 Trace element and isotope modelling of the contamination process 81
3.2.7 Relationship of the dolerites to the flood basalts of the lava pile 85
3.2.8 Conclusions 88
3.3 The dolerites of the Ubatuba magma type 88
3.3.1 Introduction 88
3.3.2 Petrography and mineral chemistry 89
3.3.3 Major and trace element geochemistry 91
3.3.4 Isotope geochemistry of the Ubatuba dolerites 91
3.3.5 Origin of the geochemical variation 95
3.3.5.1 Crystal fractionation, and the role of plagioclase 95
3.3.5.2 The role of magma mixing processes 98
3.3.6 Conclusions 99
3.4 The dolerites of the Sao Sebastiao magma type 99
3.4.1 Introduction 99
3.4.2 Petrography and mineral chemistry 100
3.4.3 Whole rock major element geochemistry 102
3.4.4 Trace element geochemistry; evidence for a mantle plume at 80 Ma? 104
3.4.5 Petrogenesis of the Sao Sebastiao basanites; partial melting processes 107
3.4.5.1 Major element constraints 108
3.4.5.2 Trace element constraints 108
3.4.6 Isotope geochemistry of the Sao Sebastiao samples 111
3.4.6.1 Sr and Nd isotope geochemistry, and the role of subsolidus alteration 111
3.4.6.2 Pb isotope geochemistry 114
3.4.6.3 Petrogenetic significance of the isotope data 116
3.4.7 The role of mixing processes in South Atlantic basalt petrogenesis 118
3.4.8 Other Cretaceous alkaline intrusive rocks in Sao Paulo State 122

3.4.9 Conclusions 124
3.5 Chapter 5; summary and conclusions 125

Chapter 4 126
The age of the Parana-Etendeka flood basalt magmatism 126
4.1 Introduction 126
4.2 Summary of previous work 127
4.2.1 The age of the Parana volcanic rocks 127
4.2.2 The age of the Etendeka volcanic rocks 131
4.3 Reliability of the existing K—Ar and Rb—Sr data 132
4.4 The Ar—Ar dating method 132
4.4.1 Introduction 132
4.4.2 Previous Ar—Ar studies of the Parana flood basalts 134
4.5 The new Ar—Ar data 137
4.5.1 The Ponta Grossa dolerites 137
4.5.2 The dolerites of the Paraiba magma type 142
4.5.3 The dolerites of the Ubatuba magma type 143
4.5.3.1 Sample MR8965 144
4.5.3.2 Sample MR8951 146
4.5.3.3 Plagioclase separates 148
4.5.4 The dolerites of the Sao Sebastiao magma type 151
4.5.4.1 Sample MR8944 151
4.5.4.2 Sample MR8981 153
4.6 Summary of the new Ar—Ar data 154

Chapter 5 160
Geodynamic modelling of the Parana CFB magmatism 160
5.1 Introduction 160
5.2 The plume initiation model 162
5.3 Decompression melting during extension of the lithosphere 164
5.3.1 The volume of melt generated during continental extension 165
5.4 The timing of rifting and flood basalt magmatism in the South Atlantic 171
5.5 Melt generation during continental rifting in the South Atlantic 175
5.6 The major element geochemistry of decompression melts 177
5.6.1 Major element geochemistry of flood basalts 180
5.7 Geochemical evolution of the Parana magmatism 188
5.8 Conclusions 191

Chapter 6 193
Summary; flood basalt magmatism in the South Atlantic 193
6.1 The geochemistry of the Parana dolerites 193

6.2 Petrogenesis of the Parana dolerites 194
6.3 The age of the Parana-Etendeka CFB event 195
6.4 Melt generation and flood basalt magmatism in the South Atlantic 198

List of figures

Chapter 1

fig. 1.1 Map showing the distribution of Phanerozoic CFB provinces 2
fig. 1.2 Position of Africa with respect to South America and the Tristan da Cunha mantle plume at 130 Ma, and at the present day 3
fig. 1.3 εSr—εNd variation within flood basalts and oceanic basalts 6
fig. 1.4 Simplified geological map of southern Brazil 9
fig. 1.5 Predrift reconstruction of South America and Africa, to show the asymmetric distribution of the Parana Etendeka flood basalts 12
fig. 1.6 Three dimensional structure of the Parana lava field 13
fig. 1.7 Histogram showing the bimodal distribution of SiO2 contents in the Parana lavas 14
fig. 1.8 Geological map of the Etendeka volcanic province, Namibia 15
fig. 1.9 TiO_2/Zr—Zr/Y variation within the Parana basalts 18
fig. 1.10 Map showing the distribuition of the Parana basalt types, and the location of the boreholes 19
fig. 1.11 Schematic north—south section through the Parana lava field 20
fig. 1.12 Stratigraphical relationships between the Parana magma types 21
fig. 1.13 Map showing the distribution of the dykes associated with the Parana basalts 25

Chapter 2

fig. 2.1 Simplified geological map of the Ponta Grossa region of southern Brazil 29
fig. 2.2 Photomicrograph of sample MR-8988 30
fig. 2.3 Photomicrograph of sample MR-8932 31
fig. 2.4 Compositions of Fe—Ti oxides from the Ponta Grossa dolerites 32
fig. 2.5 Major element variation within the Ponta Grossa dolerites 35
fig. 2.6 Classification of the Ponta Grossa dolerites 36
fig. 2.7 CIPW normative compositions of the Ponta Grossa dolerites 37
fig. 2.8 Trace element variation within the Ponta Grossa dolerites 38
fig. 2.9 Rare earth element compositions of the Ponta Grossa dolerites 39
fig. 2.10 Incompatible trace element profiles of observed and modelled melts 49
fig. 2.11 Comparison of (a) major element, (b) trace element compositions of the Ponta Grossa dolerites with lavas from the northern Parana 52
fig. 2.12 Zr/Y—Sr variation within the Ponta Grossa dolerites and Parana basalts 53
fig. 2.13 Classification of the Ponta Grossa dolerites using discriminant function analysis 54

fig. 2.14 εSr—εNd variation within the Ponta Grossa dolerites 57
fig. 2.15 Variation in the isotope composition of Sr and Nd with MgO 58
fig. 2.16 Pb isotope compositions of the Ponta Grossa dolerites 59
fig. 2.17 Histogram to show Sr and Nd model age distributions of the Ponta Grossa dolerites 64
fig. 2.18 Comparison of the measured and time integrated Rb/Sr values of the Ponta Grossa dolerites 65

Chapter 3

fig. 3.1 Simplified geological map of Sao Paulo State 69
fig. 3.2 Zr/Nb—Ba/Y variation within the Sao Paulo dolerites and other basaltic rocks from the Parana province 70
fig. 3.3 Classification of the Sao Paulo dolerites using discriminant function analysis 71
fig. 3.4 Photomicrograph of sample MR-8950 72
fig. 3.5 Major element variation within the Paraiba dolerites 73
fig. 3.6 Trace element variation within the Paraiba dolerites 75
fig. 3.7 Rare earth element compositions of the Paraiba dolerites 76
fig. 3.8 Comparison of εSr and εNd values of the Paraiba dolerites and the Parana basalts 77
fig. 3.9 Variation of $^{87}Sr/^{86}Sr$ and $^{143}Nd/^{144}Nd$ with MgO in the Paraiba dolerites 78
fig. 3.10 Rb/Sr—$^{87}Sr/^{86}Sr$ variation within the Paraiba dolerites and the Urubici basalts 87
fig. 3.11 Photomicrograph of sample MR-8952 89
fig. 3.12 Photomicrograph of sample MR-8954 90
fig. 3.13 Major element variaiotn within the Ubatuba dolerites 92
fig. 3.14 Trace element variation within the Ubatuba dolerites 93
fig. 3.15 Rare earth element compositions of the Ubatuba dolerites 94
fig. 3.16 $^{206}Pb/^{204}Pb$ and $^{87}Sr/^{86}Sr$ values of the Ubatuba dolerites and plagioclase separates 95
fig. 3.17 Photomicrograph of sample MR-8981 100
fig. 3.18 Photomicrograph of sample MR-8944 101
fig. 3.19 Major element variation within samples of the Sao Sebastiao magma type 103
fig. 3.20 Trace element variation within samples of the Sao Sebastiao magma type 105
fig. 3.21 Rare earth element compositiosn of the Sao Sebastiao samples 106
fig. 3.22 Incompatible trace element profiles of representative samples of the Paraiba, Ubatuba and Sao Sebastiao magma types 107
fig. 3.23 Ce—Yb variation within the Sao Sebastiao samples 109

fig. 3.24 Sr and Nd isotope compositions of the Sao Sebastiao samples and oceanic basalts from the South Atlantic 112
fig. 3.25 Variation of the loss on ignition (at 1000°C) with MgO within the Sao Sebastiao samples 113
fig. 3.26 Variation of the percentage decrease in measured $^{87}Sr/^{86}Sr$ during leaching, with percentage weight loss on ignition at 1000°C 114
fig. 3.27 Pb isotope compositions of the Sao Sebastiao samples and South Atlantic basalts 115
fig. 3.28 Nd isotope evolution of basalts from the South Atlantic 117
fig. 3.29 Zr/Nb—Zr/Y variation within South Atlantic basalts and the Sao Sebastiao samples 119
fig. 3.30 Zr/Nb—Ba/Nb variation within South Atlantic basalts and the Sao Sebastiao samples 120
fig. 3.31 Variation in Ba/Nb with the degree of alteration of the Sao Sebastiao samples 121
fig. 3.32 Distribution of Mesozoic alkaline intrusive rocks in southern Brazil 122
fig. 3.33 Histogram to show age distribution of the intrusive alkaline rocks 123

Chapter 4

fig. 4.1 K—Ar ages of whole rock samples and plagioclase separates from rocks from the Parana province 128
fig. 4.2 K—Ar ages of intrusive and extrusive rocks from (a) north, (b) south of latitude 25°S 130
fig. 4.3 Inverse isochron analysis of Ar—Ar data 136
fig. 4.4 Argon isotope composition and age of sample MR-8917 138
fig. 4.5 Argon isotope composition and age of sample MR-8930 139
fig. 4.6 Argon isotope composition and age of sample MR-899 140
fig. 4.7 Argon isotope composition and age of sample MR-8928 141
fig. 4.8 Argon isotope composition and age of sample MR-8931 142
fig. 4.9 Argon isotope composition and age of sample MR-8950 143
fig. 4.10 Argon isotope composition and age of the groundmass material from sample MR-8965 145
fig. 4.11 Argon isotope composition and age of plagioclase crystals from sample MR-8965 146
fig. 4.12 Argon isotope composition and age of sample MR-8965 147
fig. 4.13 Argon isotope composition and age of sample MR-8951 148
fig. 4.14 Argon isotope composition and age of plagioclase crystals from sample MR-8954 149
fig. 4.15 Argon isotope composition and age of plagioclase crystals from sample MR-8957 149
fig. 4.16 Argon isotope composition and age of plagioclase crystals from

sample MR-8959 150
fig. 4.17 Argon isotope composition and age of biotite and kaersutite crystals with sample MR-8944 152
fig. 4.18 Argon isotope composition and apparent age of an amphibole xenocryst from sample MR-8981 153
fig. 4.19 Schematic north—south section through the lava pile, showing the relative stratigraphic positions of the dated samples 155
fig. 4.20 Variation in Ar—Ar age with relative stratigraphic position 156
fig. 4.21 Variation in Ar—Ar age with latitude and longitude for samples from the Ponta Grossa region, and Sao Paulo State 158

Chapter 5

fig. 5.1 Position of South America with respect to Africa and the Tristan da Cunha mantle plume at 180 Ma, and at the present time 161
fig. 5.2 Illustration of a thermally driven initiating mantle plume in glucose 163
fig. 5.3 Cooling paths followed by upwelling mantle at various mantle potential temperatures beneath a mid ocean ridge 165
fig. 5.4 Cooling paths followed by upwelling mantle beneath extending continental lithosphere 166
fig. 5.5 Variation in total melt thickness with extension factor β for various values of MBL thickness 168
fig. 5.6 Geothermal gradients, and solidus temperatures for hydrous and anhydrous peridotite 169
fig. 5.7 Cooling paths followed by mantle material during pure and simple shear of the continental lithosphere 171
fig. 5.8 Position of Africa with respect to South America at 106 Ma 172
fig. 5.9 Plate configuration in the South Atlantic at 132 Ma, showing inferred lava flow directions 174
fig. 5.10 Major element compositions of decompression melts generated at a midocean ridge, calculated using McKenzie and Bickle's (1988) parameterisation 178
fig. 5.11 Point and depth average melt compositions generated during extension of the continental lithosphere 180
fig. 5.12 Comparison of the major element compositions of flood basalts and decompression melts calculated using McKenzie and Bickle's (1988) parameterisation 182
fig. 5.13 Comparison of the major element compositions of Karoo picrites, South Atlantic basalts, and decompression melts 184
fig. 5.14 Comparison of the major element compositions of the Sao Sebastiao basanites with decompression melts calculated using McKenzie and Bickle's (1988) parameterisation 186

fig. 5.15 Variation in the fraction of the total melt volume derived from the MBL as a function of β 189

Chapter 6

fig. 6.1 South America and Africa at 150 Ma, showing present outcrop of the flood basalts 194
fig. 6.2 Schematic north—south section through the Parana lava field 197

Appendix

fig. A.1 Location of the samples collected from the Ponta Grossa region 217
fig. A.2 Location of the samples collected from Sao Paulo State 219

List of tables

Chapter 2

Table 2.1 Least squares modelling of the major element variation within the Ponta Grossa dolerites 44
Table 2.2 Bulk distribution coefficients used in trace element modelling, Stage 1 fractionation 46
Table 2.3 Bulk distribution coefficients used in trace element modelling, Stage 2 fractionation 48
Table 2.4 Pb isotope evolution of the source to the Ponta Grossa dolerites 62
Table 2.5 Sr and Nd model ages, measured and time integrated Rb/Sr and Sm/Nd values of the Ponta Grossa dolerites 66

Chapter 3

Table 3.1 Least squares modelling of the major element variation within the Paraiba dolerites 74
Table 3.2 Major element modelling of the AFC process 80
Table 3.3 Bulk distribution coefficients used in the AFC modelling, and calculated assimilant compositions 83
Table 3.4 Mean and standard deviation of the Paraiba dolerites and the Urubici basalts 86
Table 3.5 Least squares modelling of the major element variation within the Ubatuba dolerites 96
Table 3.6 Least squares modelling of the major element variation within the Ubatuba dolerites 97

Appendix

Table A.1 Whole rock geochemistry of the Parana dolerites 240
Table A.2 Representative mineral analyses from the Parana dolerites 244
Table A.3 Trace element data obtained by INAA 245

Table A.4 Geochemistry of the samples collected by A. C. Vasconcellos 246
Table A.5 Major and trace element compositions of the borehole samples 247
Table A.6 Sm, Nd, Rb and Sr concentrations by isotope dilution 248
Table A.7 Isotope compositions of the leached samples 248
Table A.8 Sr isotope composition of the leached sample MR-8967 248
Table A.9 Argon isotope data for the samples dated by the Ar—Ar method 256

Chapter 1

Introduction; the Parana-Etendeka flood basalt province

1.1 Physical characteristics of continental flood basalt magmatism

Continental flood basalt (CFB) eruptions are major igneous events, in which very large volumes (typically between 1 and 2 x 10^6 km^3) of dominantly tholeiitic basalt of relatively uniform composition are erupted from fissures over large areas of the continents. Although flood basalt eruption is not occurring at the present, at least fifteen CFB events can be recognised in the geological record, and examples are known from all periods of Earth's history, from the Archaean to the Tertiary (see fig. 1.1). These are therefore significant crust-forming events, and although flood basalts are generally erupted with little pyroclastic activity, the accompanying ejection of gases and aerosols may have important ecological consequences (Officer and Drake, 1985; Rampino and Stothers, 1988).

A characteristic feature of flood basalt magmatism is the rapidity with which the lavas were erupted. For example, the age of the Deccan flood basalt lava field, which originally covered an area of over 1.25 x 10^6 km^2 in southern India (Devey and Stephens, 1991), is relatively well-constrained by Ar—Ar dating to lie between 66.6 and 68.5 Ma (Courtillot et al., 1988; Duncan and Pyle, 1988). This implies that the bulk of the magma was erupted at a rate of about 1.5 km^3/y (Richards et al., 1989). Thompson (1977) has shown that average magma production rates for the Columbia River CFB province of the western USA were similar to those of comparable length segments of the mid-ocean ridge system, and the eruption rates of individual flows (some of which have volumes of over 700 km^3) may have been several times greater than even the fastest-spreading sections of mid-ocean ridge (Swanson et al., 1975).

The geodynamic significance of flood basalt volcanism is currently attracting much debate. Morgan (1981) first drew attention to the close association in space and time between CFB magmatism, continental rifting, and mantle plume activity. Most flood basalts are located on passive continental margins, and appear to have been erupted at the time of continental separation. Plate reconstructions indicate that a currently active hotspot lay close

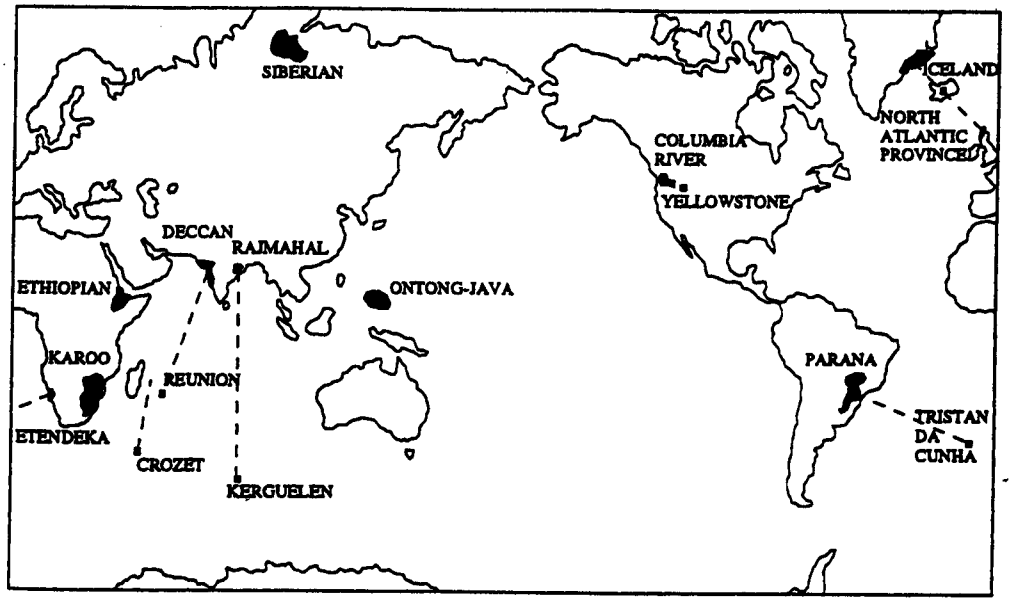

Fig. 1.1
Distribution of the Phanerozoic CFB provinces and associated mantle plumes.

to each CFB province at the time of magmatism. In the case of the Parana-Etendeka flood basalt event, the magmatism occurred at the time of rifting of Africa from South America, and the volcanics are preserved on both continental margins of the South Atlantic (fig. 1.2). Plate reconstructions place the mantle plume that is presently beneath the South Atlantic island of Tristan da Cunha, in the region of the Parana at that time (Duncan, 1984). Several recent papers have attempted to explain the relationship between these phenomena (Richards et al., 1988; White and McKenzie, 1989; and see Chapter 5), however, the processes by which such enormous volumes of magma can be produced in such a short period of time are not well understood.

This thesis presents the results of a geochemical and Ar—Ar dating study of the intrusive rocks associated with the Parana-Etendeka flood basalt province of South America and Africa. The aims of this research were firstly; to constrain the geochemical and mineralogical variation within the dykes associated with this flood basalt event, and to investigate the petrogenesis of the various dolerite magma types; secondly, to date precisely the age of the magmatism, using the Ar—Ar method; and to use these data to constrain

possible geodynamic models for the origin of the Parana-Etendeka CFB province. The intrusive rocks are particularly important in this respect, because they are more closely related to the processes of continental rifting in the South Atlantic (section 1.5).

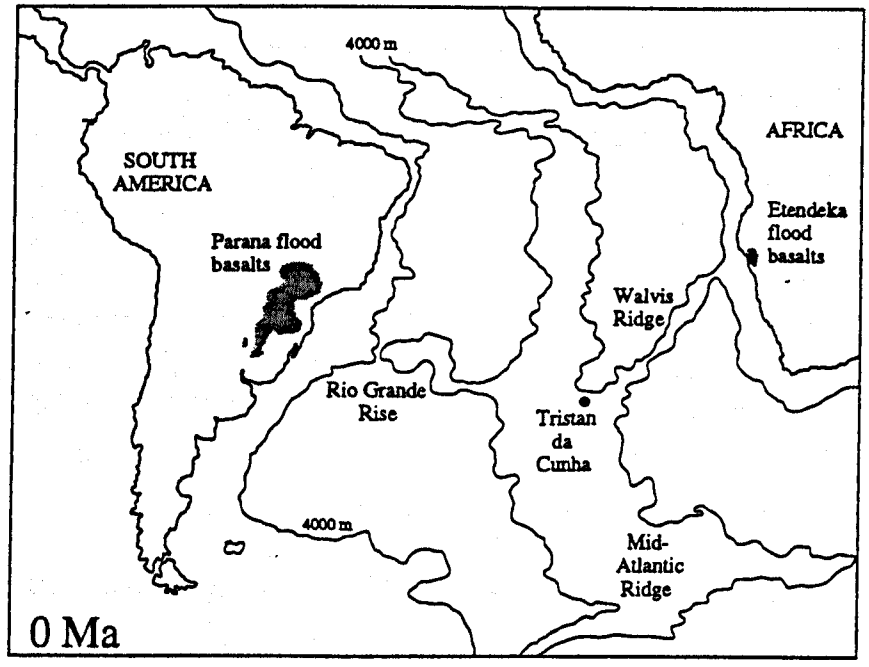

Fig. 1.2
South Atlantic bathymetry, and location of the Tristan da Cunha mantle plume relative to the Parana Etendeka flood basalts. Note positions of the Walvis Ridge and the Rio Grande Rise, which suggest that the Tristan plume lay in the region of the Parana Etendeka Province prior to continental breakup.

1.2 Geochemical characteristics of CFB magmatism

1.2.1 . The major element geochemistry of CFB

The lavas of CFB provinces are dominated by tholeiitic basalts which have $Mg:Fe^{2+}$ ratios which are too low for them to represent primary magmas that have been in equilibrium with olivine compositions that are typical of the upper mantle as inferred from mantle xenoliths (Roeder and Emslie, 1970; Gurney and Harte, 1980; Cox, 1980; Harte, 1983). Wilkinson and Binns (1977) argued that CFB represent partial melts of an Fe-rich mantle source, but xenoliths of such material are rare, and thought to be unrepresentative of the upper mantle. Many CFB lavas have major element compositions which plot close to the experimentally-determined low pressure olivine-clinopyroxene-plagioclase-liquid cotectic (Thompson et al., 1983). It is therefore generally accepted that CFB have undergone extensive low-pressure fractionation before eruption, and are descended from primary

magmas of picritic composition (Cox, 1980; Thompson et al., 1983). This idea is supported by the fact that small volumes of picrite have been recorded from several flood basalt provinces, including the Karoo (Cox and Jamieson, 1974), the Deccan (Krishnamurthy and Cox, 1977), the North Atlantic Province (Clarke, 1970), the Siberian Traps (Basaltic Volcanism Study Project, 1981), though not as yet from the Parana. The $Mg:Fe^{2+}$ ratios of many of these picrites are high enough for them to have been melts in equilibrium with mantle compositions, and Thompson (1974) demonstrated that one such rock from the North Atlantic Province is in experimental equilibrium with olivine, orthopyroxene and clinopyroxene at 16.5 kb.

Thompson et al. (1983) pointed out that many of the high $Mg:Fe^{2+}$ lavas from the Karoo and Deccan are too SiO_2-saturated to be melts of an anhydrous mantle, but could represent partial melts of hydrous lherzolite, at pressures of around 25 kb. Hergt et al. (1991) and Hawkesworth et al. (1992) have argued that the major element chemistry of many of the Gondwana CFB requires them to have been derived from a source which is both hydrous, and depleted in the major elements Ca, Al, Ti, Na and P, relative to the source of oceanic basalts. Fertile mantle can accommodate up to 0.4% water in the form of amphibole produced by the hydration of clinopyroxene (Olafsson and Eggler, 1983), and melts of hydrous peridotite are silica saturated, at least at higher degrees of melting (Kushiro, 1990). However, the subcontinental lithospheric mantle, which is considered to play an important part in the generation of CFB (section 1.2.2), is relatively depleted in the major element constituents of basalt, such as Ca, Al, Ti and P (Hawkesworth et al., 1990), and is likely to contain less than 10% amphibole. Melts of such depleted material are dominated by the orthopyroxene component, and will be silica saturated. This effect is enhanced in the presence of water, because orthopyroxene then melts incongruently to yield olivine and a silica-rich melt (Kushiro et al., 1968).

A characteristic feature of flood basalts is their relatively restricted range in major element chemistry, and Cox (1980) has shown that the major element variations of many flood basalt suites are consistent with their having undergone extensive low pressure (0—15 kb) crystal fractionation of a mineral assemblage of olivine, clinopyroxene and plagioclase, prior to eruption. This process has the effect of buffering the concentration of major

elements such as SiO_2 and Al_2O_3 in the residual melt. If flood basalts are descended from primary liquids of picritic composition, then the volume of cumulate material that is required to have fractionated is of the order of the total volume of magma erupted at the surface (Cox, 1980).

1.2.2 Trace element and isotope geochemistry, and the nature of the mantle source

In contrast to their relatively uniform major element compositions, the trace element and Sr, Nd and Pb isotope geochemistry of continental flood basalts are very variable, both within and between different provinces. Most CFB have relatively low concentrations of the compatible trace elements such as Ni and Cr, which is further evidence for their having undergone extensive low-pressure fractionation. Typically, flood basalts are enriched in the more incompatible elements, and have high concentrations of the large-ion lithophile elements Rb, K, Th, U, Ba relative to the high field strength elements Nb, Ta, Zr, P, compared with oceanic basalts. Many exhibit positive εSr and negative εNd values (fig. 1.3), which means that they include a contribution from a source with time-integrated high Rb/Sr and low Sm/Nd relative to both the bulk earth, and the source of most oceanic basalts.

The high Rb/Sr and low Sm/Nd of average continental crust has, with time, generated variable, high $^{87}Sr/^{86}Sr$ and low $^{143}Nd/^{144}Nd$, and many early studies of CFB assumed that their geochemical characteristics were the result of crustal contamination of mantle-derived magmas (Carter et al., 1978; Thompson et al., 1984). However, recent studies of xenoliths (Menzies and Murthy, 1980; Erlank et al., 1987; Hawkesworth et al., 1990) and inclusions in diamonds (Richardson et al., 1984), have revealed that parts of the subcontinental lithospheric mantle, which is isolated from the convection system of the deeper mantle, has high Rb/Sr, low Sm/Nd, and $^{87}Sr/^{86}Sr$ and $^{143}Nd/^{144}Nd$ ratios that are similar to those previously regarded as typical of the continental crust. The 'enriched' component of CFB may therefore have been derived either from the crust, or from the mantle lithosphere. Bowen (1928) and DePaolo (1981) have demonstrated that because magmas are rarely superheated, assimilation of significant amounts of crustal material can only occur when accompanied by fractional crystallisation. Many of the Parana flood basalts

show no evidence for having undergone assimilation-fractional crystallisation, and of those that do, the inferred isotopic composition of the parental magma is enriched relative to the bulk earth (e.g. Mantovani and Hawkesworth, 1990). The distinctive trace element and radiogenic isotopic composition of CFB therefore appears to be a feature that was inherited from the mantle source of these basalts.

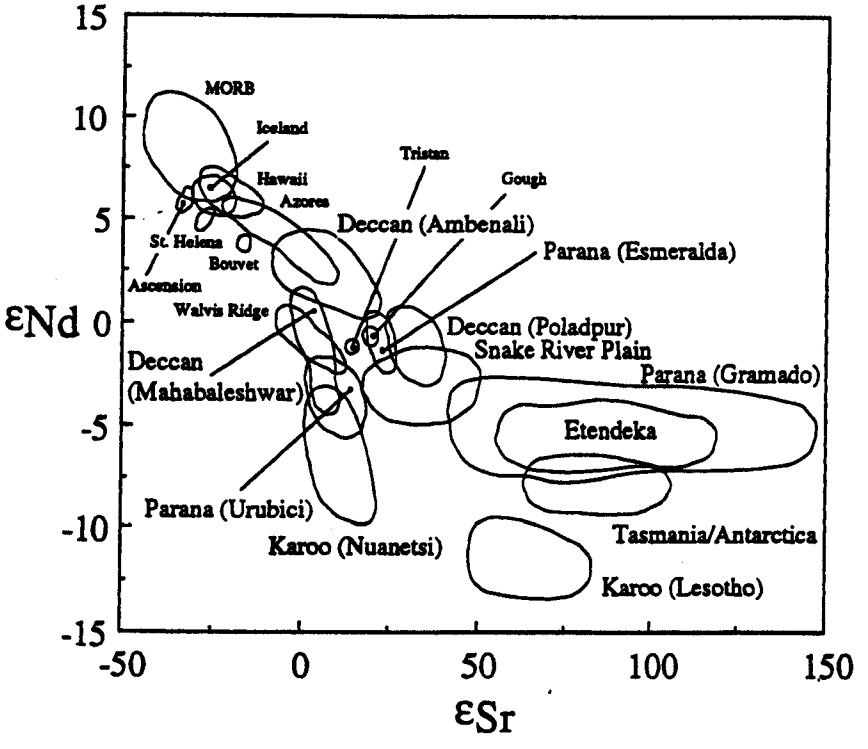

Fig. 1.3
Sr and Nd isotope compositions of selected CFB (in bold type) and oceanic basalts. Data from Lightfoot (1985), Peate (1989), Hawkesworth et al. (1986 and 1988), Cox (1988), Hergt et al. (1991), le Roex et al. (1990), Dupre and Allegre (1983), Erlank et al. (1984).

Although most geochemists now agree that the trace element and isotopic geochemical characteristics of CFB are derived from the subcontinental lithospheric mantle (SCLM), the processes by which the SCLM contributes to CFB magmatism are much less well understood.

1.3 Geodynamic origins of CFB magmatism

Any hypothesis which attempts to account for the origin of CFB provinces must be able to explain firstly, the large volume and rapid eruption rate of flood basalts and

secondly, the close association in space and time between CFB magmatism, continental rifting and mantle plumes.

Morgan (1981) noted that many CFB provinces appear to represent the earliest surface manifestations of currently active mantle plumes, which led Richards et al. (1989) to propose that CFB are erupted as a result of the initiation of a mantle plume from the lower mantle. Scaled fluid dynamic experiments (Whitehead and Luther, 1975; Griffiths and Campbell, 1990) predict that an initiating plume from the deeper mantle will ascend as a large spherical vortex approximately 1000 km in diameter, followed by a narrow feeder conduit. Melt is generated within the plume vortex by decompression melting, and Campbell and Griffiths (1990) have estimated that melt volumes of the order of 10^7 km^3 may be produced in this way. The density anomaly introduced into the upper mantle results in up to 1 km of surface uplift immediately above the plume axis, and the stresses induced in the lithosphere as a result of this uplift are sufficient to cause continental rifting (Griffiths and Campbell, 1991; Houseman and England, 1986).

One consequence of the plume initiation model is that flood basalts should also occur in the ocean basins. Large accumulations of basalt, of comparable volume to CFB have in fact been found in both the Indian and Pacific Oceans (the Kerguelen and Ontong-Java plateaus), and the Wrangellia terrain of western North America may represent an accreted oceanic flood basalt province (Richards et al., 1991). The Ontong-Java plateau (fig. 1.1) has a volume in excess of 20×10^6 km^3, and appears to have been erupted at a rate of between 8 and 22 km^3/yr (Tarduno et al., 1991).

The plume initiation model can account for many of the physical characteristics of flood basalt magmatism. However, the model predicts that most of the melt that is erupted at the surface is derived from the abnormally hot upper mantle immediately below the SCLM (Campbell and Griffiths, 1990). This is at odds with the geochemical characteristics of CFB magmatism discussed in section 1.2, which implies that a large proportion of the melt is derived from the subcontinental mantle lithosphere.

White and McKenzie (1989) investigated the consequences of continental rifting above upper mantle at the elevated temperatures associated with an existing mantle plume. They showed that melt thicknesses of approximately 17 km can be produced from the

uppermost mantle as a result of decompression melting during continental breakup above mantle at a potential temperature of 1480°C. In this model, it is the rifting process that is the driving force for melt production, and therefore the magmatism cannot precede the main rifting event. Arndt and Christensen (1992) assumed that the SCLM is anhydrous, and showed that less than 4% of the total melt volume can be produced from it during extension and adiabatic decompression. They therefore concluded that the trace element and isotope budgets of CFB are derived from the SCLM as a result of complex reaction and melt percolation processes. However, Gallagher and Hawkesworth (1992) have shown that if the lithospheric mantle can accommodate up to 0.4% water in the form of amphibole or phlogopite, then considerable volumes of melt can be generated from it at the relatively low temperatures of the hydrous peridotite solidus during continental extension.

These models are discussed more quantitatively in Chapter 5, and the new geochemical data for the Parana dolerites presented in Chapters 2, 3 and 4 are used to investigate which of these models can best explain the physical and chemical characteristics of the Parana magmatism.

1.4 The Parana-Etendeka CFB province

1.4.1 Regional geology of southeastern Brazil

The South American Platform of southeastern Brazil, upon which the sediments and associated volcanics of the Parana Basin were deposited, consists of fault bounded units of metasedimentary and metavolcanic material of Mid to Late Proterozoic age, which were subjected to deformation and metamorphism during the 500—650 Ma Brasiliano Orogeny. These surround cratonic blocks of Archaean and Mid Proterozoic age, which remained largely unaffected by the events of the Brasiliano Orogeny (fig. 1.4).

Remnants of the Amazon Craton are exposed to the NW of the Parana Basin, and consist mainly of a suite of granites, granodiorites, tonalite gneisses and quartzites and amphibolites of mid to high metamorphic grade. These have yielded Rb—Sr ages of 1680 ± 80 Ma and are intruded by late- and post-tectonic granites, associated with volcanic rocks which have been dated at between 1650 and 1600 Ma (Araujo et al., 1982). The southern part of the Parana Basin is underlain by rocks of the Curitiba Massif, which are in thrust

contact with the Luis Alves Craton to the SE, and comprise high grade metamorphic units, including granulitic charnockites, amphibolites and granitoids (Girardi, 1976; Kaul, 1979; Kaul and Teixeira, 1982). Locally, these are covered by volcanic and sedimentary rocks, and intruded by granitoids. The granulites have yielded Rb—Sr ages of 1.8 to 2.7 Ga; the gneisses and migmatites have been dated at 650 Ma (Girardi et al., 1974; Kaul and Teixeira, 1982). The Lui Alves Craton is dominated by calkalkaline granitoids and granulites of Archaean age, which underwent high grade metamorphism in the Early Proterozoic (Basei, 1985; Mantovani et al., 1987).

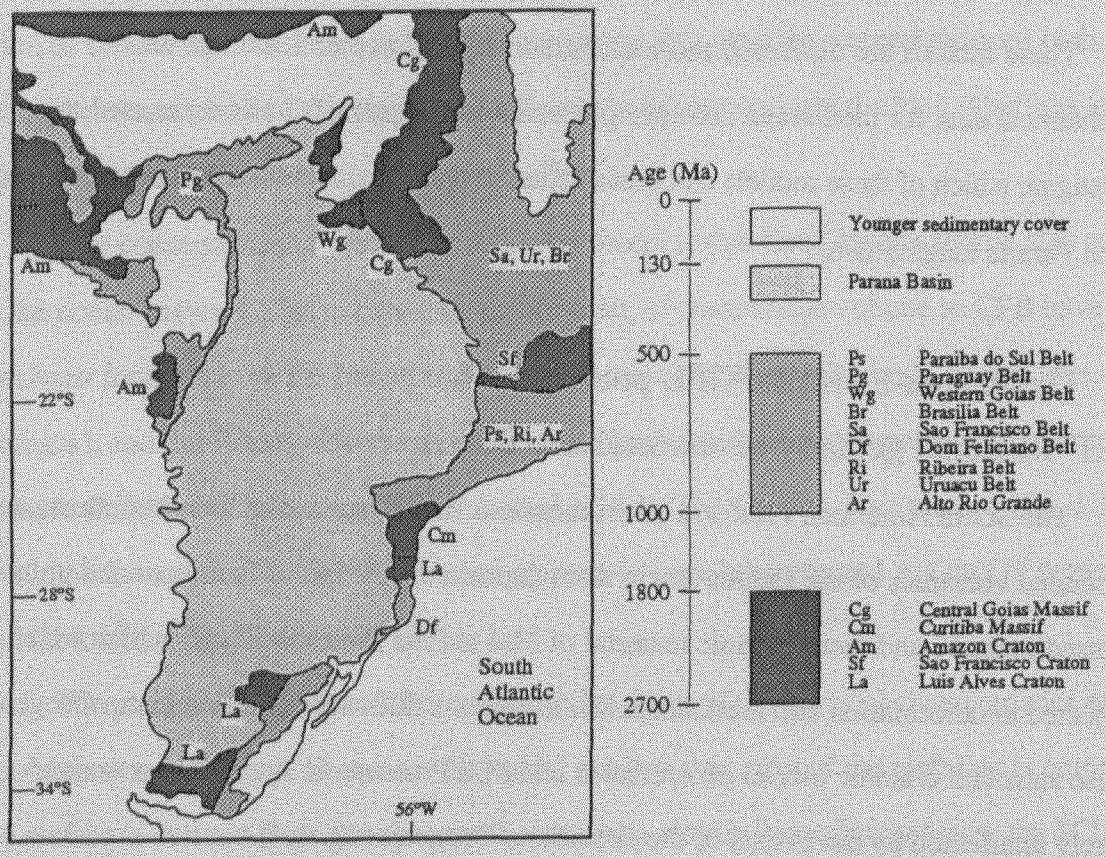

Fig. 1.4
Simplified geological map of southern Brazil (adapted from Mantovani et al., 1991).

In the region of the Parana basin, rocks of Proterozoic age outcrop in four main belts. The Paraguay Belt consists of a sequence of clastic sediments and minor carbonates, which on the basis of palaeontological evidence is thought to have been deposited in the Late Proterozoic or Early Cambrian (Fairchild, 1984). These were metamorphosed to incipient and medium grade at 480—550 Ma, and were intruded by late- to post-tectonic granites which yield ages of between 480 and 500 Ma. The Western Goias Belt, which is thought to underlie much of the Parana Basin, consists largely of a sequence of volcanic and sedimentary rocks of low to medium metamorphic grade, intruded by calcalkaline granitoids which have been dated at between 550 and 650 Ma. The Ribeira Belt consists of continental and shallow-marine metasediments, including carbonates and stromatolites (Scholl et al., 1980; Lopes, 1981; Biondi, 1983), which are interbedded with andesitic and rhyolitic metavolcanics of Mid and Late Proterozoic age, and have suffered low to medium grade regional metamorphism. Granitoids were intruded at various stages in the evolution of this belt, and yield ages of 580 to 650 Ma. The Dom Feliciano Belt consists of three thrust-bounded units (Basei, 1985). To the south, highly deformed granitoids and migmatites (U—Pb age of 624 ± 16 Ma (Basei, 1985)), were intruded by quartz-monzonitic granitoids at 520 to 600 Ma. The central unit consists of a series of metasediments and metavolcanics of low to medium grade which yield Rb—Sr and K—Ar metamorphic ages in the range 600 to 800 Ma, and which are intruded by porphyritic biotite granites and quartz-monzonites. The northernmost unit, which is in thrust contact with the Luis Alves Craton, consists of a sequence of clastic sediments with occasional rhyolite and tuff bands. These have been dated at 570 ± 20 Ma, and were metamorphosed to incipient metamorphic grade at between 500 and 550 Ma (Macedo et al., 1984; Basei, 1985; Basei et al., 1987), and the intrusive Subida Granite has yielded a Rb—Sr isochron age of 546 ± 10 Ma (Basei, 1985).

In summary, the basement rocks of this region of southern Brazil comprise a complex of high-grade Archaean gneisses and granitoids, together with supracrustal rocks of Proterozoic age which were deformed, metamorphosed and intruded by granitoids during the Brasiliano Orogeny at 500—650 Ma. Following the events of the Brasiliano Orogeny, the intracratonic Parana Basin was established in the Late Ordovician, and sedimentation continued until the Late Jurassic. The pattern of sedimentation was strongly controlled by

the structures of the basement; the earliest sediments are largely marine, but the Early Cretaceous Parana flood volcanics were erupted subaerially onto the aeolian sandstones of the late Jurassic Botucatu Formation, with which the lowermost flows of the lava pile are interbedded.

1.4.2 The flood basalt magmatism

The Parana-Etendeka CFB province is one of the largest preserved flood basalt provinces. In South America, the main lava field covers an area estimated to be in excess of 1.2×10^6 km^2 (Maack, 1952), in southern Brazil, Paraguay, Uruguay and northern Argentina (fig. 1.5). The lavas have yielded K—Ar ages of between 120 and 140 Ma (see Chapter 4 for a detailed discussion of the published age data), and the presence of several small basalt outliers lying on Jurassic sediments in Mato Grosso State close to the Brazilian-Bolivian border, suggests that a considerable area of the lava field has been removed by erosion since the Early Cretaceous. Schobbenhaus et al. (1984) recorded a 310 m thick outcrop of basalt, covering an area of approximately 3900 km^2, about 150 km to the north of Cuiaba (fig. 1.5). These rocks have yielded K—Ar ages in the range 112—126 Ma, similar to ages obtained from the central Parana. To the northwest, close to Vilhena in Rondonia State, basaltic lavas outcrop over an area of approximately 4400 km^2, and have apparent K—Ar ages of between 140 and 210 Ma. The main lava field may therefore have originally extended over 900 km to the northwest of its present limit.

In addition, the volume of basalt which exists to the south in northern Argentina is not well known, due to an extensive Quaternary alluvial sedimentary cover. Leinz et al. (1968) report that a 1 km thickness of lava was encountered in a borehole at Nogoya, to the northwest of Buenos Aires. Zambrano and Urien (1974) recorded pre-Middle Cretaceous basalt from a well near Samborombon Bay on the River Plate, some 200 km southeast of Buenos Aires. They assumed these basalts to be of Parana age, although seismic data suggests that these basalts are restricted to the Saledo Basin, and are isolated from the main Parana lava field. However, Emery and Uchapi (1984) state that the Parana lavas extend through the Saledo Basin to the south of Buenos Aires, and as far south as the Cuyo Basin, which lies about 750 km west of Buenos Aires. Unfortunately, there are no K—Ar data for

either of these basalt occurences, which could shed light on their relationship to the main Parana lava field.

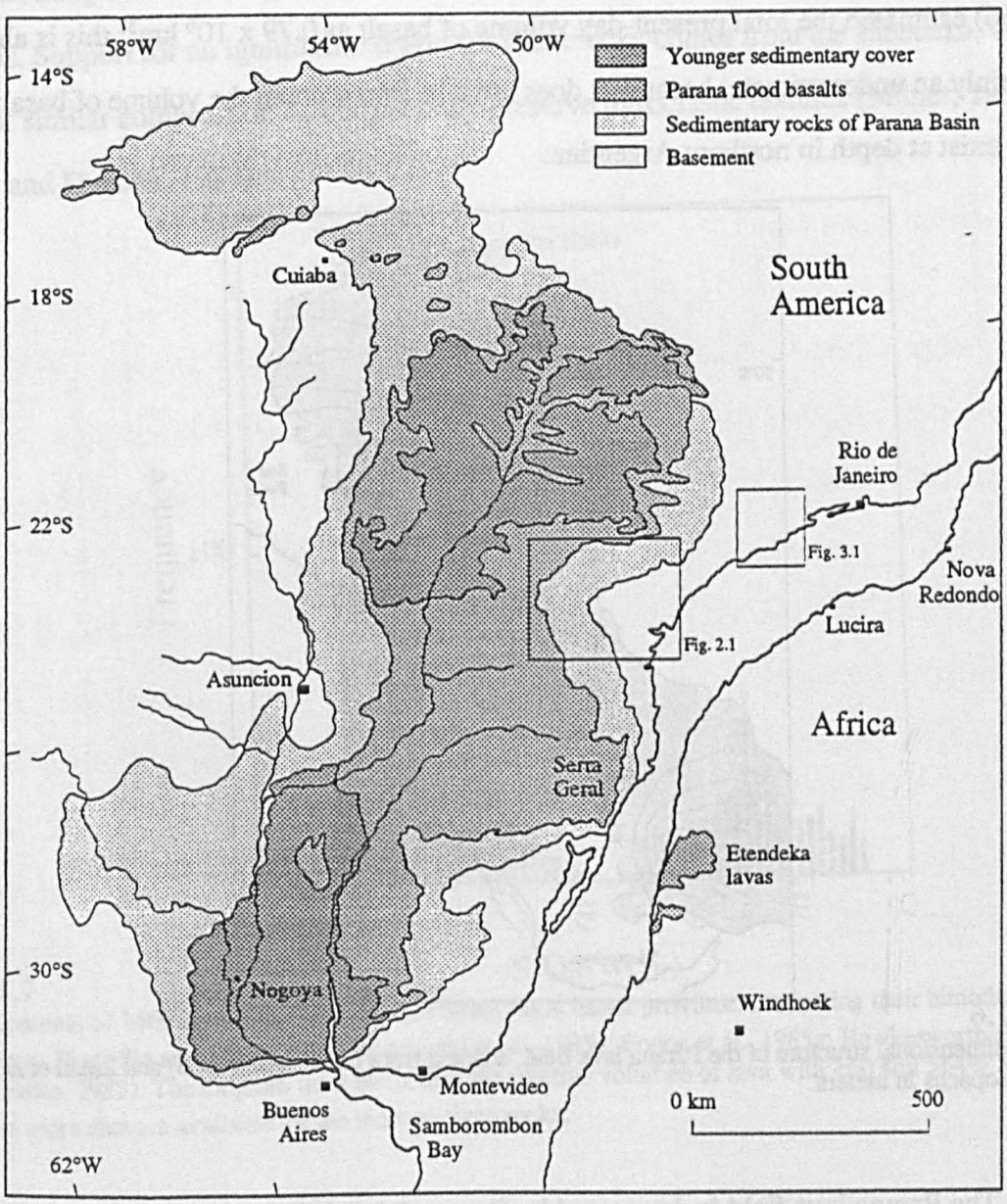

Fig. 1.5
Approximate position of Africa with respect to South America at 150 Ma, and the present day distribution of the Parana Etendeka flood basalts. The locations of Fig. 2.1 and Fig. 3.1 are also shown.

The 3-dimensional structure of the lava pile is known in some detail from exploratory borehole data (Zalan et al., 1987). The thickest preserved accumulation of lavas is in the northern part of the Parana province, and Peate et al. (1988) reported a 1723 m thickness of basalt in the CB borehole in Parana state. The axis of maximum lava thickness extends southwards parallel to the direction of elongation of the Parana basin (fig. 1.6). Leinz et al. (1966) estimated the total present-day volume of basalt as 0.79 x 10^6 km^3; this is almost certainly an underestimate, because it does not take into account the volume of basalt that may exist at depth in northern Argentina.

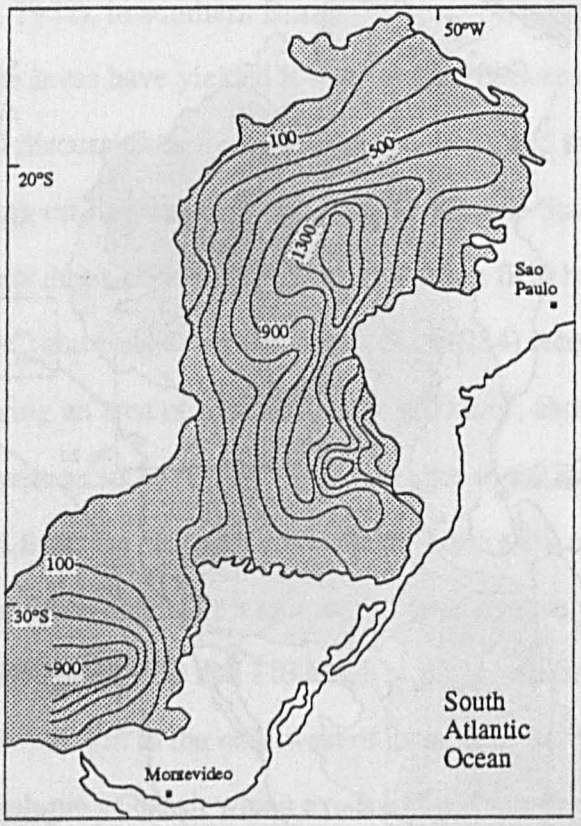

Fig. 1.6
Three dimensional structure of the Parana lava field, adapted from Leinz et al. (1968) and Zalan et al. (1987). Lava isopachs in meters.

The Parana lava field is dominated by flows of tholeiitic 'basalt' (containing 49—59% SiO_2), but the SiO_2 content of the volcanics is markedly bimodal (fig. 1.7), and significant quantities of more evolved lavas (rhyolites and rhyodacites) occur in the uppermost parts of the lava pile (Leinz, 1949; Bellieni et al., 1984). These more evolved rocks outcrop over an area of approximately 0.15 x 10^6 km^3 (Marimon et al., 1983), and are concentrated towards the continental margin of Brazil, particularly in the southeast, where they reach a thickness of 400 m. Bellieni et al. (1986) drew attention to the lateral persistence of these evolved

lavas; individual units can be traced for over 60 km. The eruption temperatures (1000—1150°C) calculated from pyroxene geothermometry are unusually high for rhyolitic lavas, and Bellieni et al. (1986) therefore concluded that these rocks are ignimbrites, rather than lava flows. They explained the observed lack of pyroclastic textures as being a result of strong welding due to the high eruption temperatures and low volatile contents of the magmas. Support for an ignimbritic origin for these rocks comes from the Etendeka, where rocks of similar composition do occasionally preserve pyroclastic textures (Milner, 1986; Milner and Duncan, 1987).

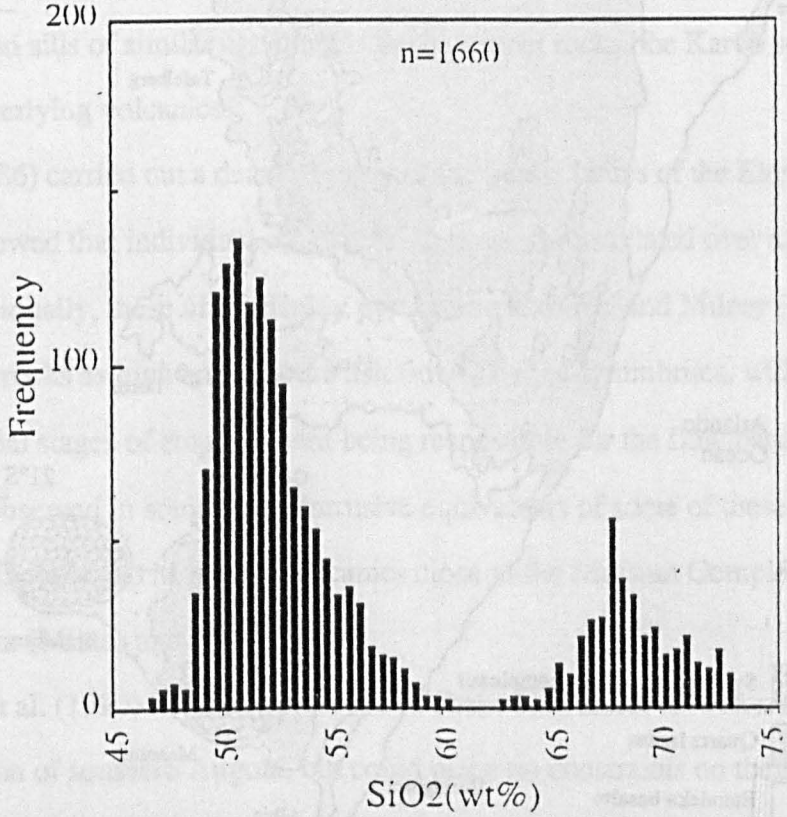

Fig. 1.7
SiO_2 contents of 1660 lava samples from the Parana flood basalt province, illustrating their bimodal nature (data from Piccirillo and Melfi, 1988; Mantovani et al., 1985a; Fodor et al., 1985a; Hawkesworth et al., 1988; Peate, 1989). The diagram does not reflect the relative volumes of lava with <60 and >64% SiO_2, because more data are available for the more evolved rocks.

The Etendeka volcanic rocks of northern Namibia lay adjacent to the Parana lavas at 130 Ma, prior to the opening of the South Atlantic (fig. 1.5). An early K—Ar dating study by Siedner and Miller (1968) revealed that these volcanics are of early Cretaceous age, and are therefore related to the Parana flood basalt province, rather than to the Karoo flood province of southern Africa. Recent geochemical studies (Erlank et al., 1984; Peate, 1989) have shown that the volcanics rocks of the two provinces are also very similar in terms of their geochemistry. The Parana and Etendeka volcanics are therefore generally accepted to be

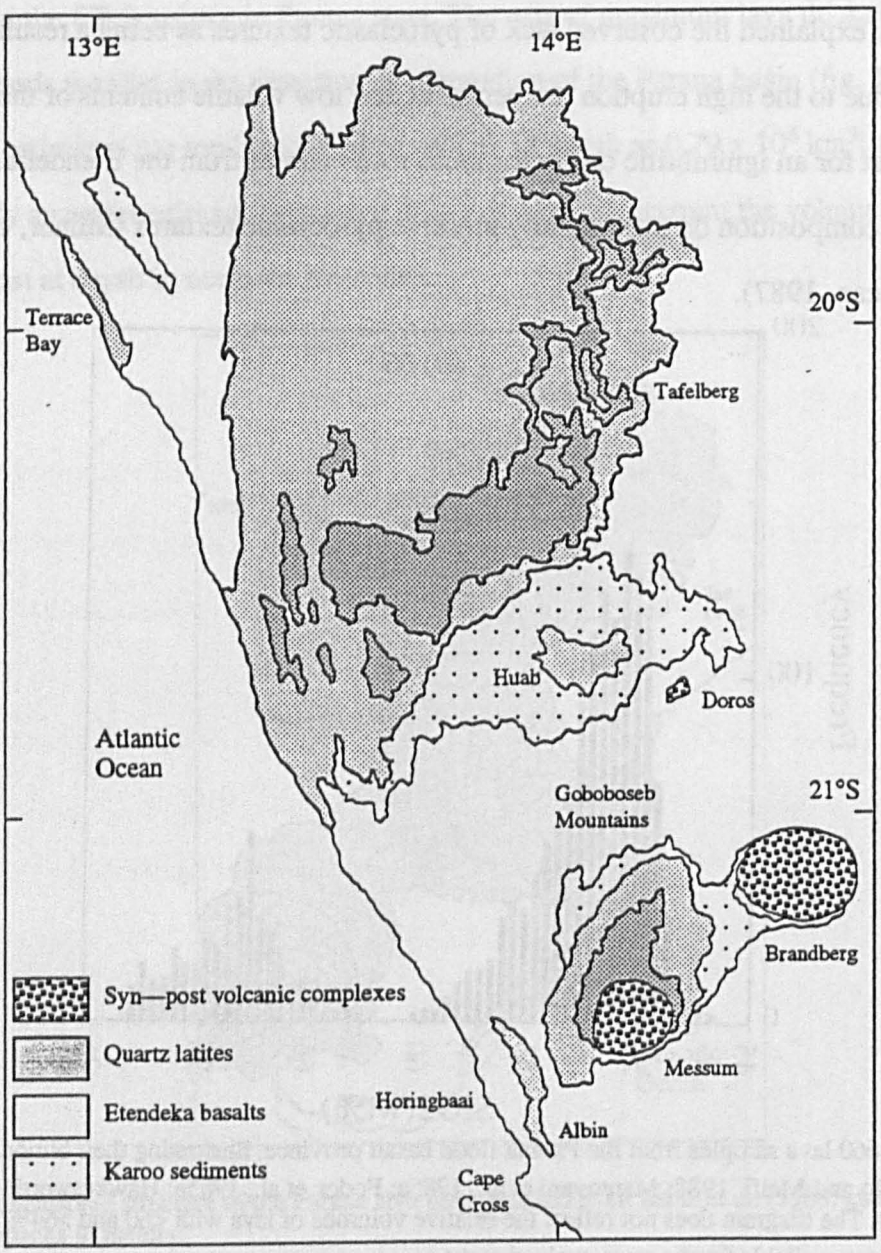

Fig. 1.8
Geological map of the Etendeka volcanic province, Namibia, showing the distribution of volcanic rocks and related intrusive complexes (from Milner et al., 1992).

part of the same igneous event, the Etendeka volcanics having become stranded on the African plate as a result of the development of the South Atlantic Ocean in the Early Cretaceous. K—Ar dating of the Etendeka volcanics has yielded ages of between 115 and 145 Ma (Siedner and Mitchell, 1976; Erlank et al., 1984). However, much of this age range

is likely to be a result of the loss or gain of radiogenic argon, and the significance of the published age data is discussed in detail in Chapter 4.

The Etendeka volcanics form the uppermost unit of the Karoo sequence in Namibia. The basalts conformably overlie the laterally impersistent deposits of the Karoo sedimentary sequence, and frequently overstep the latter to lie directly on the pre-Karoo basement of Pan-African (Damara) and mid- to early-Proterzoic age. The Etendeka volcanics consist of a series of interbedded basalts, quartz latites and rare intermediate rocks, which today cover an area of about 78,000 km^2, and reach a maximum observed thickness of 880 m at Tafelberg. Basaltic dykes and sills of similar age intrude the basement rocks, the Karoo sedimentary strata, and the overlying volcanics.

Milner (1986) carried out a detailed study of the quartz latites of the Etendeka province, and showed that individual eruptive units could be correlated over areas as great as 8800 km^2. Occasionally, these units display pyroclastic textures, and Milner (1986) interpreted these rocks as high temperature ash flows or rheo-ignimbrites, with viscous flowage in the final stages of emplacement being responsible for the flow banding and autobrecciation observed in some units. Intrusive equivalents of some of these quartz latite units intrude the Goboboseb Mountain volcanics close to the Messum Complex of the southern Etendeka (Milner and Ewart, 1987).

Piccirillo et al. (1990) noted the presence of sheet-like, acidic lava flows in the Mocamedes region of southern Angola, but could place no constraints on their age. Torquato and Amaral (1973) dated tholeiitic basalts from near Novo Redondo and Lucira in southern Angola by the K—Ar method, and obtained ages of 114—140 Ma. These volcanics therefore appear to be related to the Parana-Etendeka event; plate reconstructions place them at the latitude of Rio de Janeiro prior to continental rifting (fig. 1.5).

1.4.3 Geochemistry and stratigraphy of the flood basalts

1.4.3.1 Classification of magma types

Recent geochemical studies of the lavas from other CFB provinces, notably the Deccan and Columbia River provinces, has revealed that analyses of individual flows tend to cluster into groups on variation diagrams (Cox and Hawkesworth, 1985; Swanson et al.,

1979). Packets of flows belonging to a particular goup, or magma type, tend to behave as relatively coherent stratigraphic units, and allow the subdivision of the monotonous piles of very similar-looking lava flows that are characteristic of flood basalt provinces. This stratigraphical approach has proved valuable in the subdivision of the Deccan (Cox and Hawkesworth, 1985; Beane et al., 1986; Devey and Lightfoot, 1986) and Columbia River CFB (Swanson et al., 1979; Mangan et al., 1986), and such studies are important because they can reveal the internal structure and sequential development of the lava pile, and how magmatic sources and processes have varied in response to the changing tectonic conditions during eruption.

Preliminary geochemical studies of the Parana lavas were carried out by Bellieni et al. (1984) and Mantovani et al. (1985), and revealed significant and systematic variations in the geochemistry of the Parana volcanics, according to their geographical location. Bellieni et al. (1984) subdivided the basalts into a northern, high-Ti group, and a southern, low-Ti group. Subsequent work by Fodor et al. (1985a), Petrini et al. (1987) and Piccirillo et al. (1988a) revealed that the situation is more complex, and that several distinct geochemical types of basalt are present. Peate et al. (1992) reviewed the existing database for Parana lavas (over 2000 major and trace element analyses), and found that over 90% of the basalt samples could be classified in a scheme involving only 6 magma types, which they termed the Gramado, Urubici, Esmeralda, Ribeira, Pitanga and Paranapanema magma types (fig. 1.9). A discussion of the geochemical criteria upon which this classification is based is presented in Peate et al. (1992).

Unfortunately, many of the early geochemical studies of the Parana lavas were carried out with little regard to the stratigraphic relationships between the different sampling sites. In addition, the thick vegetation, the lack of incised river systems or significant topographic relief, and the younger sedimentary cover in the northern Parana and in Argentina, combine to limit sampling to scattered outcrops over most of the province (fig. 1.10), with the result that the stratigraphic relationships between these magma types is not well known. Only in the Serra do Mar escarpment in the southeastern part of the province, are continuous sections of up to 800 m through the lava sequence exposed, and the geochemical

stratigraphy of the basalts in this part of the Parana has therefore been extensively investigated (Bellieni et al., 1986b; Mantovani et al., 1985a; Hawkesworth et al., 1988; and Fodor et al., 1985a). In 1988, Peate and coworkers began a detailed geochemical study of drill chippings recovered from exploratory boreholes drilled through the lava pile. This approach has yielded valuable new insight into the geochemical stratigraphy of the lava pile, particularly in the northern part of the province, where the three-dimensional geochemical variation of the lavas was previously poorly known (Peate et al., 1988, 1992).

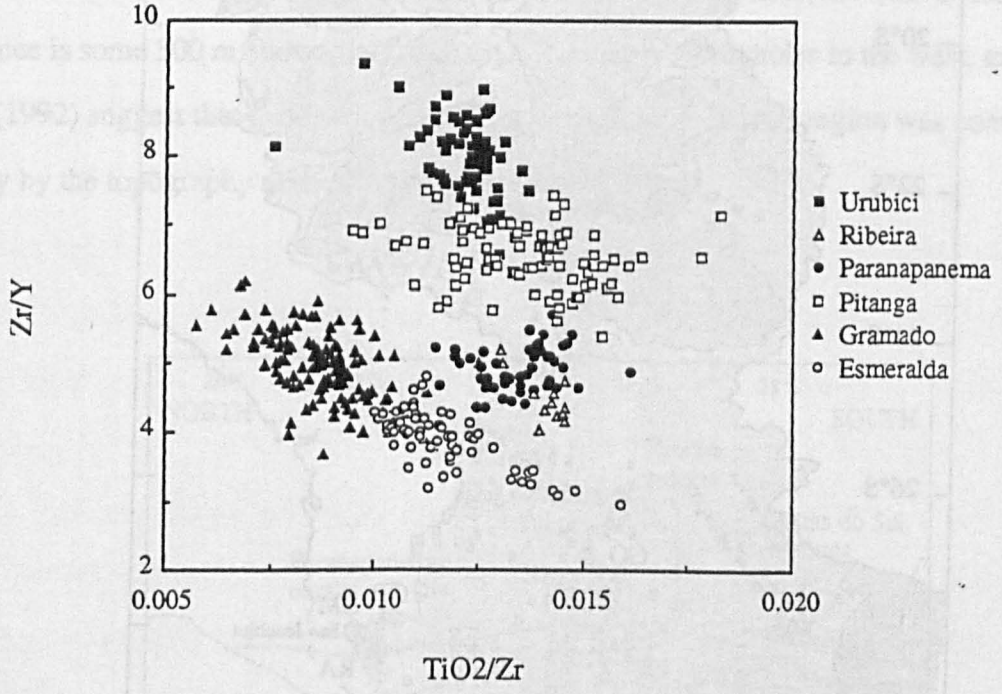

Fig. 1.9
Zr/Y—TiO_2/Zr values of Parana basalts, illustrating how the lavas may be subdivided into a number of different magma types on the basis of their major and trace element compositions. A detailed discussion of the geochemical criteria used in the classification of the Parana magma types is given in Peate et al. (1992).

1.4.3.2 Geochemical stratigraphy of the Parana basalts

Most of the early geochemical studies of the Parana volcanics (Mantovani et al., 1985a; Bellieni et al., 1986; Hawkesworth et al., 1988; Peate et al., 1990) were carried out on samples from the Serra Geral escarpment of the southeastern part of the province, where the lavas are relatively well exposed over an area of about 120,000 km^2.

In this region, the contact between the lavas and the underlying sandstones climbs from about 50 m above sea level at the TA section (fig. 1.10), to 1200 m above sea level near Sao Joachim, some 200 km to the north. In the region of Sao Joachim, the lavas

progressively overstep the sediments to the northeast, and appear to have 'ponded-up' against existing topographical features.

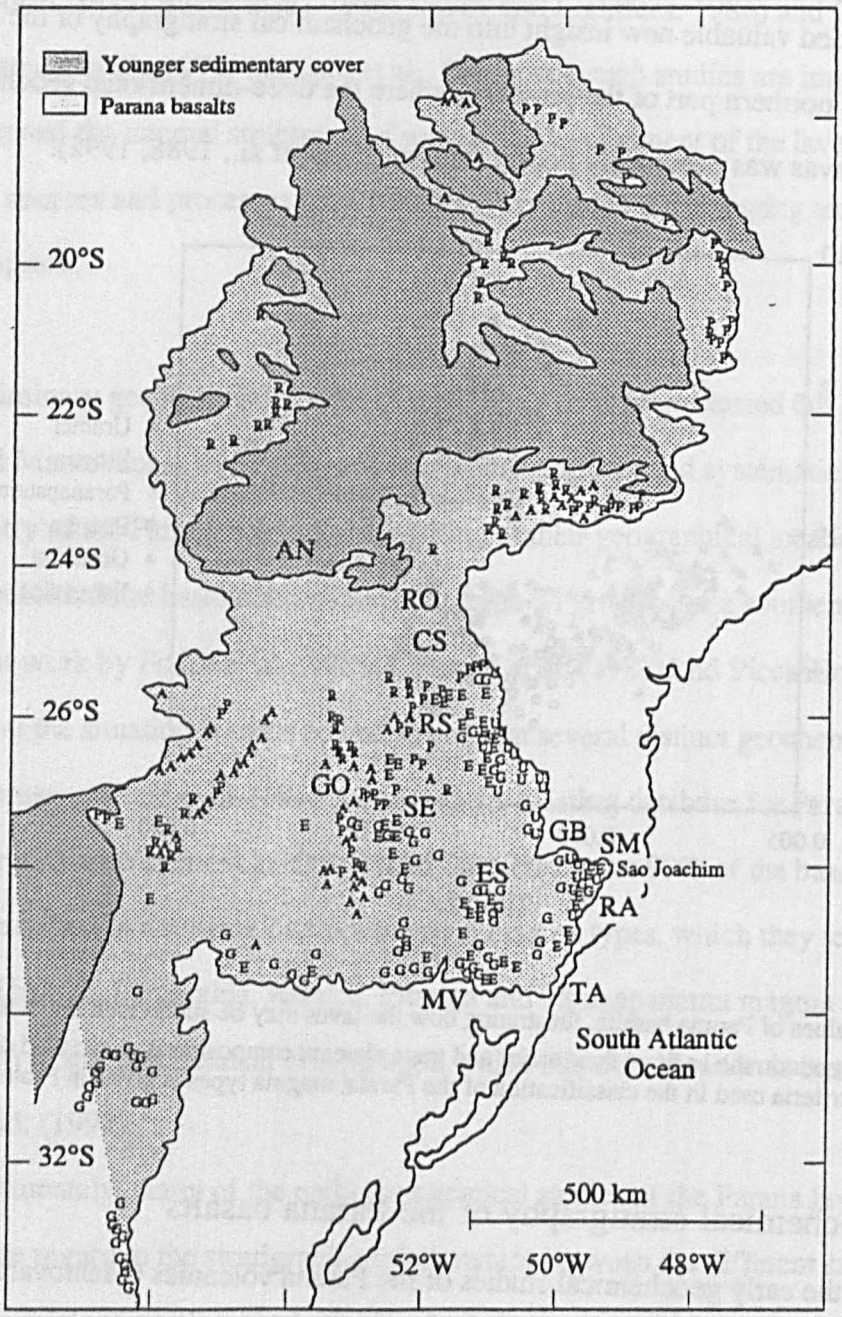

Fig. 1.10

Distribution of Parana magma types, based on the available published geochemical data. The location of boreholes (AN, RO, CS, RS, GO, SE, ES) and road sections (MV, TA, RA, SM, GB) that were studied in detail by Peate (1989) are also shown. Adapted from Peate et al. (1992). Key; G, Gramado; U, Urubici; E, Esmeralda; R, Ribeira; P, Pitanga; A, Paranapanema.

In the southern and western parts of the escarpment, basalt flows of the Gramado magma type dominate the sections. North of about latitude 29°S, basalts of Gramado type are interbedded with flows of the Urubici magma type, and the latter become progressively more abundant to the north, suggesting that their source lay to the north. Single flows of the Urubici type have been recorded from the ES borehole, about 50 km to the SW of the surface exposures, and from the GO, AV and RO boreholes (fig. 1.10), where they are interbedded with Gramado type basalts near the base of each sequence. No Urubici type flows were encountered in the nearby SE, RS or CS boreholes; here, the base of the lava sequence is some 300 m above that in the GO, RO and AV boreholes to the west, and Peate et al. (1992) suggest that the distribution of the earliest flows in this region was controlled largely by the topography at the time of eruption.

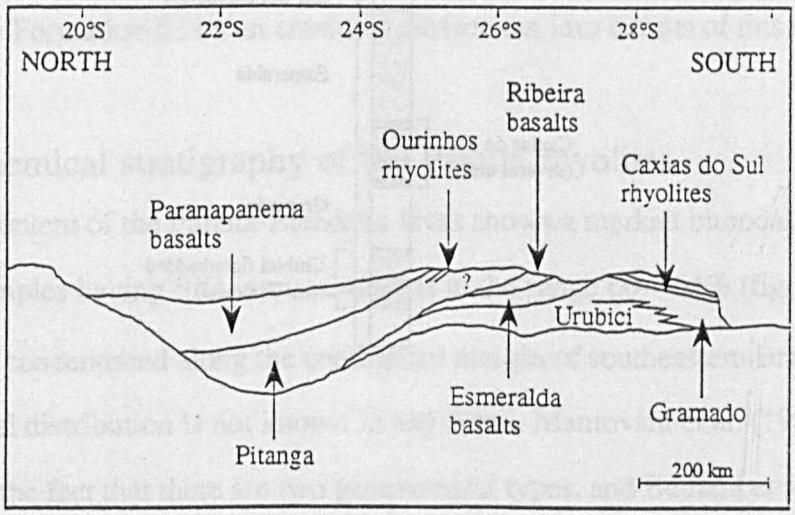

Fig. 1.11
Schematic north—south section through the lava field at 52°W, illustrating the internal stratigraphy of the lava pile as inferred from the borehole data. Vertical exaggeration x100. Adapted from Peate et al. (1992).

The uppermost flows of the SM and MV sections and the ES borehole are composed of basalts of the Esmeralda magma type. Flows of this type are also found interbedded with rhyolites in the upper part of the RA section, and many of the late-stage dykes and sills

which intrude the lava pile in this region are of the Esmeralda magma type. Scattered surface samples reveal that basalts of the Esmeralda and Gramado type occur inland between 25 and 30°S, and Esmeralda type flows overlie those of Gramado type in the CS, RS, GO and SE boreholes. Further to the south, in Uruguay, the basalts appear to be exclusively of Gramado type, although there are very few geochemical data for the basalts south of latitude 30°S (fig. 1.10).

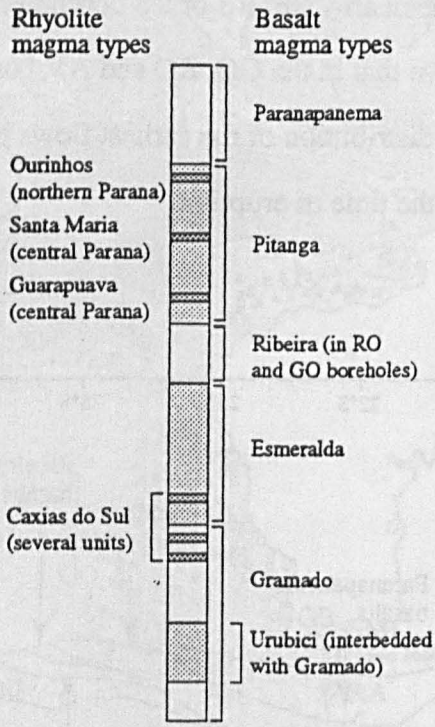

Fig. 1.12
Schematic stratigraphic column of the Parana lava field (the relative thicknesses of the different units are not to scale.

Away from the Serra Geral escarpment, the geochemical stratigraphy of the lava pile is known largely from the work of Peate et al. (1989 and 1992), who used rock chippings recovered from exploratory boreholes in the central part of the province to investigate the subsurface structure of the lava pile (fig. 1.11). In the GO borehole, a 150 m thick unit of flows of the Ribeira magma type directly overlies basalts of the Esmeralda type, and in turn is overlain by flows of the Pitanga magma type (fig. 1.12). One Ribeira type flow was

encountered near the base of the RO borehole, where it is overlain by basalts of the Pitanga magma type. However, Petrini et al. (1987) have reported basalts of the Ribeira type from surface localities to the north, east and west of the CB borehole in the central Parana, where they appear to overlie basalts of the Paranapanema type.

The basalts of the Paranapanema type are widespread at the surface in the region of the Parana river, whereas flows of Pitanga type are concentrated around the eastern and northeastern margins of the lava field. This suggests that the lavas have a regional northwesterly component of dip, and this is supported by the borehole data; in the central part of the province, the contact between the Pitanga and Paranapanema magma types occurs at a successively deeper level towards the north, corresponding to a northerly component of dip of about 0.5°.

The basalts of the Paranapanema type appear to have been the last to have been erupted, for in Mato Grosso do Sul and Sao Paulo states, the sandstones of the Upper Cretaceous Bauru Formation lie on an erosional surface cut into basalts of this magma type.

1.4.3.3 Geochemical stratigraphy of the Parana rhyolites

The SiO_2 content of the Parana-Etendeka lavas shows a marked bimodal distribution, with very few samples having SiO_2 concentrations in the range 60—64% (fig. 1.7). The evolved lavas are concentrated along the continental margin of southeastern Brazil, but their exact geographical distribution is not known in any detail. Mantovani et al. (1985b) first drew attention to the fact that there are two geochemical types, and Bellieni et al. (1986) divided the rhyolites into a Palmas type, which are largely concentrated in the southern part of the province; and a northern, Chapeco type, which are restricted to the northeastern part of the lava field, north of about latitude 28°S. Piccirillo et al. (1987) showed that regional compositional variations exist within the Chapeco rhyolites, and more recently, Peate et al. (1992) divided the Chapeco rhyolites into the Guarapuava and Ourinhos subgroups, and the Palmas rhyolites into the Caxias do Sul and Santa Maria subgroups. The age of these rhyolites, relative to the basalts, is not well constrained. In the RS borehole, rhyolites of the Guarapuava type lie towards the base of the Pitanga basalt unit, whereas at the surface, the rhyolites of the Ourinhos type are closely associated with basalts of both Pitanga and

Paranapanema type, which suggests that the Ourinhos rhyolites may lie at a slightly higher stratigraphic level (fig. 1.12). The rhyolites of the Santa Maria subgroup outcrop only in the southwestern extremity of the rhyolite exposure, and overlie rhyolites of the more dominant Caxias do Sul type in the region of Santa Maria. In the central part of the Parana province, the Guarapuava-type rhyolites form an approximately 90 m thick unit which appears to overlie the rhyolites of the Caxias do Sul type, and to be overlain by the rhyolites of the Santa Maria type (fig. 1.12).

Whittingham (1991) carried out a detailed study of the rhyolites from a 200 by 100 km area in the southeastern corner of the Serra Geral escarpment. He found that these rhyolites could be divided into seven subunits, which he considered to correspond to individual eruptive events. In this area, the lowermost unit is petrographically and compositionally identical to the Lower Springbok unit of the Etendeka (Milner, 1986). If the two represent the products of the same eruptive event, then this unit has a lateral extent of over 200 km, which is further evidence for an ignimbritic origin for these rocks.

1.4.4 Geochemical stratigraphy of the Etendeka lavas

The first detailed geochemical study of the Etendeka volcanics was carried out by Erlank et al. (1984). More recent work by Erlank, Duncan, Milner and co-workers has revealed a greater geochemical variation within the lavas than suggested by the earlier study.

Most of the basalts of the Etendeka have been assigned to a low-TiO_2 magma type named the Tafelberg. Flows of this type make up the entire 800 m basalt sequence at the type locality at Tafelberg. Erlank et al. (1984) noted that these basalts are very similar in terms of their geochemistry to the low-TiO_2 basalts of the Parana, and Peate (1989) has since demonstrated that the Tafelberg magma type is in fact the African equivalent of the Gramado magma type of the southern Parana. In places, notably in the Albin remnant near the coast at Cape Cross, the lowermost flows of the lava pile consist of highly plagioclase-phyric basalts, and these have been assigned to the Albin magma type. Basalts of the Albin and Tafelberg magma types show complete compositional overlap, and the distinction between the two is made merely on petrographic terms.

In the Sarusas and Khumib lava remnants of the northern Etendeka, basalt flows of the Tafelberg magma type are interbedded with flows of a high-TiO_2 type named the Khumib magma type (Duncan et al., 1988). Flows of this type become more common towards the north, and do not occur south of Terrace Bay. Peate et al. (1992) have shown that these basalts are geochemically identical to the Urubici basalts of the southern Parana.

Our understanding of the stratigraphy of the acidic volcanic rocks of the Etendeka has been greatly improved by the recent work of Milner and co-workers. Milner and Duncan (1987) demonstrated that individual quartz latite units have extremely uniform chemical compositions, and show no significant lateral geochemical variation over several hundred kilometers. However, significant compositional differences do exist between individual units, and Milner (1986) recognised six distinct geochemical units (believed to represent separate eruptive events) which could be correlated across the province. Of these, most have similar geochemistry to the Palmas-type rhyolites of the southern Parana, but those from the Sarusas remnant of the northern Etendeka have similar, though not identical, geochemistry to the Chapeco type rhyolites of the northern Parana. Small plugs, dykes and sills of quartz monzonite, which are thought to be intrusive equivalents of some of the quartz latite units, intrude the Goboboseb Mountain volcanics around the margins of the Messum Complex in the southern Etendeka (Milner and Ewart, 1989), which implies that some of these quartz latite units originally extended over an area of at least 2000 km^2.

1.4.5 Intrusive rocks of the Parana-Etendeka province

The eruption of the Parana-Etendeka flood basalts was accompanied by the intrusion of significant volumes of magma, in the form of both dykes and sills (fig. 1.13). The sediments of the Parana Basin, upon which the flood basalts were erupted, are host to numerous sills of between 2 and 200 m in thickness (Bellieni et al., 1984). These have a combined thickness of over 1000 m in the northern part of the basin (Bellieni et al., 1984), and are emplaced mainly within the Palaeozoic sediments. Bellieni et al. (1984) carried out geochemical analysis of dolerite samples recovered from boreholes drilled into the northern and eastern parts of the basin, and showed that all were tholeiitic, and had similar geochemical characteristics to the overlying lavas. Peate et al. (1990) demonstrated that the

distribution of dolerite magma types mirrors that of the basalts of the surface lava pile, in that the sills of the southern part of the basin belong mainly to the Gramado magma type, whilst those south of about latitude 26°S are composed dominantly of the Pitanga and Paranapanema magma types.

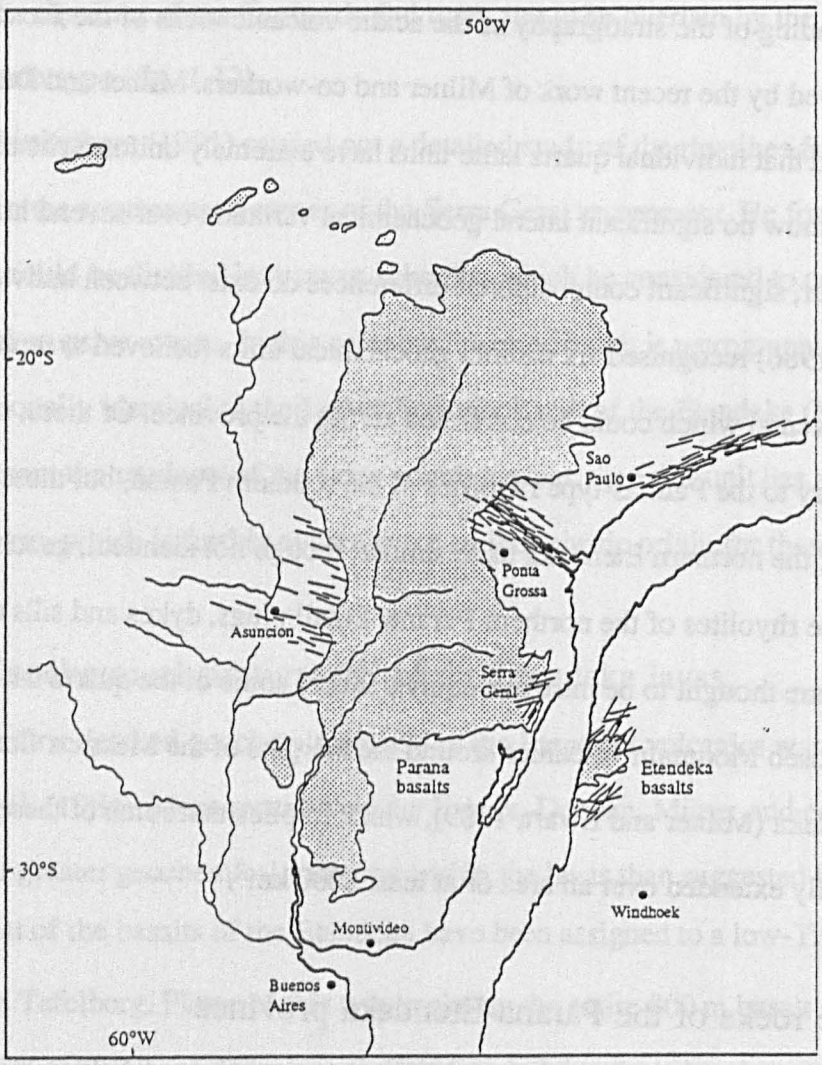

Fig. 1.11
Distribution of the dykes associated with the Parana flood basalts. The geochemistry of the dolerites from the Ponta Grossa and Sao Paulo regions are discussed in Chapters 2 and 3 respectively.

Scattered dykes intrude the sediments and the overlying volcanics in the region of the Serra Geral escarpment in Santa Caterina State (fig. 1.13). In the Ponta Grossa region of Parana State, NW—SE trending dykes intrude the basement rocks, the sediments of the Parana Basin, and locally, the overlying volcanics. To the northeast, in Sao Paulo and Rio de Janeiro States, the basement rocks of the coastal region between Santos and Rio de

Janeiro are host to numerous NE—SW trending dykes (Comin-Chiaramonti et al., 1983). Because of the poor exposure, the exact extent of these dyke swarms, and the lateral persistence of individual dykes is not known in any detail. A recent aeromagnetic survey (Druecker and Gay, 1985) has revealed the presence of numerous E—W striking dykes in eastern Paraguay, to the west of the main lava field, but as yet no geochemical data are available for these dolerites.

In Namibia, basaltic dykes and sills of similar age to the Etendeka flood volcanics intrude the basement, the Karoo sedimentary strata, and the overlying basalts. Dense dyke swarms cut the Damara granites to the southeast of the Ugab River, and a complex of dolerite sills intrudes both basement rocks and the overlying Karoo sediments in the region of the Huab River. The Namibian dolerites are the subject of a detailed study by workers from the Universities of Cape Town and Grahamstown, South Africa (Marsh et al., in prep.).

In the course of this study, dolerite samples were collected from scattered localities in Namibia; and in Brazil, from the Serra Geral escarpment, the Ponta Grossa region, and from Sao Paulo State. The sampling localities are described in more detail in Chapters 2 and 3.

1.5 Aims of study, and structure of this thesis

The aims of this research can be summarised as follows;

1. To investigate in detail the geochemistry of the dykes associated with the Parana-Etendeka CFB magmatism.

Although the geochemical variation within the surface lavas is now fairly well-constrained, less attention has been paid to the associated intrusive rocks. This thesis presents new major and trace element data for dolerites from the Ponta Grossa (Chapter 2) and Sao Paulo State (Chapter 3) southern Brazil. The mineral chemistry of a representative suite of samples was examined, and the isotopic composition of Sr, Nd and Pb measured for selected samples.

2. To investigate the petrogenesis of the various dolerite magma types.

The new geochemical data are used to identify the processess responsible for the geochemical variation within each magma type, and to examine the relationships between these dolerites and the basalt flows of the lava field to the west (Chapters 2 and 3).

3. To date precisely the age of the Parana-Etendeka CFB event.

The age of the magmatism is presently rather poorly constrained by K—Ar data to lie between 125 and 140 Ma. In contrast, recent Ar—Ar dating of other flood basalt provinces, notably the Deccan (Cortillot et al., 1988; Duncan and Pyle, 1988) and Columbia River (Long and Duncan, 1983) has revealed that these volcanics were erupted very rapidly, probably in a period of less than about two million years. This suggests that the range of K—Ar ages obtained for the Parana rocks is largely the result of the loss or gain of radiogenic ^{40}Ar. In the course of this study, whole-rock and mineral separates from 13 samples were dated using the laser ablation Ar—Ar technique. The relatively coarse crystal size of the Parana dolerites make them more suitable than the overlying basalts for dating by this method, and it was therefore possible to determine more accurately the absolute age range of the Parana magmatism, and hence its age relative to the opening of the South Atlantic. The new data are presented in Chapter 4.

4. To develop a geodynamic model for the origin of the Parana-Etendeka CFB province.

The dykes are particularly important in this respect, because the distribution of these intrusive rocks will be more closely linked to the rifting processes that led to the development of the South Atlantic Ocean. The dykes can provide a crude estimate of the amount of extension in a particular area, and their orientation will be related to that of the regional stress field at the time of emplacement. The dolerites can also provide information about the location of the feeder system to the lava pile, and how this migrated with time. The migration of the site of magmatism, relative to the developing South Atlantic rift and the inferred position of the Tristan da Cunha mantle plume can place important constraints on the geodynamic models for the origin of the Parana-Etendeka flood basalt province discussed in section 1.3.

Chapter 2

Geochemistry and petrogenesis of the Ponta Grossa dolerites

2.1 Introduction

The Precambrian basement rocks of the Ponta Grossa region of southern Brazil, and the overlying sediments of the Parana Basin to the west (fig. 2.1) are intruded by numerous NW—SE striking dykes (Amaral et al., 1966; Piccirillo et al., 1990). In the region of Pitanga, scattered dykes have been observed to intrude the Parana volcanics (Piccirillo et al., 1990), which suggests that they were intruded at, or shortly after the time of eruption of the flood basalts. This is supported by the existing K—Ar data; Amaral et al. (1966) obtained apparent ages of between 120 and 161 Ma for three dolerite samples from the Ponta Grossa dyke swarm, and Pinese (unpublished) obtained ages in the range 114—144 Ma. In this study, four of these dolerites were dated by the Ar—Ar method, and these yielded ages of between 130.5 ± 2.9 and 134.1 ± 1.3 Ma (Chapter 4). The flood basalts have yielded similar ages (Rocha Campos et al., 1988; Renne et al., 1992b), and Piccirillo et al. (1990) drew attention to the close geochemical similarities between the Ponta Grossa dolerites and the flood basalts of the northern Parana, and suggested that the dykes may have fed the surface flows of the lava field north of latitude 26°S (the relationship between the intrusive rocks and the lavas to the northwest is investigated in more detail in sections 2.7 and 2.8). Palaeomagnetic studies by Ernesto and Pacca (1988) and Raposo and Ernesto (1989) have revealed dykes of both normal and reversed polarity, which implies that they were intruded over a period of at least 0.8 Ma (Kent and Gradstein, 1985). Palaeomagnetic pole positions suggest that the dolerites were intruded after most of the flood basalt lavas had been erupted (Ernesto and Pacca, 1988), however the new Ar—Ar data (Chapter 4) indicate that these dolerites and the surface lavas are of similar age.

The poor exposure in the Ponta Grossa region means that the precise extent of the dyke swarm is not known in detail. A magnetic survey by Ferreira (1987) suggests that the dykes are more or less restricted to an approximately 100 km-wide, NW—SE trending belt

between the towns of Ponta Grossa to the SW, and Guapiara to the NE. The 54 dolerite samples analysed during this study were collected from an area of approximately 2 x 10^4 km^2 between Curitiba, Londrina and Ourinhos, in the northern part of the Ponta Grossa swarm (fig. 2.1).

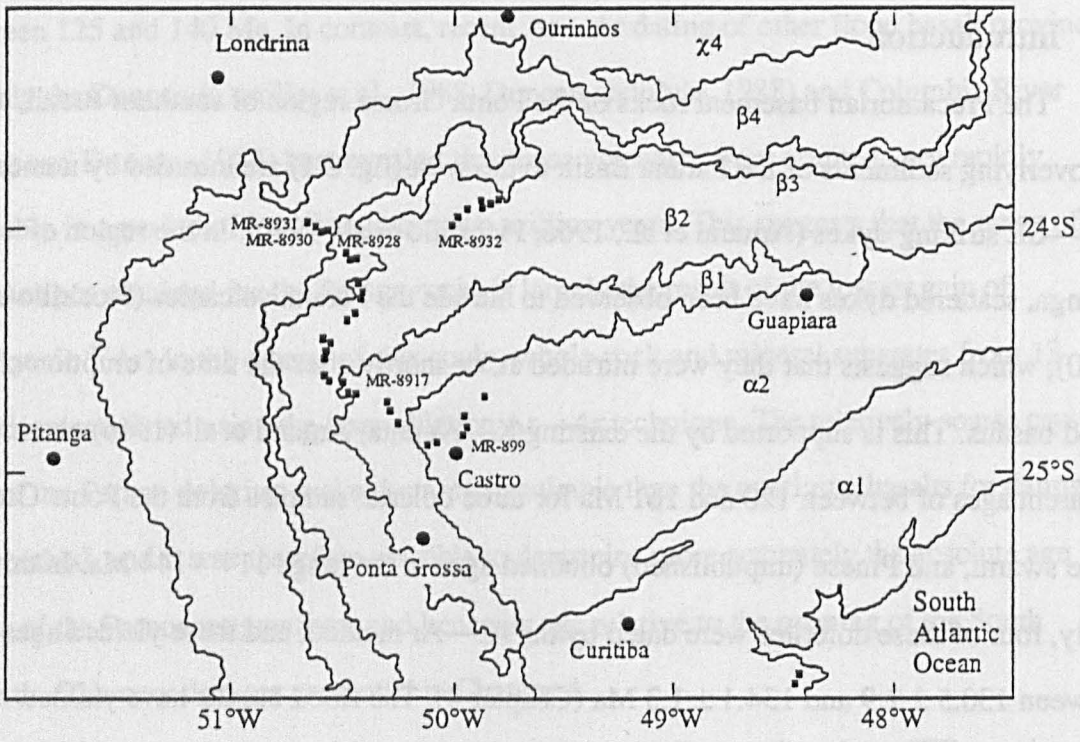

Fig. 2.1
Simplified geological map of the Ponta Grossa region of southern Brazil. The location of the samples selected for Ar—Ar analysis (Chapter 4) are shown. Key; α1, Archaean high grade metamorphic rocks of the Curitiba Massif; α2, late Proterozoic metasediments intruded by Cambrian granitoids; β1—β4, Devonian—Jurassic sediments of the Parana Basin; χ4, Parana flood basalts and rhyolites.

A previous geochemical study of the Ponta Grossa dolerites by Piccirillo et al. (1988 and 1990) investigated the mineralogy and whole-rock major and trace element geochemistry of these dykes, and presented limited Sr and Nd isotope data. This Chapter presents new major and trace element data for the Ponta Grossa dolerites (sections 2.3 and 2.4); these data, together with mineral compositions determined by microprobe analysis (section 2.2), are used to investigate the geochemical effects of low-pressure crystal fractionation (section 2.6). The isotopic composition of Sr, Nd and Pb in selected samples, and the implications of these data for the age and location of the source of the magmas, are discussed in section 2.9.

2.2 Petrography and mineral chemistry

The dolerites of the Ponta Grossa region exhibit very little petrographic variation. Most are fine-grained (crystal size <2 mm), aphyric, and composed dominantly of plagioclase, augite, titanomagnetite, with or without olivine (usually highly altered), and pigeonite. Rutile, apatite, biotite and amphibole are common accessory minerals, and chlorite occurs occasionally as an alteration product of clinopyroxene. Quartz is present in the more evolved samples. Some samples contain phenocrysts of plagioclase and/or clinopyroxene, and partially devitrified glass is present in some of the finer-grained samples. There is generally very little petrographic variation within an individual intrusion.

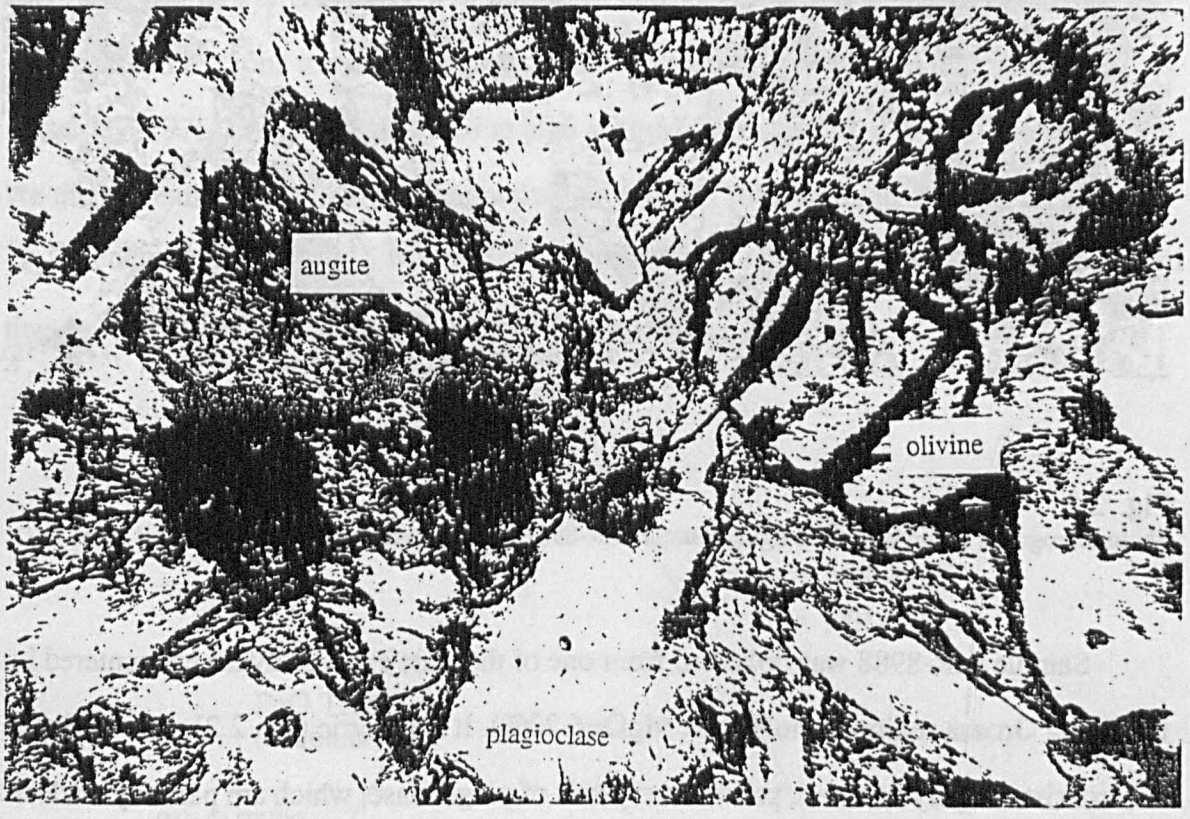

Fig. 2.2
Photomicrograph (plain polarised light) of sample MR-8988, one of the samples selected for microprobe analysis. Field of view approximately 3 x 4 mm.

The mineral chemistry of selected samples was investigated in detail by electron microprobe analysis (see Appendix), in order to model more quantitatively the fractionation history of these dolerites (section 2.6). Three samples with very different MgO

concentrations were chosen for analysis, in order to obtain a representative range of mineral compositions.

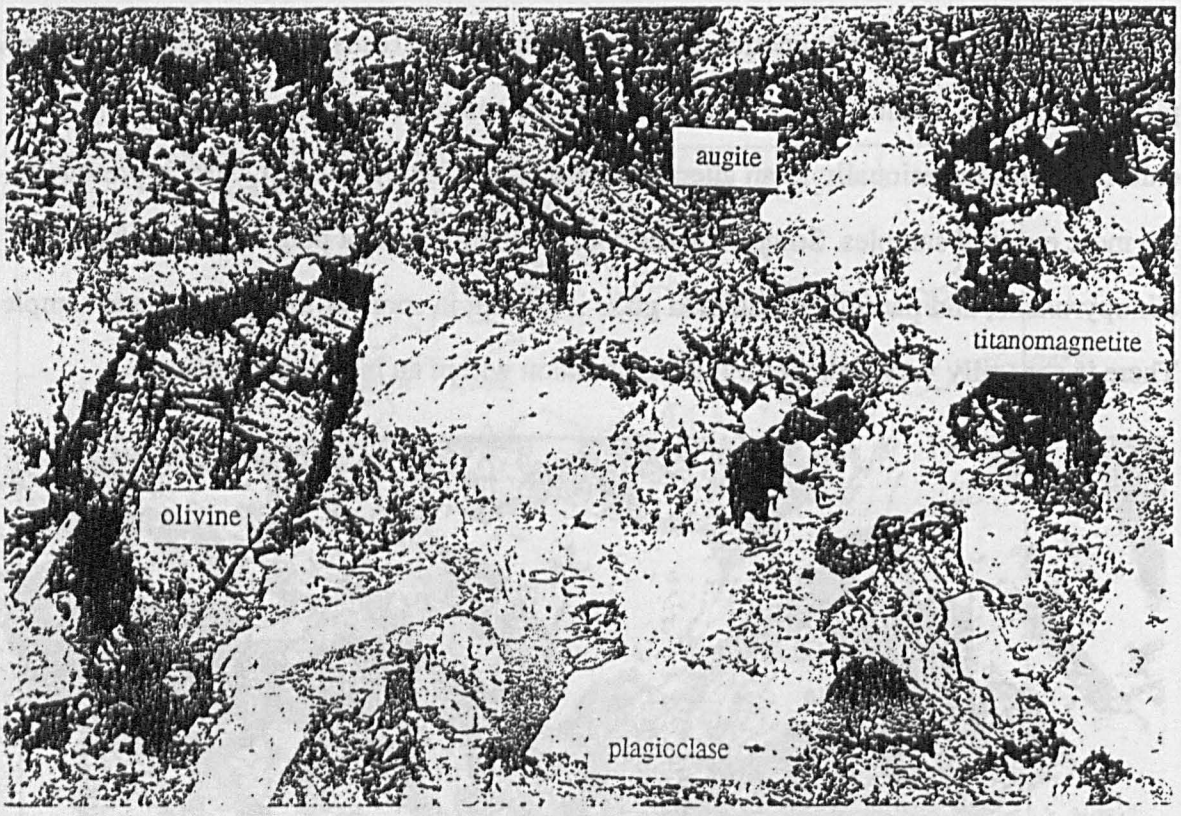

Fig. 2.3
Photomicrograph (plain polarised light), sample MR-8932. Field of view approximately 3 x 4 mm.

Sample MR-8988 was collected from one of the least evolved dykes encountered in the Ponta Grossa region (whole-rock MgO=6.20%). It is aphyric (fig. 2.2), fine-grained, and consists largely of small, prismatic crystals of plagioclase, which are partially enclosed by large, anhedral crystals of clinopyroxene in a subophitic texture. The plagioclase crystals (An_{61-65}, Ab_{35-39}, Or_{0-2}) display slight normal compositional zoning, and are generally extensively sericitised along cracks in the crystal structure. The dominant clinopyroxene in the rock is augite (Wo_{40-41}, En_{40-45}, Fs_{15-18}). There is no significant chemical variation within individual crystals. Occasional small, cracked crystals of pigeonite (Wo_{9-10}, En_{51-53}, Fs_{38-40}) are also present. The pyroxene compositions have been used to calculate approximate crystallisation temperatures in section 2.2.1.

Small, rounded grains of olivine (Fo_{39-41}) are also present; these are often almost completely replaced by fine-grained alteration products ('iddingsite').

The opaque mineral phase in this sample is a titanomagnetite, which contains between 21 and 23% weight TiO_2. Multiple analysis of single grains reveals that many are significantly heterogeneous, which appears to be due to the exsolution of a Ti rich phase (ulvospinel). Analysis totals are significantly less than 100% (generally in the range 94—96%), when reduced on the basis of 6 oxygen atoms, and these low totals are most likely to be due to the presence of maghemite, a cation-deficient spinel which is non-stoichiometric. The magnetite to maghemite reaction occurs at low pressures, between 400 and 600°C, and involves oxidation of Fe^{2+} to Fe^{3+}. The charge balance of the crystal lattice is restored by diffusion of Fe^{3+} ions towards the grain boundary, resulting in a cation deficiency (Lindsley, 1976). When recalculated to take account of the presence of Fe^{3+}, the analyses are therefore displaced from the magnetite—ulvospinel solid solution series towards the Fe_2O_3 endmember (fig. 2.4). Milner (1986) has reported the presence of similarly oxidised titanomagnetites from the quartz latites of the Etendeka.

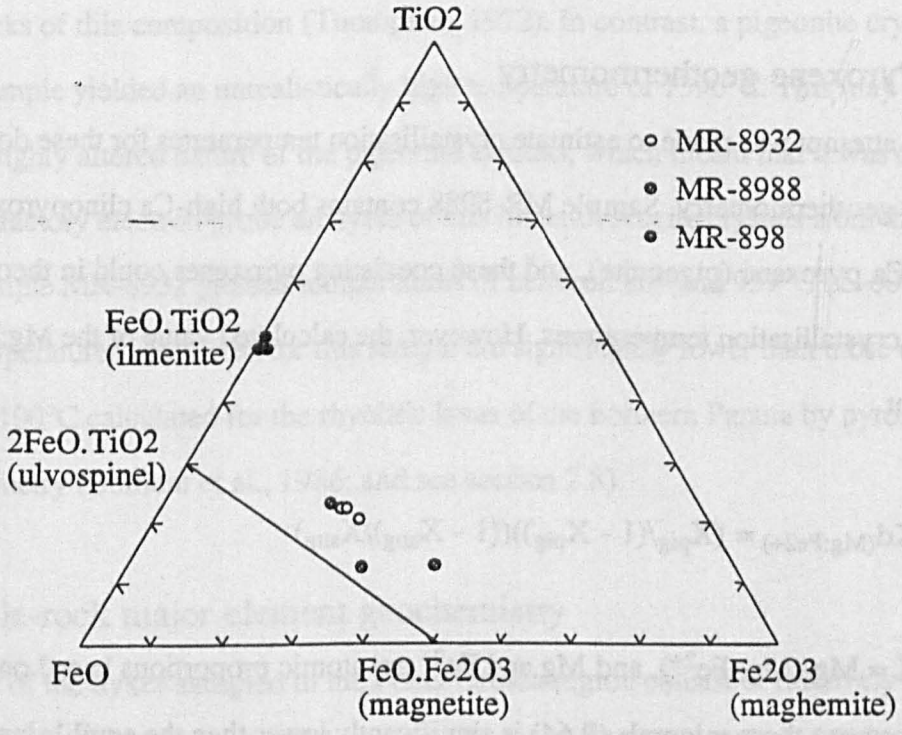

Fig. 2.4
Compositions of Fe—Ti oxides from the Ponta Grossa rocks (data obtained by electron microprobe analysis). Both ilmenite and titanomagnetite are present in different samples; crystals of the latter are variably oxidised, and contain a significant amount of the maghemite component. The proportions of the FeO and Fe_2O_3 components was calculated using the method of Lindsley (1976).

The intermediate sample MR-898 (whole-rock MgO=4.23%) consists largely of small, prismatic crystals of plagioclase (An_{53-57}). Augite (Wo_{37-39}, En_{41-44}, Fs_{18-21}) occurs as large, anhedral crystals commonly with melt-seived cores. In some cases, these possess thin overgrowths of amphibole (hornblende). The opaque mineral phase is ilmenite, rather than titanomagnetite (fig. 2.4).

Sample MR-8932 (fig. 2.3) was collected from the most evolved dyke encountered in the Ponta Grossa region (whole-rock SiO_2=60.7%; MgO=0.91%). The rock consists largely of crystals of relatively fresh, sodic plagioclase (An_{37-45}, Ab_{53-60}, Or_{0-4}), which show a slight normal compositional zoning. Large, anhedral crystals of Fe-rich augite (Wo_{39-42}, En_{16-23}, Fs_{36-42}), many of which possess thin overgrowths of amphibole, and small, rounded grains of fayalitic olivine (Fa_{92-95}), which are partially iddingsitised, are the dominant ferromagnesian minerals. Titanomagnetite (containing up to 22% TiO_2), and ilmenite are present as distinct phases. Free quartz occupies the interstices, and in places is intergrown with plagioclase in a myrmekitic texture. Apatite and biotite are common accessory minerals.

2.2.1 Pyroxene geothermometry

An attempt was made to estimate crystallisation temperatures for these dolerites using pyroxene geothermometry. Sample MR-8988 contains both high-Ca clinopyroxene (augite), and low-Ca pyroxene (pigeonite), and these coexisting pyroxenes could in theory be used to calculate crystallisation temperatures. However, the calculated value of the $Mg:Fe^{2+}$ partition coefficient

$$Kd_{(Mg:Fe2+)} = (X_{pig}/(1 - X_{pig}))((1 - X_{aug})/X_{aug}) \quad (1)$$

(where $X = Mg/(Mg+Fe^{2+})$, and Mg and Fe^{2+} are atomic proportions based on 6 oxygen atoms) between these minerals (0.64) is significantly lower than the equilibrium value of 0.75 reported by Nakamura and Kushiro (1970). This suggests that these pyroxenes are not in equilibrium (this is supported by petrographic evidence, in that the pigeonite crystals are

frequently overgrown by augite), and therefore cannot be used to calculate reliable crystallisation temperatures.

Piccirillo et al. (1990) used the single pyroxene geothermometer of Kretz (1982) to estimate crystallisation temperatures for the Ponta Grossa dolerites. This geothermometer is based upon the temperature dependence of the solubility of the enstatite component in pyroxenes. Kretz (1982) used the experimental data of Lindsley and Dixon (1976) to determine the position of the solvus in the diopside-enstatite system, and hence calibrate a thermometer which can be used to estimate the crystallisation temperatures of individual pyroxene crystals (see Appendix). The same thermometer is used here for consistency.

Augite crystals from sample MR-8988 yielded crystallisation temperatures of between 1073 and 1108°C (±~60°C). These temperatures are similar to those reported by Piccirillo et al. (1990) for the Ponta Grossa dolerites (1182—1162°C for the most basic dolerites, and 1115—1136°C for more evolved samples), using the same thermometer. These crystallisation temperatures agree well with the available experimental data which suggest that clinopyroxene will begin to crystallise at temperatures of approximately 1150—1180°C in basic rocks of this composition (Thompson, 1972). In contrast, a pigeonite crystal from the same sample yielded an unrealistically high temperature of 1396°C. This may in part be due to the highly altered nature of the pigeonite crystals, which meant that it was difficult to obtain satisfactory electron probe analyses of this mineral. Augite crystals from the more evolved sample MR-8932 yielded temperatures of between 889 and 959°C (±~60°C). Note that the temperatures calculated for this sample are significantly lower than those of between 1000 and 1100°C calculated for the rhyolitic lavas of the northern Parana by pyroxene geothermometry (Bellieni et al., 1986; and see section 2.8).

2.3 Whole-rock major element geochemistry

Most of the dykes sampled in the Ponta Grossa region consist of relatively evolved rocks which have MgO contents of between 3.18 and 6.51% (fig. 2.5) and SiO_2 contents of between 50.0 and 54.5% (basalts and basaltic andesites, fig. 2.6) although two samples with higher SiO_2 contents were also analysed. $Mg/(Mg+Fe^{2+})$ ratios of the least evolved samples are between 35 and 52, whereas magmas in equilibrium with mantle olivine (Fo_{92})

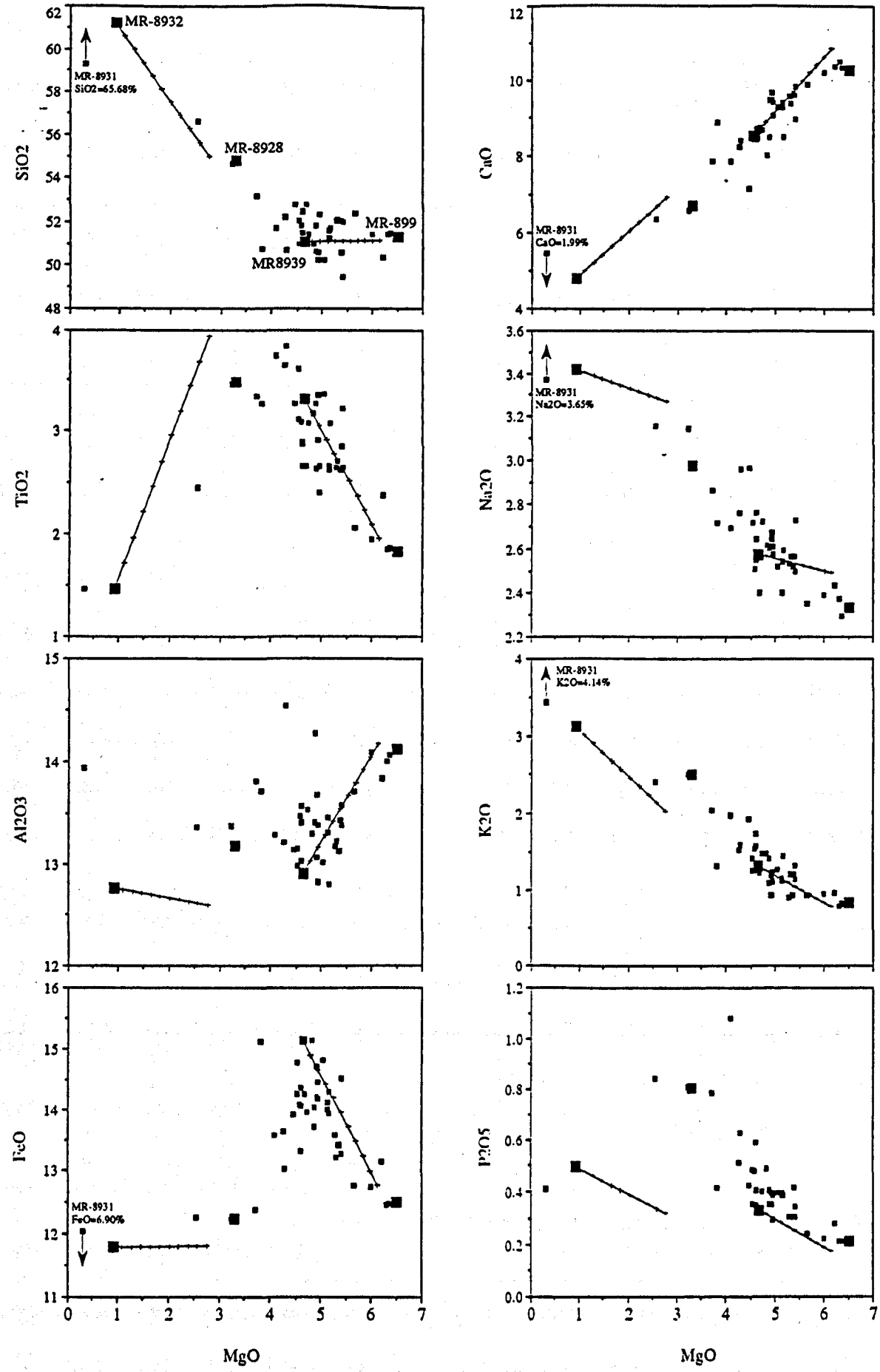

Fig. 2.5
Major element variation within the Ponta Grossa dolerites and the evolved sample MR-8931. Fractionation paths between samples MR-899 and MR-8939, and MR-8928 and MR-8932 were calculated using the least squares mixing approach of Wright and Doherty (1975), and mineral compositions determined by electron microprobe analysis.

are expected to have ratios of 68—72 (Frey et al., 1978). None of these dolerites can therefore be considered to represent primary magmas. All samples are quartz, diopside and hypersthene CIPW normative (calculated assuming 15% of the total Fe to be in the Fe^{3+} state), and their normative compositions lie close to the experimentally-determined olivine-clinopyroxene-plagioclase-liquid cotectic at between 0 and 5 kb pressure (fig. 2.7). This is further evidence that these rocks have suffered a considerable degree of low-pressure fractional crystallisation.

Cox (1980) has shown that the lavas erupted in many flood basalt provinces have undergone extensive low-pressure crystal fractionation of olivine, clinopyroxene and plagioclase. This process tends to buffer the concentration of SiO_2 and Al_2O_3, cause a marked decrease in MgO and CaO, and an increase in the FeO concentration of the residual magma. The major element variations within the more magnesian (MgO >4%) Ponta Grossa

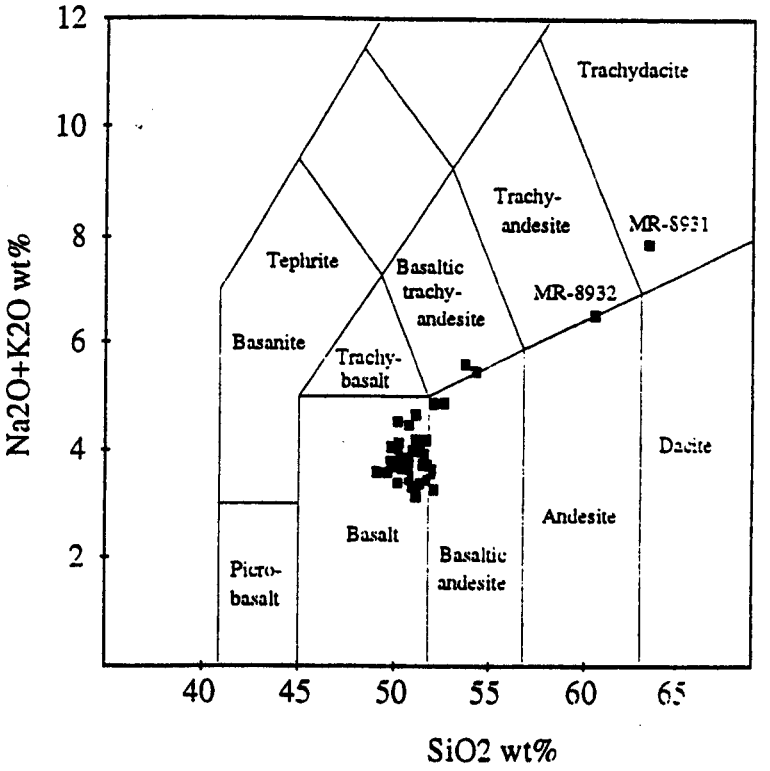

Fig. 2.6
Classification of the Ponta Grossa rocks according the the scheme of le Bas et al. (1986).

dolerites have many of the features that are characteristic of gabbro fractionation. The inflection in several of the major element trends at between 4 and 5% MgO imply that a change in the fractionating assemblage took place at this point. The decrease in TiO_2 and Fe_2O_3 with MgO for samples with less than about 4.5% MgO suggests that titanomagnetite fractionation became important, and the relatively low P_2O_5 concentrations of samples with less than about 3% MgO suggests that apatite joined the fractionating assemblage at this point. However, note that the major element variation at MgO contents of less than about 4% is relatively poorly constrained by the small number of samples. The role that fractional crystallisation has played in generating the major element variations displayed by these dolerites is discussed more quantitatively in section 2.6.

Note that the most silicic sample (MR-8931; SiO_2=65.7%) is displaced from the main array of data to higher FeO and CaO and lower SiO_2 and K_2O (fig. 2.5), which suggests that it may not be related to these less evolved samples by crystal fractionation. It will be argued in section 2.8 that sample MR8931 is an intrusive equivalent of the Ourinhos rhyolites, which outcrop on the eastern margin of the lava field north of latitude 24°S.

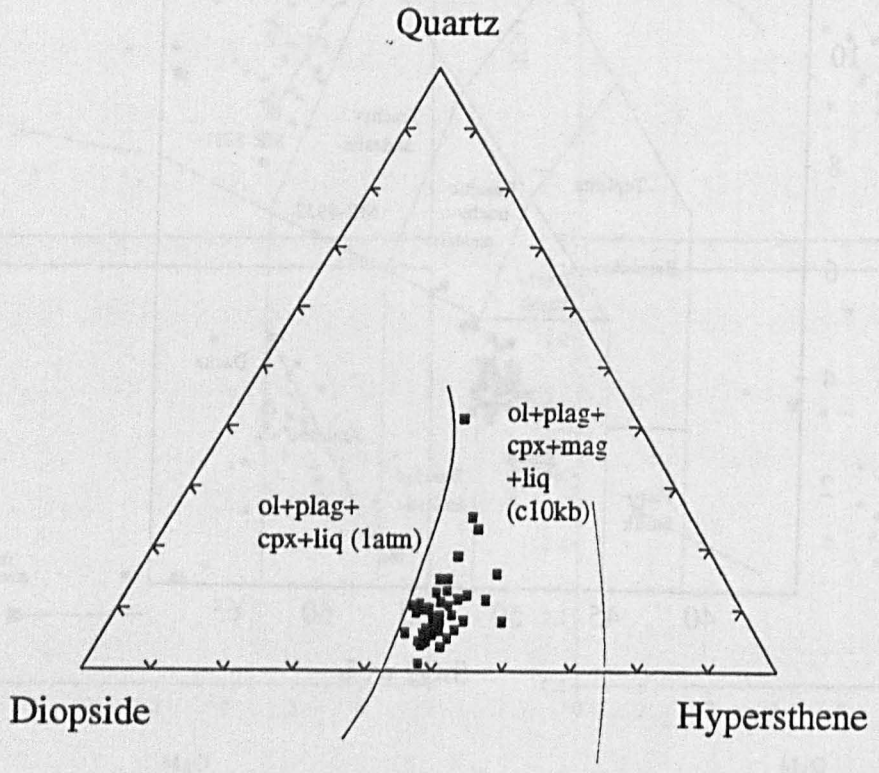

Fig. 2.7
CIPW normative compositions of the Ponta Grossa dolerites (calculated assuming that 15% of the total Fe is in the Fe3+ state). Note that the data lie close to the olivine+plagioclase+clinopyroxene+liquid cotectic at 1 atmosphere pressure (Thompson et al., 1983), suggesting that these samples have undergone extensive low pressure crystal fractionation.

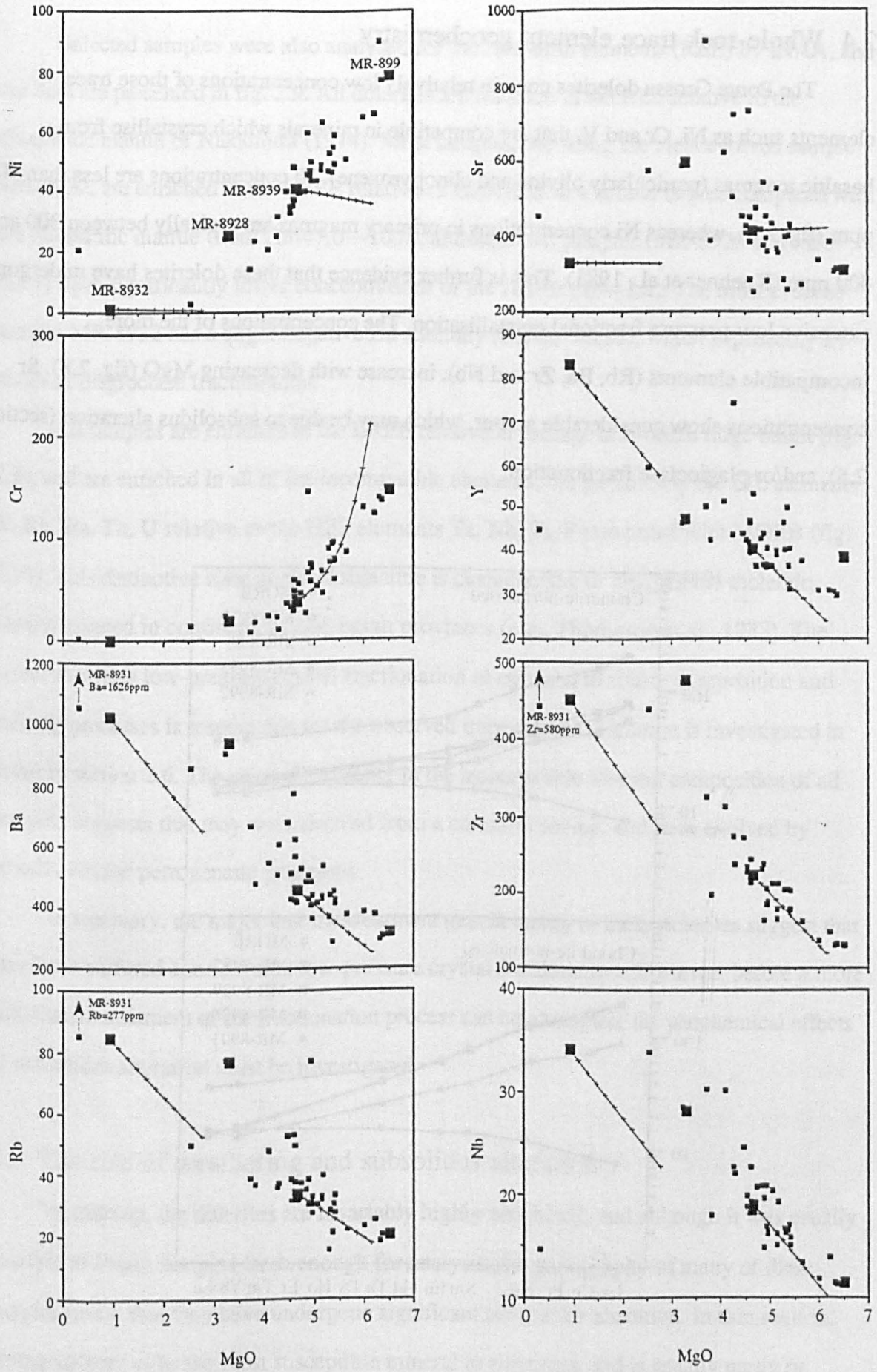

Fig. 2.8
Trace element compositions of the Ponta Grossa dolerites and the more evolved sample MR-8931. Fractionation paths were calculated using the solutions obtained from least squares modelling of the major element variaion, together with mineral melt distribution coefficients taken from the literature (see Appendix).

2.4 Whole-rock trace element geochemistry

The Ponta Grossa dolerites contain relatively low concentrations of those trace elements such as Ni, Cr and V, that are compatible in minerals which crystallise from basaltic magmas (particularly olivine and clinopyroxene). Ni concentrations are less than 90 ppm (fig. 2.8), whereas Ni concentrations in primary magmas are typically between 300 and 400 ppm (Kuehner et al., 1981). This is further evidence that these dolerites have undergone extensive low-pressure fractional crystallisation. The concentrations of the more incompatible elements (Rb, Ba, Zr and Nb), increase with decreasing MgO (fig. 2.8). Sr concentrations show considerable scatter, which may be due to subsolidus alteration (section 2.5), and/or plagioclase fractionation.

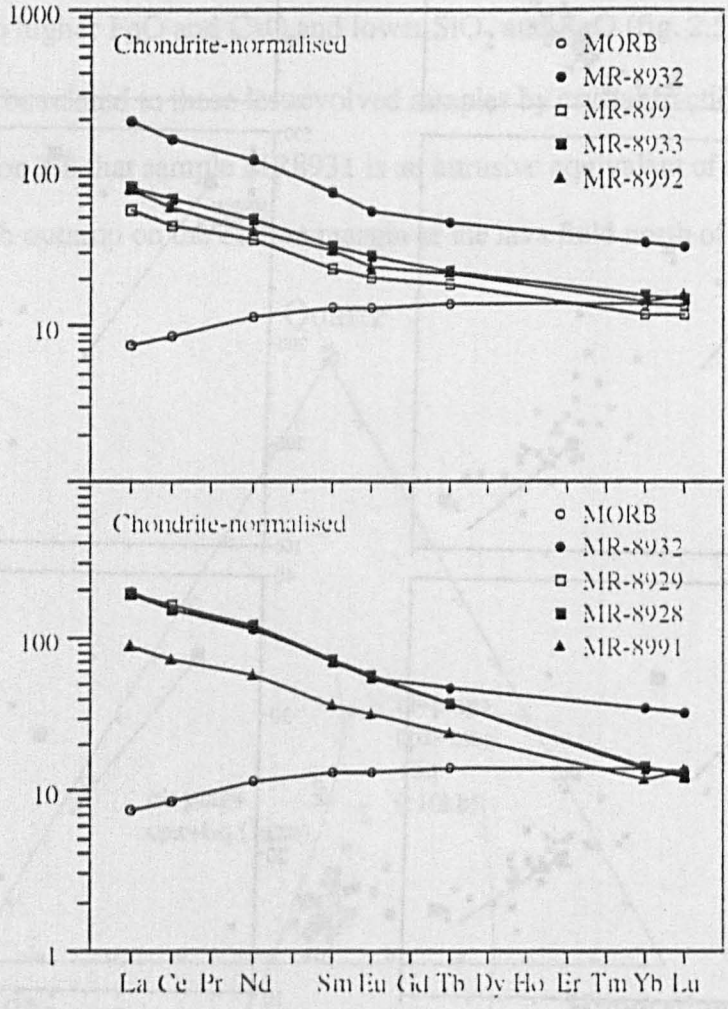

Fig. 2.9
Rare earth element compositions of the Ponta Grossa dolerites. Data obtained by INAA, and normalised to the chondritic composition of Nakamura (1974). The average NMORB composition is taken from Sun and McDonough (1989).

Selected samples were also analysed for the rare-earth elements (REE) by INAA, and the data are presented in fig. 2.9. All dolerites are enriched in the REE relative to the chondritic mantle of Nakamura (1974). Most samples, including the most evolved sample MR-8932, are enriched in the LREE relative to the HREE to a similar degree compared with the chondritic mantle (Lan/Ybn=7.0—10.0), although two samples (MR-8928 and MR-8991) have significantly lower concentrations of the HREE (Tb—Lu). The most evolved sample MR-8932 has a slight negative Eu anomaly (Eu/Eu*=0.89), which is probably a result of plagioclase fractionation.

All samples are enriched in the LREE relative to average mid-ocean ridge basalt (fig. 2.9), and are enriched in all of the incompatible elements, but particularly the LIL elements K, Rb, Ba, Th, U relative to the HFS elements Ta, Nb, Ti, P compared with MORB (fig. 2.10). This distinctive trace element signature is characteristic of many of the tholeiitic basalts erupted in continental flood basalt provinces (e.g., Thompson et al., 1983). The extent to which low-pressure crystal fractionation as opposed to source composition and melting processes is responsible for the observed trace element variation is investigated in detail in section 2.6. The general similarity in the incompatible element composition of all samples suggests that they were derived from a common source, and have evolved by broadly similar petrogenetic processes.

In summary, the major and trace element geochemistry of these dolerites suggest that they have suffered considerable low-pressure crystal fractionation. However, before a more quantitative treatment of the fractionation process can be attempted, the geochemical effects of subsolidus alteration must be investigated.

2.5 The role of weathering and subsolidus alteration

At outcrop, the dolerites are invariably highly weathered, and although it was usually possible to obtain samples fresh enough for analysis, the petrography of many of these samples reveal that they have undergone significant subsolidus alteration. In thin section, olivine appears to be the most susceptible mineral to alteration, and is usually partly or wholly iddingsitised. Plagioclase is generally extensively sericitised along cracks in the crystal structure. These alteration effects are likely to have taken place shortly after

crystallisation and were probably contemporaneous with titanomagnetite oxidation. It is important to assess the geochemical effects of these alteration processes before investigating in more detail the role that fractional crystallisation has played in the evolution of these rocks.

Studies of basalts from other CFB provinces suggest that in most cases post-eruptive weathering and alteration processess have had a limited effect upon the concentrations of most major and trace elements in these rocks. Wood et al. (1976) and Marsh and Eales (1984) demonstrated that the high field-strength elements (Ti, Zr, Hf, Nb, Ta and Y), V, Co, Zn and most REE were relatively immobile during subsolidus alteration of the Karoo CFB. Cox and Hawkesworth (1985) and Lightfoot (1985) showed that Rb, Ba and K were the only elements whose concentrations were significantly affected by alteration of the Deccan flood basalts. Milner (1986) found significant variation of K, Sr, Cs and to a lesser extent Ca and Na within individual rhyolite units from the Etendeka, which he ascribed to the effects of plagioclase alteration and divitrification.

Peate (1989) showed that the variation of Rb, Sr, Ba, K and Na within individual basaltic lava flows from the southern Parana is greater than the analytical precision of the XRF technique as determined by repeated analysis of standards, and interpreted these variations as the effects of weathering and subsolidus alteration. The isotopic composition of Nd and Pb, and to a lesser extent Sr, were found to be unaffected by these processes.

Several of the Ponta Grossa dolerites contain significant amounts of glass, which has been devitrified to varying degrees. Devitrification involves low-temperature hydration and ion-exchange reactions, and these may have had a significant effect upon the distribution of the more incompatible elements (K, Rb, Sr and Ba), which are likely to be concentrated in the glass phase of these dolerites. Sample MR-8921, which contains a large amount of devitrified glass, has a relatively high loss on ignition (L.O.I.=5.61%), and the highest $^{87}Sr/^{86}Sr$ value of any of the Ponta Grossa dolerites (section 2.8). This suggests that Sr was mobile during the alteration process.

In conclusion, although a detailed study of the geochemical effects of subsolidus alteration on these dolerites was not attempted, weathering is likely to have had little effect upon major element and most trace element concentrations, especially for non-glassy

samples with less than about 2% L.O.I. Those elements most likely to have been affected by devitrification and plagioclase alteration are Sr, Rb, Ba, K and U. Plagioclase alteration may also have had a significant effect upon the distribution and isotopic composition of Ar in these samples, (Chapter 4), because the fine-grained alteration products will tend to lose radiogenic ^{40}Ar more readily than unaltered plagioclase, even at relatively low temperatures (McDougall and Harrison, 1988).

2.6 The role of fractional crystallisation

The major and trace element data presented in sections 2.3 and 2.4 suggest that the Ponta Grossa dolerites have undergone considerable low-pressure fractionation. In the following section, the nature of this fractionation is investigated more quantitatively, using the major element compositions of the observed phenocryst and groundmass phases, and least-squares mixing calculations.

2.6.1 Major element modelling

The least-squares mixing programme SUPERMIX (based on the least-squares approach of Wright and Doherty (1970), and adapted for the O.U. VAX mainframe by D. W. Wright) was used to investigate more quantitatively the nature of the low-pressure fractionation that these rocks have undergone. The programme adds mineral compositions to an evolved endmember, in proportions such as to match as closely as possible the composition of a less evolved endmember. A measure of the fit of the model to the data is given by the value of the sum of the squares of the residuals (Σr^2); the lower the value of Σr^2, the better the fit. The mineral compositions used in the calculations were obtained from microprobe analysis (section 2.2). The inflections in several of the major element trends at between 3 and 4% MgO imply that a significant change in the mineralogy of the fractionating assemblage took place at this point, and therefore the fractionation process was modelled separately for samples with more than 4.5% MgO (Stage 1), and less than 3.5% MgO (Stage 2).

The major element variation within the least evolved Ponta Grossa dolerites (MgO >4.5%), in particular the relatively uniform SiO_2 and Al_2O_3 contents of these samples, the

sympathetic behaviour of CaO and MgO, and the increase in FeO with decreasing MgO, are consistent with the effects of olivine, clinopyroxene and plagioclase fractionation (Cox, 1980). The rapid increase in TiO_2, FeO and P_2O_5 with decreasing MgO constrain titanomagnetite and apatite to have had a minor role in the fractionating assemblage. The major element variation between samples MR-899 and MR-8939 (Stage 1) can be satisfactorily modelled using the least-squares technique (Σr^2=0.60) by 48.5% fractionation (F=0.515) of augite (39.0%), olivine (11.3%), and plagioclase (49.7%). The mineral compositions used in the calculations were obtained from microprobe analysis of samples MR-898 and MR-8988 (table 2.1), and the calculated fractionation paths are illustrated in fig. 2.5. Negative solutions were obtained for apatite and titanomagnetite, if these minerals were included in the calculations.

The decrease in FeO, TiO_2 and P_2O_5 with decreasing MgO within the more evolved samples suggests that titanomagnetite and apatite joined the fractionating assemblage at MgO ~4%. This is supported by the least-squares calculations; the best-fit solution to the major element variation between the most evolved sample MR-8932 and the intermediate sample MR-8928 (Stage 2) can be explained by 38.9% fractional crystallisation of augite (37.5%), plagioclase (46.9%), ilmenite (15.5%) and apatite (0.1%). The mineral compositions used in the calculations for this Stage were obtained from samples MR-8932 and MR-898 by microprobe analysis. Note that the value of Σr^2 (1.67) is significantly higher for Stage 2, despite the fact that the value of F is similar in each case, and more minerals were included in the calculations for Stage 2. Note also the good fit to the variation in TiO_2 obtained by including ilmenite in the fractionating assemblage. The calculations predict less than 1% apatite in the fractionating assemblage, which is too small an amount to repreduce the P_2O_5 content of sample MR-8928. The proportion of apatite in the fractionating assemblage is constrained to be less than about 1% by the variation in CaO, which is also controlled by plagioclase and clinopyroxene fractionation. The least-squares calculations overestimate the CaO concentration of sample MR-8928, and may therefore have overestimated the proportion of augite, relative to apatite, in the fractionating assemblage.

STAGE 1 (MR-8939 to MR-899)

	SiO_2	TiO_2	Al_2O_3	FeO	MgO	CaO	Na_2O	K_2O	P_2O_5	Quantity
MR-8939	51.1	3.31	12.9	15.1	4.66	8.68	2.58	1.31	0.33	51.5
augite	51.1	1.14	3.22	11.2	14.5	18.6	0.25			19.1
plagioclase	54.1	0.13	28.4	0.76		11.6	4.55	0.43		24.4
olivine	34.0	0.07	0.05	47.7	17.8	0.38	0.02			5.53
MR-899	51.3	1.83	14.1	12.5	6.52	10.3	2.33	0.84	0.21	
product	51.1	1.96	14.2	12.8	6.15	10.9	2.49	0.87	0.17	100.51
residual	-0.162	+0.126	+0.045	+0.251	-0.375	+0.570	+0.151	-0.061	+0.039	
Sum of squares of residuals			0.600							

STAGE 2 (MR-8932 to MR-8928)

	SiO_2	TiO_2	Al_2O_3	FeO	MgO	CaO	Na_2O	K_2O	P_2O_5	Quantity
MR-8932	61.2	1.47	12.8	11.8	0.92	4.79	3.42	3.13	0.49	61.1
augite	51.3	1.00	2.18	12.2	14.9	18.1	0.27			14.1
plagioclase	58.9		25.5	0.49		8.01	6.49	0.60		17.6
ilmenite	0.05	49.7	0.17	48.2	1.88	0.02				5.82
apatite				0.03	0.02	57.1			42.9	0.03
MR-8928	54.8	3.49	13.2	12.3	3.31	6.69	2.97	2.50	0.81	
product	55.0	3.93	12.6	11.8	2.77	6.91	3.27	2.02	0.30	98.62
residual	+0.198	+0.445	-0.582	-0.436	-0.540	+0.217	+0.296	-0.481	-0.497	
Sum of squares of residuals			1.670							

Table 2.1
Least-squares modelling of the major element variation. Mineral compositions from electron microprobe analysis of samples MR-898, MR-8932 and MR-8988, except for apatite (data from Deer et al., 1966).

2.6.2 Trace element modelling

It is important to establish whether the fractionation history predicted for these rocks on the basis of least-squares modelling of the major element variation can also account for the observed trace element variation. This was investigated by using the composition of the fractionating assemblage and the value of F calculated from the least-squares model, together

with partition coefficients from the literature (see Appendix), to calculate the fractionation paths followed by the more evolved endmembers MR-8939 and MR-8932 (the theoretical fractionation path was back-calculated from the more evolved sample in each case, in order to be consistent with the major element calculations).

The concentration of an element i in a melt which is undergoing perfect Rayleigh fractionation is given by (Shaw, 1970);

$$C_l^i/C_o^i = F^{(K_d^i-1)} \quad (2)$$

$$K_d^i = X_a D_a^i + X_b D_b^i + \ldots\ldots X_n D_n^i \quad (3)$$

where C_o^i is the initial concentration of element i in the melt; X_a is the fraction of mineral a in the fractionating extract; D_a^i is the distribution coefficient for element i between a and the melt; and C_l^i the concentration of element i in the residual melt.

The theoretical fractionation paths between samples MR-8939 and MR-899 are illustrated in fig. 2.8, and were calculated using the value of F=0.515 and the composition of the fractionating assemblage obtained from the major element modelling in section 2.6.1, and K_d^i values (table 2.2b) calculated from the values of D^i from the literature (see Appendix).

Clearly, the calculated path between samples MR-895 and MR-8988 provides a reasonably good fit to the observed incompatible trace element variations for samples with greater than about 4% MgO, and this suggests that the least-squares modelling provides a good estimate both of F, and of the composition of the fractionating assemblage for Stage 1. This being so, the poor fit to the data for the more compatible elements Ni, Cr and Sr is likely to be due to a poor choice of partition coefficients. K_d^{Ni} appears to have been underestimated, and K_d^i for Sr and Cr somewhat overestimated. The values of K_d^i for these elements that are required to fit the data can be calculated from equation (2) by assuming F=0.515 (from the major element modelling), and these values are listed in table 2.2a.

The K_d^i values calculated for Stage 1 are within the range expected for gabbro fractionation; all elements other than Ni and Cr behave incompatibly; Sr and Y, which partition into plagioclase and pyroxene, behave slightly less incompatibly.

The calculated fractionation paths between samples MR-8928 and MR-8932 (Stage 2), assuming F=0.571, and using values of D^i taken from the literature (fig. 2.8) are illustrated in fig. 2.8. Note that these fractionation paths do not fit the observed trace element variation as well as those calculated for Stage 1. There are several possible explanations for this. The fractionation calculations consistently underestimate the incompatible trace-element content of the less evolved endmember (MR-8928), which suggests that the least-squares calculations have underestimated the value of F for Stage 2. This is unlikely however, because the best-fit solution to the major element variation considerably underestimates the MgO concentration of sample MR-8928, which implies that the least-squares calculations have in fact overestimated the value of F. The least-squares calculations appear to be relatively insensitive to the exact mineral compositions used, and should therefore provide a reasonable estimate of the relative proportions of the minerals in the fractionating assemblage. It is possible that, because relatively few samples with MgO concentrations of <3% were encountered, sample MR-8932 is not representative of the composition of more evolved rocks. Alternatively, the values of D^i used in the calculations for Stage 2 are too low. Mineral-melt partition coefficients were assumed not to change as the SiO_2 content of the melt increased from 51.2 to 61.2%, although there is evidence that D^i may increase significantly as the residual melt becomes more silicic and increasingly polymerised (Watson, 1979; Mahood and Hildreth, 1983).

The variation of the more incompatible elements within this group of rocks can be used to place constraints upon the degree of fractionation that they have undergone, and hence provide an independent estimation of K_d^i. Of those elements considered to behave incompatibly during crystallisation of basaltic melts (Ba, Rb, Zr, Y), the greatest enrichment in MR-8932 compared to MR-8928 is shown by Y. Assuming Y to be perfectly

incompatible, and that crystal fractionation took place by a Rayleigh fractionation process, then equation (2) reduces to

$$C_1^H = C_o^H/F \qquad (4)$$

(Allegre et al., 1977), where C^H is the concentration of a highly incompatible, or hygromagmatophile element (in this case, Y).

Equation (4) yields a value of F for Stage 2 of 0.571 (42.9% crystallisation). Note that this is slightly lower than the value of F=0.611 obtained from least-squares modelling of the major element data. Y is unlikely to be perfectly incompatible, and thus the value of F calculated from (4) will be an overestimate. However, in this case the least-squares calculations appear to have overestimated F, as discussed above. The value of 0.571 is therefore probably closer to the true value. Having obtained an estimate of F, the bulk distribution coefficient for any less incompatible element i can then be calculated by substituting the value of F from (4) into (2);

$$K_d^i = (\log C_1^i - \log C_o^i)(\log C_o^H - \log C_1^H) + 1 \qquad (5)$$

Note that because Y is unlikely to be behaving perfectly incompatibly, the K_d^i values calculated in this way (table 2.3a) will represent lower limits on their true values.

All elements other than Y behave more compatibly during Stage 2 than Stage 1. Note that Sr is compatible in Stage 2, even though the proportion of plagioclase in the crystal extract for each stage is similar (49.7% in Stage 1; 46.9% in Stage 2). It is possible that the least squares calculations have underestimated the proportion of plagioclase in the fractionating assemblage for Stage 2, because the best-fit solution considerably underestimates the Al_2O_3 concentrationof sample MR-8928. Strangely, Y behaves more incompatibly during Stage 2 than Stage 1, although the least squares modelling predicts a small amount of apatite fractionation in Stage 2, and the proportion of clinopyroxene in Stages 1 and 2 are similar (39.0% and 37.9% respectively). Thus the trace element variation

suggests that D^i values for all elements other than Y increased significantly as the SiO_2 concentration of the residual melt increased.

The effect upon the trace element composition of the least evolved sample (MR-899) of combined Stage 1 + Stage 2 fractionation (68% fractionation of olivine, clinopyroxene, plagioclase, ilmenite and apatite) is illustrated in fig. 2.10. The residual liquid has a very similar trace element composition to the most evolved sample MR-8932. Clearly, fractional crystallisation can satisfactorily account for the trace element variation within the Ponta Grossa dolerites. However, note that this process has little effect upon the relative concentrations of the more incompatible trace elements in the residual liquid, and therefore

	(a) F=0.515	(b)
Zr	0.198	0.045
Rb	0.274	0.025
Ba	0.442	0.094
Sr	0.570	1.033
Y	0.920	0.201
Ni	1.988	0.809
Cr	1.454	3.616
Nb	0.243	0.044

Table 2.2

Trace element bulk distribution coefficients calculated for Stage 1 fractionation; (a), calculated assuming F=0.515 (from the least-squares modelling) using equation (2); (b), values used to calculate the fractionation paths in fig. 2.8, using F=0.515 and mineral proportions from the least-squares modelling, and mineral-melt distribution coefficients from the literature.

	(a) F=0.571	(b) F=0.611	(c)
Zr	1.096	1.110	0.058
Rb	0.824	0.799	0.025
Ba	0.846	0.825	0.091
Sr	2.060	2.206	0.977
Y	0.000	0.000	0.236
Ni	6.276	7.001	0.294
Cr			4.951
Nb	0.763	0.731	0.166

Table 2.3

Trace element bulk distribution coefficients calculated for Stage 2 fractionation; (a), assuming $K_d^Y=0$, hence F=0.571; (b), calculated assuming F=0.611 (from the least-squares modelling), using equation (2); (c), values used to calculate the fractionation paths in fig. 2.8, using F=0.611 and mineral proportions from the least-squares modelling, and mineral-melt distribution coefficients from the literature.

fractionation cannot have been responsible for either the enrichment of the LIL elements relative to the HFS elements compared with oceanic basalts, nor the HREE depletion of certain samples. This implies that these features were either derived from the mantle source of the Ponta Grossa dolerites, or they were inherited during the melting process (this is discussed further in section 2.9.5).

In summary, the major and trace element variation within the least evolved Ponta Grossa dolerites are consistent with some 50% fractionation of olivine, clinopyroxene and plagioclase. The major element variation within the more evolved samples can be modelled in terms of an additional 53% fractionation of clinopyroxene, plagioclase, ilmenite and apatite, although the fit of the model to the data is less good. The trace element variation is consistent with this model, and implies that mineral-melt partition coefficients increased

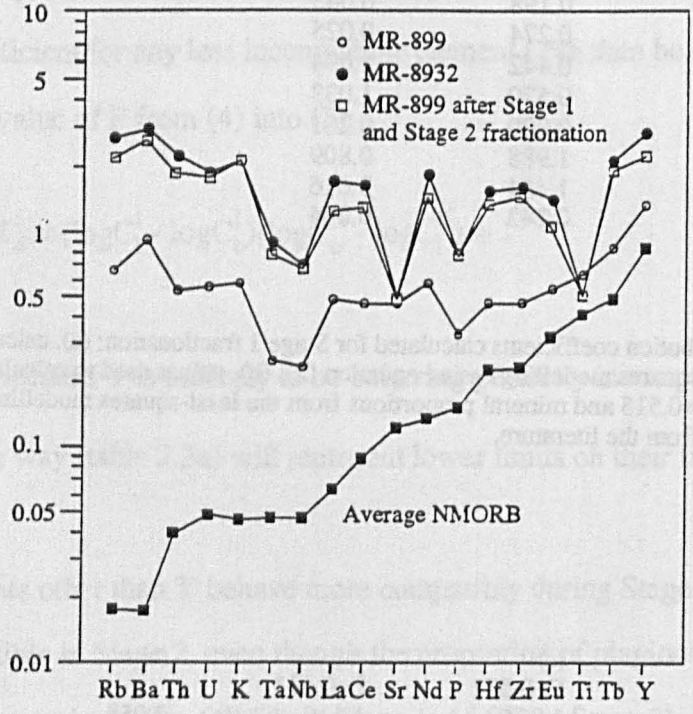

Fig. 2.10
Trace element compositions of the least and most evolved endmembers used in the major element modelling (samples MR-899 and MR-8932 respectively), and the predicted composition of sample MR-899 after 67.4% fractionation (based on the results of the least squares modelling), using mineral melt distribution coefficients taken from the literature. Sample compositions are normalised to the average oceanic island basalt composition of Sun and McDonough (1989), and the average NMORB composition of Sun and McDonough (1989) is also shown.

significantly as the SiO_2 concentration of the residual magma increased. The calculations indicate that the Ponta Grossa dolerites cannot have been derived from a parental magma of MORB composition by fractional crystallisation, and that the high concentrations of the LIL elements relative to the HFS elements of these dolerites are likely to have been derived from their source.

2.7 Relationship of the intrusive rocks to the basaltic lavas of the northern Parana

Piccirillo et al. (1990) first drew attention to the fact that the Ponta Grossa dolerites have very similar composition to the basalts of the northern Parana. Peate et al. (1992) have shown that, north of about latitude 26°S, the lava pile is composed of an older unit consisting of flows of the Pitanga magma type, overlain by a unit consisting of flows of the Paranapanema magma type (Chapter 1). The geochemistry of the Ponta Grossa dolerites and the basalts of the Pitanga and Paranapanema magma types are compared in fig. 2.11. Not only do the Ponta Grossa dolerites and the Pitanga and Paranapanema basalts have very similar concentrations of all major and trace elements, but also the inflections in the variation of TiO_2 and Fe_2O_3 of the Ponta Grossa dolerites, which reflect changes in the fractionating assemblage, are mirrored in the major element variations of the basalt magma types. This suggests that the surface lavas of the northern Parana and the Ponta Grossa dolerites have evolved by similar petrogenetic processes, and that the dykes fed the surface lava flows of the northern Parana.

The geochemical differences between basalts of the Pitanga and Paranapanema magma types are small, and the two are difficult to separate using simple discriminant diagrams such as fig. 2.12. The basalts of the Pitanga type tend to contain slightly higher concentrations of TiO_2, P_2O_5, and the incompatible trace elements (fig. 2.11). Most of the Ponta Grossa dolerites have very similar trace element concentrations to basalts of the Paranapanema magma type, although the Ba concentrations of the dolerites are somewhat high, and fall within the field defined by the basalts of the Pitanga magma type.

In order to highlight the subtle geochemical differences between the Pitanga and Paranapanema magma types, discriminant function analysis was used to calculate two

(a)

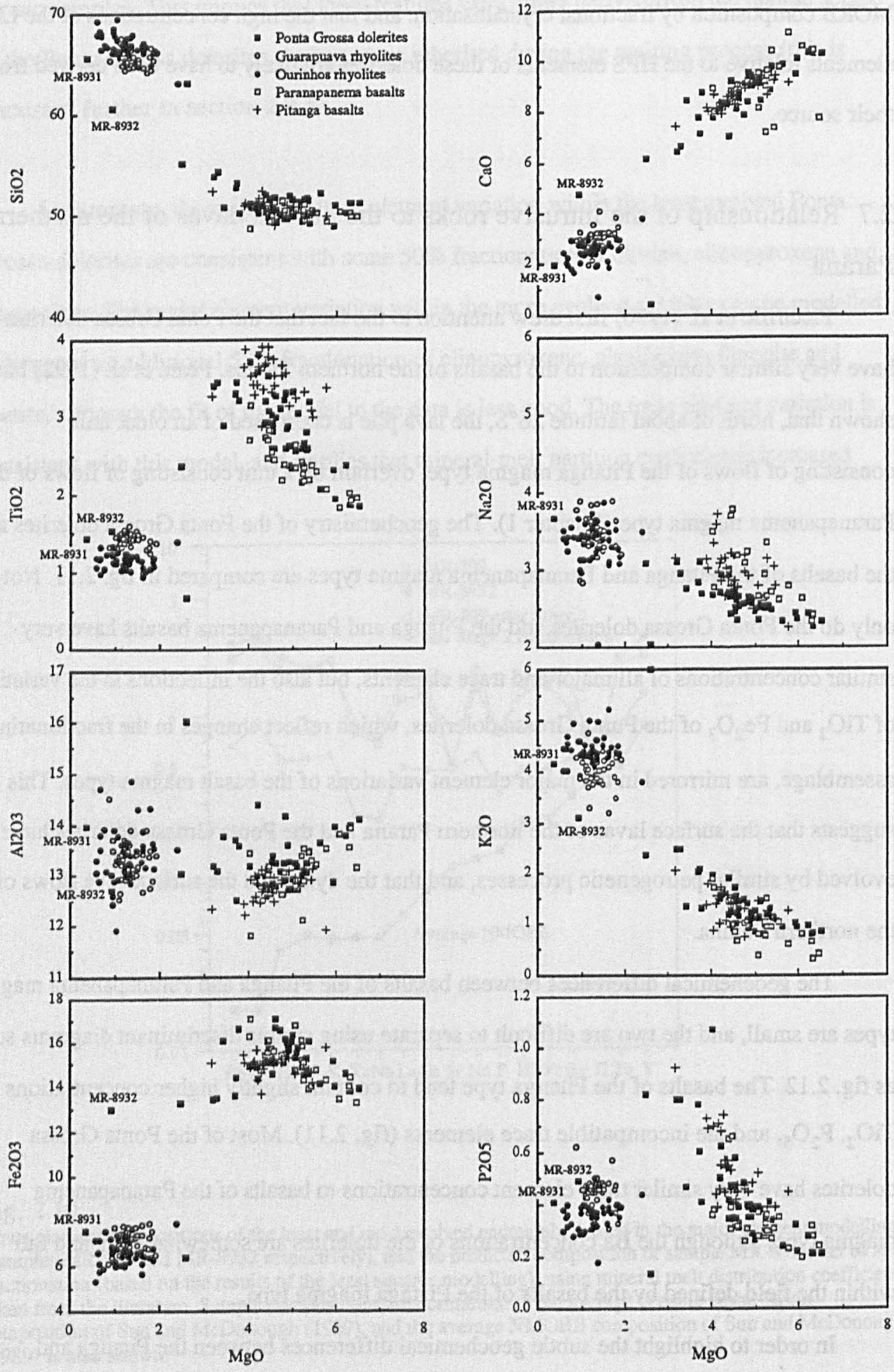
Ponta Grossa dolerites
Guarapuava rhyolites
Ourinhos rhyolites
Paranapanema basalts
Pitanga basalts
SiO2
TiO2
Al2O3
Fe2O3
CaO
Na2O
K2O
P2O5
MgO
MgO
MR-8931
MR-8932

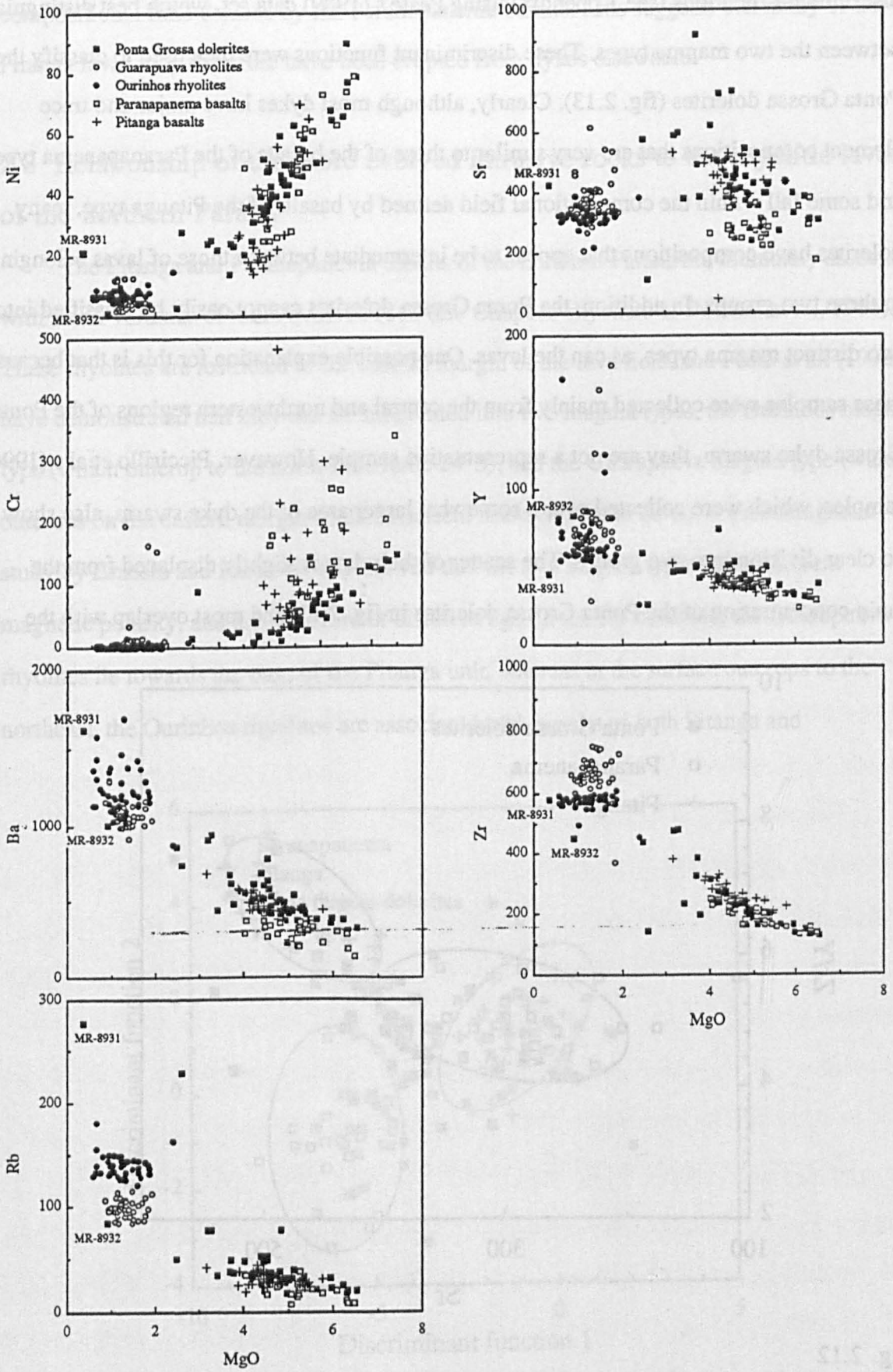

Fig. 2.11
Comparison of (a) the major element and (b) the trace element geochemistry of the Ponta Grossa dolerites with the extrusive basalt and rhyolite magma types of the northern Parana (data from Peate, 1989; Peate et al., 1992).

discriminant functions (see Appendix) using Peate's (1989) data set, which best distinguish between the two magma types. These discriminant functions were then used to classify the Ponta Grossa dolerites (fig. 2.13). Clearly, although most dykes have major and trace element compositions that are very similar to those of the basalts of the Paranapanema type, and some fall within the compositional field defined by basalts of the Pitanga type, many dolerites have compositions that appear to be intermediate between those of lavas belonging to these two groups. In addition, the Ponta Grossa dolerites cannot easily be classified into two distinct magma types, as can the lavas. One possible explanation for this is that because these samples were collected mainly from the central and northwestern regions of the Ponta Grossa dyke swarm, they are not a representative sample. However, Piccirillo et al's (1990) samples, which were collected over a somewhat larger area of the dyke swarm, also show no clear division into two groups. The scatter of their data is slightly displaced from the main concentration of the Ponta Grossa dolerites in fig. 2.13, and most overlap with the

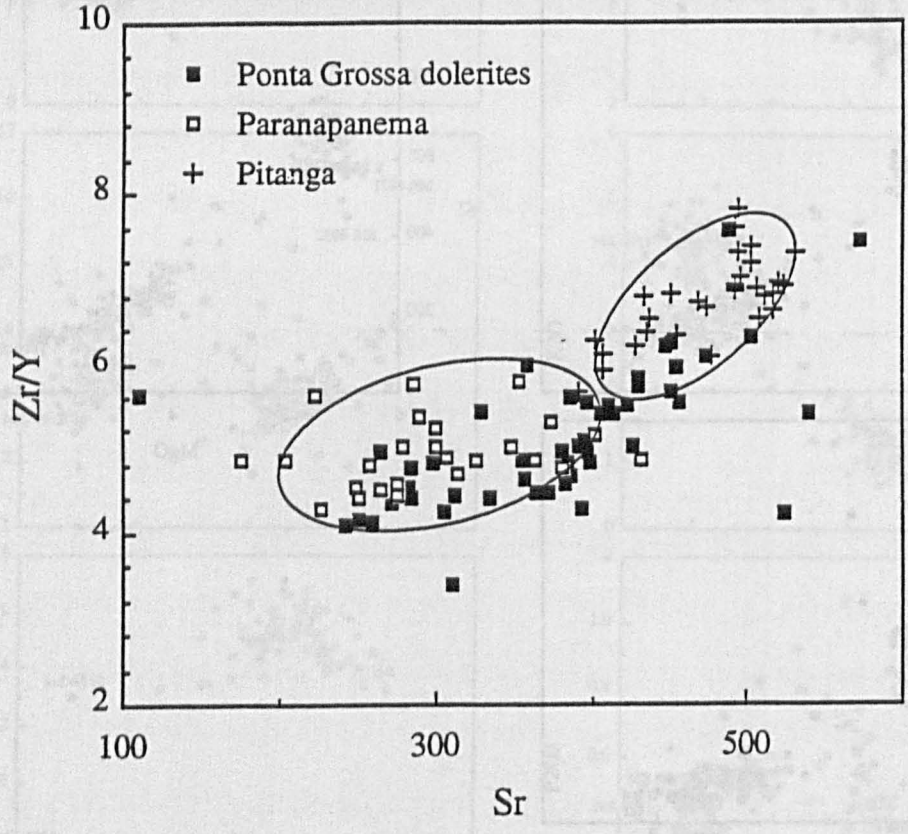

Fig. 2.12
Zr/Y—Sr variation within basalts of the Pitanga and Paranapanema magma types (data from Peate, 1989), and the dolerites of the Ponta Grossa. Note that although many of the dolerite samples have similar compositions to basalts of the Paranapanema magma type, the former have more variable Sr concentrations, and are not easily divisible into two magma types.

compositional field defined by the Paranapanema basalts. This suggests that many of the Pitanga lavas may therefore have been erupted from dykes elsewhere.

2.8 Relationship of the more evolved intrusive rocks to the rhyolitic lavas of the northern Parana

The Pitanga and Paranapanema basalts of the northern Parana are intimately associated with small volumes of more evolved rock (the Chapeco rhyolites of Bellieni et al., 1986). These rhyolites are restricted to the eastern margin of the lava field, and Peate et al. (1992) have demonstrated that they can be subdivided into two magma types, the Ourinhos magma type (which outcrop to the north of latitude 24°S), and the Guarapuava magma type (which outcrops on the eastern margin of the lava field between 25 and 28°S). A paleomagnetic study by Ernesto and Pacca (1988) showed that the two magma types have different magnetic polarity, and are therefore of different age. In the RS borehole, the Guarapuava rhyolites lie towards the base of the Pitanga unit, whereas at the surface outcrops to the northeast, the Ourinhos rhyolites are associated with basalts of both Pitanga and

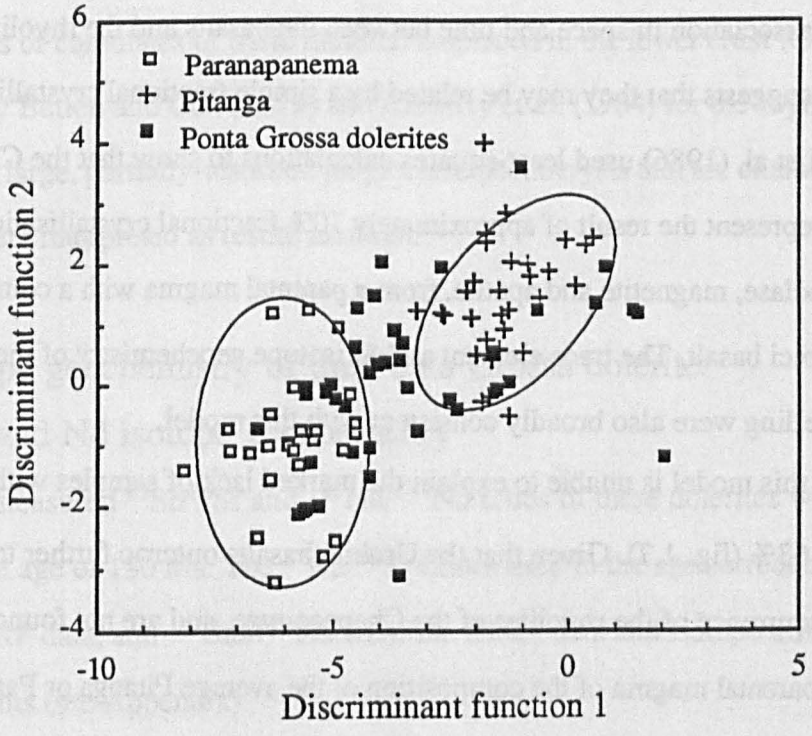

Fig. 2.13
Attempt to classify the Ponta Grossa dolerites using discriminant functions calculated such as to give maximum discrimination between basalts of the Pitanga and Paranapanema magma types (see Appendix). Basalt data from Peate (1989).

Paranapanema type (Piccirillo et al., 1987), which suggests that the Ourinhos rhyolites lie at a slightly higher stratigraphic level (Peate et al., 1992).

The most silicic intrusive rock analysed in this study (MR-8931) is displaced from the fractionation controlled data array defined by the Ponta Grossa dolerites to lower SiO_2 and K_2O and higher FeO and CaO (fig. 2.5). Unlike most of the Ponta Grossa dolerites, sample MR-8931 is highly plagioclase phyric (approximate plagioclase composition An_{45}). Most of the rhyolites of the northern Parana also contain large plagioclase phenocrysts of similar composition (An_{45-50}) (Bellieni et al., 1986). Fig. 2.11 illustrates the similarity in major and trace element composition of sample MR-8931 to the rhyolites of the Ourinhos magma type, which outcrop ~100 km to the north of the point at which this sample was collected. Piccirillo et al. (1990) encountered dykes of acidic composition (both Ourinhos and Guarapuava type) in the Ponta Grossa region, and have reported rhyolite xenoliths (Ourinhos type) from a basaltic dyke of the Paranapanema magma type. Sample MR-8931 yielded an Ar—Ar age of 131.7 ± 0.8 Ma (Chapter 4), and this suggests that these rhyolites were erupted from dykes in the Ponta Grossa region at approximately the same time as the basalts of the northern Parana.

The close association in space and time between the basalts and the rhyolites of the northern Parana suggests that they may be related by a simple fractional crystallisation process. Bellieni et al. (1986) used least-squares calculations to show that the Chapeco rhyolites could represent the result of approximately 70% fractional crystallisation of augite, pigeonite, plagioclase, magnetite and apatite, from a parental magma with a composition of the average Urubici basalt. The trace element and Sr isotope geochemistry of the rhyolites used in the modelling were also broadly consistent with this model.

However, this model is unable to explain the marked lack of samples with SiO_2 between 54 and 63% (fig. 1.7). Given that the Urubici basalts outcrop further to the south than the main occurrence of the rhyolites of the Chapeco type, and are not found north of latitude 26°S, a parental magma of the composition of the average Pitanga or Paranapanema basalt type would probably be more realistic. Although least-squares calculations can in fact force a reasonable solution to the major element data, assuming a parental magma with the composition of the average Ponta Grossa dolerite, the fractionation trends defined by the

more evolved of the Ponta Grossa dolerites do not pass through the rhyolite data, but are displaced to lower SiO_2, K_2O and higher CaO and Fe_2O_3 (fig 2.11). This suggests that the rhyolites are not related to these less evolved samples by crystal fractionation.

The Chapeco rhyolites yield relatively high pyroxene crystallisation temperatures of between 1133 ± 24°C and 1126 ± 23°C (Bellieni et al., 1986). In contrast, augite crystals from the evolved sample MR-8932 from the Ponta Grossa yielded significantly lower temperatures of 890—960°C (±~60°C) using the Kretz (1982) geothermometer (section 2.2.1). The relatively high eruption temperatures of the rhyolites led Bellieni et al. (1986) to suggest that these rocks are not fractionates of a more basic magma, but instead represent partial melts of a source of basic to intermediate composition under H_2O undersaturated conditions. Precambrian granulites of basic and intermediate composition have been recorded from this part of southern Brazil (Hasui, 1982; Almeida and Hasui, 1984), but these have very variable compositions (Oliveira, 1982), and have high Rb/Sr ratios (Bellieni et al. (1986) showed that the Rb/Sr values of the Chapeco rhyolites constrain their source to have had Rb/Sr values of about 0.05), and do not represent a suitable source material. Bellieni et al. (1986) therefore proposed that the rhyolites of the northern Parana represent partial melts of cumulates of basic material emplaced in the lower crust (Cox, 1980), as proposed by Betton and Cox (1979) and Cleverly et al. (1984) for the rhyolites of the Karoo. The large, partially-resorbed plagioclase phenocrysts that are characteristic of these rhyolites were interpreted as restite material.

2.9 Isotope geochemistry of the Ponta Grossa dolerites

2.9.1 Sr and Nd isotope geochemistry

The measured $^{87}Sr/^{86}Sr$ and $^{143}Nd/^{144}Nd$ ratios of these dolerites were age corrected assuming an age of 130 Ma. The $^{87}Rb/^{86}Sr$ values used in the age correction were calculated from the XRF data, and $^{147}Sm/^{144}Nd$ from the INAA data and isotope dilution measurements (see Appendix).

The new data are presented in fig. 2.14, together with the data for 8 dolerite samples reported by Piccirillo et al. (1990). The dolerites have Sr and Nd isotopic compositions which are very different from the Gramado and Esmeralda basalts of the southern Parana,

and most have higher εSr values than basalts of the Urubici magma type. Unfortunately there are at present no Nd isotope data for the basalts of the northern Parana, but the range in Sr isotope composition of these basalts (Petrini et al., 1987; Cordani et al., 1988; Peate, 1989) is similar to that of the Ponta Grossa dolerites (fig. 2.14).

All samples have positive εSr and negative εNd values, which means that they contain a contribution from a source with time-integrated high Rb/Sr and low Sm/Nd relative to the bulk earth. Note that there is no systematic variation of $^{87}Sr/^{86}Sr$ of $^{143}Nd/^{144}Nd$ with degree of fractionation (fig. 2.15), which suggests that the magmas did not undergo significant crustal-level contamination. This implies that the high εSr and low εNd values of these dolerites were inherited from their mantle source (this is discussed further in section 2.9.5).

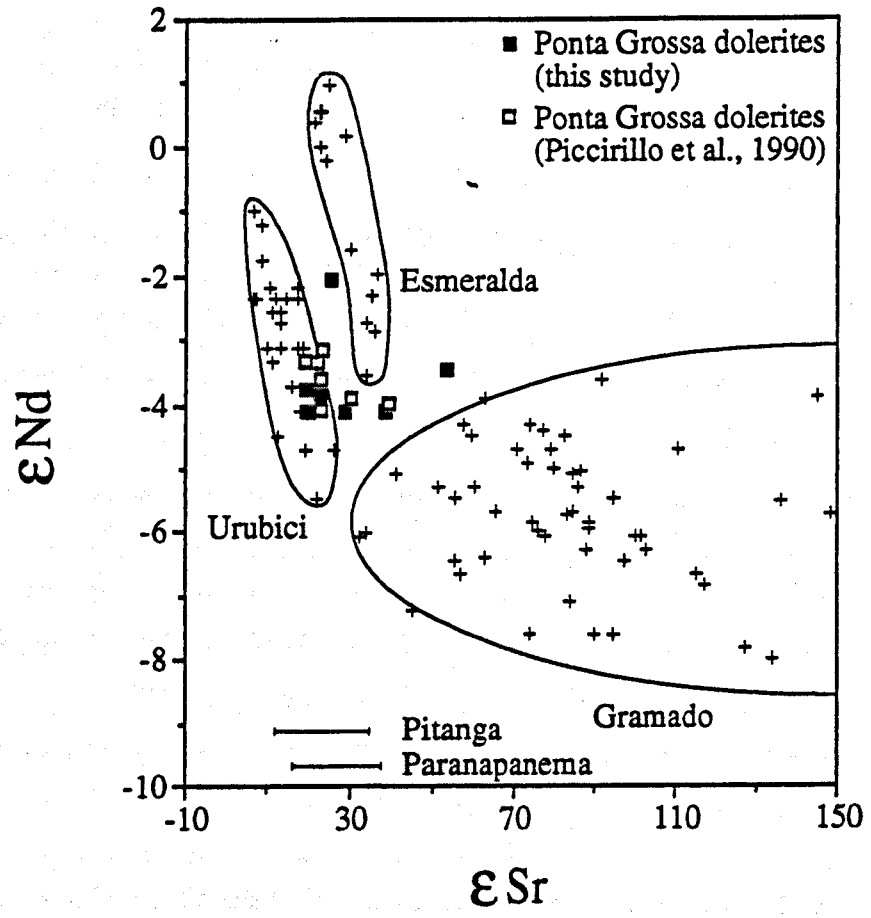

Fig. 2.14
Sr and Nd isotope compositions of the Ponta Grossa dolerites (data from Piccirillo et al., 1988; and this study), compared with those of the Parana lavas (data from Peate, 1989). Age corrections were applied assuming an age of 130 Ma for all samples.

The leaching experiments described in Chapter 3 suggest that subsolidus alteration will have had little effect upon samples with L.O.I.<2%. Care was taken to use only the

freshest samples (L.O.I.<1.5%) for isotope analysis, although one dolerite with a relatively high L.O.I. (5.61%; sample MR-8921) was also analysed, in order to estimate the effects of alteration upon the isotopic composition of Sr and Nd in these dolerites. The high L.O.I. of this sample is due to the fact that it contains a large amount of partially devitrified glass,

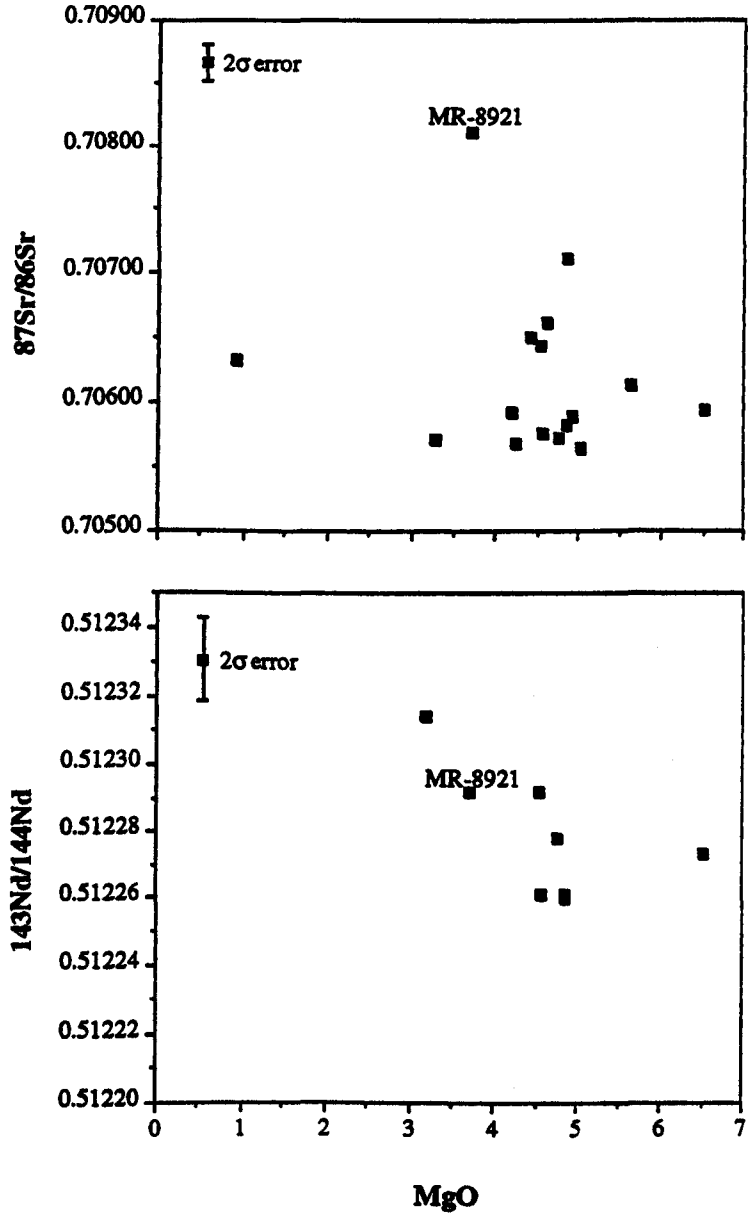

Fig. 2.15
Variation in the Sr and Nd isotope composition of the Ponta Grossa dolerites with weight percent MgO. Errors represent average 2s error on the isotope measurements. Note that there is no evidence for open system behaviour. The relatively high 87Sr/86Sr value of sample MR-8921 is due to the effects of subsolidus alteration (section 2.9.1); note that the Nd isotope composition of this sample appears not to have been affected by the alteration process.

which has been partially replaced by secondary minerals. This sample has the highest $^{87}Sr/^{86}Sr$ ratio of all those analysed (fig. 2.15), but note that the alteration process appears to have had no significant effect upon the isotopic composition of Nd.

2.9.2 Pb isotope geochemistry

There have been no previous Pb isotope studies of the Ponta Grossa dolerites. Pb isotope data for 18 samples are reported here as measured ratios (corrected for mass spectrometer fractionation) rather than initial ratios. This is because precise U and Th data by

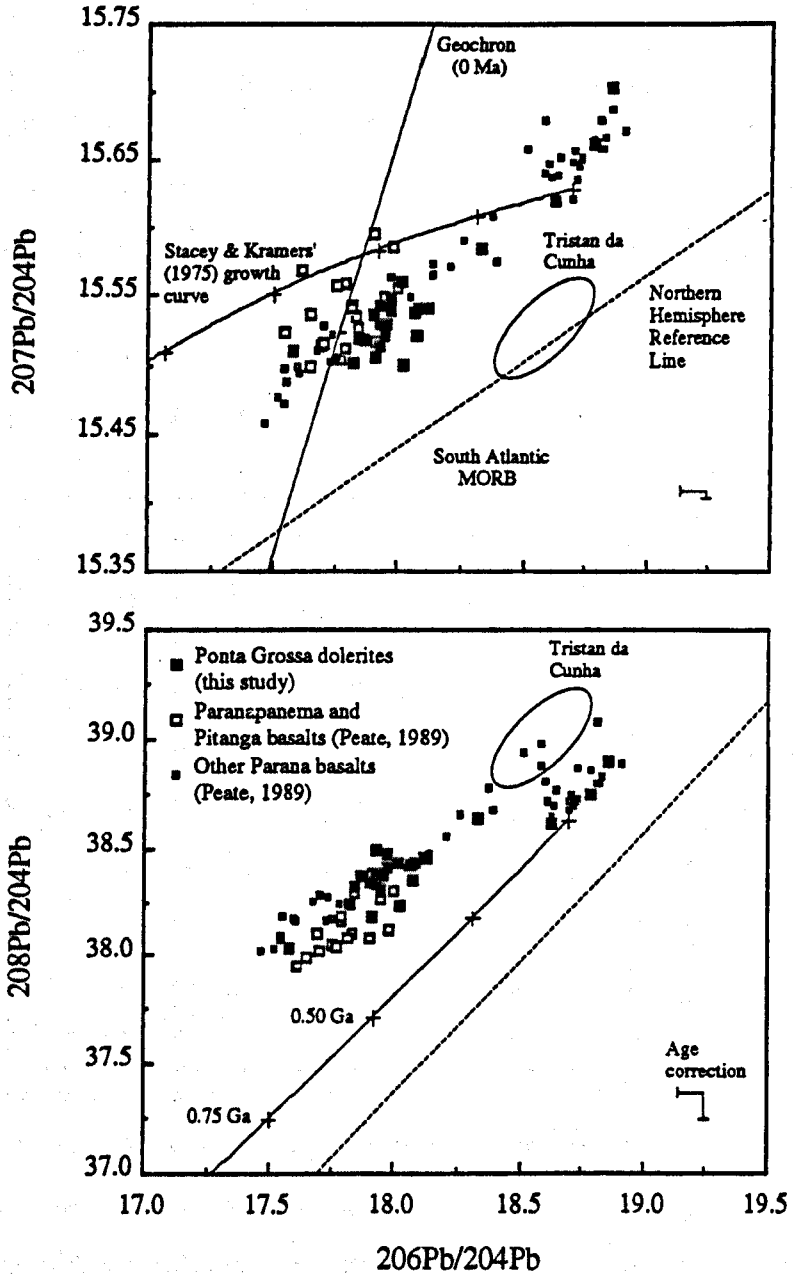

Fig. 2.16
Pb isotope compositions of the Ponta Grossa dolerites, the Pitang and Paranapanema basalts, and the flood basalts of the southern Parana (basalt data from Peate, 1989). The Pb isotope composition of oceanic basalts from Tristan da Cunha in the South Atlantic (data from le Roex, 1989), and the Northern Hemisphere Reference Line of Hart (1984) are shown for reference.

INAA were not available for all samples; the concentrations of U and Th in these rocks are close to their detection limits for the XRF technique and the XRF data are therefore likely to be inaccurate. The average U/Pb and Th/Pb ratios for these samples are 0.166 and 0.588 respectively (average of 15 samples), which correspond to relatively small age corrections of 0.251, 0.011 and 0.216 for $^{208}Pb/^{204}Pb$, $^{207}Pb/^{204}Pb$ and $^{206}Pb/^{204}Pb$ respectively, assuming an age of 130 Ma for all samples (fig. 2.16).

The Pb isotope composition of most samples fall to the right of the 0 Ma geochron in fig. 2.16a, which means that the Pb in the Ponta Grossa dolerites has had a complex, multi-stage history, and has evolved in a system with high U/Pb relative to the bulk earth at some time in the past. The data lie close to the fields defined by Parana basalts of the Pitanga and Paranapanema magma types (data from Peate, 1989). The basalt data do not include the borehole samples which Peate considered to have had their Pb isotopic compositions modified as a result of contamination introduced during the drilling process. Note that an age correction has also not been applied to Peate's data because of the lack of accurate U and Th data for these samples, but because there is little variation in U/Pb and Th/Pb either within or between the various magma types, an age correction would have little effect upon the relative positions of these magma types in fig. 2.16.

The dolerites are displaced to higher $^{207}Pb/^{204}Pb$ and $^{206}Pb/^{204}Pb$ than the NHRL of Hart (1984), and lie within the field defined by DUPAL basalts from the South Atlantic. Dupre and Allegre (1983) first drew attention to the fact that oceanic basalts from the South Atlantic are anomalous in terms of their Pb (and Sr and Nd) isotope compositions. DUPAL basalts are characterised by higher $^{208}Pb/^{204}Pb$, $^{207}Pb/^{204}Pb$ and $^{87}Sr/^{86}Sr$ than 'normal' oceanic basalts, and their source region must therefore have high time-integrated Th/U, $^{235}U/Pb$ and Rb/Sr relative to the source of most oceanic basalts. Hart pointed out that this cannot be the result of recent (<300 Ma) contamination by crustal material, since this would lead to steep mixing arrays in the $^{208}Pb/^{204}Pb$, $^{206}Pb/^{204}Pb$ diagram. Hart (1984) argued that this anomalous mantle domain was produced early in the Earth's history by core-mantle-crust differentiation processes. In an alternative explanation (Hawkesworth et al., 1986), the Pb of DUPAL basalts is derived from ancient lithospheric mantle material that was

remobilised during the Parana event, and the $^{207}Pb/^{206}Pb$ array therefore has age significance, in that it represents the age of this material.

2.9.3 Age significance of the Pb isotope data

The gradient (m) of the best-fit line to the data in fig. 2.16a is controlled by the time since U/Pb was last fractionated, and the isotopic composition of Pb homogenised;

$$m=^{235}U/^{238}U \times (e^{\lambda 2T} - e^{\lambda 2t})/(e^{\lambda 1T} - e^{\lambda 1t})$$

where t is the age of the dolerites, T the age of the source, and λ_2 and λ_1 are the decay constants of ^{235}U and ^{238}U respectively.

The ratio $^{235}U/^{238}U$ will not have been fractionated during partial melting or subsequent fractional crystallisation. $^{207}Pb/^{206}Pb$ secondary isochron ages are therefore likely to provide a reasonably accurate estimate of the age of the source of the Pb. The variation in $^{238}U/^{204}Pb$ (μ) of the source determines the distribution of the samples along the secondary isochron, and the approximation to a straight line is determined by the degree of homogenisation of the Pb isotope ratios at the time of formation of the source.

The Sr and Nd isotope data presented in section 2.8.1 were used to show that the Ponta Grossa dolerites have not undergone significant crustal level contamination. Therefore, the Pb isotope variation within the Ponta Grossa dolerites is likely to be a result of source heterogeneity, and can provide information upon the age of the source.

The Pb isotope data lie upon a line in fig. 2.16a, which if interpreted as a secondary isochron, and assuming $^{235}U/^{238}U=1/137.88$, corresponds to a $^{207}Pb/^{206}Pb$ age of approximately 2.1 Ga. Note that the data are not well correlated ($r^2=0.841$), and that the slope of the isochron is determined mainly by a few samples which are displaced to high $^{206}Pb/^{204}Pb$ and $^{207}Pb/^{204}Pb$. However, the isochron age calculated from these data is very similar to the Pb secondary isochron ages of 1.8 and 2.2 Ga obtained by Hawkesworth et al. (1986) for basalts from the southern Parana (the Urubici and Gramado magma types respectively), and an age of 2.18 Ga obtained by Mantovani et al. (1986) for 9 samples of the basement rocks from the region of the Parana. Hawkesworth et al. (1986) considered

their Pb data to have age significance, and suggested that 'the major crust-forming event in this area took place at about 2200 Ma ago, and in the following 200—300 Ma, mantle material stabilised within the continental lithosphere'.

Although the $^{207}Pb/^{206}Pb$ secondary isochron age is somewhat older than the model source ages calculated using the Nd data (section 2.9.5), the T^{Nd} ages are quite likely to represent underestimates of the true age of the source, because Sm/Nd ratios will be significantly fractionated (decreased) during melting.

2.9.4 Pb isotope evolution

The Pb isotope data presented in section 2.9.2 suggests that the Pb in the Ponta Grossa dolerites has had a multi-stage history, the Pb having evolved in systems with different $^{238}U/^{204}Pb$ (μ) and $^{232}Th/^{204}Pb$ (ω) for different lengths of time. A minimum of 3 stages are required to account for the observed Pb isotope variation; Stage 1, from 4.57 Ga to 2.1 Ga; Stage 2, from 2.1 Ga to 130 Ma; and Stage 3, from 130 Ma to the present. Note that there is no direct evidence for the conditions of the earliest stage of evolution. At 2.1 Ga a major crust-forming event occurred, and the Pb that was later incorporated into the dolerites evolved in a number of isolated systems, each characterised by different μ and ω. If the measured Pb isotope ratios of the dolerites are corrected for U and Th decay during the last 130 Ma, and if it is assumed that the Pb evolved according to Stacey and Kramers' (1975) two stage model prior to 2.1 Ga, then the range in μ and ω in the source that is

	STAGE 1	STAGE 2	STAGE 3	STAGE 4
Time	4.57 Ga	3.70 Ga	2.10 Ga	0.13 Ga	0.00 Ga
$^{206}Pb/^{204}Pb$	9.307	11.15	15.16	16.74—18.57	16.95—18.35
$^{208}Pb/^{204}Pb$	29.48	31.23	34.80	37.30—37.49	37.55—37.74
$^{238}U/^{204}Pb$	7.192	9.735	4.409—9.543	10.63	10.63
$^{232}Th/^{204}Pb$	32.21	36.84	24.43—26.29	38.89	38.89

Table 2.4
Model for the Pb evolution of Pb in the Ponta Grossa dolerites. Source compositions at 4.57 and 3.70 Ga after Stacey and Kramers (1975). Average μ and ω values at 0.13 Ga calculated from the INAA data.

required to account for the observed variation in the $^{206}Pb/^{204}Pb$ and $^{208}Pb/^{204}Pb$ of these rocks can then be calculated (table 2.4).

The μ and ω values of the dolerite source correspond to elemental U/Pb and Th/Pb ratios of between 0.068 and 0.148, and 0.367 and 0.395 respectively. The present-day average U/Pb and Th/Pb ratios of these dolerites are 0.166 and 0.588, which suggests that both Th/Pb and U/Pb were increased during partial melting of the source at 130 Ma. This is consistent with the relative compatibilities of these elements in mantle minerals. For comparison, average continental crust has U/Pb=0.114, Th/Pb=0.438, and average lower crust has U/Pb=0.070, Th/Pb=0.265.

Note that the calculations imply that the dolerite source was depleted in both U and Th relative to Pb during its lithospheric residence time of 1.97 Ga, most likely as a result of a melt extraction event during this period. Alternatively, the model assumed for Pb evolution prior to 2.1 Ga is incorrect, and the Pb that was later incorporated into the Ponta Grossa dolerites evolved in a reservoir with lower μ and ω at some time before 2.1 Ga.

2.9.5 Sr and Nd isotope evolution

Nd model ages of the Ponta Grossa dolerites are presented in table 2.4. The Nd model age (T^{Nd}) of an igneous rock is often taken to represent the time of residence in the lithosphere since melt extraction from the mantle (McCulloch and Wasserburg, 1978). The measured Sm/Nd of the dolerites is assumed to represent that of their source, which is assumed to have been extracted from mantle of known composition in a single event, and to have remained unfractionated since that time (Arndt and Goldstein, 1987). The model age obtained by this method is sensitive to the composition assumed for the mantle source. DePaolo and Wasserburg (1976) used a chondritic mantle composition (CHUR), whereas Jacobsen and Wasserberg (1979) and DePaolo (1981) used a depleted mantle composition (DM). Using CHUR yields model ages for the dolerites of between 630 and 720 Ma. If a depleted mantle composition is used in the calculations, model ages of between 1280 and 1340 Ma are obtained (table 2.4). Of these ages, those obtained using DM are most similar to (but significantly younger than) the source ages calculated using the Pb isotope data. The

T^{Nd}_{DM} ages should be regarded as underestimates of the true source age, because Sm/Nd is likely to have been fractionated (decreased) during the melting event at 130 Ma.

T^{Sr}_{DM} ages can be calculated in a similar manner, but these are less likely to represent

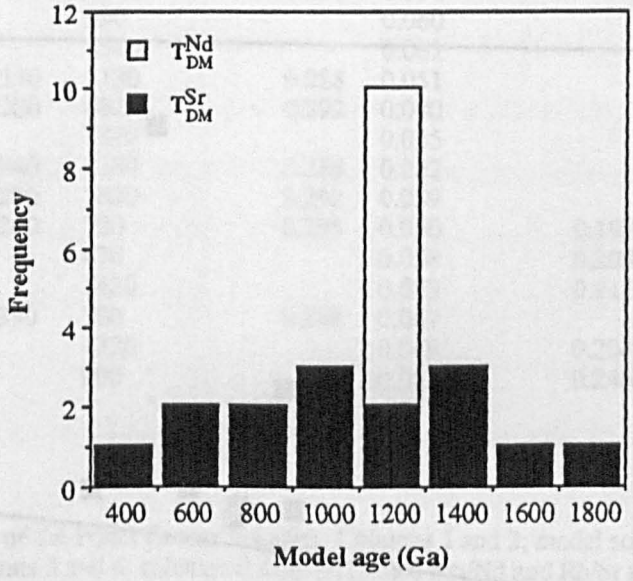

Fig. 2.17
Sr and Nd model ages of the Ponta Grossa dolerites (calculated relative to the depleted mantle of DePaolo, 1987). Note the relatively large range of the T^{Sr}_{DM} values, which suggests that Rb/Sr values were significantly fractionated during partial melting and subsequent fractional crystallisation at 132 Ma, and therefore do not represent source ages.

true source ages, because Rb/Sr is likely to have been fractionated both during melting at 130 Ma, and also during subsequent fractional crystallisation of the magmas. The two more evolved samples (MR-8928 and MR-8932) yielded relatively young T^{Sr}_{DM} ages of 720 and 470 Ma respectively. T^{Sr}_{DM} ages of the less evolved samples are between 990 and 1980 Ma; a much greater range than for the T^{Nd}_{DM} ages of the same samples (fig. 2.17). Note that the altered sample MR-8921 yielded an impossibly old source age of 4.82 Ga.

The time-integrated Rb/Sr and Sm/Nd values of the dolerite source was calculated using the source age of 2.1 Ga obtained from the Pb isotope data. The time-integrated Rb/Sr ratios are consistently lower (between 0.049 and 0.061) than the measured Rb/Sr in the rocks today (0.052—0.257) (fig. 2.18), whereas the time integrated Sm/Nd values of the

source (0.288—0.295) are significantly higher than the measured Sm/Nd values of the dolerites (0.192—0.236).

The calculated time-integrated Rb/Sr and Sm/Nd ratios suggest that the source of the Ponta Grossa dolerites was more depleted than average continental crust (Rb/Sr=0.123,

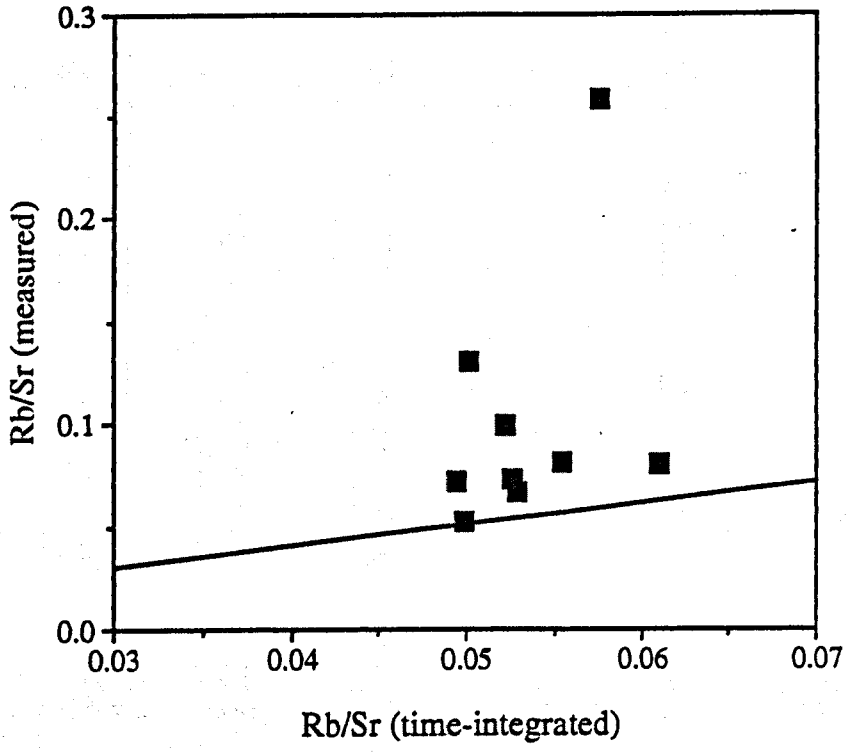

Fig. 2.18
Measured and time integrated (source) Rb/Sr values of the Ponta Grossa dolerites. The time integrated values were calculated assuming the source age of 2.1 Ga obtained from the Pb isotope data.

Sm/Nd=0.219), but significantly enriched relative to the bulk earth (Rb/Sr=0.029, Sm/Nd=0.327). The fact that the dolerites yield Proterozoic T_{DM}^{Nd} (and $^{207}Pb/^{206}Pb$) ages, yet have not undergone crustal-level contamination is evidence that they were derived from a source from within the subcontinental lithospheric mantle.

2.10 Conclusions

The Ponta Grossa dykes are composed of petrographically and mineralogically rather uniform dolerites, which underwent closed-system crystallisation at relatively shallow levels in the crust. Least-squares modelling of the major element variation has been used to

Sample	1 T^{Nd}_{DM}	2 T^{Sr}_{DM}	3 Sm/Nd	4 Rb/Sr	5 Sm/Nd	6 Rb/Sr
MR-898		1980		0.050	0.211	0.052
MR-899	1310	1560	0.290	0.053	0.236	0.067
MR-8915	1300	1100	0.291	0.051		0.086
MR-8914		990		0.060		
MR-8918		1540		0.061		0.079
MR-8919	1330	1130	0.288	0.051		0.084
MR-8921	1280	4820	0.292	0.080		0.043
MR-8922		1320		0.055		0.081
MR-8925	1340	1180	0.288	0.052		0.082
MR-8926	1280	1620	0.292	0.059		0.073
MR-8928	1240	720	0.295	0.050	0.192	0.130
MR-8932		470		0.058	0.203	0.257
MR-8942		1420		0.053	0.211	0.072
MR-8990	1330	780	0.288	0.067		0.171
MR-8991		1320		0.049	0.204	0.071
MR-8992		990		0.052	0.240	0.098

Table 2.5
Sr and Nd isotopic evolution of the Ponta Grossa dolerites. Columns 1 and 2; model source ages of the Ponta Grossa dolerites. Columns 3 and 4; calculated time-integrated Sm/Nd and Rb/Sr ratios of the dolerite source. Columns 5 and 6; measured Sm/Nd and Rb/Sr ratios of the dolerites.

constrain the composition of the fractionating assemblage (clinopyroxene+plagioclase±olivine±magnetite± apatite), and the trace element variation displayed by these dolerites is broadly consistent with this model. The Ponta Grossa dolerites appear to be intrusive equivalents of the Pitanga and Paranapanema basalt magma types, and to have fed the youngest basalt flows of the lava field which outcrop to the north of latitude 26°S. The dolerites do not represent parental magmas to the rhyolitic lavas of the northern Parana.

The dolerites have positive εSr and negative εNd values, which means that they have received a contribution from a source with time-integrated high Rb/Sr, low Sm/Nd relative to the bulk earth. These rocks have not undergone significant crustal-level contamination, and this suggests that their isotope and trace element signatures were derived largely from the subcontinental lithospheric mantle. This conclusion is supported by the new Pb isotope data; a $^{207}Pb/^{206}Pb$ secondary isochron yielded an age of approximately 2.1 Ga, similar to

ages obtained by previous authors for the basement rocks of this part of Brazil. An attempt to model the isotopic evolution of Sr, Nd and Pb in these samples suggests that the source of these dolerites was enriched in U relative to Pb, and had variable, time-integrated high Rb/Sr and low Sm/Nd (0.05—0.06 and 0.29—0.30 respectively) relative to the bulk earth. The isotopic evidence therefore suggests that the dolerites were derived from a source within the subcontinental lithospheric mantle. The high LILE:HFSE ratios of these dolerites, and the HREE depletion of certain samples have been shown not to be an artifact of low-pressure crystal fractionation, which implies that these characteristics were inherited from the mantle source.

Chapter 3

Geochemistry of the dykes from Sao Paulo State

3.1 Introduction

The Precambrian basement rocks of Sao Paulo and Rio de Janeiro States are intruded by numerous SW—NE oriented basaltic dykes (Damasceno, 1966). These dykes extend westwards as far as Serra dos Itatins (approximately 400 km east of the most easterly occurrences of the Ponta Grossa dolerites), and eastwards to the coast north of Rio de Janeiro (Comin-Chiaramonti et al., 1983; Piccirillo et al., 1988). Amaral et al. (1966) obtained K—Ar ages of between 127 and 137 Ma for six samples of these dykes collected from the region of Ubatuba, and an age of 119 Ma for a dolerite from the nearby island of Sao Sebastiao. Several samples were dated by the Ar—Ar technique in the course of this study, and these yielded ages of between 80.9 ± 0.4 and 135.8 ± 1.1 Ma (see Chapter 4). These ages suggest that although many of the dolerites have ages similar to those of the flood basalts to the west, some are considerably younger than the lavas.

The dolerite samples analysed in this study were collected from an area of approximately 7000 km^2 to the north and east of the town of Sao Sebastiao (fig. 3.1). Geochemically, these dolerites differ from those of the Ponta Grossa region in that they have higher Nb concentrations (lower Zr/Nb values), and relatively high concentrations of the LIL elements Rb, Ba and Sr (fig. 3.2a). The Sao Paulo dolerites do not appear to be intrusive equivalents of any of the Parana flood basalts (fig. 3.2b) although a few of the samples have similar trace element concentrations to the basalts of the Urubici magma type (see detailed discussion in section 3.2.7).

The dolerites of Sao Paulo State can be divided into three groups on the basis of their trace element geochemistry (fig. 3.2a), and these appear not to be related by any simple petrogenetic process. These have been termed the Paraiba, Ubatuba and Sao Sebastiao magma types, and the geochemistry and petrogenesis of these three magma types are discussed separately in this Chapter.

Very few previous geochemical studies of these dolerites have been carried out.

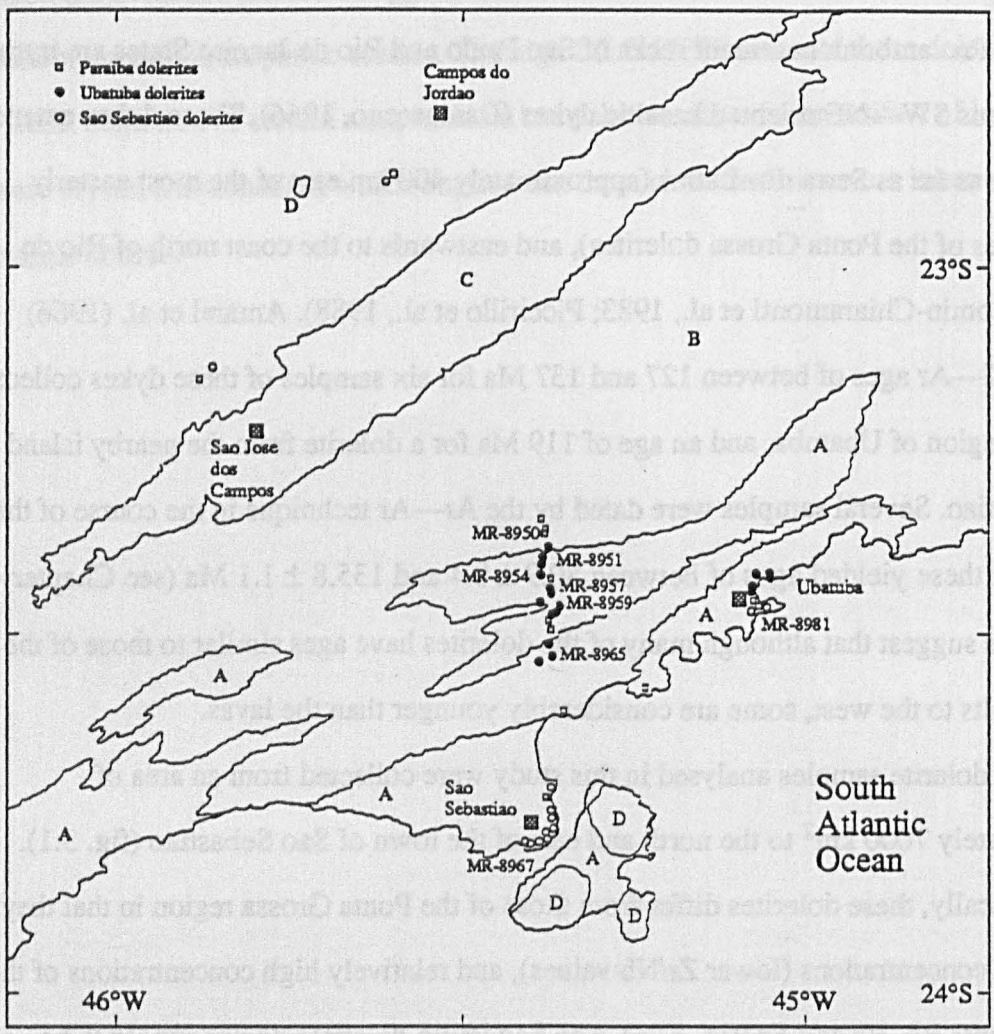

Fig. 3.1
Simplified geological map of Sao Paulo State, showing sampling localities. Key; A and B; basement rocks of Archaean and Proterozoic age respectively; C, Cenozoic sediments of the Taubate Group; D, alkalic intrusive rocks of Cretaceous age. The locations of the samples that were selected for Ar—Ar analysis are shown.

Piccirillo et al. (1988) analysed 22 dolerite samples which were collected from a somewhat larger area than was covered in this study. Significantly, most of their samples fall into the three geochemical groups defined here (fig. 3.3), and this suggests that the samples collected in this study are representative of the entire swarm.

3.2 The dolerites of the Paraiba magma type

3.2.1 Introduction

12 samples of the Paraiba magma type were collected from the region north of the town of Sao Sebastiao, and from the coastal region between Sao Sebastiao and Ubatuba (fig. 3.1). Sample MR-8950 has been dated by the Ar—Ar method at 133.3 ± 1.7 Ma

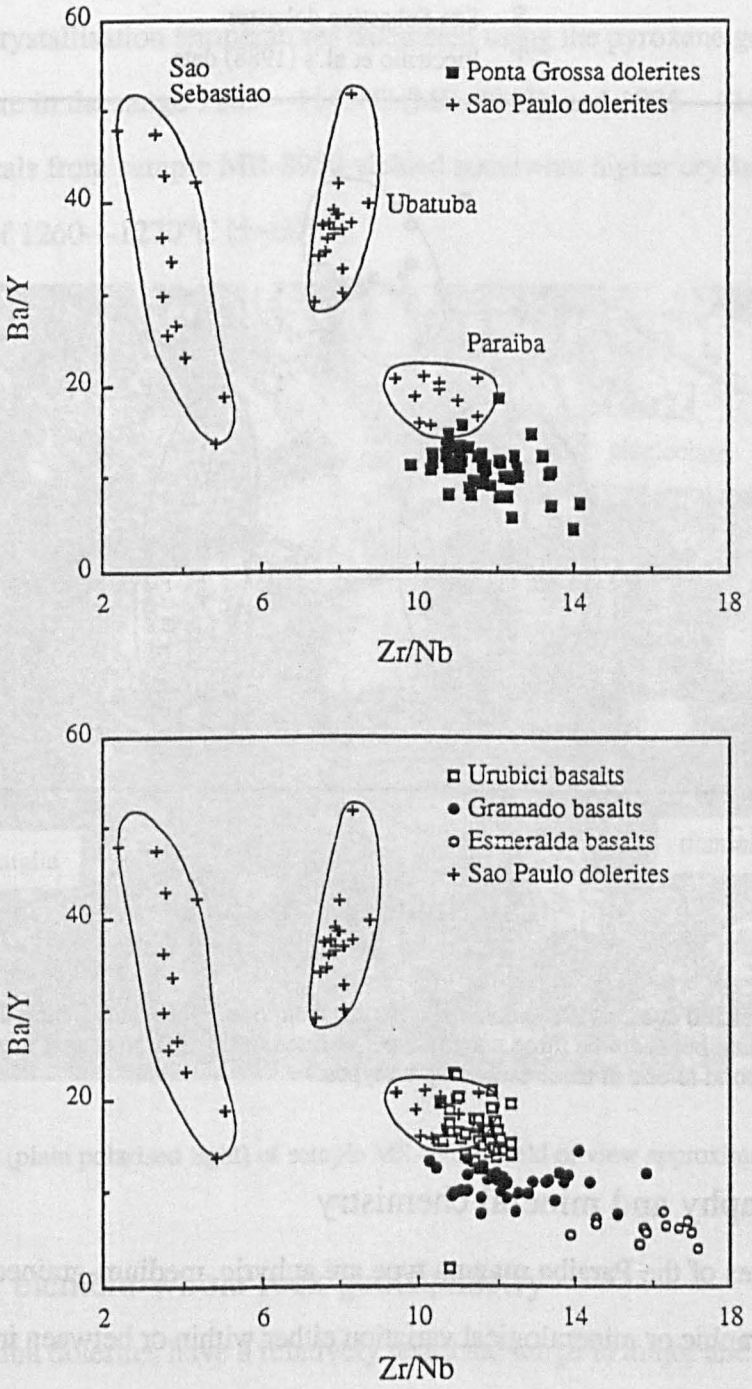

Fig. 3.2
Zr/Nb—Ba/Y variation within the Sao Paulo dolerites, the Ponta Grossa dolerites (a), and the flood basalt lavas of the southern Parana (b) (data from Peate, 1989). The Sao Paulo dolerites are divisible into three groups, which have been termed the Paraiba, Ubatuba and Sao Sebastiao magma types.

(Chapter 4), which suggests that these dolerites were intruded at the time of the Parana flood basalt magmatism and continental rifting in the South Atlantic. Despite this, it will be argued in section 3.2.7 that these dolerites do not have extrusive equivalents in the Parana lava pile, and that the dykes therefore do not represent feeders to the flood basalts to the west.

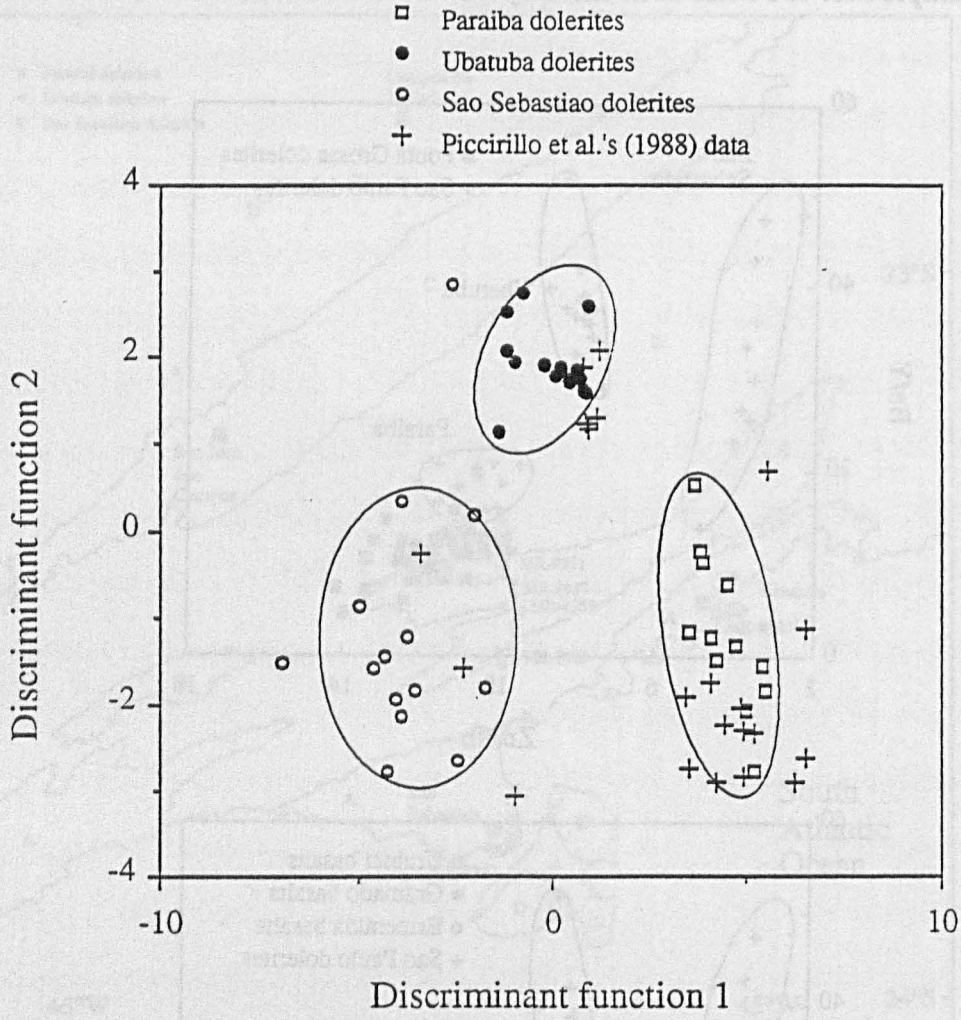

Fig. 3.3
Classification of Piccirillo et al.'s (1988) data for dolerites from Sao Paulo State, using discriminant funcion analysis to discriminate between the three magma types defined in fig. 3.2. Note that most of Piccirillo et al.'s samples correspond to one of these three magma types.

3.2.2 Petrography and mineral chemistry

The dolerites of the Paraiba magma type are aphyric, medium-grained, and there is very little petrographic or mineralogical variation either within or between individual intrusions. The mineral chemistry of three samples (MR-8943, MR-8950, and MR-8982) was investigated in detail using electron microprobe analysis (see Appendix). MR-8943 and MR-8982 were respectively, the least and most evolved samples of this magma type encountered, but all three samples were very similar in terms of their mineral chemistry. The

dolerites display a subophitic texture, in which large anhedral crystals of augite (En_{40-44}, Wo_{35-38}, Fs_{12-25}) partially enclose sericitised prismatic crystals of plagioclase (An_{47-56}) and partially oxidised titanomagnetite (fig. 3.4). Small grains of pigeonite (En_{47-52}, Wo_{9-10}, Fs_{38-43}) are present in samples MR-8943 and MR-8950. Hornblende occurs as overgrowths on augite in samples MR-8950 and MR-8982. A small amount of quartz is present in all samples, and apatite, biotite and sphene are common accessory minerals.

Augite crystallisation temperatures calculated using the pyroxene geothermometer of Kretz (1982) are in the range 1105—1145°C (MR-8943), and 1085—1115°C (MR-8982). Pigeonite crystals from sample MR-8950 yielded somewhat higher crystallisation temperatures of 1260—1270°C (±~60°C).

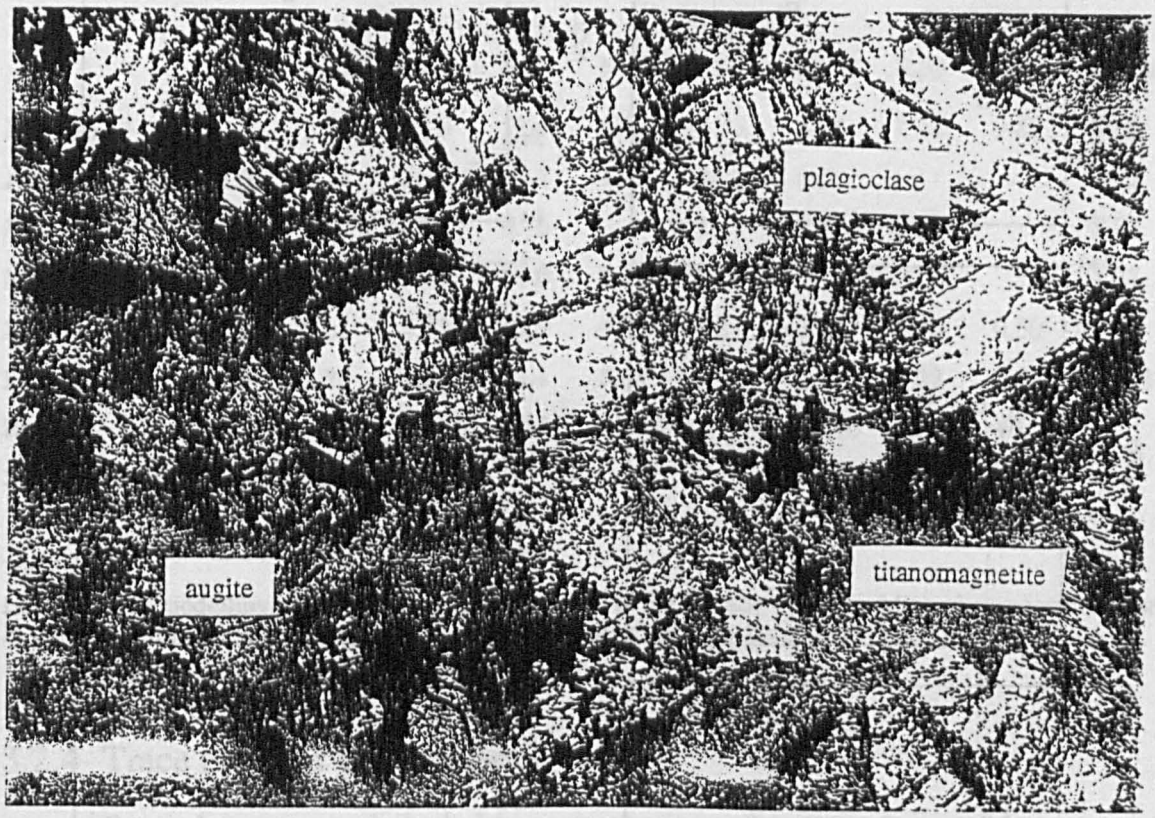

Fig. 3.4
Photomicrograph (plain polarised light) of sample MR-8950. Field of view approximately 2 x 3 mm.

3.2.3 Major element whole rock geochemistry

The Paraiba dolerites have a relatively restricted range in major and trace element geochemistry. SiO_2 concentrations vary between 50.4 and 52.8%, MgO between 4.04 and 4.90%, and all samples have $Mg/(Mg+Fe^{2+})$ ratios of between 41 and 47. These dolerites are therefore relatively evolved rocks, and none can be considered to represent primary

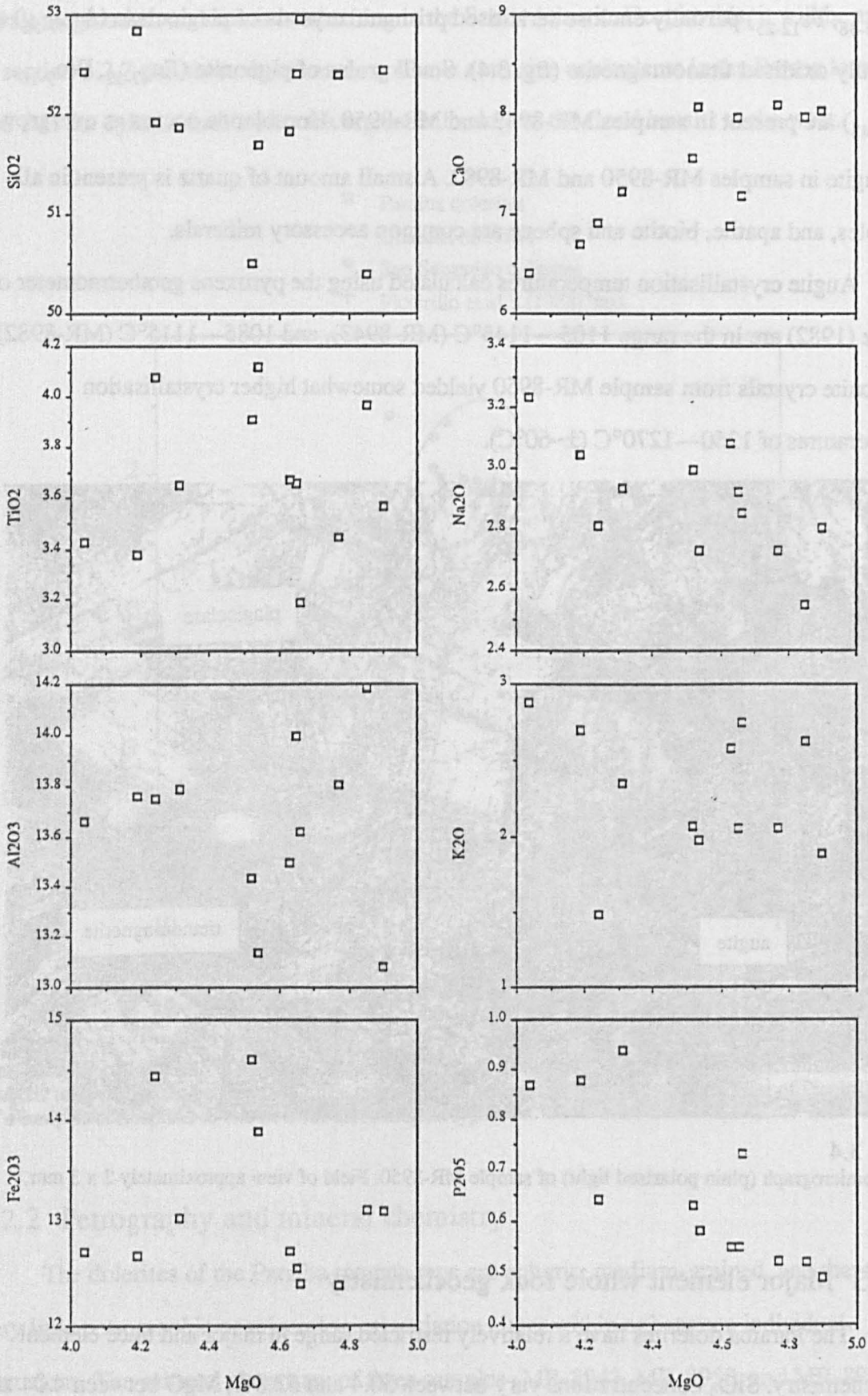

Fig. 3.5
Major element variation within samples of the Paraiba magma type

magma compositions. CIPW normative compositions (calculated assuming that 15% of the total Fe is in the Fe^{3+} state) are quartz and hypersthene normative, and cluster around the low-pressure olivine-clinopyroxene-plagioclase-liquid cotectic of Thompson et al. (1983). The major element variation displayed by the group as a whole is broadly consistent with the effects of low-pressure fractionation of an assemblage of clinopyroxene, plagioclase and magnetite (fig. 3.5), although these fractionation trends are not well defined due partly to the relatively restricted compositional range. The major element variation between samples MR-8943 and MR-8962 can be satisfactorily modelled by the least-squares approach, which predicts 19% crystallisation (F=0.81) of an assemblage of augite (59.7%), plagioclase (32.8%), and titanomagnetite (7.5%) (Σr^2=0.914; see table 3.1).

	SiO_2	TiO_2	Al_2O_3	FeO	MgO	CaO	Na_2O	K_2O	P_2O_5	Quantity
MR-8962	53.3	3.49	13.9	11.6	4.11	6.52	3.28	2.93	0.88	80.8
Augite	51.3	1.24	2.42	13.1	15.5	16.2	0.27			14.7
Plagioclase	62.1		29.5	0.76		1.11	5.96	0.65		7.92
Magnetite	3.99	24.2	1.41	67.0	0.10	3.36				1.27
MR-8943	53.0	3.61	13.2	11.9	4.95	8.11	2.83	1.90	0.50	
Product	52.9	3.25	13.2	12.1	5.49	7.54	2.99	2.22	0.65	100.39
Residual	-0.02	-0.35	+0.01	+0.16	+0.54	-0.57	+0.16	+0.32	+0.16	

Sum of squares of residuals 0.914

Table 3.1
Least-squares modelling of the major element variation in the Paraiba dolerites. Mineral compositions used in the calculations were obtained from microprobe analysis of samples MR-8943 and MR-8982.

3.2.4 Trace element geochemistry

All samples possess relatively low concentrations of the more compatible trace elements Ni (between 28 and 73ppm) and Cr (between 22 and 91ppm), which is further evidence that these dolerites have undergone extensive low-pressure fractionation (fig. 3.6). The elements Ba, Rb, Zr and Nb behave incompatibly. However, the incompatible trace element variation is not easily explained in terms of the simple fractional crystallisation model discussed in section 3.2.3. For example, assuming the least compatible element (Ba) to be perfectly incompatible, requires 35.6% crystallisation to have taken place between samples MR8943 and MR-8962 (F=0.65). Ba is unlikely to be perfectly incompatible, and

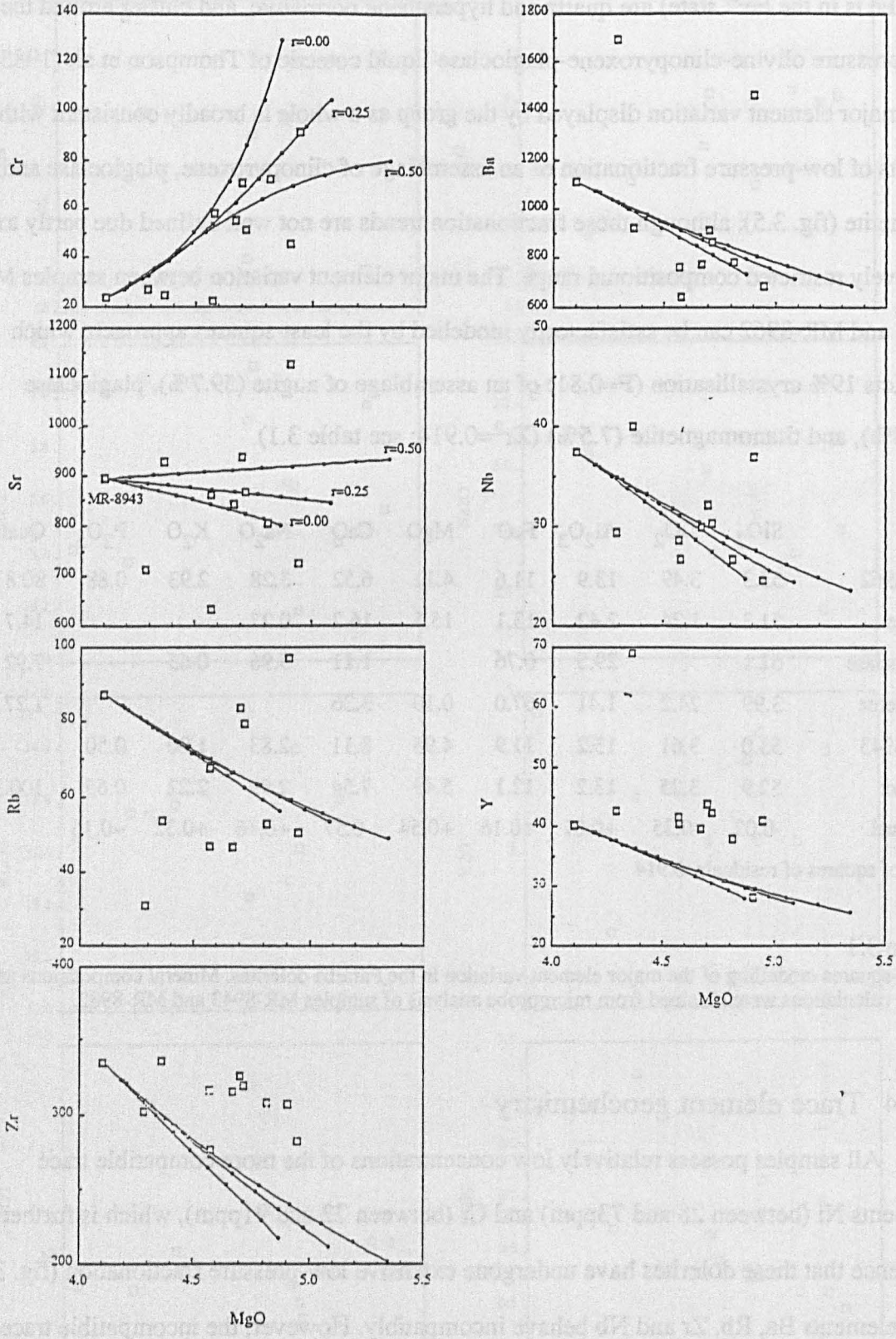

Fig. 3.6
Trace element variation within samples of the Paraiba magma type. AFC trajectories were calculated between F=0.00 and F=0.63 for r=0.00, r=0.25 and r=0.50, using the average continental crust composition of Taylor and McLennan (1981) as a contaminant, and the mineral composition of the fractionating assemblage estimated from least squares modelling of the major element variation.

hence this estimate is likely to represent an upper limit on the true value of F. However, this is significantly lower than the estimate obtained from the major element variation (F=0.81), in spite of the fact that the least-squares calculations overestimate the MgO content of sample MR-8943, and therefore have probably underestimated the value of F. This suggests that simple fractional crystallisation was not primarily responsible for the trace element variation within these dolerites, and this conclusion is supported by the variation in the Sr and Nd isotope composition of these samples (section 3.2.5).

Six samples were analysed for the rare-earth elements (REE) by INAA. All samples have very similar concentrations of the REE, which suggests that they were derived from a common source and have evolved by broadly similar petrogenetic processes. The dolerites are enriched in the LREE relative to the chondritic mantle of Nakamura (1974), and MORB (fig. 3.7). The two more evolved samples (MR-8962 and MR-8982) have slightly higher concentrations of the more incompatible LREE than the less evolved samples.

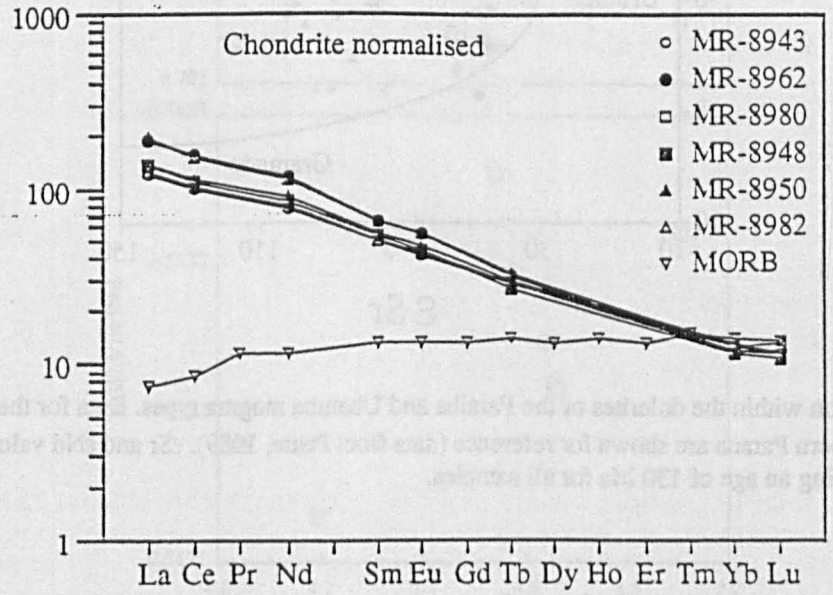

Fig. 3.7
Rare earth element concentrations of the Paraiba dolerites, normalised to the chondritic composition of Nakamura (1974). The average NMORB composition is taken from Sun and McDonough (1989).

3.2.5 Sr and Nd isotope geochemistry

In contrast with the relatively restricted major and trace element compositions, the Sr and Nd isotope compositions of the Paraiba dolerites are very variable. All samples have positive εSr and negative εNd values, which differ from those of basalts from the southern Parana (fig. 3.8). The more evolved samples have higher $^{87}Sr/^{86}Sr$ and lower $^{143}Nd/^{144}Nd$ values than the less evolved samples (fig. 3.9). Simple closed system fractionation of plagioclase, augite and magnetite cannot account for the observed Sr and Nd isotope variation, which suggests that crustal contamination has played an important role in the evolution of these rocks.

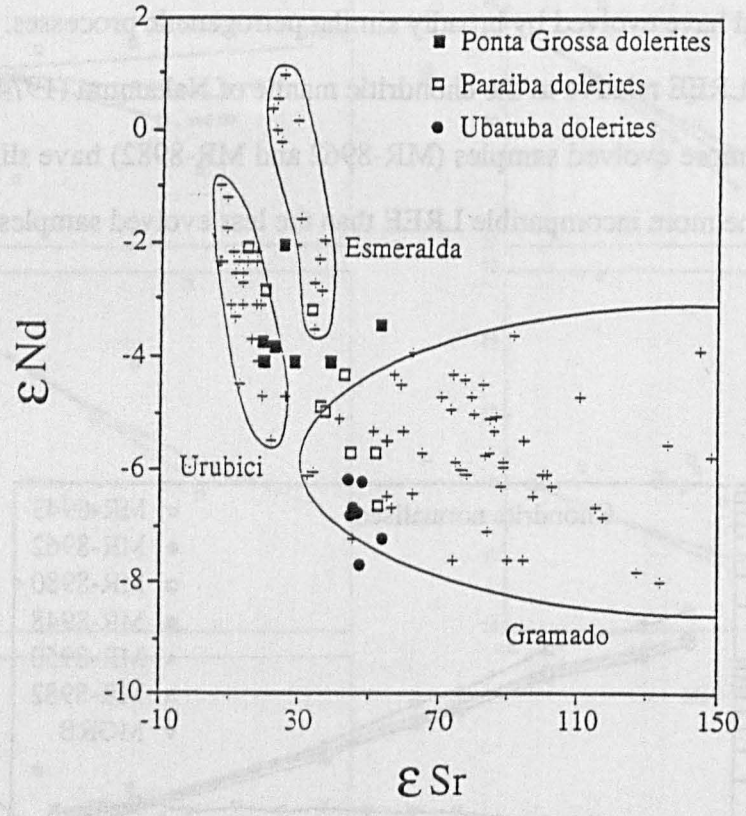

Fig. 3.8
εSr—εNd variation within the dolerites of the Paraiba and Ubatuba magma types. Data for the flood basalt lavas of the southern Parana are shown for reference (data from Peate, 1989). εSr and εNd values were calculated assuming an age of 130 Ma for all samples.

Crustal contamination of a basaltic magma may occur in several different ways. Bulk assimilation of crustal material is possible, but more frequently assimilation is accompanied by crystal fractionation (DePaolo, 1981), because the latent energy released during crystalisation increases the amount of material that can be assimilated. The contaminant may be a crustal melt, and Dickin (1981) appealed to a contamination process involving a crustal

fluid (Patchett, 1980) in order to explain the geochemical variation within basaltic lavas from the North Atlantic CFB province, which appear to have been selectively enriched in certain elements. Watson (1982) has shown that selective contamination can also occur during incomplete dissolution of minerals into a basaltic melt, because the chemical diffusivities of different elements vary by over an order of magnitude.

The nature of the contamination processs that was responsible for the geochemical variation within the Parana dolerites is investigated in detail in section 3.2.6.

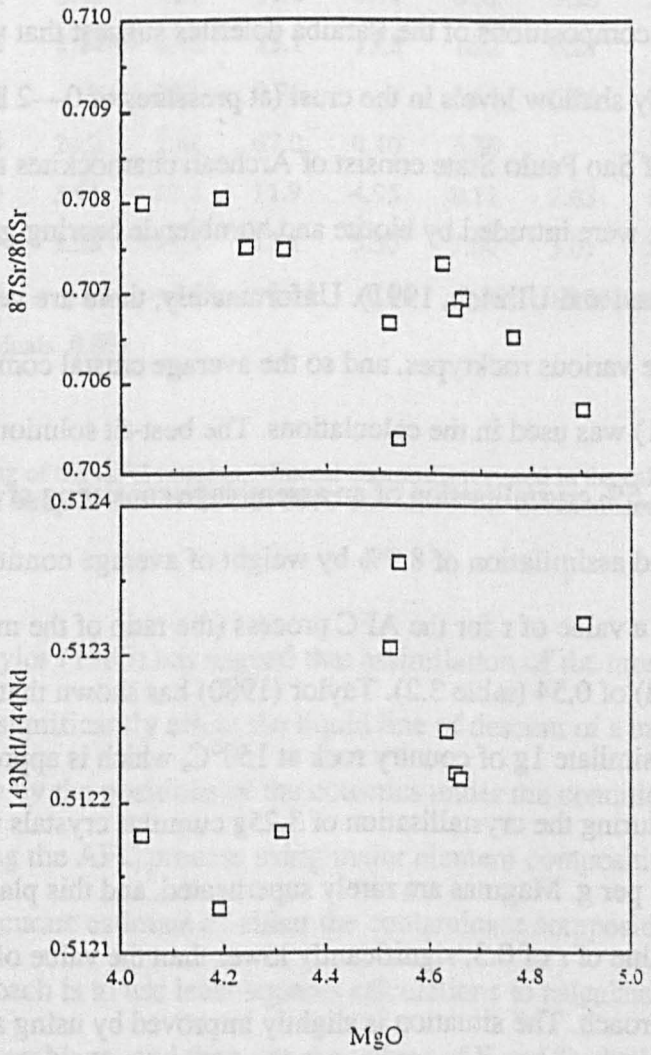

Fig. 3.9
Variation of $^{87}Sr/^{86}Sr$ and $^{143}Nd/^{144}Nd$ (at 130 Ma) with MgO, for samples of the Paraiba magma type.

3.2.6 Geochemical constraints on the contamination process

3.2.6.1 Major element constraints

The isotope variation within the Paraiba dolerites is consistent with control by an AFC process, in that the most evolved basalts are also the most contaminated. It is possible to use the major element compositions of the phenocryst and groundmass phases (section 3.2.2) to constrain the parameters of the AFC process. If some constraints can be placed on the composition of the contaminant, then least squares mixing calculations can be used to estimate the mineral composition of the fractionating assemblage and the value of r (the ratio of the mass rate of assimilation to the mass rate of fractional crystallisation), using the least and most evolved samples (MR-8943 and MR-8962 respectively).

The normative compositions of the Paraiba dolerites suggest that the AFC process took place at relatively shallow levels in the crust (at pressures of 0—2 kb). The basement rocks in this region of Sao Paulo State consist of Archean charnockites and Proterozoic metasediments which were intruded by biotite and hornblende bearing granites at between 980 and 650 Ma (Janasi and Ulbrich, 1991). Unfortunately, there are very few major element data for these various rocktypes, and so the average crustal composition of Taylor and McLennan (1981) was used in the calculations. The best-fit solution using this approach (table 3.2) required 7.5% crystallisation of an assemblage consisting of 35.2% plagioclase and 64.8% augite, and assimilation of 8.9% by weight of average continental crust. However, this yields a value of r for the AFC process (the ratio of the mass assimilated to the mass fractionated) of 0.54 (table 3.2). Taylor (1980) has shown that approximately 325 cal are required to assimilate 1g of country rock at 150°C, which is approximately equivalent to the heat released during the crystallisation of 3.25g cumulus crystals with an aggregate latent heat of 100 cal per g. Magmas are rarely superheated, and this places an approximate upper limit on the value of r of 0.3; significantly lower than the value of 0.54 obtained from the least-squares approach. The situation is slightly improved by using a more silicic contaminant in the calculations; assuming a contaminant with the composition of the upper crustal average of Taylor and McLennan (1981), yields r=0.22 for 19% crystallisation of augite (61.6%), plagioclase (33.1%) and magnetite (5.3%).

	SiO_2	TiO_2	Al_2O_3	FeO	MgO	CaO	Na_2O	K_2O	P_2O_5	Quantity
Av. crust	64.0	0.61	16.3	4.96	2.83	4.76	4.25	2.13	0.19	-10.7
MR-8962	53.3	3.49	13.9	11.6	4.11	6.52	3.28	2.93	0.88	91.9
Augite	51.3	1.24	2.42	13.1	15.5	16.2	0.27			13.2
Plagioclase	62.1		29.5	0.76		1.11	5.96	0.65		6.51
MR-8943	53.0	3.61	13.2	11.9	4.95	8.11	2.83	1.90	0.50	
Product	53.0	3.30	13.3	11.9	5.51	7.69	2.99	2.51	0.79	100.91
Residual	-0.03	-0.30	+0.04	+0.02	+0.56	-0.43	+0.16	+0.61	+0.30	

Sum of squares of residuals 1.072

	SiO_2	TiO_2	Al_2O_3	FeO	MgO	CaO	Na_2O	K_2O	P_2O_5	Quantity
U. crust 65.9	0.60	16.0	4.49	2.30	3.49	3.79	3.29	0.17	-4.03	
MR-8962	53.3	3.49	13.9	11.6	4.11	6.52	3.28	2.93	0.88	80.8
Augite	51.3	1.24	2.42	13.1	15.5	16.2	0.27			14.7
Plagioclase	62.1		29.5	0.76		1.11	5.96	0.65		7.92
Magnetite	3.99	24.2	1.41	67.0	0.10	3.36				1.27
MR-8943	53.0	3.61	13.2	11.9	4.95	8.11	2.83	1.90	0.50	
Product	52.9	3.28	13.3	12.1	5.50	7.64	3.01	2.29	0.71	100.69
Residual	-0.05	-0.32	+0.07	+0.14	+0.55	-0.48	+0.18	+0.39	+0.21	

Sum of squares of residuals 0.891

Table 3.2
Least-squares modelling of the AFC process. Mineral compositions used in the calculations were obtained by microprobe analysis of samples MR-8943, MR-8950 and MR-8982. Contaminant compositions from Taylor and McLennan (1981).

However, Taylor (1980) has argued that assimilation of the more common crustal rock types will not significantly affect the liquid line of descent of a magma, which is controlled primarily by the positions of the cotectics under the conditions of crystallisation. Therefore, modelling the AFC process using major element compositions alone is unlikely to provide a very accurate estimate of either the contaminant composition or the value of r. An alternative approach is to use least-squares calculations to calculate the composition of the fractionating assemblage, and then use the values of F and D obtained in this way to constrain r and the composition of the assimilant using the trace element approach of DePaolo (1981) (see section 3.2.6.2).

The isotope variation within the Paraiba dolerites is also consistent with contamination having occurred by a mixing process involving a silicic crustal melt. The Palmas rhyolites of the southern Parana are widely accepted to represent crustal melts (Bellieni et al., 1986), and so the average Caxias do Sul rhyolite composition was used in the modelling. The major element composition of sample MR-8962 can be reasonably modelled (by the least squares method) in terms of a mixture of 10.7% average Caxias do Sul rhyolite, and 89.3% of sample MR-8943.

These calculations indicate that it is not possible to place very tight constraints upon either the nature of the contamination process or the composition of the assimilant, using the major element variation alone.

3.2.6.2 Trace element and isotope modelling of the contamination process

The concentration and isotope composition of a trace element i in a melt that is undergoing AFC are given by

$$C_m^i = F^{-z} C_{mo}^i + \frac{rC_a^i(1 - F^{-z})}{z(r - 1)} \qquad (1)$$

$$\varepsilon_m^i = \frac{(r/r - 1)(C_a^i/z)(1 - F^{-z})\varepsilon_a^i + C_{mo}^i F^{-z}\varepsilon_{mo}^i}{(r/r - 1)(C_a^i/z)(1 - F^{-z}) + C_{mo}^i F^{-z}} \qquad (2)$$

where C_{mo}^i is the initial concentration of the element in the magma, C_a^i its concentration in the assimilant, and ε_a^i and ε_{mo}^i are the isotope compositions of the assimilant and the uncontaminated magma respectively. F is the mass proportion of liquid remaining, and $z = (r + K_d^i - 1)/(r - 1)$, where K_d^i is the bulk distribution coefficient of the element (DePaolo, 1981).

The values of F and K_d^i are constrained by the least squares calculations (table 3.1). However, it is not possible to obtain a unique solution to the AFC process, because both the value of r, and the composition of the contaminant are unknown.

The basement rocks in this region of Sao Paulo State consist largely of gniesses and charnockites which have been dated by the Rb—Sr method at ~550 Ma (Gasparini and Mantovani, 1979). To the north, these are faulted against supracrustal rocks of Archaean and mid Proterozoic age, which were deformed and metamorphosed during the Brasiliano Orogeny at 500—700 Ma. These various lithologies were intruded by numerous granitoids at between 650 and 540 Ma. However, the lack of published trace element and isotope data for most of these different rocktypes means that it is difficult to estimate a representative contaminant composition. AFC trajectories calculated assuming the contaminant to have the composition of average continental crust (Taylor and McLennan, 1981), are shown in fig. 3.6 for reference. Note that there is little difference between the AFC paths for r=0.0 (fractional crystallisation) and r=0.5, reflecting the limited degree of crystallisation (less than about 20%) between the least and most evolved samples.

The alternative approach to modelling the AFC process is to assume a value for r. The composition of the fractionating assemblage (and hence the bulk distribution coefficients) are constrained by the major element variation, and equation (1) can therefore be solved for the trace element composition of the assimilant. The value of r is likely to be less than 0.3, and thus the concentrations of trace elements calculated assuming that r=0.3 will represent lower limits on their true values. The trace element composition of the assimilant calculated assuming a range of values for r are presented in table 3.3. These should not be regarded as very precise estimates of the composition of the assimilant, partly because of the relatively restricted major element variation within the Paraiba dolerites (fig. 3.5), which means that the composition of the fractionating assemblage calculated from the major element data is unlikely to be very accurate. There will therefore be uncertainties in estimating bulk distribution coefficients from the least squares calculations (particularly for the less incompatible elements such as Y and Sr). The AFC paths are not well constrained by the limited trace element variation between samples MR8943 and MR8962, and the scatter of the

data in fig. 3.6 suggests that both endmembers in the AFC process had variable compositions.

	(a) K_d^i	(b) C_a^i (r=0.3)	(c) C_a^i (r=0.2)	(d) C_a^i (r=0.1)	(e) C_{melt}^i
Zr	0.072	-247	-438	-1013	803
Nb	0.125	39.1	64.3	140.0	153
Y	0.322	-57.5	-107.9	-259.1	33.1
Rb	0.034	131	223	499	419
Sr	0.727	1347	1888	3514	2387
Ba	0.081	1421	2385	5277	4935
Rb/Sr		0.097	0.118	0.142	0.176
$^{87}Sr/^{86}Sr$		0.7175	0.7198	0.7225	0.7143
$\varepsilon^{Sr}_{assimilant}$		185	218	255	140

Table 3.3
(a), bulk distribution coefficienta used in the AFC calculations, estimated from the least-squares modelling of the major element variation between samples MR-8943 and MR-8962; (b), (c), (d), trace element and isotope composition of the contaminant calculated assuming values for r of 0.3, 0.2 and 0.1 respectively. (e) is the composition of the crustal melt assuming that contamination occurred by a magma mixing process.

The $^{87}Sr/^{86}Sr$ value calculated for the assimilant is within the range of 0.708—0.850 obtained for the basement rocks (recalculated to 132 Ma) by Gasparini and Mantovani (1979). However, the contaminant is required to have significantly higher concentrations of Sr, and higher Rb/Sr values than are typical of those basement rocks for which trace element data are available. This could be explained in terms of selective enrichment in Sr. Note that negative solutions were obtained for C_a^{Zr} and C_a^Y. This is unlikely to be due to an underestimate of the values of K_d^{Zr} and K_d^Y for the fractionating assemblage, because assuming that $C_a^Y=0$, places a minimum constraint upon K_d^Y of 1.01. This relatively high value is difficult to explain in view of the incompatible behaviour of P, which implies that apatite fractionation has not taken place. These negative solutions are instead attributed to the errors associated with calculating assimilant compositions using the limited trace element variation within the Paraiba dolerites.

Thus the trace element and isotope composition of the assimilant that is required to explain the observed variation within the Paraiba dolerites is at least consistent with

contamination having occurred by AFC, but it is difficult to obtain an accurate estimate of the composition of the assimilant.

The least squares mixing calculations (3.2.6.1) indicate that the major element variation within the Paraiba dolerites can be satisfactorily explained in terms of a contamination process involving a crustal melt. The trace element composition of the contaminating melt (table 3.3) was calculated assuming 10% contamination between samples MR-8943 and MR-8962 (section 3.2.6.1). Again, it is difficult to obtain an accurate quantitative estimate of the composition of the contaminant, because of the limited trace element variation within these samples, and because of the scatter in the data (fig. 3.6), which suggests that both endmembers in the mixing process had variable compositions. The melt is required to have relatively high concentrations of all of the incompatible trace elements, and lower Rb/Sr values than are considered typical of crustal melts (the Palmas rhyolites have Rb/Sr values of 1.24—1.93).

In summary, the trace element and isotope variation within the Paraiba dolerites is most consistent with a model in which low pressure crystal fractionation of augite, plagioclase and titanomagnetite in upper crustal magma chambers was accompanied by assimilation of the basement rocks, although it is not possible to rule out the possibility that contamination occurred by a magma mixing process involving a crustal melt. There is some evidence that selective enrichment in certain elements may have occurred, although the uncertainties associated with estimating K_d^i values from the major element modelling means that there are considerable errors on the calculated assimilant composition. The relatively restricted compositional range of these dolerites will increase the magnitude of these errors, because the compositions of the endmembers are less well constrained by the data. It also appears that both endmembers in the AFC process were significantly heterogeneous, which means that it is very difficult to obtain an accurate estimate of the composition of the contaminant.

3.2.7 Relationship of the dolerites to the flood basalts of the lava pile

The Paraiba dolerites have similar Zr/Nb and Ba/Y values to the basalts of the Urubici magma type of the southern Parana (fig. 3.2; section 3.1). The major element chemistry of these two groups of rocks are also very similar (table 3.4), which suggests that the surface lava flows of the Urubici magma type may have been fed from dykes in Sao Paulo State.

The Urubici basalts outcrop in the Serra Geral escarpment north of about latitude 29°S, and are not found north of about latitude 26°S, some 500 km to the south of the main occurence of the dolerites of the Paraiba type (Chapter 1). In the Etendeka province, basaltic lava flows of the African equivalent of the Urubici magma type (the Khumib magma type) occur only in the northern parts of the lava field between latitudes 18 and 20°S (between 27 and 29°S at 130 Ma). Scattered dykes of the Urubici magma type have been recorded from the Serra Geral escarpment in the region around Urubici and Sao Joaquim (Peate, 1989). The stratigraphical distribution of the Urubici flows do suggest that they were fed from a source that lay to the north of latitude 28°S (Peate et al., 1992), and there is evidence from the Columbia River CFB Province (Hooper, 1982), that in some cases, basaltic lava flows can travel distances of over 550 km. Sample MR-8950 yielded an Ar—Ar isochron age of 133.3 ± 1.7 Ma (see Chapter 4), which is within error of Ar—Ar ages recently obtained from two basalt samples of the Urubici magma type (S. Turner, pers. comm.).

In order to determine whether or not the dolerites are intrusive equivalents of the Urubici basalts, the mean and standard deviation of the dolerites, and of the Urubici basalts (data from Peate, 1989) were calculated, and the significance of the differences between the means was measured (table 3.4) using standard statistical techniques (Hoel, 1976). Although these XRF analyses and those of Peate (1989) were carried out on different instruments, interlaboratory bias can be monitored and corrected for by the analysis of standards (see Appendix). Note that there are significant differences between the means at the 95% confidence level for not only the more mobile elements such as Rb and Ba (which might possibly behave differently during the alteration of intrusive and extrusive rocks), but

	Paraiba dolerites Mean (n=12)	s.d.	Urubici basalts Mean (n=59)	s.d.	Significant difference between means at the 95% confidence level
SiO_2	52.0	0.81	51.7	0.79	No
TiO_2	3.67	0.29	3.76	0.28	No
Al_2O_3	13.7	0.32	13.3	0.32	Yes
Fe_2O_3	13.1	0.77	13.3	0.52	No
MgO	4.53	0.27	4.56	0.34	No
CaO	7.41	0.60	8.19	0.50	Yes
Na_2O	2.89	0.18	2.80	0.28	No
K_2O	2.29	0.43	1.70	0.35	Yes
P_2O_5	0.66	0.16	0.54	0.0	Yes
Zn	105	15	118	9	Yes
Cu	107	55	162	30	Yes
Ni	55	15	55	14	No
V	300	60	355	21	Yes
Ba	974	319	638	92	Yes
Ga	24	1	26	2	Yes
Rb	64	20	38	11	Yes
Sr	854	127	773	105	Yes
Y	43	9	39	3	No
Zr	314	21	319	28	No
Nb	32	5	28	3	Yes

Table 3.4
Mean and standard deviation of the Urubici basalts (data from Peate, 1989), and the dolerites of the Paraiba magma type from Sao Paulo State.

also for elements such as Al and Nb, the concentrations of which are generally unaffected by subsolidus alteration processes.

In addition, the Paraiba dolerites and the Urubici basalts have significantly different Sr isotope compositions. The former have initial $^{87}Sr/^{86}Sr$ values of greater than 0.7055 (fig. 3.10), and in section 3.2.7 it has been argued that the dolerites underwent AFC at shallow levels in the crust. In contrast, most of the Urubici basalts have initial $^{87}Sr/^{86}Sr$ values of less than 0.7053, except a few initial lava flows of anomalous composition, and the very youngest flows of the SM and GB sections, which have $^{87}Sr/^{86}Sr$ values of between 0.7053 and 0.7062 (fig. 3.10). Peate (1989) considered these flows to have been contaminated by crustal material, but the Urubici basalts on the whole show no evidence of having undergone AFC. Another possibility is that the Paraiba dolerites represent contaminated varieties of the Urubici basalts. As discussed above, it is difficult to place constraints on the composition of the parental magma to the Paraiba dolerites. However, note that the AFC paths defined by the Paraiba dolerites and by the most contaminated samples of the Urubici magma type cannot be explained in terms of variations in the value of r, and require different contaminant compositions (fig. 3.10). Although all of these samples

could in theory have been derived from the same parental magma composition, the fact that different contaminants were involved suggests that the two magma types evolved within different magma chambers in different crustal provinces, and that the Paraiba dolerites are not contaminated varieties of the Urubici basalts.

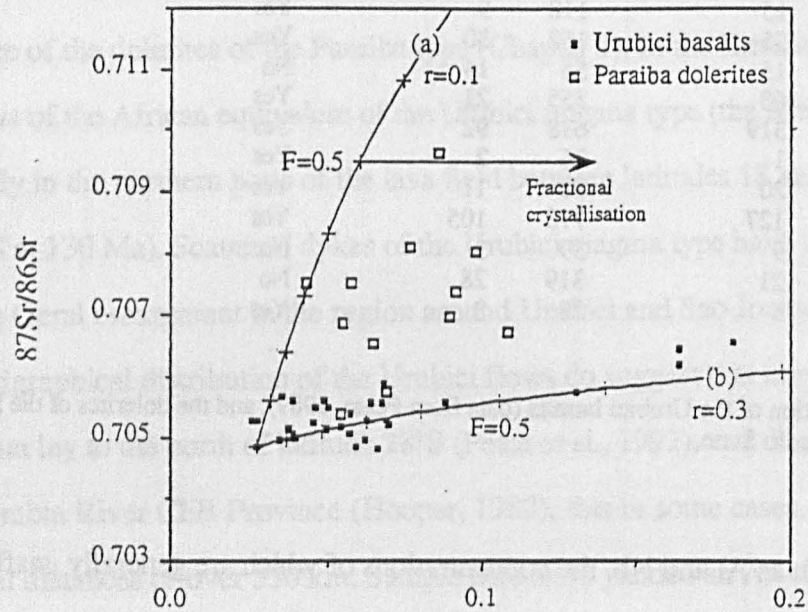

Contaminant composition

(a)
Rb=110ppm
Sr=350ppm
87Sr/86Sr=0.850

(b)
Rb=110ppm
Sr=350ppm
87Sr/86Sr=0.711

Parent composition

Rb=22ppm
Sr=780ppm
87Sr/86Sr=0.705

Fig. 3.10
Rb/Sr—$^{87}Sr/^{86}Sr$ variation within the Paraiba dolerites and the Urubici basalts (data from Peate, 1989). AFC trajectories were calculated assuming the contaminant to have the trace element composition of average upper crust (Taylor and McLennan, 1981); the mineral composition of the fractionating assemblage was calculated by least squares modelling of the major element variation within the Paraiba dolerites. The geochemical variation within these two suites of rocks cannot be explained in terms of variations in the value of r, and require at least two different contaminants with different $^{87}Sr/^{86}Sr$ values.

3.2.8 Conclusions

The dolerites of the Paraiba magma type have undergone assimilation-fractional crystallisation (AFC) at relatively shallow levels in the crust. The major element variation within this group of dolerites is consistent with crystal fractionation of augite, plagioclase and magnetite. Fractionation was accompanied by assimilation of a high SiO_2, high $^{87}Sr/^{86}Sr$ contaminant. Attempts to model the contamination process more quantitatively were hampered by the limited major and trace element variation within these dolerites, and by the fact that several contaminant compositions appear to have been involved.

The Paraiba dolerites do not have extrusive equivalents in the lava pile, although the new Ar—Ar data presented in Chapter 4 indicate that they have similar ages to the flood basalts to the west.

3.3 The dolerites of the Ubatuba magma type

3.3.1 Introduction

Dolerites of the Ubatuba magma type were encountered in the Serra Geral escarpment to the north of the town of Sao Sebastiao, and further to the east where they outcrop on the coast close to Ubatuba (fig. 3.1). These dolerites have significantly higher Ba/Y (higher Ba concentrations) than either the dolerites of the Paraiba magma type or the flood basalt lavas to the west, and higher Zr/Nb (lower Nb concentrations) than the dolerites of the Sao Sebastiao magma type (fig. 3.2). Most possess large phenocrysts of plagioclase and augite. Amaral et al. (1966) dated several dolerite samples collected from this region by the conventional K—Ar technique, and although they did not report whole-rock geochemical data for the same samples, their description of the petrography of these dolerites suggest that in fact several belonged to the Ubatuba magma type. Amaral et al. (1966) obtained ages of between 132 and 139 Ma for three such samples. Five samples of this magma type, in the form of both whole-rock samples and plagioclase separates were dated by the Ar—Ar method in the course of this study (Chapter 4), and these yielded isochron ages of between 129.4 ± 0.6 and 135.8 ± 1.1 Ma, which suggests that they were intruded at approximately the same time as the flood basalt magmatism was taking place to the west.

3.3.2 Petrography and mineral chemistry

The dolerites of this magma type have a complex petrography, although there is very little mineralogical variation within the group as a whole. All samples contain phenocrysts of plagioclase, augite and ilmenite, which display evidence of mineral disequilibrium. The mineral chemistry of three samples was investigated in detail by microprobe analysis.

The least evolved sample (MR-8952) (MgO=4.64%) is highly porphyritic, consisting of 2—3 mm sized, rounded and embayed phenocrysts of plagioclase (Ab_{45-48}, Or_{6-8}, An_{44-48}), augite (En_{41-43}, Wo_{37-39}, Fs_{19-21}), ilmenite and apatite which are set in a fine-grained groundmass of partially devitrified glass containing small crystals of ilmenite and quench

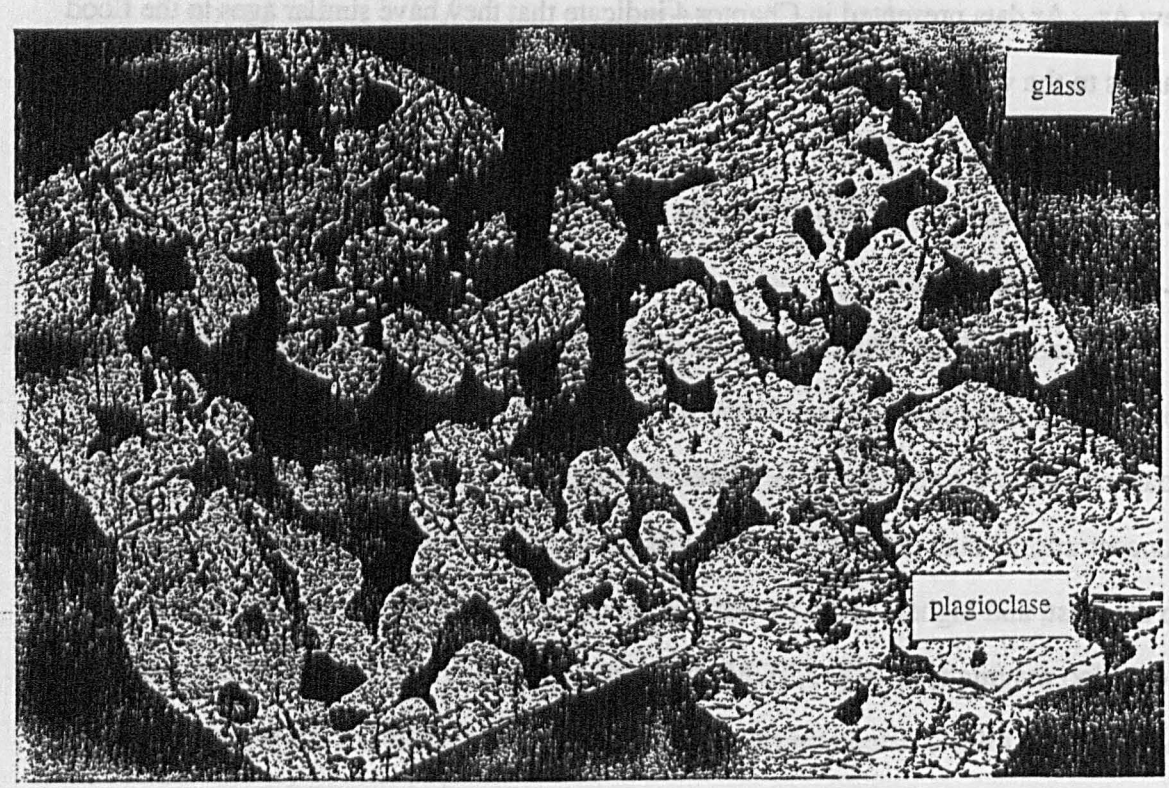

Fig. 3.11
Photomicrograph (plain polarised light) of sample MR-8952, showing a large plagioclase phenocryst enclosed in a glassy matrix. Note the rounded and embayed crystal margins, and the melt sieved core of the phenocryst. Field of view 4 x 6 mm.

crystals of felspar (fig. 3.11). Occasional small, highly altered phenocrysts of pigeonite are also present.

Sample MR-8984 (MgO=4.42%) contains occasional microphenocrysts of plagioclase (An_{44-50}, Ab_{44-49}, Or_{5-8}) which are generally overgrown by small blocky crystals of

potassium felspar, and the indistinct twinning and melt sieved cores of the plagioclase crystals suggest that they are not in equilibrium with the groundmass. Small phenocrysts of ilmenite, augite (En_{41-43}, Wo_{38-39}, Fs_{19-20}) and pigeonite (En_{60-64}, Wo_{4-5}, Fs_{31-36}) are also present. The groundmass consists dominantly of potassium felspar, plagioclase, clinopyroxene and ilmenite. Hornblende occurs as thin overgrowths on augite, and apatite, sphene and zircon are present in accessory amounts.

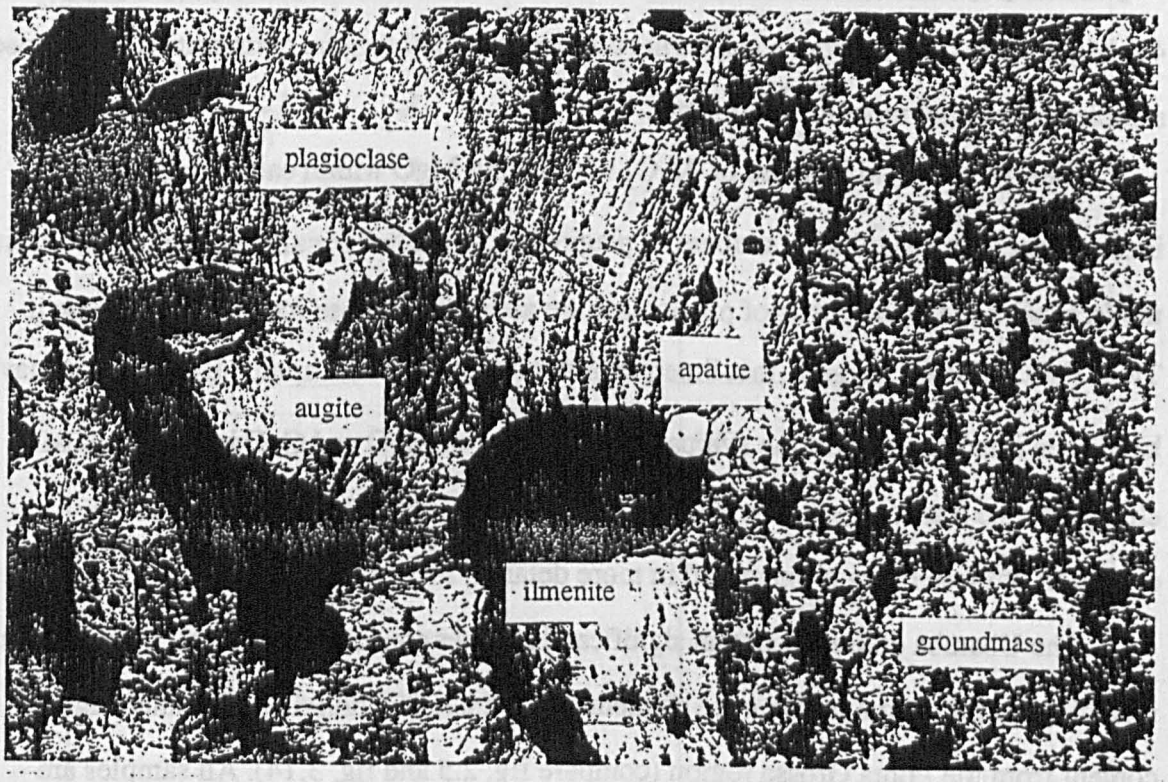

Fig. 3.12
Photomicrograph (plain polarised light) of sample MR-8954. Note glomerocrysts of plagioclase, augite, ilmenite and apatite. The groundmass consists of finegrained alkali feldspar, augite and ilmenite. The field of view is approximately 2 x 3 mm.

Sample MR-8954 (MgO=3.46%) contains rounded and embayed phenocrysts of augite (En_{41-42}, Wo_{37-39}, Fs_{19-21}), ilmenite and apatite which are clustered in aggregates (fig. 3.12). Large (up to 1 cm in diameter) phenocrysts of plagioclase (Ab_{47-49}, Or_{7-9}, An_{42-45}) are also present. These also are clearly not in equilibrium with the groundmass; most possess resorbed crystal margins, which were later overgrown by potassium felspar.

Many have extensively melt-sieved cores. The groundmass of this sample consists largely of fine-grained potassium felspar, ilmenite and clinopyroxene.

3.3.3 Major and trace element geochemistry

The dolerites of the Ubatuba magma type are relatively evolved rocks (trachyandesites and basaltic trachyandesites), containing 2.5—4.6% MgO and 54.4—58.0% SiO_2 (fig. 3.13). All samples are 5.1—6.3% quartz normative. Note that the variation in TiO_2, FeO, Na_2O and P_2O_5 suggests that the more evolved samples (those containing less than about 4% MgO) were derived from a somewhat different parental magma composition from those samples containing more than 4% MgO.

Clearly, the rapid increase of Al_2O_3 with falling MgO within each subgroup is inconsistent with a significant amount of plagioclase in the fractionating assemblage, despite the fact that large phenocrysts of plagioclase are abundant in these rocks. The decrease in TiO_2, FeO and P_2O_5 suggests that ilmenite or titanomagnetite and apatite fractionation may have been important, whilst the sympathetic variation of MgO and CaO is consistent with clinopyroxene fractionation. The role that fractional crystallisation has played in the evolution of these rocks is examined in more detail in section 3.3.5.1.

The Ubatuba dolerites contain significantly higher concentrations of all trace elements, including the more compatible trace elements Ni and Cr, than dolerites of similar MgO content from the Ponta Grossa region (compare fig. 2.5 and fig. 3.14). All samples are enriched in the REE relative to the chondritic mantle composition of Nakamura (1974), and in the LREE relative to MORB (fig. 3.15).

3.3.4 Isotope geochemistry

The Ubatuba dolerites have relatively uniform Sr and Nd isotope compositions (fig. 3.9), which are similar to those of the least evolved basalts of the Gramado magma type from the southern Parana. However, the relatively high Ba/Y and low Zr/Nb values of the Ubatuba dolerites (fig. 3.2) indicate that the latter do not represent intrusive equivalents of these basalts. The uniform Sr and Nd isotope compositions of these rocks, together with the lack of any significant variation with MgO, suggests that crustal contamination has not

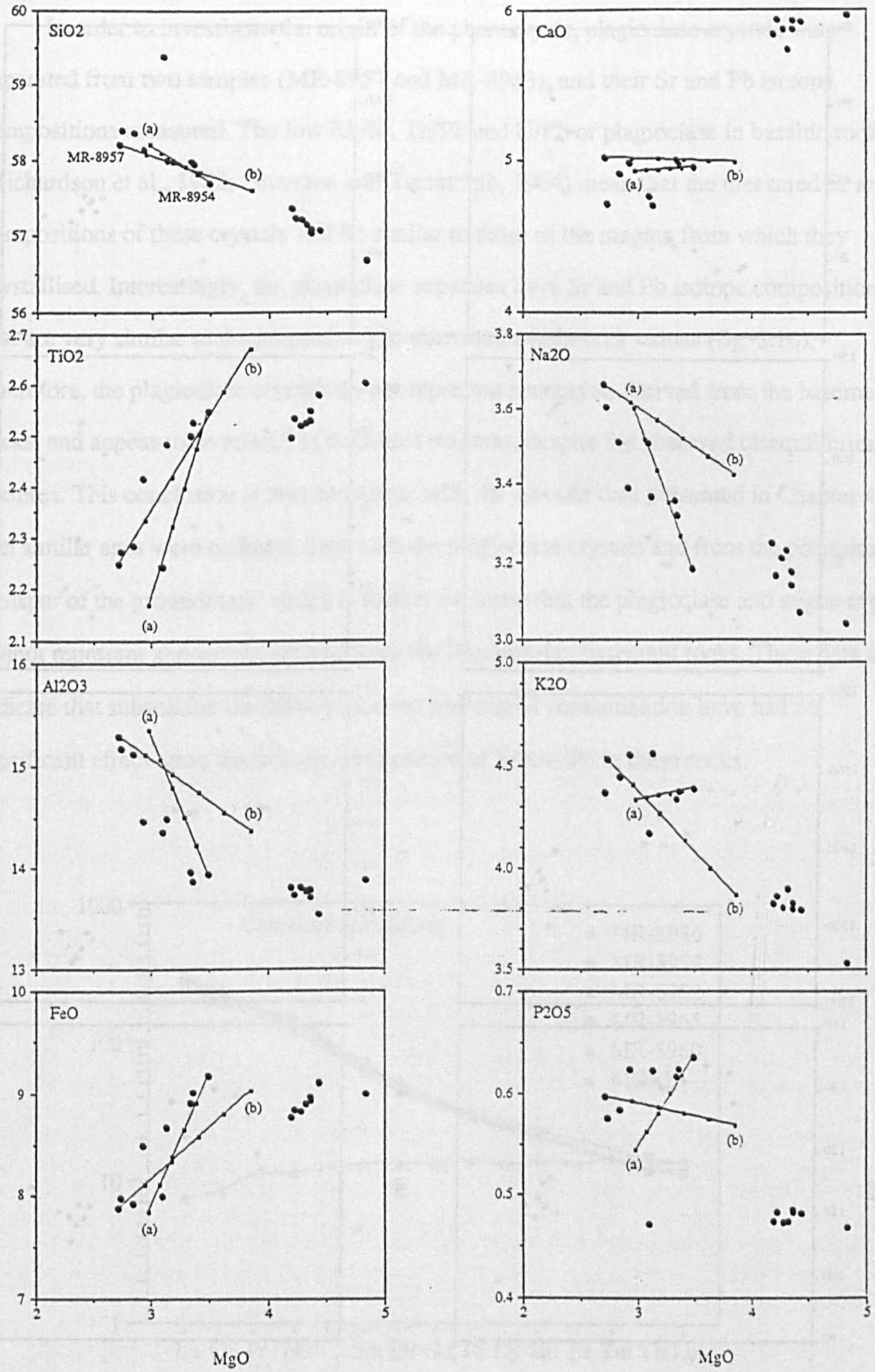

Fig. 3.13
Major element variation within the Ubatuba dolerites. (a), best fit solution to the major element variation within the more evolved samples assuming that samples MR-8954 and MR-8957 are related by fractional crystallisation of pigeonite, augite, ilmenite and apatite; (b), illustrates effect of adding 12% plagioclase to sample MR-8954.

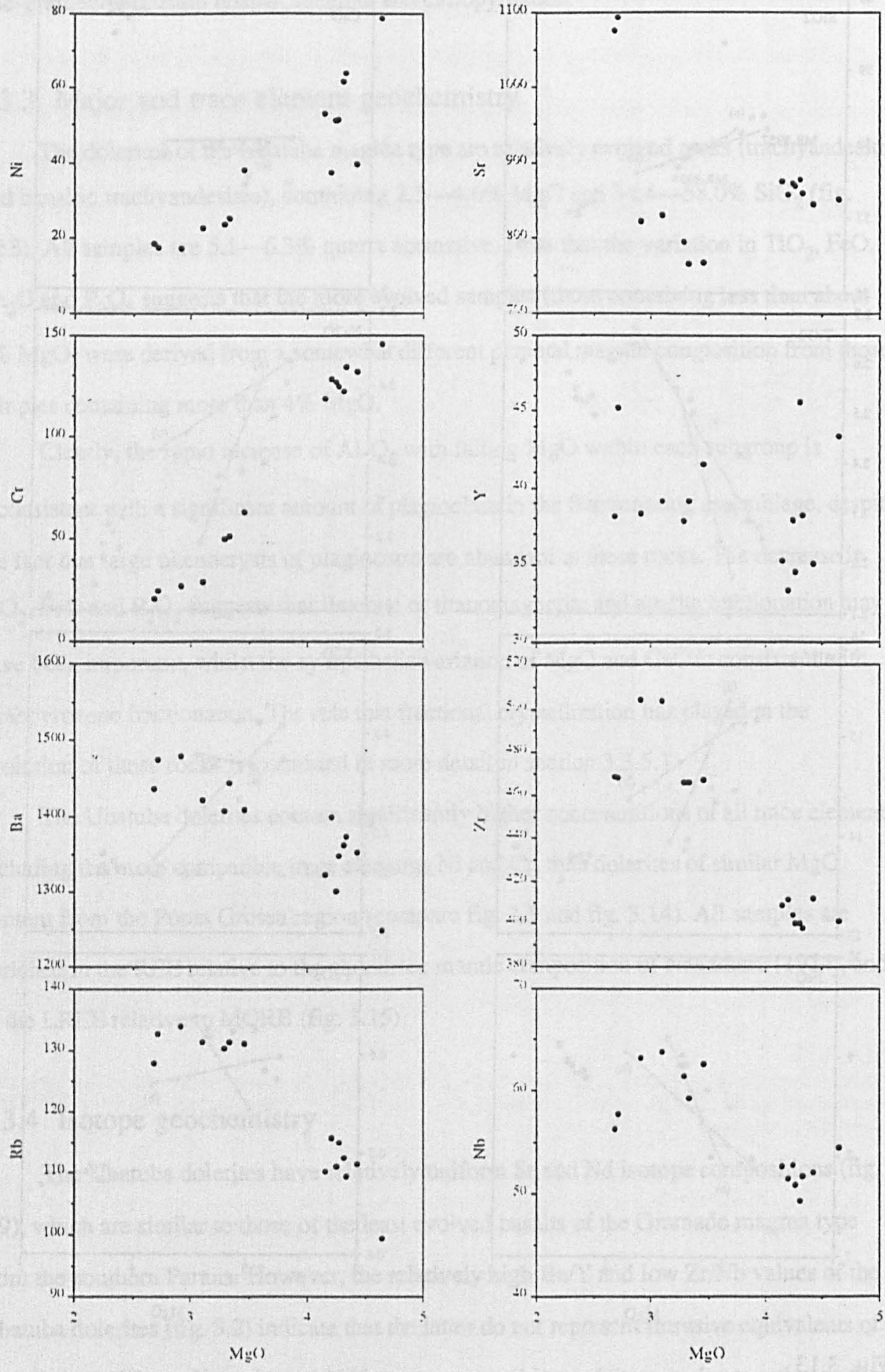

Fig. 3.14
Trace element variation within the Ubatuba dolerites

influenced the geochemistry of these dolerites.

In order to investigate the origin of the phenocrysts, plagioclase crystals were separated from two samples (MR-8957 and MR-8983), and their Sr and Pb isotope compositions measured. The low Rb/Sr, Th/Pb and U/Pb of plagioclase in basaltic rocks (Richardson et al., 1982; Patterson and Tatsumoto, 1964) mean that the measured Sr and Pb compositions of these crystals will be similar to those of the magma from which they crystallised. Interestingly, the plagioclase separates have Sr and Pb isotope compositions that are very similar to the respective age-corrected whole-rock values (fig. 3.16). Therefore, the plagioclase crystals do not represent xenocrysts derived from the basement rocks, and appear to be related to their host magmas, despite the observed disequilibrium textures. This conclusion is also consistent with the Ar—Ar data presented in Chapter 4, in that similar ages were obtained from both the plagioclase crystals and from the potassium feldspar of the groundmass, which is further evidence that the plagioclase and augite crystals cannot represent xenocrysts derived from the Precambrian basement rocks. These data also indicate that subsolidus alteration processes and crustal contamination have had no significant effect upon the isotope composition of Sr and Pb in these rocks.

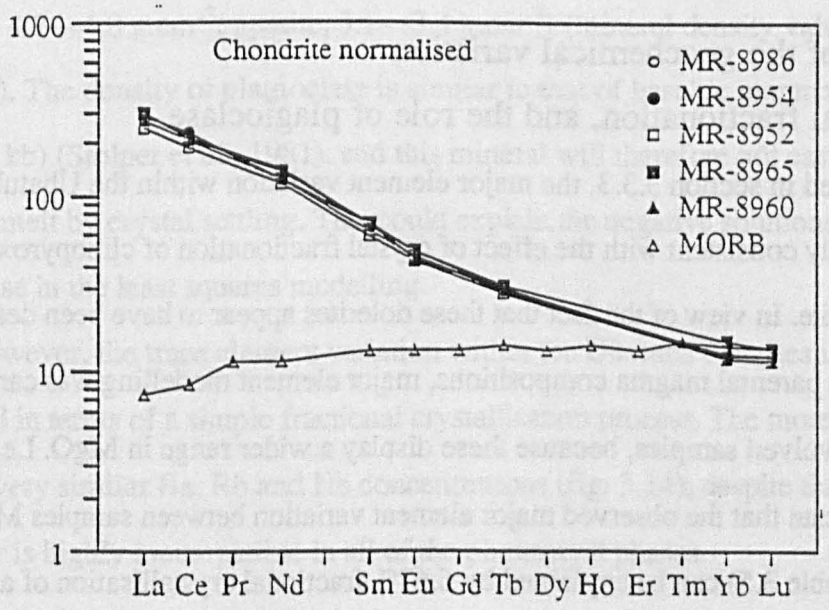

Fig. 3.15 ·
REE concentrations of the Ubatuba dolerites, normalised to the chondritic composition of Nakamura (1974). The average NMORB of Sun and McDonough (1989) is shown for reference.

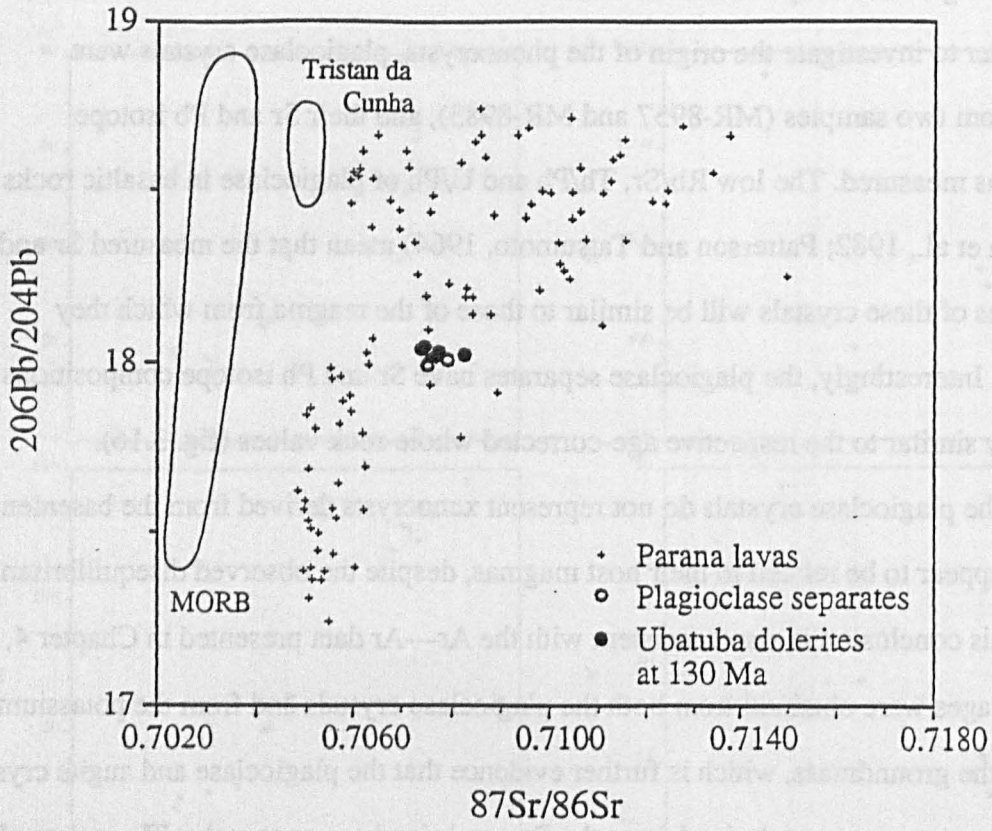

Fig. 3.16
$^{206}Pb/^{204}Pb$—$^{87}Sr/^{86}Sr$ variation within the Ubatuba dolerites (age corrected assuming an age of 130 Ma for all samples) and separated plagioclase phenocryst fragments from two of these samples. Data for the Parana flood basalts (Peate, 1989), Tristan da Cunha (le Roex et al., 1990) and MORB are shown for reference.

3.3.5 Origin of the geochemical variation

3.3.5.1 Crystal fractionation, and the role of plagioclase

As discussed in section 3.3.3, the major element variation within the Ubatuba dolerites is broadly consistent with the effect of crystal fractionation of clinopyroxene, ilmenite and apatite. In view of the fact that these dolerites appear to have been descended from two distinct parental magma compositions, major element modelling was carried out using the more evolved samples, because these display a wider range in MgO. Least-squares calculations indicate that the observed major element variation between samples MR-8957 and MR-8954 (table 3.5) can be explained by 6.67% fractional crystallisation of augite (13.5%), pigeonite (70.6%), ilmenite (15.7%), and apatite (0.3%) (Σr^2=0.536).

	SiO_2	TiO_2	Al_2O_3	FeO	MgO	CaO	Na_2O	K_2O	P_2O_5	Quantity
MR-8957	58.2	2.25	15.3	7.88	2.72	5.01	3.67	4.38	0.60	93.3
Augite	50.9	1.23	3.12	12.1	14.0	18.3	0.39			0.98
Pigeonite	53.6	0.49	0.97	20.2	22.5	2.15	0.04			5.12
Ilmenite	2.24	46.9	0.80	47.0	3.07	0.02				1.14
Apatite				0.03	0.02	57.1			42.9	0.03
MR-8954	57.7	2.55	13.9	9.19	3.49	4.95	3.19	4.39	0.62	
Product	57.6	2.67	14.4	9.04	3.86	4.98	3.43	4.08	0.57	100.6
Residual	-0.11	+0.12	+0.44	-0.15	+0.37	+0.04	+0.24	-0.31	-0.48	

Sum of squares of residuals 0.536

Table 3.5
Least-squares modelling of the major element variation between samples MR-8954 and MR-8957, assuming these samples to be related by fractional crystallisation. Apatite data from Deer et al. (1966); all other mineral compositions used in the calculations were obtained by microprobe analysis of samples MR-8954 and MR-8984.

The rapid increase in Al_2O_3 with decreasing MgO in the melt is evidence that plagioclase fractionation has not occurred, and indeed negative solutions were obtained for plagioclase, if this mineral was included in the least squares calculations. This is despite the fact that large plagioclase phenocrysts are present in all samples. A possible explanation for the apparent lack of plagioclase fractionation is the relatively low density of this mineral (2.62—2.76 $g.cm^{-3}$) relative to the other phenocryst phases (augite, 2.96—3.52 $g.cm^{-3}$; ilmenite, 4.7—4.8 $g.cm^{-3}$; apatite, 3.1—3.4 $g.cm^{-3}$) (mineral density values from Deer et al., 1966). The density of plagioclase is similar to that of basaltic magmas (2.5—2.7 $g.cm^{-3}$ at 0—10 kb) (Stolper et al., 1981), and this mineral will therefore not easily be removed from the melt by crystal settling. This could explain the negative solutions obtained for plagioclase in the least squares modelling.

However, the trace element variation within the Ubatuba dolerites is less easily explained in terms of a simple fractional crystallisation process. The more evolved samples all have very similar Ba, Rb and Nb concentrations (fig. 3.14), despite the fact that Rb in particular is highly incompatible in all of the phenocryst phases.

The plagioclase phenocrysts within these dolerites have relatively uniform compositions (Ab_{46-48}, An_{42-46}, Or_{7-9}) (section 3.3.2), and it is interesting that sample MR-

8957 can be satisfactorily modelled as a mixture of 87.8% liquid with the composition of sample MR-8954 and 12.2% by volume of plagioclase (Σr^2=0.568) (table 3.6).

(a)	SiO_2	TiO_2	Al_2O_3	FeO	MgO	CaO	Na_2O	K_2O	P_2O_5	Quantity
MR-8954	57.7	2.55	13.9	9.19	3.49	4.95	3.19	4.39	0.62	88.3
Plagioclase	58.2		25.9	0.54		8.48	5.38	1.50		12.2
MR-8957	58.2	2.25	15.3	7.88	2.72	5.01	3.67	4.38	0.60	
Product	58.1	2.25	15.5	8.18	3.08	5.41	3.47	4.07	0.55	100.6
Residual	-0.11	+0.00	+0.18	+0.31	+0.37	+0.39	-0.21	-0.31	-0.05	
Sum of squares of residuals 0.568										

(b)	SiO_2	TiO_2	Al_2O_3	FeO	MgO	CaO	Na_2O	K_2O	P_2O_5	Quantity
MR-8957	58.2	2.25	15.3	7.88	2.72	5.01	3.67	4.38	0.60	103.6
Plagioclase	58.2		25.9	0.54		8.48	5.38	1.50		-8.05
Augite	50.9	1.23	3.12	12.1	14.0	18.3	0.39			1.97
Pigeonite	53.6	0.49	0.97	20.2	22.5	2.15	0.04			2.06
Ilmenite	2.24	46.9	0.80	47.0	3.07	0.02				0.64
Apatite				0.03	0.02	57.1			42.9	0.04
MR-8954	57.7	2.55	13.9	9.19	3.49	4.95	3.19	4.39	0.62	
Product	57.7	2.66	13.9	9.07	3.58	4.94	3.38	4.42	0.64	100.3
Residual	+0.00	+0.11	-0.05	-0.12	+0.09	-0.02	+0.19	+0.03	+0.02	
Sum of squares of residuals 0.073										

Table 3.6
Least-squares modelling of the major element variation between samples MR-8954 and MR-8957, assuming these samples to be related by (a) accumulation of plagioclase, (b) plagioclase accumulation accompanied by fractional crystallisation of the other phenocryst phases. Apatite composition from Deer et al. (1966); all other mineral compositions obtained from microprobe analysis of sample MR-8954.

The major element calculations suggest that approximately 12% volume of plagioclase is required to explain the major element variation between sample MR-8954 and MR-8957, but this is too small an amount to account for the variation of Ni and Cr. Assuming the plagioclase crystals to contain no Cr, requires ~30% plagioclase to have been added to sample MR-8954.

A better fit to the trace element variation was obtained for a model in which 8.1% plagioclase accumulation is accompanied by 4.7% fractionation of clinopyroxene, ilmenite and apatite (table 3.6), because fractional crystallisation of clinopyroxene and ilmenite will rapidly deplete the residual melt in the compatible elements such as Ni and Cr. However,

although such a model is physically possible, given the relative densities of these minerals, it cannot account for the observed mineral textures. Disequilibrium textures are displayed by all the phenocryst phases. Small crystals of augite are occasionally observed within larger plagioclase crystals, and commonly augite, ilmenite and plagioclase crystals are grouped together in glomerocrysts (as in sample MR-8954; fig. 3.12). These textures indicate that both phases crystallised at approximately the same time, and that plagioclase cannot have behaved independently of the other phenocryst phases. In addition, there is no significant compositional variation between the phenocrysts within the least and most evolved samples (section 3.3.2), as would be expected had crystal fractionation and accumulation been responsible for the geochemical variation between these samples.

3.3.5.2 The role of magma mixing processes

An alternative petrogenetic model for the low-pressure evolution of these dolerites, which can account for the mineral disequilibrium textures and the uniform compositions of the phenocrysts, involves magma mixing processes.

The petrographic evidence suggests that the mixing process involved a relatively basic melt, containing phenocrysts of plagioclase, augite, ilmenite and apatite, and a less basic, potassium-rich aphyric melt. This model can explain the disequilibrium textures displayed by the phenocrysts, and the fact that the plagioclase crystals commonly possess thin overgrowths of potassium felspar. Samples with less than 3.5% MgO and more than 4% MgO lie upon different mixing arrays in fig. 3.13, which do not intersect at a common composition. This suggests that the mixing process involved slightly different magma compositions in each case.

The relatively restricted range in isotope composition and the relative concentrations of incompatible trace elements implies that the mixing endmembers were derived from the same batch of magma, and may therefore be related by fractional crystallisation or partial melting processes. The Ni and Cr variation within those samples with less than 4% MgO requires one endmember to have a MgO concentration of between 2.0 and 2.6%, whilst the Na_2O variation requires the other endmember to have a MgO concentration of less than about 6.5%. The mixing process therefore appears to have involved relatively evolved melt

compositions, and the normative compositions of these dolerites indicates that mixing took place at shallow levels in the crust.

3.3.6 Conclusions

The trachyandesites of the Ubatuba magma type were intruded at approximately 132 Ma (Chapter 4), but do not have extrusive equivalents in the flood basalt lava field to the west. The major and trace element variation within this suite of dolerites is most satisfactorily explained in terms of magma mixing processes at shallow levels in the crust. This model can also explain the fact that the phenocryst phases are in disequilibrium with the groundmass material. The relatively restricted range in Sr, Nd and Pb isotope composition implies that the mixing endmembers were derived from a similar source, and this makes it difficult to constrain the endmember compositions very precisely. However, the subparallel data arrays defined by samples with less than and more than 4% MgO suggests that several melt compositions were involved, and that these had relatively evolved compositions.

3.4 The dolerites of the Sao Sebastiao magma type

3.4.1 Introduction

The dolerites of the Sao Sebastiao magma type intrude the basement rocks of Sao Paulo State close to the town of Sao Sebastiao. Three samples of similar composition were also encountered further inland to the southwest of Campos do Jordao (fig. 3.1).

At Ubatuba, a dyke of the Sao Sebastiao magma type (MR-8981) intrudes a dyke of the Paraiba magma type. A different sample of the latter type has been dated at 133.3 ± 1.7 Ma (Chapter 4), which places an upper limit upon the age of the Sao Sebastiao dolerites. An Ar—Ar age of 134.0 ± 0.4 Ma was obtained from an amphibole xenocryst separated from sample MR-8981, but this is unlikely to represent the intrusion age (see Chapter 4). Crystals of biotite separated from sample MR-8944 yielded an isochron age of 80.9 ± 0.4 Ma. These ages suggest that the Sao Sebastiao dolerites were intruded some 50 Ma after the flood basalts were erupted to the west. Fodor and Vetter (1984) reported a single sample of very similar composition from a drill site (SPS—10) 150 km off the Brazilian coastline in the Santos Basin. This is further evidence that the Sao Sebastiao dolerites were intruded at a

relatively late stage in the rifting process, and are considerably younger than the flood basalts.

3.4.2 Petrography and mineral chemistry

The dolerites of the Sao Sebastiao magma type are extremely variable in terms of their mineralogy and petrography, reflecting the variable bulk-rock major element compositions of these rocks (section 3.4.3). Most are porphyritic, containing phenocrysts of clinopyroxene ± olivine ± amphibole, which often display complex zoning. The clinopyroxene phenocrysts are unusually Ca rich, containing 45—50% of the Wo component, and as such differ markedly in composition from the pyroxenes which occur in the flood basalts. Electron microprobe analysis has been used to examine the mineral chemistry of three of these samples in more detail.

Sample MR-8967 (MgO=14.2%) contains large phenocrysts of olivine (Fo_{84-87}), which are generally highly altered to a fine-grained grey material. Large, euhedral

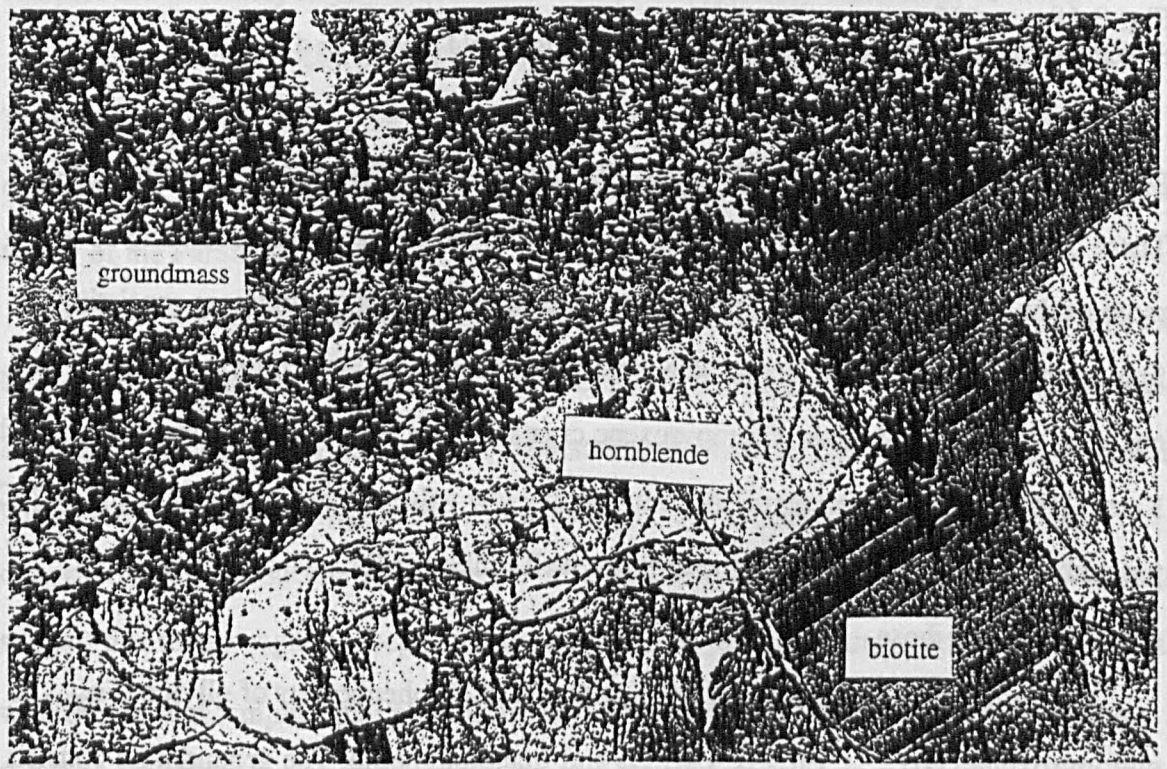

Fig. 3.17
Photomicrograph (plain polarised light), sample MR-8981. Large crystals of biotite and hornblende, which display cumulate textures and which are interpreted as xenocrysts, are enclosed in a fine grained matrix consisting of clinopyroxene, titanomagnetite and amphibole. Field of view 3 x 4 mm.

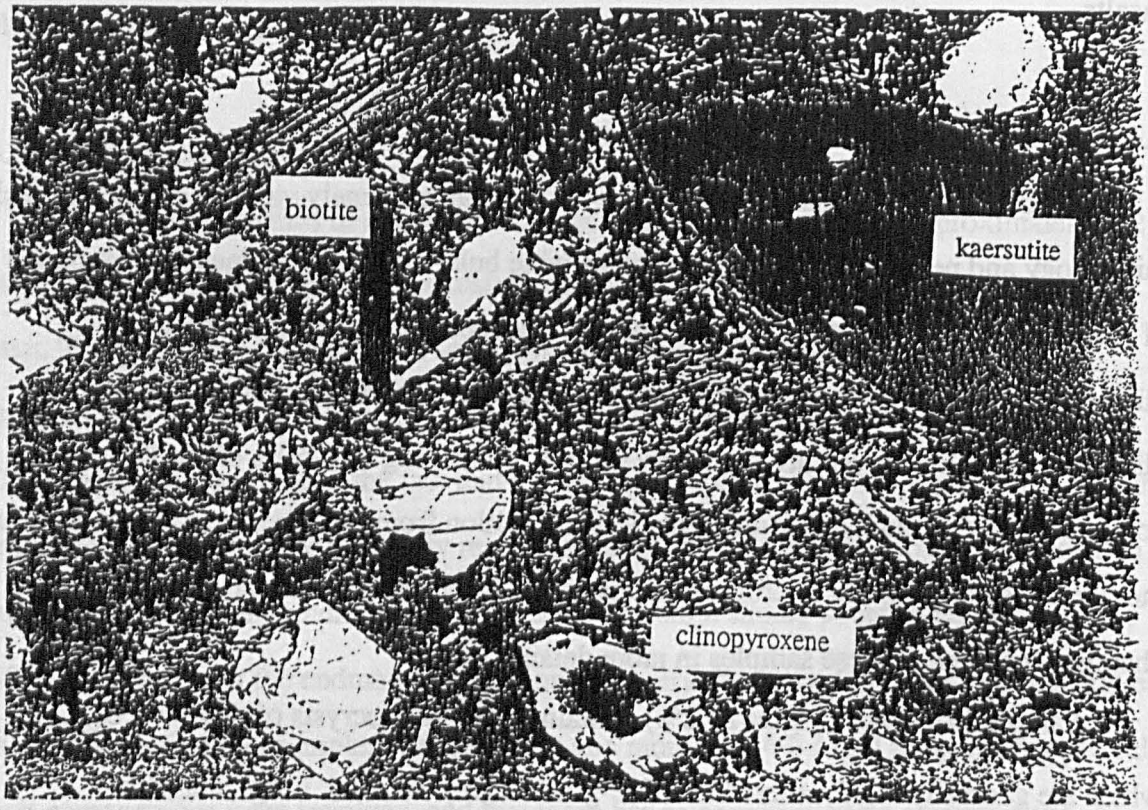

Fig. 3.18
Photomicrograph of sample MR-8944. Plain polarised light, field of view 3 x 4 mm.

phenocrysts of clinopyroxene (Wo_{46-50}, En_{40-48}, Fs_{4-10}) constitute ~30% of the rock. These commonly display compositional zoning, with the crystal cores containing up to 8% more of the En component. The phenocrysts are contained in a groundmass consisting of fine-grained clinopyroxene, amphibole, titanomagnetite and glass. Rutile and analcite are common accessory minerals. Clinopyroxene crystallisation temperatures calculated using the Kretz (1982) geothermometer yielded improbably low values of between 835°C and 962°C, probably because this geothermometer is not well calibrated for such calcic pyroxene compositions as these.

Sample MR-8981 (MgO=11.9%), contains small phenocrysts of olivine (Fo_{83-86}), clinopyroxene (Wo_{46-48}, En_{40-42}, Fs_{11-13}) and titanomagnetite. The groundmass consists largely of Ca rich clinopyroxene, titanomagnetite and small prismatic crystals of a pale brown amphibole. Occasional coarse-grained aggregates of biotite and hornblende are also present. These display cumulate textures (fig. 3.17), and are interpreted as xenocrysts

derived from the hornblende and biotite-bearing granitoids of late Proterozoic age which intrude the basement rocks in this region (Janasi and Ulbrich, 1991).

Sample MR-8944 (MgO=5.58%) was collected from a dyke to the north of the town of Sao Jose dos Campos. Phenocrysts of amphibole (kaersutite), Ti rich biotite, and clinopyroxene (Wo_{46-47}, En_{39-41}, Fs_{12-15}) are enclosed in a groundmass consisting of finegrained clinopyroxene, titanomagnetite, amphibole and interstitial glass. The biotite and amphibole crystals in this sample are generally euhedral (fig. 3.18), and do not exhibit cumulate textures. These are therefore considered to be phenocrysts, rather than xenocrysts. The kaersutite crystals commonly display complex compositional zoning.

3.4.3 Whole-rock major element geochemistry

The Sao Sebastiao dolerites have very variable major element compositions. Most samples are basanites or picritic basalts, although two samples of more evolved composition (SiO_2=59.1 and 66.8%) were collected to the southwest of Sao Sebastiao. The latter samples are extremely highly altered, and little of their primary mineralogy remains.

Many of these rocks are considerably less evolved than any of the basalts of the Parana lava pile. However, the Ar—Ar data suggest that the Sao Sebastiao basanites are considerably younger than the flood basalts, and cannot therefore represent parental magmas to any of the Parana lavas.

CIPW normative compositions (calculated assuming that 15% of the total Fe is in the Fe^{3+} state), are between 4 and 14% nepheline-normative. In contrast, all of the flood basalt lavas are either quartz- or olivine- and hypersthene-normative. The major element variation within the less evolved (MgO>8%) dolerites (fig. 3.19) is consistent with olivine and clinopyroxene control. The inflections in the trends of SiO_2, FeO and TiO_2 at 5—6% MgO suggest that titanomagnetite began to crystallise at this point, and the rapid increase of Al_2O_3 with falling MgO implies that plagioclase was not present in the fractionating assemblage. Indeed, crystals of plagioclase are absent from all but the two most evolved samples of this magma type. The absence of plagioclase has implications for the pressure at which fractionation took place; experimental studies of alkalic basalts (Fisk et al., 1988), show that clinopyroxene, rather than plagioclase, becomes cotectic with olivine only at pressures of

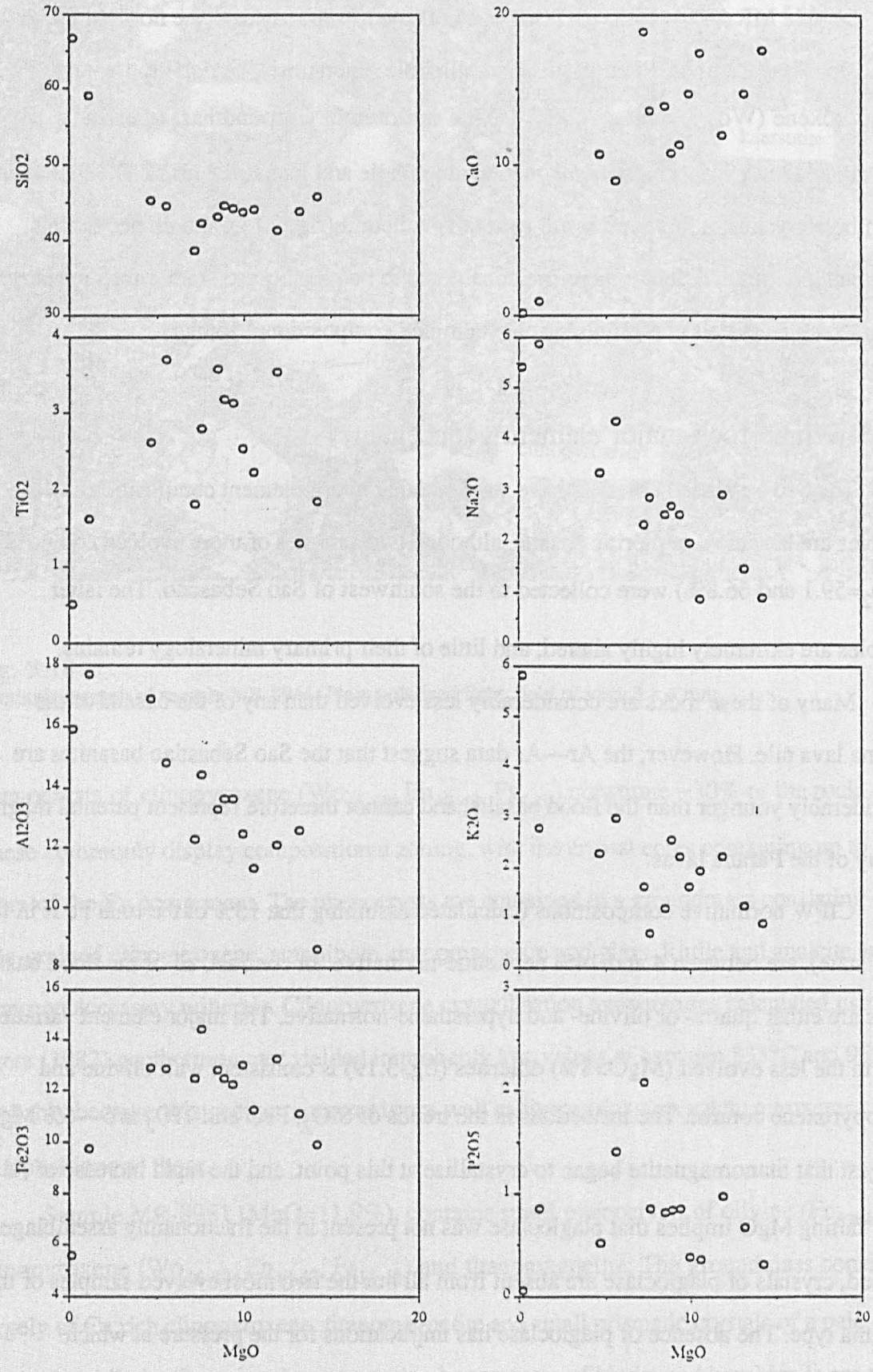

Fig. 3.19
Major element variation within samples of the Sao Sebastiao magma type.

greater than about 4kb. The presence of zoned clinopyroxene phenocrysts in several samples suggests that polybaric fractionation or magma mixing processes may also have influenced the major element variation within these rocks. The relatively high Ca content of sample MR-8972 is attributed to the growth of secondary calcite in veins and cracks.

3.4.4 Trace element geochemistry; evidence for a mantle plume at 80 Ma?

The least evolved of the Sao Sebastiao dolerites contain relatively high concentrations of the more compatible trace elements Ni (up to 400ppm) and Cr (up to 800ppm) (fig. 3.20), reflecting the fact that samples containing >10% MgO have undergone very little crystal fractionation. The incompatible behaviour of Ba, Rb, Zr, Nb and Y is consistent with the effects of olivine, clinopyroxene and titanomagnetite fractionation. These incompatible elements are present in higher concentrations than in many of the more fractionated basalts of the lava pile.

Sample MR-8944 was collected from the central part of an intrusion, in which phenocrysts of biotite and kaersutite appear to have been concentrated by flow differentiation. This would explain the high concentrations of Rb and Ba in this sample (fig. 3.20). The highly altered sample MR-8972 has a relatively high Sr content, due to the growth of secondary calcite. Leaching experiments (described in section 3.4.7.1) suggest that some mobilisation of Rb and Sr has also occurred in many of the other samples as a result of subsolidus alteration.

All samples are enriched in the REE relative to chondritic mantle, and in the LREE relative to MORB (fig. 3.21). The pronounced negative Eu anomaly (Eu/Eu*=0.718), and relatively low Sr concentration of sample MR-8969 suggests that the most evolved samples have fractionated plagioclase.

The Sao Sebastiao basanites contain high concentrations of the elements Ta and Nb, hence their low Zr/Nb values relative to the Parana flood basalts and to the other dolerites discussed in Chapters 2 and 3 (fig. 3.2). In this respect, these rocks are very similar to basalts erupted on oceanic islands (fig. 3.22).

Plate reconstructions place the mantle plume that is at present beneath the South

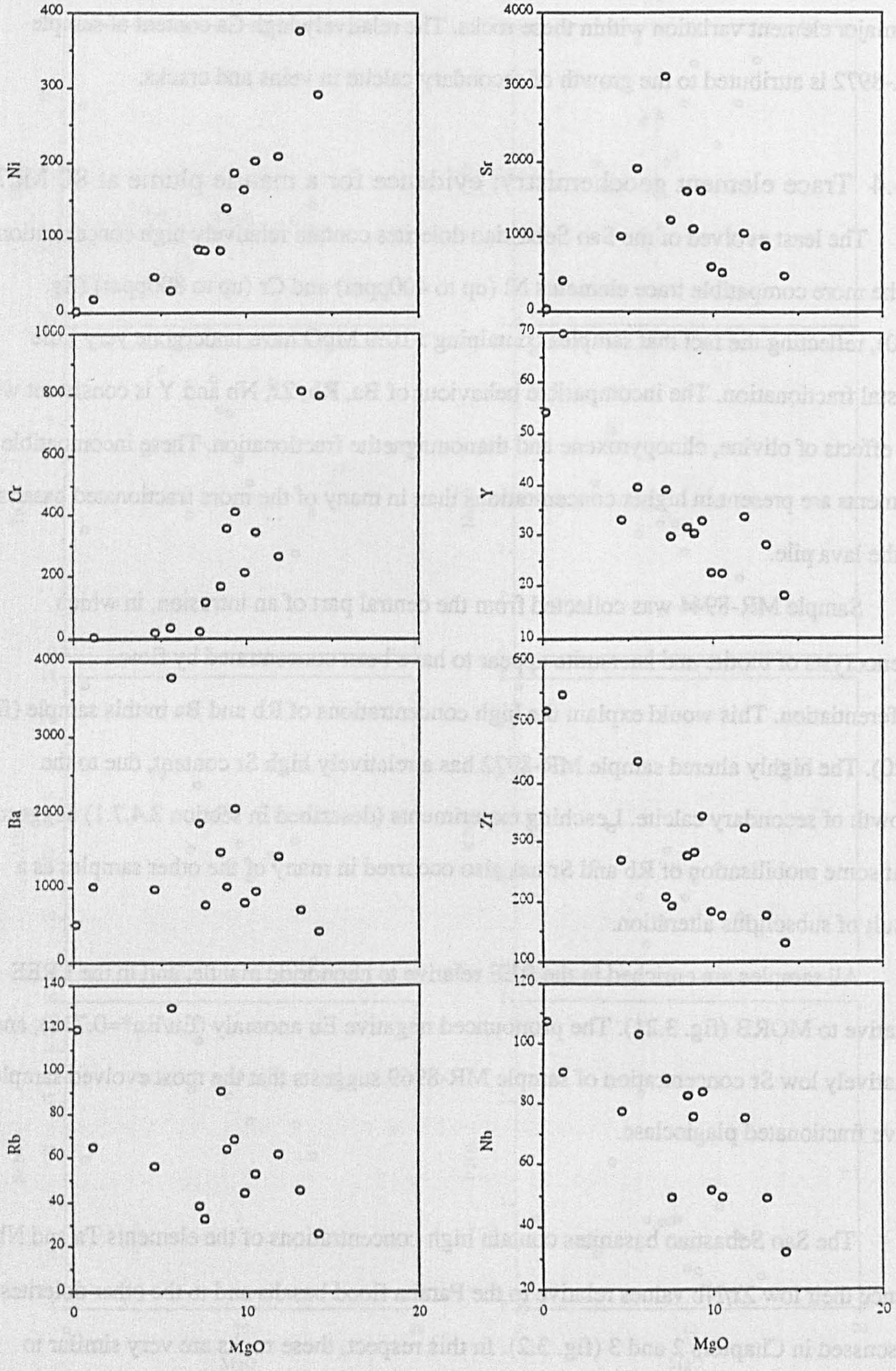

Fig. 3.20
Trace element variation within samples of the Sao Sebastiao magma type.

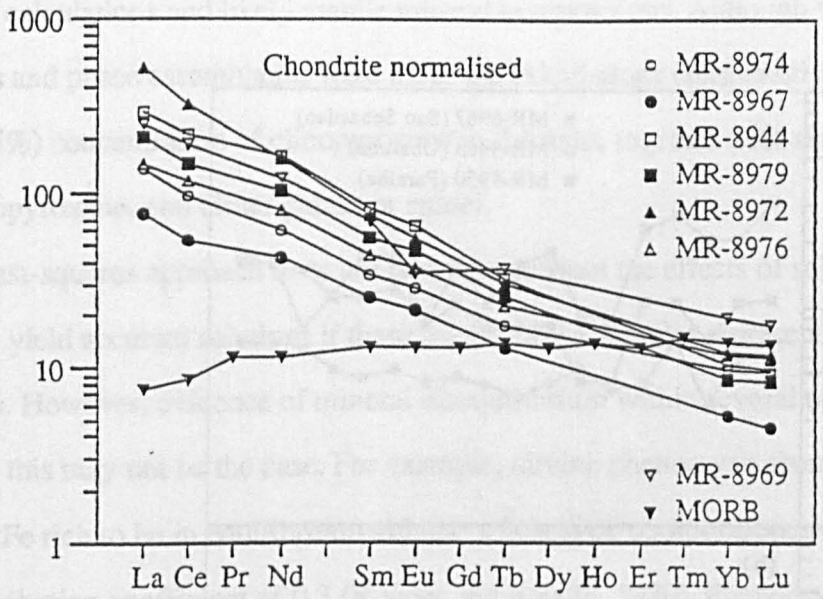

Fig. 3.21
REE concentrations of the Sao Sebastiao samples, normalised to the chondritic composition of Nakamura (1974). The average NMORB composition is taken from Sun and McDonough (1989).

Atlantic island of Tristan da Cunha in the region of the Parana at the time of continental rifting and flood basalt magmatism at around 130 Ma (Duncan, 1984), and the volume of the magmatism in this part of the South Atlantic is generally attributed to the thermal effect of this plume (White and McKenzie, 1989; Richards et al., 1989; and see Chapter 5).

Apart from slight anomalies for the elements Rb, Ba and U, the Sao Sebastiao basanites have very similar relative concentrations of the incompatible trace elements to Recent basanites erupted on Tristan da Cunha (fig. 3.22). The similarity is remarkable, given that there is an 80 Ma age difference between these two groups of rocks, and this implies that the Sao Sebastiao basanites represent the expression of the Tristan plume at 80 Ma. The high concentrations of Rb, Ba and U in these basanites relative to lavas from Tristan may reflect the influence of subsolidus alteration processes (sections 3.4.5.2, 3.4.6.1).

The Sr, Nd and Pb isotope compositions of basanites from Tristan and from the Brazilian mainland are compared in section 3.4.6, and the relationship between the basanites and oceanic basalts from the South Atlantic is examined in more detail in section 3.4.7.

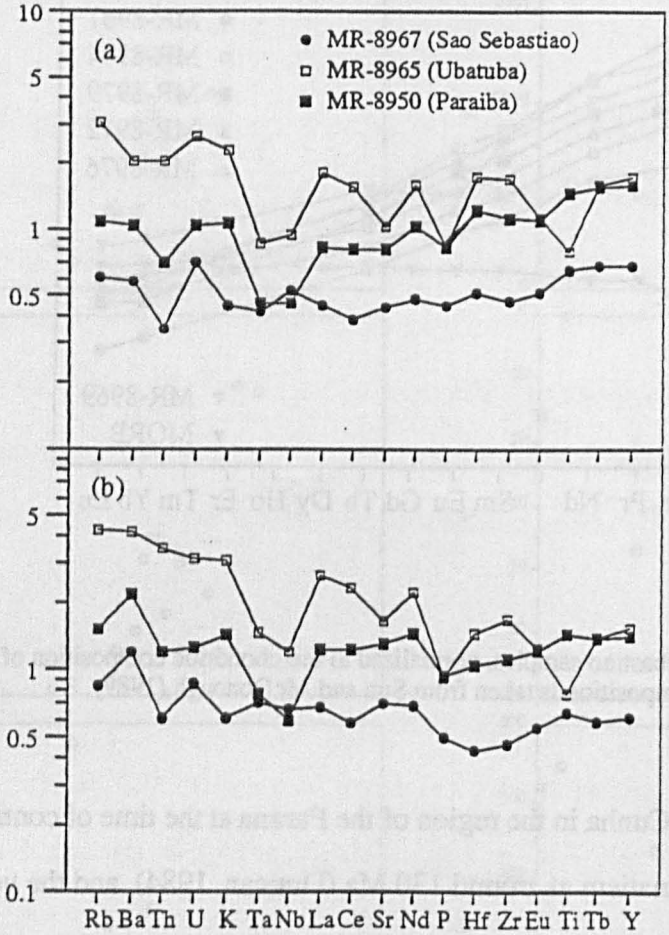

Fig. 3.22
Trace element compositions of representative samples of the Paraiba, Ubatuba and Sao Sebastiao magma types, normalised to (a), average Tristan da Cunha basanite (data from le Roex et al., 1990); (b), the average oceanic island basalt composition of Sun and McDonough (1989).

3.4.5 Petrogenesis of the Sao Sebastiao basanites; partial melting processes

Samples containing less than 10% MgO have $Mg/(Mg+Fe^{2+})$ values of 67.6—77.0 (calculated assuming that 15% of the total Fe is in the Fe^{3+} state) which are similar to those considered to be representative of primary melts in equilibrium with mantle olivine (68—76; Frey et al., 1978). These samples therefore appear to have undergone little or no fractionation, and can potentially yield insights into the mineralogy of the mantle source, and the nature of the melting processes responsible for magmatism in this region.

3.4.5.1 Major element constraints

An attempt was made to estimate the proportions of minerals entering the melt, using least-squares calculations and likely mantle mineral compositions. Although various mineral compositions and phase assemblages were used, the calculations consistently predicted a high (75—85%) concentration of clinopyroxene in the melt, together with small amounts of olivine, orthopyroxene, and either garnet or spinel.

The least-squares approach does not take into account the effects of solid solution, and will only yield accurate solutions if these least evolved samples represent liquid compositions. However, evidence of mineral disequilibrium within several of these samples suggests that this may not be the case. For example, olivine phenocrysts from sample MR-8967 are too Fe rich to be in equilibrium with the whole rock composition, assuming an Fe—Mg distribution coefficient of 0.3 (Roeder and Emslie, 1970). Phenocrysts of clinopyroxene in this sample display compositional zoning; the cores are enriched in the En component by up to 8%. The phenocryst compositions suggest that some crystal fractionation and magma mixing has occurred, and that the least evolved samples do not therefore represent liquid compositions. Any fractionation of olivine or clinopyroxene that has taken place will have the effect of decreasing the apparent contribution of these minerals to the melt. However, the high concentrations of Ni and Cr in those samples with more than 10% MgO suggests that these cannot have undergone more than about 5% olivine or clinopyroxene fractionation.

3.4.5.2 Trace element constraints

It is important to be able to place some constraints upon the behaviour of trace elements during the melting process, in order to determine the extent to which the distinctive trace element compositions of the Sao Sebastiao samples were inherited from their source. The conventional inverse approach of Hofmann and Feigenson (1983) could not be applied to the Sao Sebastiao samples, because there is evidence that the concentrations of the most incompatible elements Rb and Ba have been modified by subsolidus alteration processes (sections 3.4.6.1 and 3.4.7).

A forward modelling approach using trace element concentrations is an alternative method of investigating the conditions of the melting process. Although such an approach cannot provide a unique solution for the composition and mineralogy of the source, it can nevertheless place strong constraints upon the possible conditions of melting. During

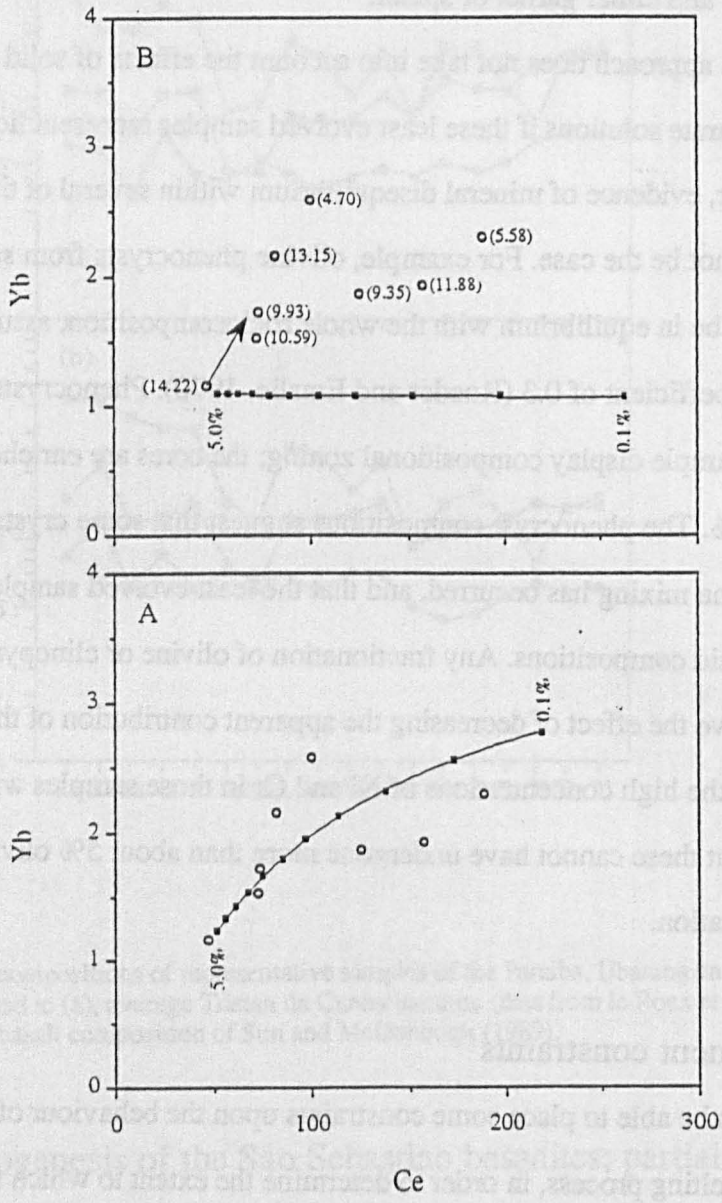

Fig. 3.23

Ce—Yb variation within the Sao Sebastiao samples (data by INAA). A vector illustrating the effect of 25% fractional crystallisation of olivine and clinopyroxene is shown in (A). Melting paths were calculated for (A), a typical spinel lherzolite, consisting of olivine (55%), orthopyroxene (27%), clinopyroxene (15%) and spinel (3%); and (B), a typical garnet lherzolite, consisting of olivine (55%), orthopyroxene (26%), clinopyroxene (6%), and garnet (11%). The mineral composition of the melt was estimated using least squares calculations, and were for (A), olivine (10%), orthopyroxene (13%), clinopyroxene (75%), spinel (2%), and for (B), olivine (10%), orthopyroxene (10%), clinopyroxene (78%) and garnet (2%). Mineral-melt distribution coefficients were taken from McKenzie and O'Nions (1992), and the source was assumed to contain Ce=9.975 ppm, Yb=1.11 ppm.

decompression melting of mantle material, melting probably occurs by a dynamic process (McKenzie, 1984; Klein and Langmuir, 1987), but useful information can be obtained by assuming equilibrium melting (Shaw, 1970), the geochemical effects of which are similar to those of more complex melting processes in many situations (Langmuir and Plank, 1988).

Melting paths were calculated using the REE elements, because mineral melt partition coefficients for these elements are relatively well known. Variations in the concentration of the more incompatible LREE can be used to estimate the extent of mantle melting, whilst the less incompatible HREE can place important constraints upon the residual source mineralogy (Feigenson, 1983). The elements Ce and Yb were therefore used in the modelling.

The Sao Sebastiao basanites have variable Ce and Yb concentrations, which cannot be explained in terms of fractional crystallisation of the observed phenocryst phases (fig. 3.23). Equilibrium melting paths were calculated using both spinel and garnet peridotite source compositions, using the estimate of the mineral composition of the melt obtained from the least squares modelling. The concentration of Yb in melts generated from garnet peridotite over likely melting intervals is buffered in the presence of residual garnet, whereas melts of spinel peridotite more closely reproduce the REE content of the Sao Sebastiao basanites. A reasonable fit to the data was obtained only by assuming that the source was enriched in the LREE relative to chondritic compositions (the melting paths in fig. 3.23 were calculated assuming that the concentration of Ce in the source was 5 times the chondritic concentration of Nakamura (1974); see caption to fig. 3.23).

Having placed some constraints upon the likely conditions of melting and the mineralogy of the mantle source to the Sao Sebastiao basanites, it is then possible to estimate the concentrations of other trace elements in the source. The Sao Sebastiao basanites were assumed to represent relatively small (0.1—5.0%) degree melts of a spinel lherzolite (the calculations are relatively insensitive to the exact mineral composition used, particularly if garnet is absent). The estimate of the mineral composition of the melt obtained from the least squares calculations (section 3.4.5.1) was used in the modelling. This approach suggests that firstly, the relatively low Zr/Nb values of the Sao Sebastiao basanites cannot be explained in terms of fractionation during partial melting or subsequent fractional

crystallisation, and appear to have been derived from their source. Secondly, the mantle source of the Sao Sebastiao basanites had Sm/Nd values of 0.18—0.23 (this can place important constraints upon models for the radiogenic isotope evolution of these rocks (section 3.4.6.3)). The Rb/Sr value of the source is more difficult to estimate, because the concentrations of both of these elements have been affected by subsolidus alteration (section 3.4.6.1).

3.4.6 Isotope geochemistry

3.4.6.1 Sr and Nd isotope geochemistry, and the role of subsolidus alteration

Initial $^{87}Sr/^{86}Sr$ and $^{143}Nd/^{144}Nd$ values were calculated assuming an age of 80 Ma for all samples (see Chapter 4). The Sao Sebastiao dolerites have initial Sr and Nd isotope compositions unlike any of the flood basalts of the southern Parana (fig. 3.24); most have significantly higher εNd values. However, note the relatively large scatter of the data, and that several samples have positive values of both εSr and εNd. This implies that the Sr isotope composition of these dolerites may have been affected by subsolidus alteration processes, which result in an increase in the whole-rock $^{87}Sr/^{86}Sr$ value, but tend to have little effect upon $^{143}Nd/^{144}Nd$ (for example; McCulloch et al., 1980). The petrography (section 3.4.2) and the relatively high values of loss on ignition of these rocks (only 2 samples have values of loss on ignition of less than 2%) suggests that alteration processes may indeed have had an important influence upon the isotopic composition of Sr in these basanites. It is interesting that most of these rocks are significantly more altered than the older dolerites of the Paraiba and Ubatuba magma types, which also occur in this region. This may be due to the fact that the Sao Sebastiao samples have a higher temperature mineralogy and contain more olivine, a mineral that appears to be particularly susceptible to alteration. This interpretation is supported by the fact that the more primitive samples of the Sao Sebastiao magma type appear to have been more severely altered (fig. 3.25).

Leaching experiments were carried out in an attempt to constrain the Sr isotope composition of these rocks prior to alteration. Whole-rock powders of four samples were leached in warm 6M HCl for 24hr, before being washed several times in distilled water in an

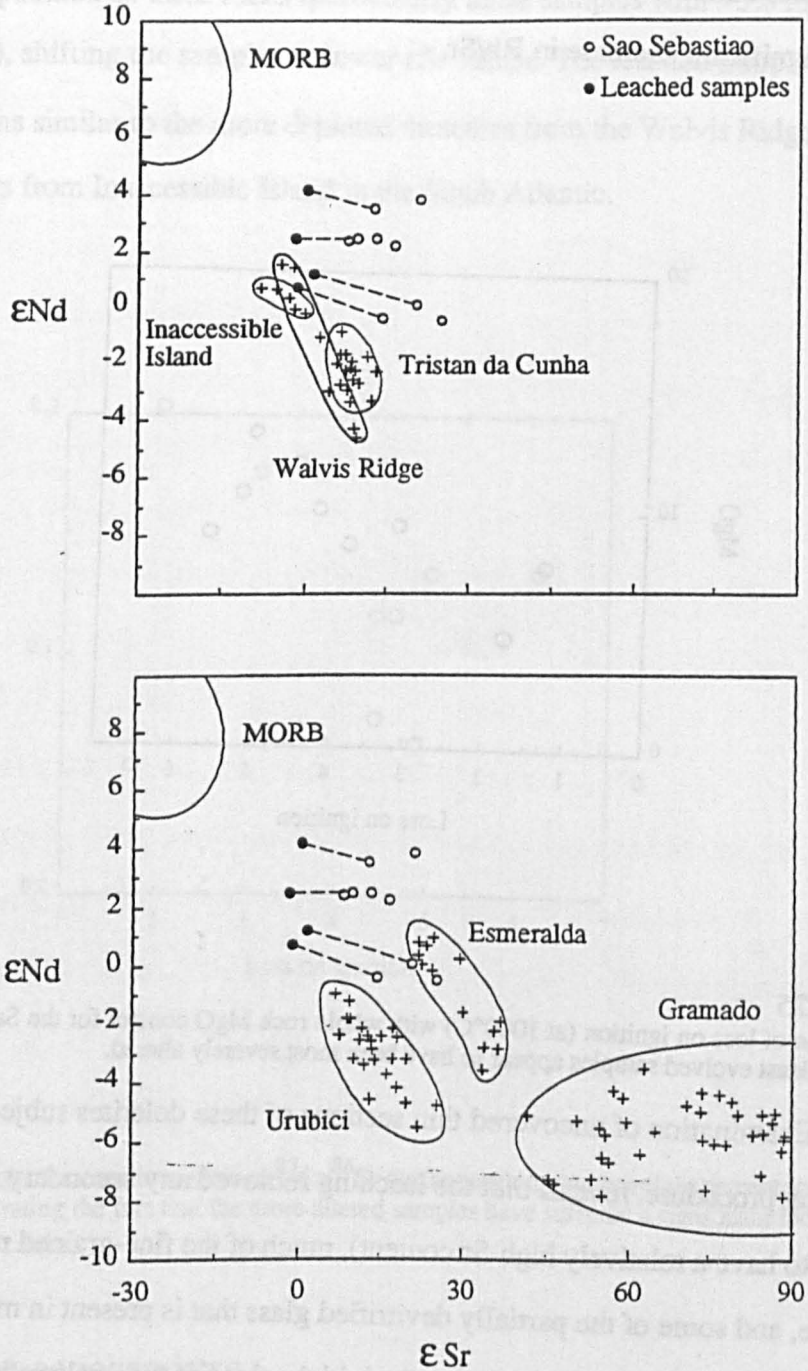

Fig. 3.24

εSr—εNd variation (at 80 Ma) within the Sao Sebastiao samples. Data for basalts from Tristan da Cunha (le Roex et al., 1990), Inaccessible Island (Cliff et al., 1991), the Walvis Ridge (Richardson et al., 1982), and the southern Parana (Peate, 1989) are shown for reference.

ultrasonic bath. No further change in the isotopic compositions of either Sr or Nd was observed if the leaching was carried out for a longer period of time (see Appendix). The Rb and Sr concentration of the leached sample was measured by isotope dilution, and these were used to calculate the initial $^{87}Sr/^{86}Sr$ value. The leaching process resulted in a decrease

in the concentration of both Sr and Rb by up to 52% and 59% respectively, and, in most cases, a significant decrease in Rb/Sr.

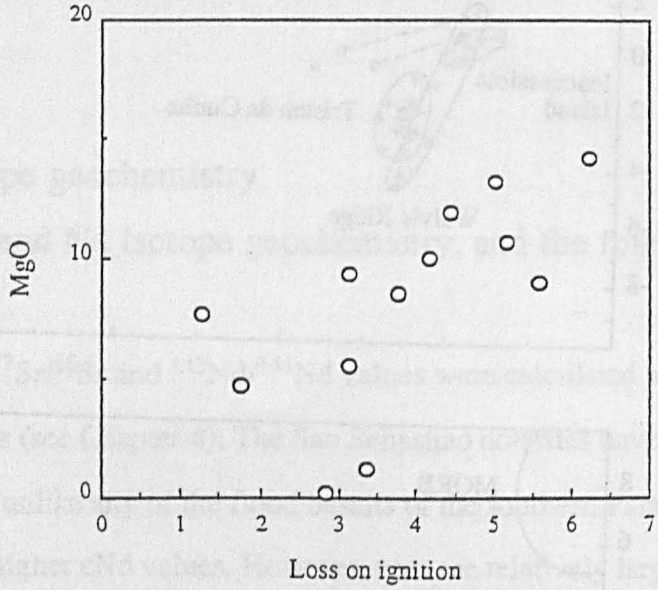

Fig. 3.25
Variation of loss on ignition (at 1000°C) with whole rock MgO content for the Sao Sebastiao samples. Note that the least evolved samples appear to have been most severely altered.

Examination of uncovered thin sections of these dolerites subjected to the same leaching procedure, reveals that the leaching removed any secondary carbonate (which is likely to have a relatively high Sr content), much of the fine-grained material which replaces olivine, and some of the partially devitrified glass that is present in many samples. The age corrected values will only represent the initial values of the unaltered rock if all of the secondary Rb and Sr has been removed, and if Rb and Sr has not been preferentially removed from the glass during leaching. The acid leachate separated from one of these samples (MR-8976) and yielded a $^{87}Sr/^{86}Sr$ value of 0.70629 ± 3. For comparison, the Precambrian basement rocks of Sao Paulo State have significantly higher values (Gasparini and Mantovani, 1979) of 0.709—0.870 (at 80 Ma).

The leaching process has little effect upon the Nd isotope composition of these samples (fig. 3.24), which suggests that the Nd isotope system has remained relatively resistant to the effects of subsolidus alteration. However, leaching has a significant effect on

the Sr isotope composition of these rocks (particularly those samples with >3% loss on ignition (fig. 3.26)), shifting the samples to lower εSr values. The leached samples have isotope compositions similar to the more depleted tholeiites from the Walvis Ridge, and to Recent alkali basalts from Inaccessible Island in the South Atlantic.

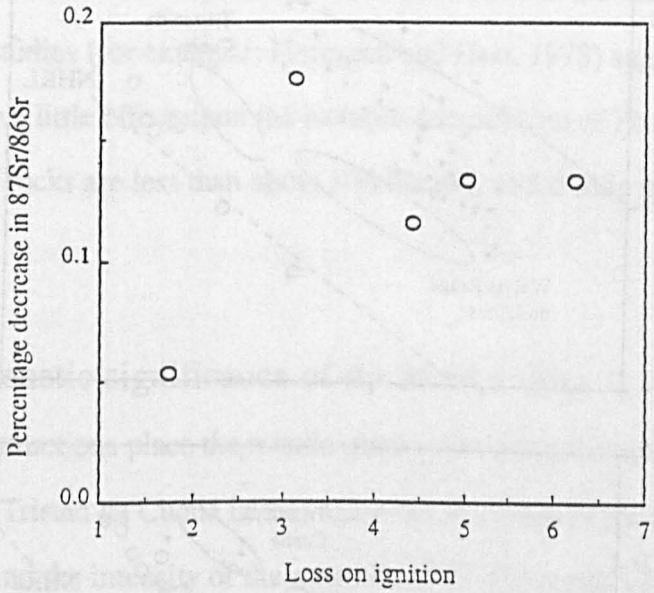

Fig. 3.26
Variation of the percentage decrease in measured $^{87}Sr/^{86}Sr$ during leaching, with weight percentage loss on ignition at 1000°C, illustrating the fact that the more altered samples have suffered a significant increase in the whole rock $^{87}Sr/^{86}Sr$ value.

3.4.6.2 Pb isotope geochemistry

The isotope composition of Pb from nine samples of the Sao Sebastiao magma type are presented in fig. 3.27. The data have been corrected for mass spectrometer fractionation, but not for the decay of the radiogenic isotopes of Th and U since crystallisation, because precise U and Th concentration data by INAA were not available for all samples. Assuming an age of 80 Ma for all samples, then the average Th/Pb and U/Pb ratios (1.07 and 0.29 respectively, by INAA) require relatively small age corrections of 0.232, 0.011 and 0.274 for $^{206}Pb/^{204}Pb$, $^{207}Pb/^{204}Pb$ and $^{208}Pb/^{204}Pb$, respectively.

The Sao Sebastiao basanites have distinctive Pb isotope compositions which are displaced to lower $^{207}Pb/^{204}Pb$ than the array defined by basalts from the Parana lava field (fig. 3.27), and have very similar isotope compositions to Recent basanites erupted on

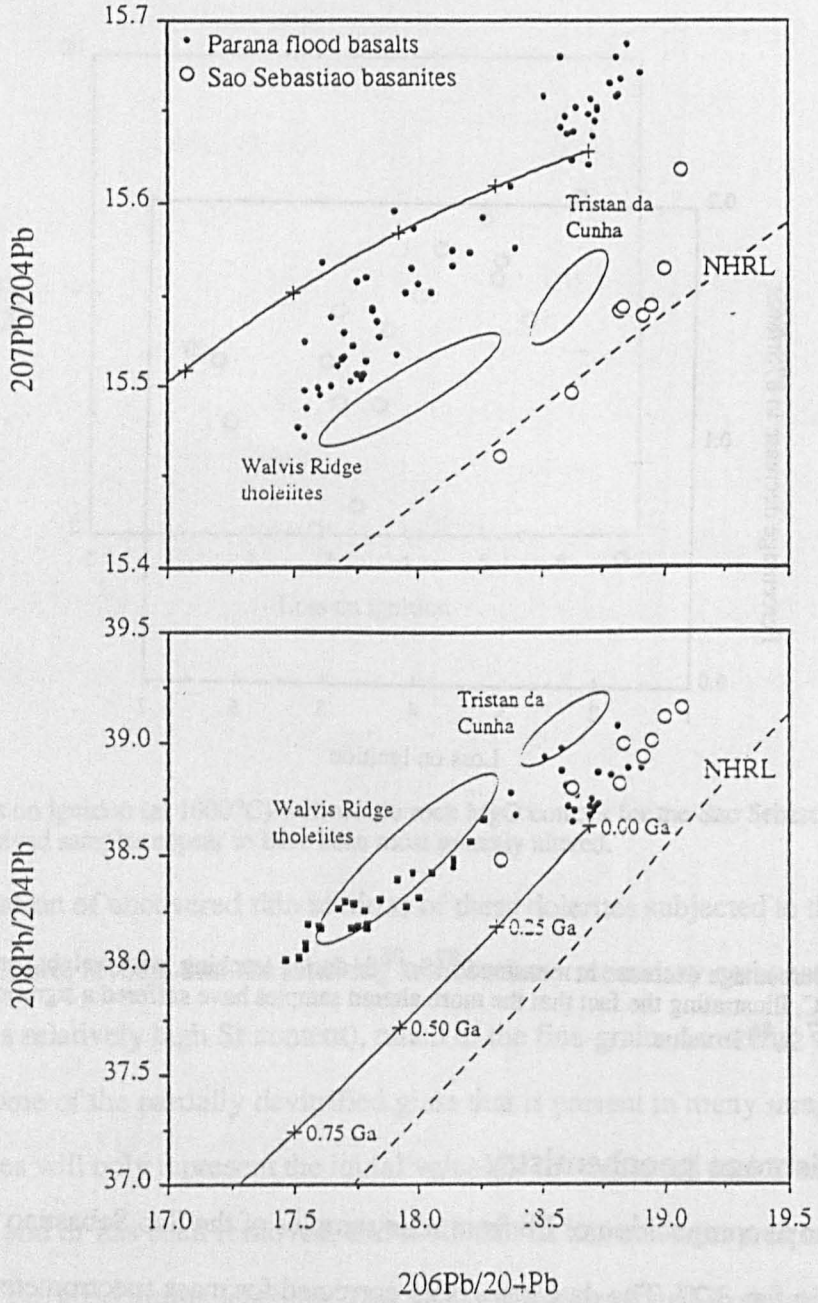

Fig. 3.27
Pb isotope compositions of the Sao Sebastiao samples. Data for basalts from Tristan (le Roex et al., 1990), the Walvis Ridge (Richardson et al., 1982), and the southern Parana (Peate, 1989), are also included. The model Pb isotope growth curve of Stacey and Kramers (1975), and the Northern Hemisphere Reference Line of Hart (1984) are shown for reference.

Tristan da Cunha (data from le Roex et al., 1990). The simplest interpretation of the data is that unlike the Parana flood basalts, the Ponta Grossa dolerites, and the other dolerite types

discussed in this Chapter, the Pb of the Sao Sebastiao dolerites does not contain a significant contribution from the lithosphere, but instead represents the expression of the Tristan da Cunha mantle plume, which is believed to have lain beneath the region at 80 Ma (section 3.4.6.3).

An attempt was made to measure the effect of leaching on the isotopic composition of Pb in these samples, but six samples subjected to the same leaching procedure as described in section 3.4.6.1 twice failed to produce stable ion beams in the mass spectrometer. However, other studies (for example; Hofmann and Hart, 1978) suggest that alteration processes will have little effect upon the isotopic composition of Pb in basaltic rocks, particularly if the rocks are less than about 100 Ma old, and if little mobilisation of U and Th has taken place.

3.4.6.3 Petrogenetic significance of the isotope data

Plate reconstructions place the mantle plume that is at present beneath the South Atlantic island of Tristan da Cunha in the region of the Parana at the time of eruption (Duncan, 1984), and the intensity of the magmatism in this region of the South Atlantic is generally attributed to the thermal effect of this plume (see Chapter 5). However, there is no clear geochemical evidence for a contribution from the Tristan plume to the Ponta Grossa dolerites or to any of the Parana flood basalts. For example, the Ponta Grossa dolerites yield $^{207}Pb/^{206}Pb$ ages that are similar to the age of the overlying lithosphere, and it has been argued in Chapter 2 that much of the Pb in these dolerites was derived from a source within the subcontinental lithospheric mantle.

In contrast, the Sao Sebastiao basanites have remarkably similar trace element geochemistry to Recent lavas erupted on oceanic islands (section 3.4.4.1), and leached samples have similar εSr and εNd values to rocks from the Walvis Ridge and Inaccessible Island (which lies ~40 km to the southwest of Tristan). Class et al. (1991, 1992) have recently interpreted the isotope array variation within basalts from Tristan and the Walvis Ridge as the result of radioactive decay in the mantle source of these basalts. If the Sao Sebastiao basanites can be regarded as the expression of the Tristan plume at 80 Ma, then the isotope compositions of these rocks can provide an important test of this model.

Assuming that the Sao Sebastiao basanites were intruded at 80 Ma, and that they were derived from the same source as basanites from Tristan, requires this source to have Rb/Sr

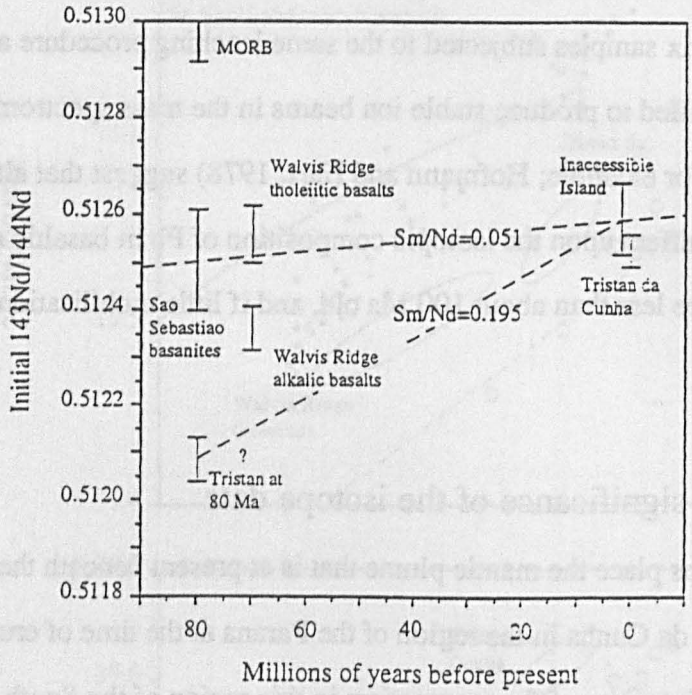

Fig. 3.28

Variation of initial $^{143}Nd/^{144}Nd$ with age within oceanic basalts from the South Atlantic Ocean (data from Cliff et al., 1991, le Roex et al., 1990; Richardson et al., 1982). In order to derive the Tristan and Inaccessible Island basalts by radioactive decay within the source of the Sao Sebastiao basanites and Walvis Ridge tholeiites, requires an unlikely source Sm/Nd value of 0.051, whereas the calculations carried out in section 3.4.5.1 suggests that in fact this source had a Sm/Nd value of approximately 0.20. An alternative explanation for the relatively high initial $^{143}Nd/^{144}Nd$ values of the Walvis and Sao Sebastiao rocks is that they were derived from a mixed mantle source containing a contribution from the Tristan plume, and a contribution from the source to MORB from the South Atlantic.

and Sm/Nd values of 0.146 and 0.051 respectively (fig. 3.28). The measured Sm/Nd of the Sao Sebastiao basanites are in the range 0.18 to 0.20 (data by isotope dilution), which requires that Sm/Nd values were increased by a factor of about 4 during partial melting of the source. This is inconsistent with the relative incompatibilities of these elements in mantle minerals (Irving and Frey, 1984), and with the calculations carried out in section 3.4.5.2, which suggest that in fact the source had a Sm/Nd value of 0.18—0.23.

Tholeiitic basalts from the Walvis Ridge which were erupted at 70 Ma have less radiogenic Pb compositions than Recent lavas erupted on Tristan (Richardson et al., 1982) (fig. 3.27). This was attributed by Class et al. (1991, 1992) to the decay of the radioactive isotopes of U and Th in the source of these oceanic basalts. Assuming that the Sao Sebastiao dolerites were derived from the same source at 80 Ma, then these should have sightly less radiogenic Pb compositions than tholeiitic basalts from the Walvis Ridge. In fact, this is not the case; the Sao Sebastiao dolerites have very similar initial Pb isotope compositions to Recent basanites erupted on Tristan da Cunha (fig. 3.27).

An alternative explanation of the variation in isotope composition of oceanic basalts from the South Atlantic is that it is the result of mixing processes, and this is discussed further in the following section.

3.4.7 The role of mixing processes in South Atlantic basalt petrogenesis

Humphris et al. (1985) have shown that basalts dredged from the Mid-Atlantic Ridge between latitudes 33 and 38°S are enriched in the LREE relative to basalts from further to the north and south, and that this represents the geochemical influence of the Tristan plume, which lies about 430 km to the east of the ridge at this point.

Basalts from the Walvis Ridge represent the expression of the Tristan plume at between 0 and about 100 Ma (le Roex et al., 1992). These have Sr and Nd isotope compositions that are intermediate between those of Recent alkalic basalts from Tristan and MORB from the South Atlantic (Richardson et al., 1982) (fig. 3.24). Humphris and Thompson (1983) have argued that the trace element composition of tholeiitic basalts from the Walvis Ridge can be explained in terms of a two-component mixing process (fig. 3.29).

In contrast, Richardson et al. (1982) have argued that several features of the trace element variation within tholeiitic basalts from the Walvis Ridge (in particular their high Ba/Nb values) cannot be explained in terms of a simple two-component mixing process (fig. 3.30). Richardson et al. (1982) proposed that the Walvis Ridge basalts represent partial melts of an inhomogenous, variably trace element enriched mantle source. They showed that

the Walvis Ridge samples define a $^{147}Sm/^{144}Nd$—$^{143}Nd/^{144}Nd$ array, which if interpreted as a secondary isochron, yields a minimum age of 800 Ma for the enrichment event. This age is similar to the ages obtained from amphibolites and volcanic rocks from the Damaran Province of Namibia (Hawkesworth et al., 1981). Alternatively, this isotope variation could be interpreted in terms of a mixing process.

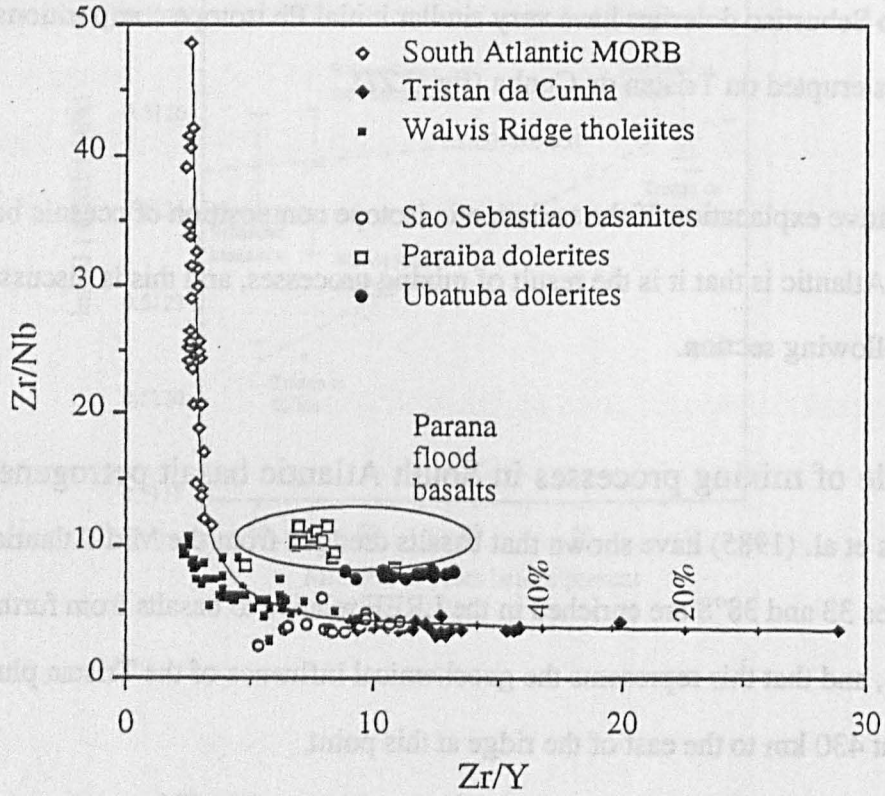

Fig. 3.29
Zr/Nb—Zr/Y variation within basalts from the South Atlantic (data sources; Cliff et al., 1991; le Roex et al., 1990; Richardson et al., 1982; Humphris and Thompson, 1983). The Sao Sebastiao samples lie upon a simple two component mixing curve between NMORB and Tristan endmembers. Data for the Parana flood basalts (Peate, 1989), and the dolerites of the Paraiba and Ubatuba magma types are displaced from this mixing line.

Richardson et al. (1982) analysed fresh glass separates from the Walvis Ridge basalts, and demonstrated that many of these samples have undergone a considerable degree of subsolidus alteration, which has resulted in an increase in the whole rock $^{87}Sr/^{86}Sr$ value by up to 0.5%. The LIL elements, including Ba, are particularly mobile during alteration of basalt (Cox and Hawkesworth, 1985; Lightfoot, 1985; Peate, 1989), which suggests that the high Ba/Nb values of the Walvis Ridge tholeiites may in part be due to the effects of

alteration processes. This is supported by new geochemical data for the Sao Sebastiao basanites.

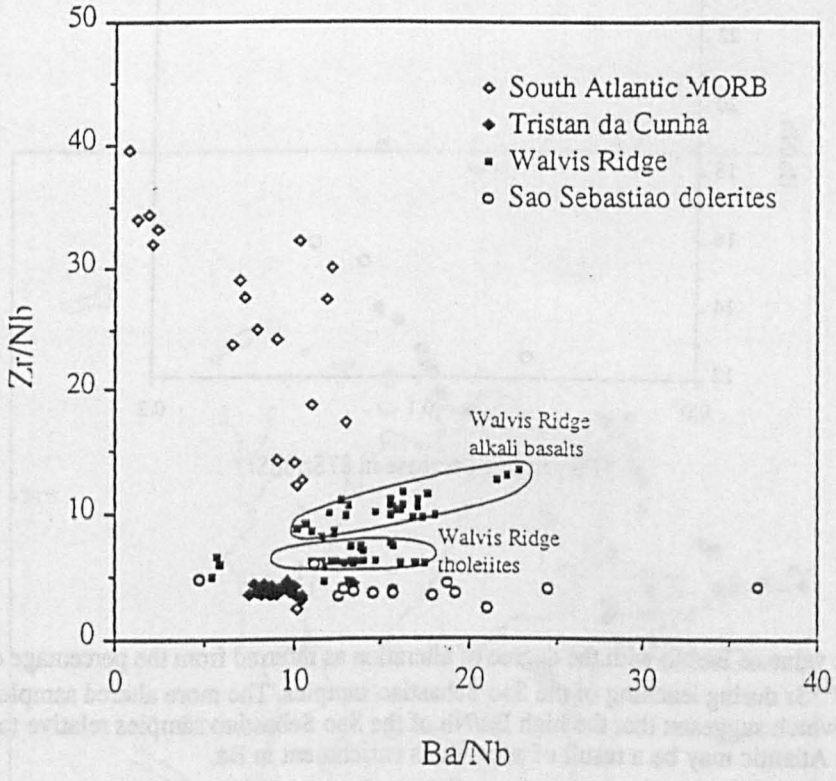

Fig. 3.30
Zr/Nb—Ba/Nb variation within oceanic basalts from the South Atlantic (data sources as for fig. 3.29). The Walvis Ridge basalts, and the Sao Sebastiao samples are displaced to higher Ba/Nb from a two component mixing array between basalts from Tristan and MORB from the South Atlantic.

The Sao Sebastiao basanites have incompatible trace element compositions that are in general intermediate between those of basanites from Tristan and tholeiitic basalts from the Walvis Ridge (for example, fig. 3.29). Note that the Sao Sebastiao samples also have variable, high Ba/Nb values relative to basanites from Tristan (fig. 3.30). However, the Ba/Nb values of the Sao Sebastiao basanites are highest in those samples which have been

most severely altered, as inferred from the extent of Sr isotope modification (fig. 3.31). This suggests that the high Ba concentrations of these basanites relative to lavas from Tristan may be due to the effects of subsolidus alteration.

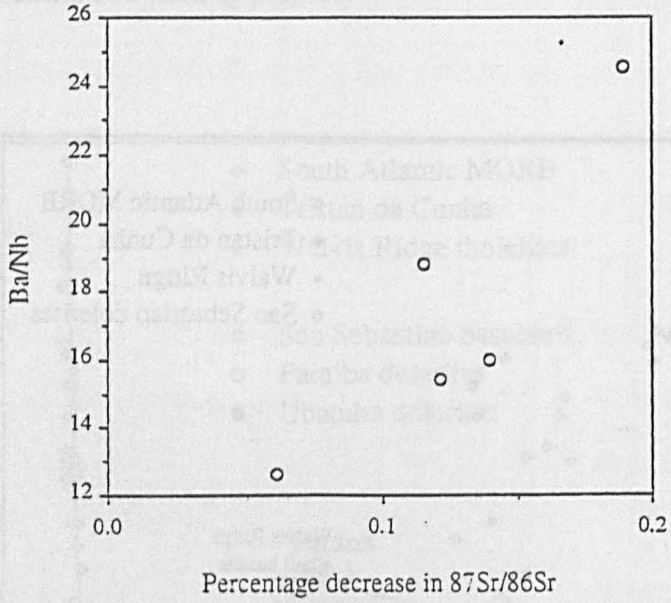

Fig. 3.31
Variation in the value of Ba/Nb with the degree of alteration as inferred from the percentage decrease in measured $^{87}Sr/^{86}Sr$ during leaching of the Sao Sebastiao samples. The more altered samples have higher Ba/Nb values, which suggeststst that the high Ba/Nb of the Sao Sebastiao samples relative to oceanic basalts from the South Atlantic may be a result of subsolidus enrichment in Ba.

In conclusion, the high εNd, low εSr and $^{207}Pb/^{204}Pb$ values of the Sao Sebastiao basanites relative to the older Parana basalts requires them to have been derived from a source of very different composition. The similarity in trace element and isotope composition to oceanic basalts from the South Atlantic implies that the Sao Sebastiao basanites do not contain a significant contribution from the lithosphere. Although there is some debate concerning the nature of the processes responsible for the trace element and isotope composition of oceanic basalts from the South Atlantic, it is generally accepted that mixing processes play an important role. The Sao Sebastiao basanites lie upon the mixing arrays defined by these oceanic basalts, and are interpreted as melts of a mixed mantle source, containing a contribution from the Tristan plume, and a contribution from the source

to the mid ocean ridge basalts of the South Atlantic Ocean. The relatively high Ba concentrations of the Sao Sebastiao basanites are due to the effect of alteration processes.

3.4.8 Other Cretaceous alkalic intrusive rocks in Sao Paulo State

Alkaline intrusive rocks of Cretaceous age are widespread in southern Brazil and Namibia, particularly around the northern and eastern margins of the Parana lava field (fig.

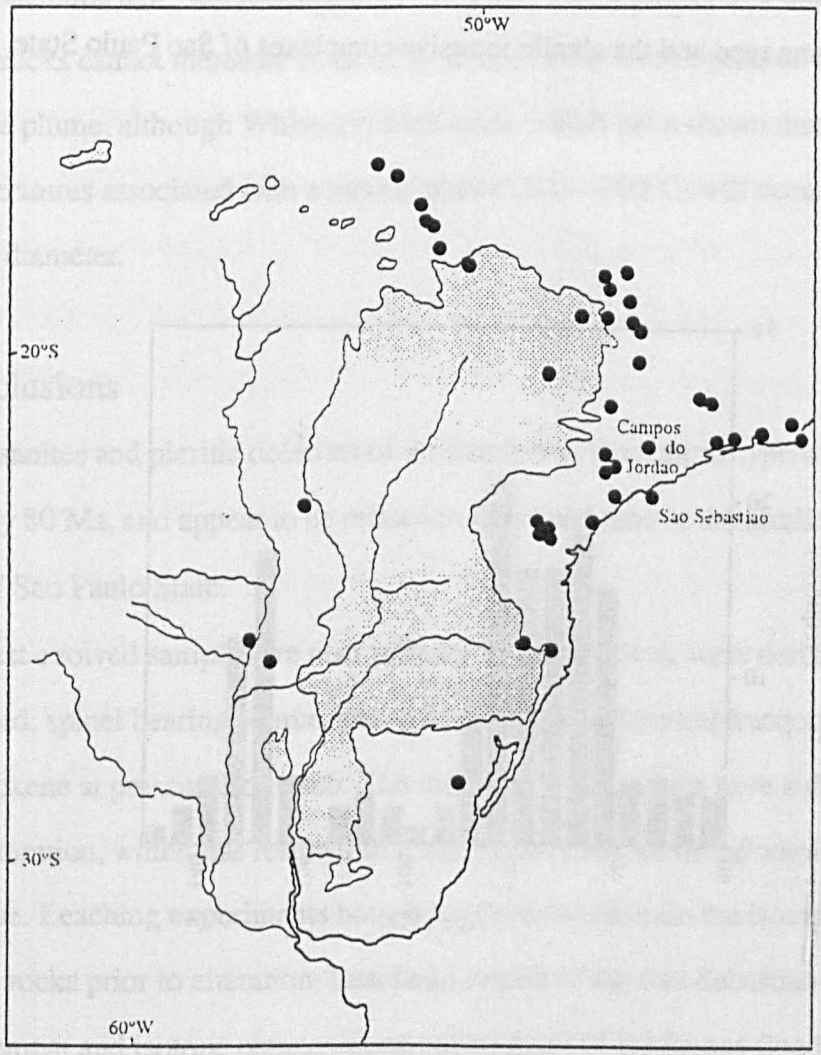

Fig. 3.32
Distribution of the Mesozoic alkalic intrusive complexes of southern Brazil (modified from Ulbrich and Gomes, 1981).

3.32). These yield K—Ar and Rb—Sr ages of between 50 and 140 Ma (Ulbrich and Gomes, 1981) (fig. 3.33).

The Sao Sebastiao dolerites were collected from the coastal region of Sao Paulo State close to the offshore alkalic complex of Sao Sebastiao Island, and were also encountered further inland close to the alkalic complex of Campos do Jordao. A biotite separate from sample MR-8944 yielded a Ar—Ar age of 80.9 ± 0.4 Ma (Chapter 4). The Sao Sebastiao alkalic complex has an age of approximately 81 Ma (Melcher and Melcher, 1972), and the intrusive complex of Campos do Jordao has been dated at 80 Ma (Amaral et al., 1967). There is therefore a close association in space and time between the dolerites of the Sao Sebastiao magma type and the alkalic intrusive complexes of Sao Paulo State.

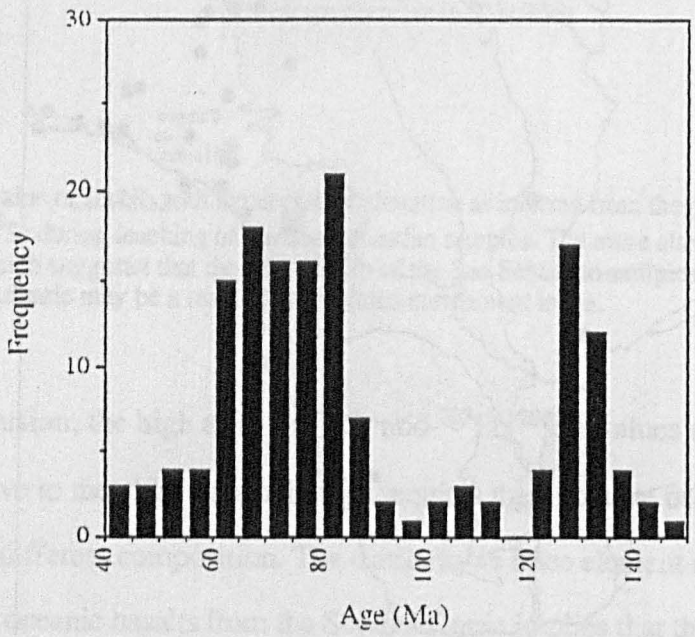

Fig. 3.33
Histogram of K—Ar and Rb—Sr ages of Mesozoic alkalic rocks from southern Brazil (data from Ulbrich and Gomes, 1981). Note the bimodal distribution of ages, and that several of these intrusions (including the Sao Sebastiao and Campos do Jordao intrusions) have ages of approximately 80 Ma.

The Sao Sebastiao complex consists of a number of stock-like intrusions, composed of nepheline syenite, pulaskite, nordmarkite and tinguaite (Guimaraes, 1960; Melcher and Melcher, 1972; S. Gibson, pers. comm.). Most of these rocks are considerably more evolved than the dolerites of the Sao Sebastiao magma type, but unfortunately there are too few trace element and isotope data for these various rocktypes for the relationship between these alkalic rocks and the Sao Sebastiao basanites to be investigated in any detail.

The alkalic rocks extend some 1200 km to the NW of Rio de Janeiro (fig. 3.32). Their emplacement was strongly controlled by the regional structure of the basement, and there is no systematic age variation along the length of their outcrop. The distribution of these alkalic rocks cannot therefore be directly related to the former position of the Tristan da Cunha mantle plume, although White and McKenzie (1989) have shown that the excess mantle temperatures associated with a mantle plume (100—200°C) will occur over an area ~2000 km in diameter.

3.4.9 Conclusions

The basanites and picritic dolerites of the Sao Sebastiao magma type were intruded at approximately 80 Ma, and appear to be related in space and time to the alkalic intrusive complexes of Sao Paulo State.

The least evolved samples are near primary in composition, were derived from a LREE enriched, spinel bearing source, and underwent limited crystal fractionation of olivine and clinopyroxene at pressures of >4kb. The more Mg rich samples have suffered extensive subsolidus alteration, which has resulted in a significant increase of the whole rock $^{87}Sr/^{86}Sr$ value. Leaching experiments have been used to constrain the isotope composition of Sr in these rocks prior to alteration. Leached samples of the Sao Sebastiao magma type have trace element and isotope compositions unlike those of the Parana flood basalts, but similar to oceanic basalts from the South Atlantic, which implies that they have not received a significant contribution from the lithosphere. The basanites lie upon mixing arrays defined by oceanic basalts from the South Atlantic, and are interpreted as melts of a mixed mantle source, containing a contribution from the Tristan da Cunha mantle plume, and a contribution from the source to the mid ocean ridge basalts of the South Atlantic. The

relatively high Ba concentrations of the Sao Sebastiao basanites are interpreted as the effects of subsolidus alteration processes.

3.5 Chapter 3; summary and conclusions

The samples discussed in this chapter were collected from an approximately 7000 km^2 area in the region to the north of the town of Sao Sebastiao, Sao Paulo State. Previous studies by Comin-Chiaramonti et al. (1983) and Piccirillo et al. (1988) have revealed that the dykes extend westwards to Serra dos Itatins, and as far east as the coastline to the north of Rio de Janeiro, but this is the first detailed geochemical and petrogenetic study of these dolerites to have been carried out.

The dolerites analysed in this study are divisible into three magma types, which cannot be related to one another, or to the flood basalts of the lava field, by any simple petrogenetic process. Dolerites of the Paraiba and Ubatuba magma types were intruded at approximately 132 Ma; the Sao Sebastiao basanites are considerably younger (80 Ma).

The geochemical variation within the Paraiba and Ubatuba dolerites reflect the control of shallow-level AFC and magma mixing processes. The most basic samples of the Sao Sebastiao magma type are primary or near primary in composition, having undergone only limited crystal fractionation of olivine and clinopyroxene at pressures of greater than about 4 kb. These dolerites appear to be related in space and time to the alkalic intrusive complexes of Sao Paulo State, and have remarkably similar trace element and isotope compositions to Recent basanites erupted on the South Atlantic island of Tristan da Cunha. Plate reconstructions place the mantle plume that is at present beneath Tristan in the region of the Parana at 80 Ma, and the Sao Sebastiao samples are interpreted as melts of a mixed source, containing a contribution from the Tristan plume, and a contribution from the source to the NMOR basalts of the South Atlantic Ocean.

Chapter 4

The age of the Parana-Etendeka flood basalt magmatism

4.1 Introduction.

As discussed in Chapter 1, two geodynamic models for the origin of continental flood basalts have recently been put forward, which attempt to explain the observed close association in space and time between CFB magmatism, continental rifting, and the location of mantle plumes (Morgan, 1981). Richards et al. (1989) have proposed that CFB are erupted when a mantle plume initiates beneath continental lithosphere. In this model, flood basalt magmatism need not be accompanied by continental breakup, and the magmatism may occur before extension and continental rifting. In contrast, White and McKenzie (1989) have shown that the large volume and rapid eruption rates of CFB can be explained by decompression melting during continental rifting and breakup above the abnormally hot upper mantle associated with a mantle plume. This model predicts that magmatism will be contemporaneous with, or slightly postdate the main period of extension (these models are discussed in more detail in Chapter 5).

In order to decide which of these models can best explain the characteristics of a particular CFB province, it is essential to have a precise knowledge of both the age range of the flood basalt magmatism, and its age relative to that of continental rifting. For example, Hooper (1989) noted that in the Deccan and Columbia River CFB provinces (the ages of which are relatively well constrained by Ar—Ar dating), magmatism appears to have preceded the main period of extension by a few million years, and therefore concluded that flood basalt eruption occurred in response to the initiation of a mantle plume, rather than being due to decompression melting during continental extension.

Most of the existing age determinations for the Parana have been carried out using the K—Ar method, and various authors have obtained apparent ages of between 80 and 165 Ma. In contrast, recent Ar—Ar dating of the Deccan (Duncan and Pyle, 1988; Courtillot et al., 1988) and the Columbia River flood basalts (Long and Duncan, 1983) suggests that other CFB were erupted rapidly in the space of only one or two million years. Much of the

apparent age range of the Parana rocks may therefore be a result of the loss or gain of radiogenic ^{40}Ar, and it was decided to date a selection of the Parana dolerites using the Ar—Ar laser fusion technique. Eight whole-rock samples, and six mineral separates from five samples have been analysed. The new data are presented in section 4.5, and their geodynamic significance is discussed in Chapter 5.

4.2 Summary of previous work.

4.2.1 The age of the Parana volcanic rocks.

Early workers in the Parana (Huene, 1933; Sanford and Lange, 1960) were able to constrain the lavas to be between Upper Triassic and Upper Cretaceous in age, on the basis of the fossil faunas of the sediments immediately below and above the lavas. Since 1965, numerous K—Ar and some Rb—Sr dating studies have been carried out on samples from all parts of the Parana-Etendeka province, and there now exists a database of over 200 age determinations, on both whole rock samples and mineral separates. Unfortunately, sampling was often carried out with little stratigraphical control, and only rarely have the dated samples been subjected to geochemical analysis, so that the variation of absolute age with stratigraphic height and geochemistry is not well constrained.

The first published K—Ar data for Parana rocks were those of Creer et al. (1965), who obtained K—Ar ages of between 124 and 149 Ma for six basalt samples from the central lava field. Amaral et al. (1966) carried out K—Ar analysis of 35 samples from localities throughout the Parana province (including both intrusive and extrusive rocks), which yielded ages of between 100 and 161 Ma. This work was followed by that of McDougall and Ruegg (1966), Vandoros et al. (1966), and Melfi (1967). These early studies established the approximate age range of the Parana, and later work (Minioli et al., 1971; Sartori et al., 1975; Pacca and Hiodo, 1976; Fodor and Vetter, 1984; Mantovani et al., 1985; Piccirillo et al., 1987; Bitschene, 1987) served to confirm the earlier results, extending the number of K—Ar analyses of Parana rocks to over 200.

Siedner and Mitchell (1976) used $^{40}Ar/^{36}Ar$—$^{40}K/^{36}Ar$ isochron analysis to reinterpret some of the earlier results of Amaral et al. (1966) and Melfi (1967). A group of basalts from Santa Catarina and Sao Paulo states (which had individual ages of between 110

and 123 Ma (Amaral et al., 1966)) yielded an isochron age of 120.3 ± 1.2 Ma. Similar analysis of dolerites from Ubatuba (individual ages 129—138 Ma (Amaral et al., 1966)) and scattered borehole samples (120—135 Ma (Melfi, 1967)), yielded isochron ages of 127.9 ± 3.6 Ma and 127 ± 1.0 Ma respectively.

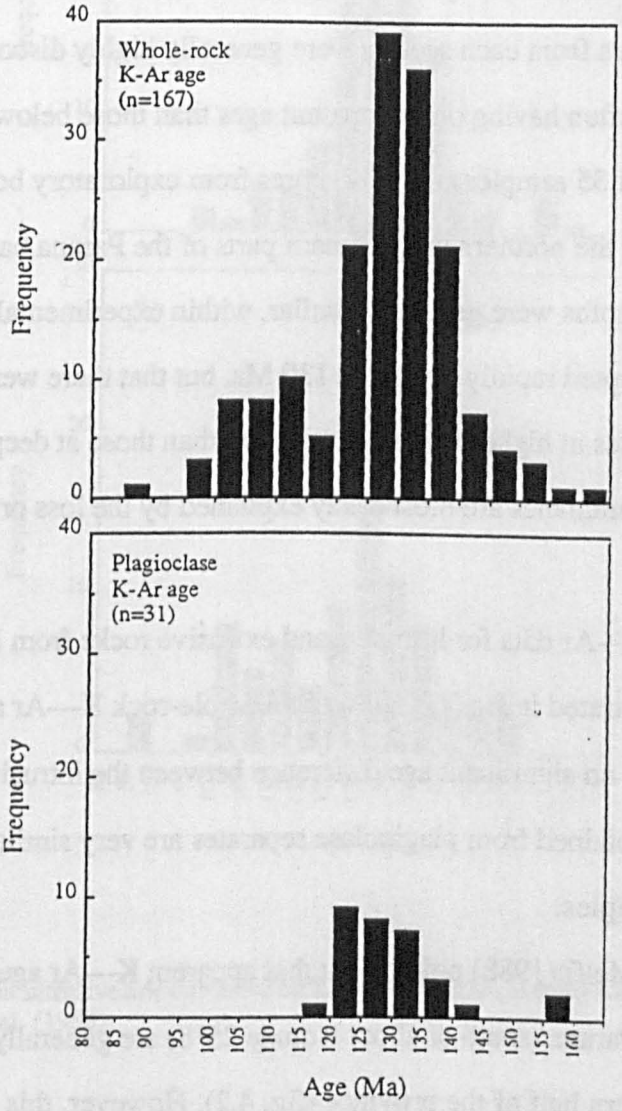

Fig. 4.1
K—Ar ages of whole-rock samples and plagioclae separates from intrusive and extrusive rocks from the Parana CFB province. Data from compilation by Rocha-Campos et al. (1988).

Mantovani et al. (1985) carried out a detailed study of three samples of porphyritic rhyodacite from the central and northern parts of the Parana which had previously been dated by the K—Ar method. Whole-rock, plagioclase and groundmass fragments were separated and dated using the Rb—Sr method. The authors assumed these samples to be

contemporaneous and cogenetic, and obtained an isochron with an age of 135.4 ± 3.5 Ma. The K—Ar ages for the same samples were 5—10% younger than the ages obtained using the Rb—Sr method. Cordani et al. (1980) attempted to date the Palmas rhyolites of the southern Parana by the Rb—Sr method, but obtained an errorchron of 118 ± 17 Ma.

Stratigraphically-controlled sampling of sections on the southeastern margin of the Parana lava field was carried out by Amaral et al. (1966), Cordani et al. (1980), and Pacca and Hioto (1976). Ages from each section were generally highly discordant, with samples higher in the section often having older apparent ages than those below. Melfi (1967) carried out K—Ar analysis of 35 samples from drill cores from exploratory boreholes drilled through the basalts of the northern and southern parts of the Parana basin, and found that the ages from different depths were generally similar, within experimental error, suggesting that these basalts were erupted rapidly at around 130 Ma, but that there were cases in which the apparent age of samples at higher levels were greater than those at deeper levels in the same borehole. These discordancies are most easily explained by the loss or gain of radiogenic argon.

The existing K—Ar data for intrusive and extrusive rocks from localities all over the Parana basin are illustrated in fig. 4.1. 70% of all whole-rock K—Ar ages lie between 120 and 135 Ma. There is no significant age difference between the intrusive and the extrusive rocks. K—Ar ages obtained from plagioclase separates are very similar to those obtained from whole-rock samples.

Piccirillo and Melfi (1988) pointed out that apparent K—Ar ages for lavas from the southern half of the Parana (south of about latitude 25°S) are generally slightly younger than those from the northern half of the province (fig. 4.2). However, this is in conflict with the geochemical stratigraphy of the lava pile as inferred from borehole data (Peate, 1989), which suggests that the basalts of the southern part of the province are in fact slightly older than those of the north. This implies that much of the apparent age range of the Parana volcanics is due to the loss or gain of radiogenic ^{40}Ar.

The results of more recent age determinations for volcanic rocks from the Parana, using the Ar—Ar technique (Baksi et al., 1991; Hawkesworth et al., 1992; Renne et al., 1992a, b), are discussed in section 4.4.2.

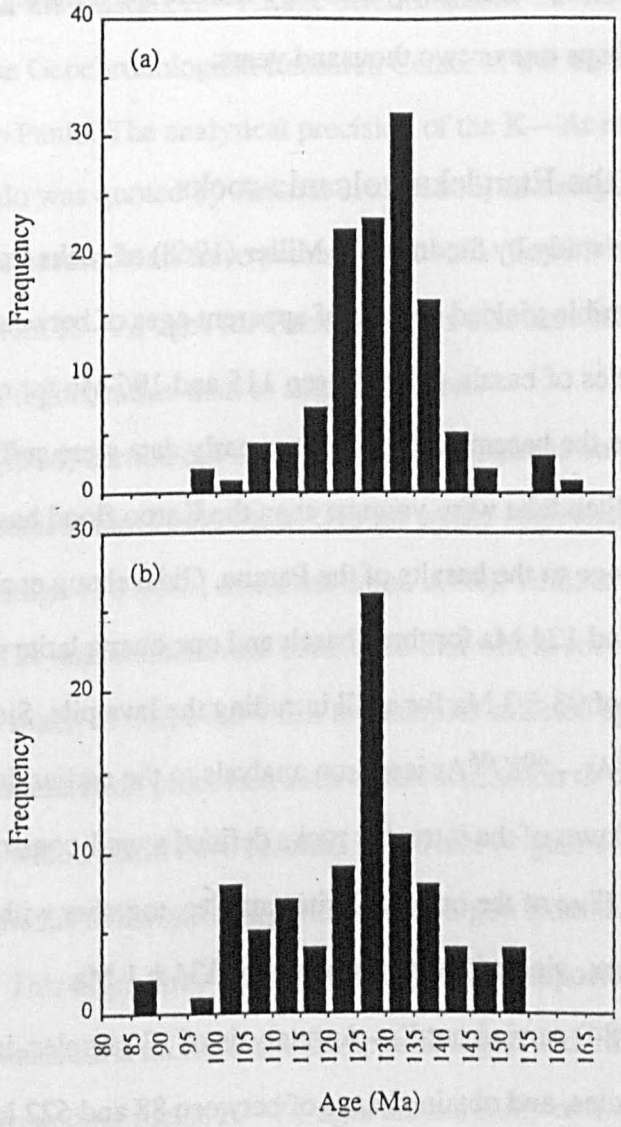

Fig. 4.2
K—Ar ages of the Parana intrusive and extrusive rocks from (a) north, and (b) south of latitude 25°S. Data from Rocha-Campos et al. (1988).

Limited palaeomagnetic data also exist for rocks from the Parana province. A preliminary regional study was carried out by Creer (1962). Pacca and Hiodo (1976), Ernesto et al. (1979), and Bellieni et al. (1983) carried out flow-by-flow sampling of the lavas from road sections in the southern Parana. Most of the sections sampled contained 2 or 3 reversals, some as many as 7. The early Cretaceous was a period of relatively rapid polarity reversal, and the mean duration of a single event has been estimated at approximately 0.4 Ma (Kent and Gradstein, 1985). This suggests that the lavas of this part of the Parana province may have been erupted in less than about 3 million years. Bellieni et

al. (1983) noted that several flow sequences show regular and gradual changes in magnetic declination and inclination, which imply that they were erupted during a single secular variation cycle of perhaps one or two thousand years.

4.2.2. The age of the Etendeka volcanic rocks.

An early K—Ar study by Siedner and Miller (1968) of rocks from the Etendeka flood basalt province of Namibia yielded a range of apparent ages of between 114 and 132 Ma for four whole-rock samples of basalt, and between 115 and 196 Ma for nine samples of the dolerites which intrude the basement rocks. These early data were sufficient to show that the volcanic rocks of the Etendeka were younger than the Karoo flood basalts of southern Africa, and similar in age to the basalts of the Parana. Gidskehaug et al. (1975) obtained ages of between 108 and 124 Ma for three basalt and one quartz latite sample from near Tafelberg, and an age of 93 ± 3 Ma for a sill intruding the lava pile. Siedner and Mitchell (1976) applied $^{40}Ar/^{36}Ar$—$^{40}K/^{36}Ar$ isochron analysis to the earlier data, and found that the eight lava samples and two of the intrusive rocks defined a well-constrained isochron with an age of 121 ± 2 Ma. Five of the other dolerite samples, together with samples from the Doros intrusive complex, yielded an isochron age of 134 ± 1 Ma.

Erlank et al. (1984) carried out K—Ar analysis of 17 samples, including basalts, dolerites and quartz latites, and obtained ages of between 88 and 622 Ma. Several of the basalt samples yielded anomalously high conventional K—Ar ages (in excess of 300 Ma) which were in conflict with their stratigraphical position, suggesting that they contain excess ^{40}Ar. This was confirmed by Ar—Ar stepped-heating analysis of crystals of plagioclase and pyroxene separated from two dolerite samples of the Horingbaai magma type. These yielded plateau ages of between 125 and 130 Ma, and both minerals were shown to contain a significant amount of excess ^{40}Ar.

Allsopp et al. (1984) attempted to date samples of the Etendeka quartz latites using the Rb—Sr method, but obtained an errorchron with an age of 154 ± 21 Ma. This anomalously old age was attributed to the effects of zeolitisation.

4.3 Reliability of the existing K—Ar and Rb—Sr data.

Over 90% of all the existing K—Ar age determinations for the Parana volcanic rocks were carried out at the Geochronological Research Center of the Institute of Geosciences at the University of Sao Paulo. The analytical precision of the K—Ar method using the apparatus at Sao Paulo was quoted by Amaral et al. (1966) as being about 3—6% (2σ). More recent K—Ar measurements have precisions of ~2% (2σ=3 Ma at 130 Ma). Much of the variation in apparent K—Ar ages for Parana rocks is therefore likely to be due to the loss or gain of radiogenic argon, rather than to analytical error.

Amaral et al. (1966) carried out K—Ar age determinations on several samples from a single dyke from Ubatuba, Sao Paulo State. Of four whole-rock analyses, three gave concordant ages (average 136.8 Ma, mean deviation 0.7%), whilst the fourth yielded a much younger age. The authors therefore concluded that whole-rock K—Ar ages of basalts can be in error by as much as 8%, even when the samples selected appear to show little or no sign of subsolidus alteration processes such as devitrification or the development of secondary minerals, which could have resulted in the loss or gain of radiogenic ^{40}Ar. This is probably because igneous rocks generally incorporate argon from their surroundings as they crystallise and cool. This argon may have the atmospheric composition, but more commonly, it will consist of a mixture of atmospheric argon and 'foreign' radiogenic ^{40}Ar derived from the surrounding rocks. K—Ar ages are normally corrected for the presence of atmospheric ^{40}Ar, but the correction procedure cannot take account of any foreign radiogenic ^{40}Ar that may have entered the rock during crystallisation. A major advantage of the Ar—Ar dating method is that under the right circumstances, the presence of excess argon can be recognised.

4.4 The Ar—Ar dating method.

4.4.1 Introduction.

The Ar—Ar method of dating is based on the natural occurrence of the radioactive isotope of potassium, ^{40}K, which decays to ^{40}Ca and ^{40}Ar with a half-life of 1250 Ma. The conventional K—Ar dating technique involves measuring the K concentration of the sample (the natural $^{40}K/K$ ratio (0.0001167) is then used to calculate the amount of ^{40}K), and the

Ar concentration, which is generally determined by isotope dilution using a ^{38}Ar spike. Gas is extracted from the sample by fusion in vacuum, and following purification of the argon, the concentration of radiogenic ^{40}Ar ($^{40}Ar^*$) is measured by mass spectrometry. The K—Ar technique allows the determination of $^{40}Ar^*$ with a precision of about 1%, if the $^{40}Ar^*$ concentration of the sample is greater than about 10%. The age calculated by this method assumes that the sample has remained closed to argon since its formation, and that any non-radiogenic argon incorporated into the rock at the time of crystallisation had the composition of atmospheric argon ($^{40}Ar/^{36}Ar$=295.5 (Nier, 1950)).

In the Ar—Ar dating technique, the sample to be dated is first irradiated in a nuclear reactor to transform a proportion of the ^{39}K atoms to ^{39}Ar by interaction with fast neutrons, through the $^{39}K(n,p)^{39}Ar$ reaction. The isotopic composition of argon in the sample is then measured by mass spectrometry, and the $^{40}Ar^*/^{39}Ar_K$ ratio of the sample (where $^{40}Ar^*$ is the amount of radiogenic ^{40}Ar, and $^{39}Ar_K$ is the amount of ^{39}Ar derived from ^{39}K) is calculated from the measured $^{40}Ar/^{39}Ar$ ratio, after correcting for the presence of isotopes of Ar that were generated during the irradiation by interfering nuclear reactions involving Ca, K, Ar and Cl (see the Appendix for details of the corrections used in this study). The age of the sample is related to its $^{40}Ar^*/^{39}Ar_K$ ratio by the standard age equation

$$t = (1/\lambda) \ln(1 + J(^{40}Ar^*/^{39}Ar_K))$$

where λ is the decay constant of ^{40}K, and J is a dimensionless irradiation parameter. The value of J for a particular irradiation is usually measured by irradiating a standard of known K—Ar age together with the samples (see Appendix).

One important advantage of the Ar—Ar technique is that the ratio of the daughter and parent isotopes is measured in a single isotopic analysis. There is no need for a separate analysis to determine the K concentration, overcoming the problem of sample inhomogeneity, and allowing smaller samples to be used. Since isotope ratios can be measured more accurately than separate analyses of K and Ar, a more precise age can be obtained. Another major advantage of the Ar—Ar technique is that stepped-heating, or laser

fusion methods can be used to release Ar from the sample. These can reveal information about the spatial distribution of K and Ar in the sample, and to what extent the sample has remained closed to argon since crystallisation.

4.4.2 Previous Ar—Ar studies of the Parana flood basalts

Previous to this work, the only existing Ar—Ar data for rocks from the Parana were those of Baksi et al. (1991), Hawkesworth et al. (1992) and Renne et al. (1992a,b).

Baksi et al. (1991) carried out stepped-heating analysis of a small selection of basalts from the Parana, and obtained ages of between 130 Ma and 135 Ma. However, the significance of these data is difficult to assess, because of recoil loss of ^{39}Ar from the samples during irradiation, and the presence of excess ^{40}Ar.

Hawkesworth et al. (1992) used the laser ablation method to date three samples of the Gramado basalt type from the southern Parana, and obtained isochron ages of 132.4 ± 1.4 and 132.0 ± 2.8 Ma for two of these samples. The third sample did not yield a sensible isochron age, but apparent ages ranged from 147 to 188 Ma.

Renne et al. (1992a,b) have recently reported Ar—Ar ages obtained by laser stepped heating analysis of whole-rock samples and plagioclase separates collected from different stratigraphic levels in the lava pile in Rio Grande do Sul State. The samples were collected from the SM, CV, TA and GB sections (fig. 1.9). Although the authors did not report whole-rock geochemical data for these samples, previous work by Peate (1989) allows some constraints to be placed upon the magma types that were dated by Renne et al. (1992b). The lowermost flows of the CV and TA sections are composed of basalts of the Gramado magma type. The rhyolites at the top of the CV section belong to the Caxias do Sul type, and basalts of the Gramado, Urubici and Esmeralda magma types occur in the SM and GB sections.

A 650 m thickness of basalt is exposed in the CV section, and includes at least two, and possibly as many as four magnetic polarity reversals (Renne et al., 1992b). A whole-rock sample taken from a basalt flow near the base of the section yielded an age of 132.6 ± 0.3 Ma, which is indistinquishable from the age of a plagioclase separate from a rhyolite

near the top of this section (132.8 ± 1.1 Ma). The basalt sample exhibited a discordant profile suggestive of ^{39}Ar loss by recoil.

A plagioclase separate from a basalt flow ~400m above the base of the TA section (Gramado?) yielded replicate plateau ages of 131.4 ± 1.6, 132.7 ± 1.2 and 132.5 ± 0.3 Ma. Of two basalt samples from the GB section, one yielded an age of 132.4 ± 0.7 Ma, but exhibited ^{39}Ar recoil loss; the other (a fine-grained sample containing secondary celadonite) did not yield a plateau age. A plagioclase separate from a basalt collected from the SM section yielded a well-defined (97.1% total argon release) plateau age of 132.9 ± 0.6 Ma. The ages obtained from these five samples were mutually indistinguishable in the range 132.9 ± 0.6—131.4 ± 1.6 Ma (2σ error). A plagioclase separate from a rhyodacite of Chapeco type further to the north in Parana State yielded replicate plateau ages of 132.0 ± 0.4, 132.4 ± 0.9 and 132.5 ± 0.6 Ma (Renne et al., 1992a).

The authors concluded from their data that the Parana flood basalt magmatism began at around 133 Ma, and lasted for approximately 1 Ma. However, none of the sections sampled in their study contain any basalt flows of the Pitanga or Paranapanema magma types, which comprise over one third by volume of the lava field, and which appear to have been the last basalts erupted in the Parana event (Peate et al., 1992). Thus Renne et al.'s (1992) data can only place an upper limit upon the age of the Parana magmatism.

In the course of this study, thirteen dolerite samples from the Parana were analysed using the Ar—Ar technique, in order to determine the reasons for the wide range of apparent K—Ar ages, when evidence from other CFB provinces such as the Deccan (Duncan and Pyle, 1988; Baksi and Farrar, 1991), suggests that these flood basalts were erupted in just a few million years. The samples were irradiated at the Ford reactor, Michigan, in a neutron flux of approximately 10^{18} fast neutrons per cm^2. At the Open University, argon is released from the irradiated sample by laser ablation. This method has several advantages over the conventional stepped-heating technique used by Baksi et al. (1991). Most importantly, stepped-heating of bulk samples averages the argon isotopic compositions from all components of the rock, whereas the laser ablation technique can be used to release argon from individual crystals, which is of great value if mixed populations of single crystals are

present in the rock, or if certain minerals tend to contain excess ^{40}Ar. A crude stepped-heating effect can in any case be achieved by varying the power of the laser. The analytical procedures used during this study are described in more detail in the Appendix, together with details of the corrections applied for the presence of background Ar, and isotopes of Ar generated by interfering nuclear reactions involving Ca and K.

The new data are presented in the form of $^{36}Ar/^{40}Ar$—$^{39}Ar/^{40}Ar$ isochron correlation diagrams (Heizler and Harrison, 1988). The isotopic composition of argon in an igneous rock that has remained closed to argon since its crystallisation can be considered as a mixture of two components (fig. 4.3). The initial, or trapped argon component, is incorporated into the rock at the time of crystallisation, and may consist of pure atmospheric argon (the isotopic composition of atmospheric argon has not changed significantly during the Phanerozoic; Cadogan, 1977), or a mixture of atmospheric argon and 'foreign' radiogenic ^{40}Ar derived from the surrounding rocks. The radiogenic component consists of ^{40}Ar

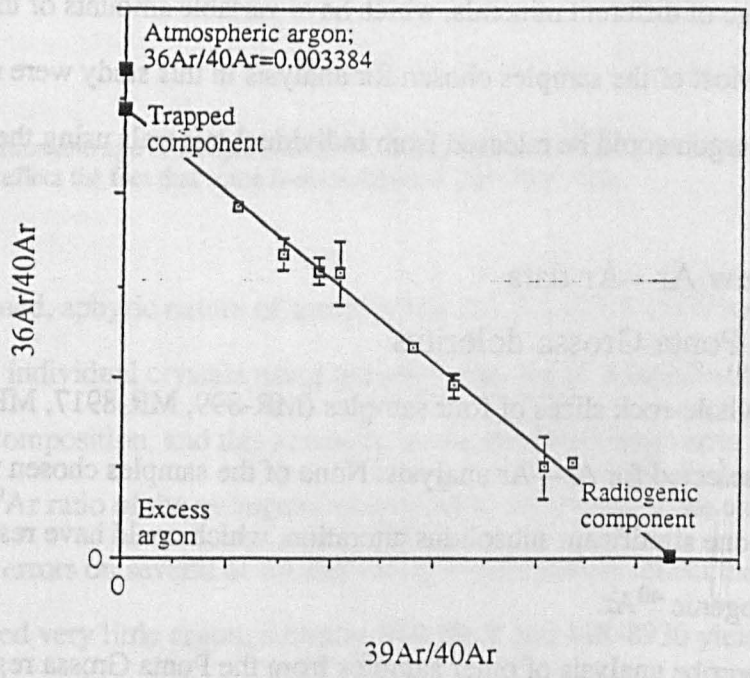

Fig. 4.3
Inverse isochron analysis (Turner, 1971) has been used in this study to obtain the best age estimate from the argon isotope data for each sample. If the sample has remained closed to argon since crystallisation, the data will lie upon a simple two component mixing array. Loss or gain of radiogenic ^{40}Ar will displace points above or below the mixing line (see discussion in text). The best fit mixing line was calculated using the least squares regression procedure of York (1969), and the age of the sample was calculated from the value of the $^{39}Ar/^{40}Ar$ intercept. The trapped component will generally have a $^{36}Ar/^{40}Ar$ value of less than the atmospheric value (0.003384), because most igneous rocks incorporate excess radiogenic ^{40}Ar, derived from the basement rocks, as they crystallise.

generated by in-situ decay of ^{40}K, and ^{39}Ar produced by irradiation of ^{39}K. Provided that the rock has remained closed to argon since crystallisation, the $^{40}Ar/^{39}Ar$ ratio of the radiogenic component, and hence the age of the sample, can be calculated from a least-squares fit to the data (York, 1969).

Many igneous rocks have not remained closed to argon since crystallisation. Some minerals may contain significant amounts of 'excess' radiogenic ^{40}Ar, derived from the surrounding rocks, and incorporated into the sample at some time after its crystallisation. Loss of radiogenic ^{40}Ar may occur as a result of later alteration processes, such as devitrification of glass (Cerling et al., 1985), or replacement of plagioclase by sericite (McDougall and Harrison, 1988). It is usually possible to recognise these effects using isochron correlation analysis, and in some cases derive a meaningful age from the data.

The accuracy to which the $^{40}Ar^*/^{39}Ar$ ratio, and hence the age, of a particular sample can be determined in this way is to a large extent controlled by the range in composition of the argon released from the sample (fig. 4.3). It is therefore an advantage to be able to analyse a range of different minerals, which have variable amounts of the radiogenic component. Most of the samples chosen for analysis in this study were relatively coarse-grained, and argon could be released from individual minerals using the laser.

4.5 The new Ar—Ar data

4.5.1 The Ponta Grossa dolerites

Thin whole-rock slices of four samples (MR-899, MR-8917, MR-8928 and MR-8930) were selected for Ar—Ar analysis. None of the samples chosen for analysis appear to have undergone significant subsolidus alteration, which could have resulted in the loss or gain of radiogenic ^{40}Ar.

Microprobe analysis of other samples from the Ponta Grossa region (Chapter 2) has revealed that these dolerites are composed dominantly of plagioclase (Ab_{36-44}, Or_{1-3}, An_{55-61}), augite and titanomagnetite, with or without olivine and pigeonite. Although olivine is often severely altered, the extremely low K content of this mineral means that this will have had little effect upon the isotopic composition of Ar in these samples. Small amounts of biotite and hornblende are present as accessory minerals in the more evolved samples, but as

a rule, these dolerites contain no primary K bearing phase, (whole-rock K_2O contents are generally less than 2.5%).

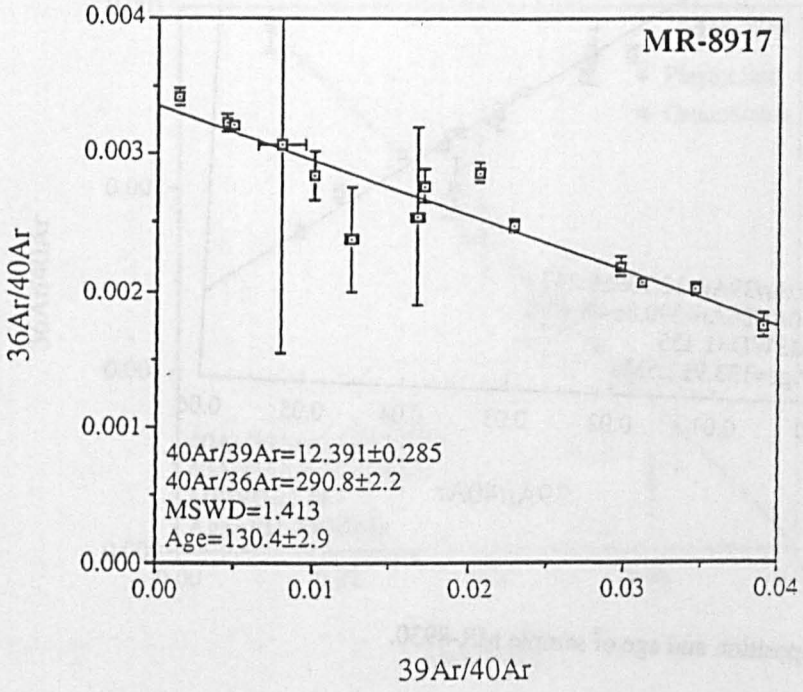

Fig. 4.4
Argon isotope composition and age of sample MR-8917. Note the relatively large errors on some of the measurements, which reflect the fact that some fusions released very little argon.

The fine-grained, aphyric nature of samples MR-8917 and MR-8930 meant that it was not possible to fuse individual crystals using the laser. The argon released was therefore of relatively uniform composition, and this accounts for the relatively large error on the extrapolated $^{40}Ar/^{39}Ar$ ratio of the radiogenic endmember, and hence of the calculated age. The relatively large errors on several of the individual measurements reflect the fact that some fusions released very little argon. Samples MR-8917 and MR-8930 yielded isochron ages of 130.5 ± 2.9 Ma (MSWD=1.413) and 133.9 ± 2.5 Ma (MSWD=1.355) respectively (fig. 4.4 and 4.5). The $^{40}Ar/^{36}Ar$ ratios of the trapped argon component (290.4 ± 2.2 and 290.8 ± 4.8 respectively) are similar to that of air, which suggests that neither sample contains a significant amount of excess ^{40}Ar.

Sample MR-899 was collected from the least evolved dyke encountered in the Ponta Grossa region, and therefore contains very little potassium (K_2O=0.84%). Small

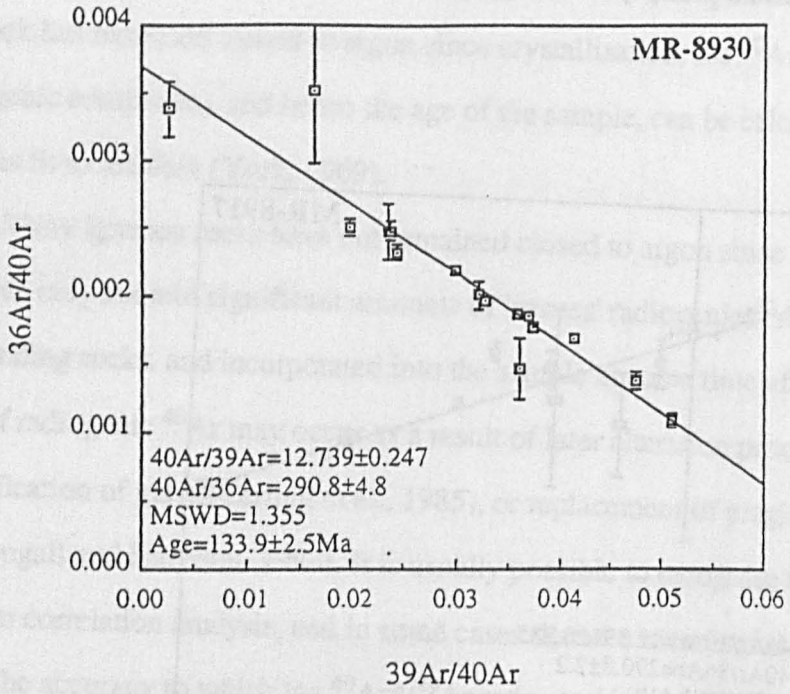

Fig. 4.5
Argon isotope composition and age of sample MR-8930.

phenocrysts of plagioclase are present, and it was possible to release argon from individual crystals using the laser. The plagioclase phenocrysts tended to contain a higher proportion of the radiogenic endmember than the groudmass material (fig. 4.6). The best-fit line through the 16 data points (MSWD=1.187) yields an age of 131.2 ± 0.5 Ma. The $^{40}Ar/^{36}Ar$ ratio of the trapped component is 311.0 ± 8.3, which means that a small amount of excess ^{40}Ar was incorporated into the sample at the time of crystallisation, and the scatter of the data about the best-fit mixing line suggests that the sample has not remained completely closed to argon since crystallisation.

Sample MR-8928 was collected from one of the more evolved dolerites encountered in the Ponta Grossa region (MgO=3.28%), and has a relatively high potassium content (K_2O=2.48%). The sample contains small phenocrysts of plagioclase (approximate composition An_{55}), set in a groundmass consisting of plagioclase, augite and titanomagnetite. A small amount of biotite, and partially divitrified yellow glass is likely to contain much of the potassium, and accounts for the fact that the plagioclase

microphenocrysts tended to contain argon of less radiogenic composition than that released from the groundmass (fig. 4.7).

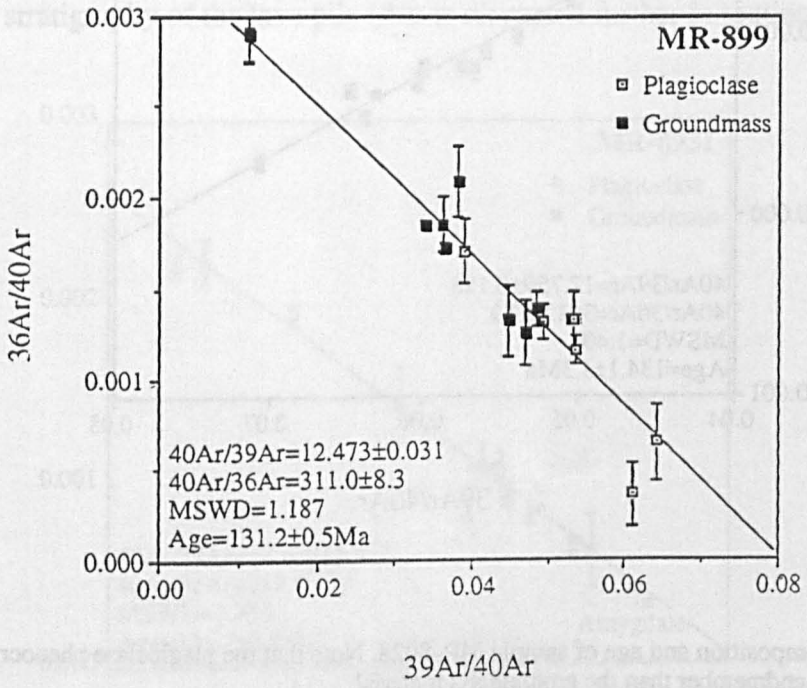

Fig. 4.6
Argon isotope composition and age of sample MR-899. The mixing line is defined by analyses of both plagioclase microphenocrysts and the groundmass material. Note that the plagioclase crystals tend to contain more of the radiogenic component.

Extrapolation of a least-squares fit line to the data (MSWD=1.403) yields a $^{40}Ar/^{39}Ar$ ratio for the radiogenic component of 12.76 ± 0.13, corresponding to an age of 134.1 ± 1.3 Ma. The $^{36}Ar/^{40}Ar$ ratio of the trapped component (301.5 ± 9.9) is close to that of air, which means that the sample contains little excess argon.

Sample MR-8931 was collected from a dyke of evolved composition which intrudes Permo-Triassic sediments in the region of Sao Jeronimo da Serra. This intrusion is very similar in terms of its geochemistry to the rhyolite lavas of the Ourinhos magma type which outcrop on the northeastern margin of the lava field (Chapter 2). Large, zoned plagioclase crystals are set in a fine-grained matrix which consists dominantly of quartz and alkali felspar.

The argon released from the plagioclase phenocrysts tended to contain a lower

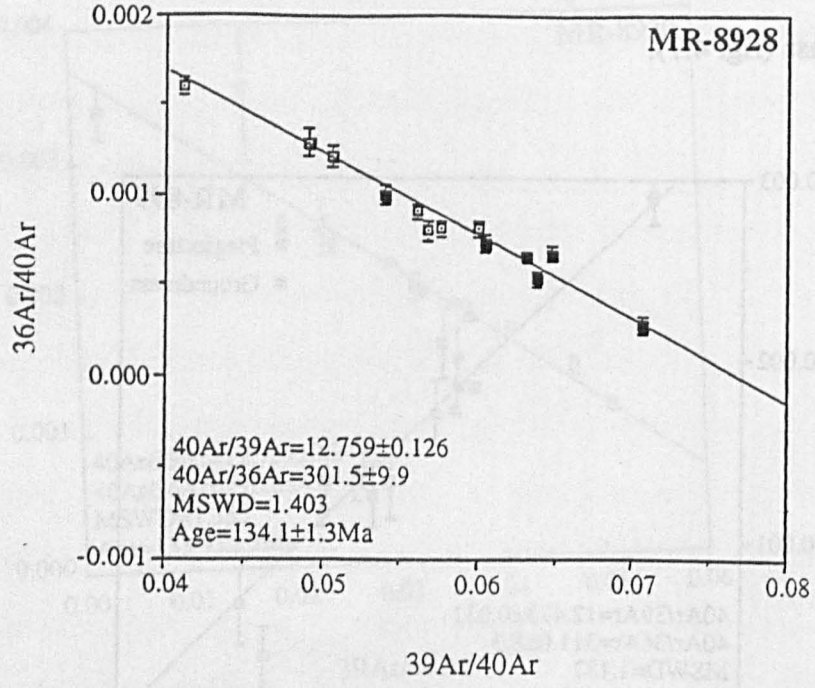

Fig. 4.7
Argon isotope composition and age of sample MR-8928. Note that the plagioclase phenocrysts contain less of the radiogenic endmember than the groundmass material.

proportion of the radiogenic component, compared to the argon released from the groundmass (fig. 4.8). Much of the potassium in this sample is likely to be concentrated in the alkali feldspar of the groundmass. Note that the argon released from the plagioclase crystals has a more variable isotopic composition than that from the groundmass. Hawkesworth et al. (1992) noted that the proportion of the trapped argon component in plagioclase crystals in basalts of the Gramado magma type was greatest in those crystals whose structure was most extensively damaged by cracks. The variable isotopic composition of the argon released from the plagioclase phenocrysts may therefore be due to heterogeneous distribution of the mixing components within the crystal structure. Fusion of a small amygdale filled with a finely crystalline material yielded argon of relatively radiogenic composition (fig. 4.8), which suggests that this material is a K rich zeolite. The $^{40}Ar/^{39}Ar$ ratio of the radiogenic endmember, calculated from a best-fit line to the data, corresponds to an age of 131.7 ± 0.8 Ma (MSWD=1.750). The $^{40}Ar/^{36}Ar$ ratio of the trapped component (289.4 ± 5.1) is similar to the atmospheric composition.

Note that sample MR-8928 appears to be significantly older than either sample MR-899 or MR-8931, but has an age which is within error of the ages of samples MR-8917 and MR-8930. This is consistent with the relative ages of these samples as inferred from the geochemical stratigraphy of the lava pile (this is discussed further in section 4.6).

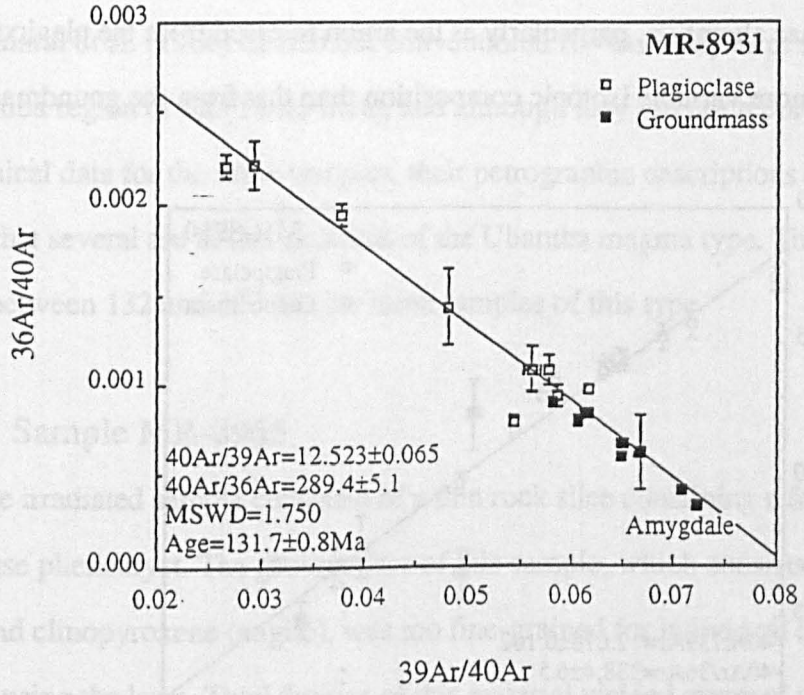

Fig. 4.8
Argon isotope composition and age of the evolved sample MR-8931.

4.5.2 The dolerites of the Paraiba magma type

Many of the dolerites of this magma type show evidence in thin section for having undergone extensive subsolidus alteration; the sample chosen for analysis (MR-8950) appears relatively fresh, and the mineral chemistry of this sample has been investigated in detail by electron probe (Chapter 3).

Microphenocrysts of highly sericitised plagioclase (An_{54-56}) are set in a groundmass consisting of plagioclase, augite (En_{42-44}, Wo_{36-39}, Fs_{17-22}), and titanomagnetite. A minor amount of highly altered pigeonite is present, in the form of small rounded grains that are usually overgrown by augite. A pale green amphibole occurs as rims on clinopyroxene, and the small crystals of biotite which are present in the groundmass.

The laser was used to release argon from individual plagioclase crystals, and these

tended to contain a lower proportion of the radiogenic argon component, compared to the argon released from the groundmass (fig. 4.9). The age calculated from the extrapolated $^{40}Ar/^{39}Ar$ ratio of the radiogenic endmember is 133.3 ± 1.7 Ma (MSWD=1.856). The trapped component has a high excess ^{40}Ar content ($^{40}Ar/^{39}Ar$=338.4 ± 6.5), and much of the scatter of the data about the best-fit mixing line is likely to be due to ^{40}Ar loss or gain as a result of plagioclase alteration, particularly as the argon released from the plagioclase phenocrysts has a more variable isotopic composition than that from the goundmass.

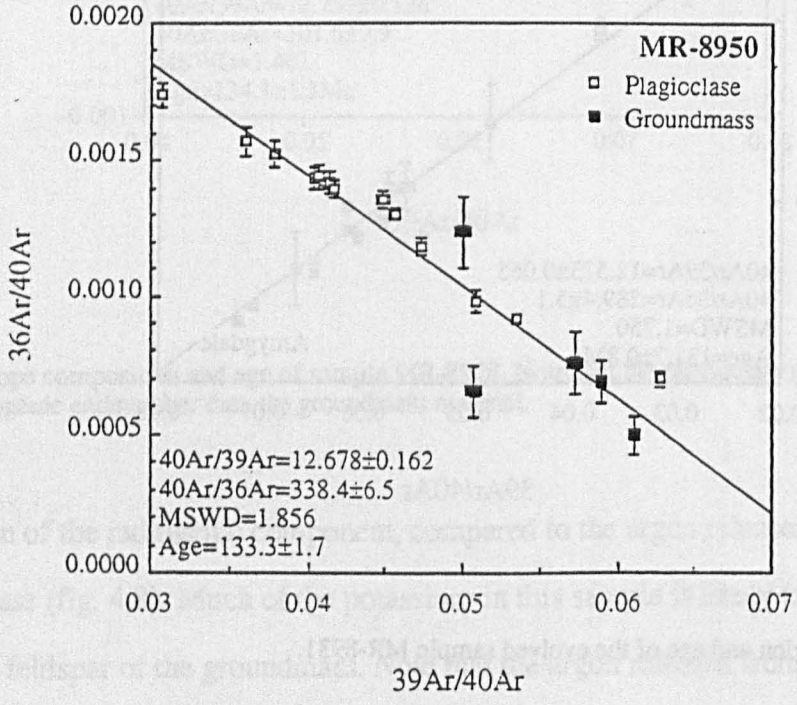

Fig. 4.9
Argon isotope composition and age of sample MR-8950 (Paraiba magma type).

4.5.3 The dolerites of the Ubatuba magma type

Five samples of this magma type were selected for Ar—Ar analysis; thin slices of samples MR-8965 and MR-8951, and plagioclase crystal fragments separated from samples MR-8957, MR-8954 and MR-8959. The petrography and mineral chemistry of this group of rocks is described in detail in Chapter 3. Most samples contain large phenocrysts of plagioclase. These have a relatively restricted compositional range (Ab_{44-50}, An_{49-43}, Or_{6-9}, 1.2—1.5% K_2O) and display complex disequilibrium textures, including resorbed crystal margins and melt-sieved cores. Many of the plagioclase crystals are overgrown by

potassium feldspar. Small glomerocrysts of augite (which contain less than about 0.1% K_2O), pigeonite, apatite and ilmenite, are set in a fine-grained groundmass consisting of potassium feldspar and augite (fig. 3.12). These dolerites have relatively high whole-rock K_2O concentrations of between 3 and 5%, and much of this K is likely to be concentrated in the potassium felspar phase of the groundmass.

Amaral et al. (1966) carried out conventional K—Ar analysis of several dolerites from the Ubatuba region of Sao Paulo State, and although they did not report whole-rock geochemical data for the same samples, their petrographic descriptions of these rocks suggest that several are in fact dolerites of the Ubatuba magma type. They obtained K—Ar ages of between 132 and 139 Ma for three samples of this type.

4.5.3.1 Sample MR-8965

The irradiated sample consisted of a thin rock slice containing a fragment of a large plagioclase phenocryst. The groundmass of this sample, which consists dominantly of K-felspar and clinopyroxene (augite), was too fine-grained for individual crystals to be analysed using the laser. Total fusions of this material yielded argon of relatively radiogenic composition, since most of the potassium in this sample (K_2O=4.49%) will be concentrated in the potassium felspar of the groundmass. The $^{39}Ar/^{40}Ar$ ratio of the radiogenic endmember calculated from a best-fit line through the data corresponds to an age of 130.2 ± 1.6 Ma (fig. 4.10), and the trapped argon component had a $^{40}Ar/^{36}Ar$ ratio of 302.2 ± 6.0 (MSWD=0.653), which is similar to the atmospheric value.

The laser was used to release argon from the plagioclase crystal; this contained argon of slightly less radiogenic composition than the argon released from the groundmass material. A best-fit line through the plagioclase data (fig. 4.11) yields an age of 117.0 ± 1.2 Ma (MSWD=2.880), significantly younger than the ages obtained from the groundmass material, and from other samples of this magma type. The $^{40}Ar/^{36}Ar$ ratio of the trapped component is 301.9 ± 2.4; slightly higher than the atmospheric value. Note that the mixing line defined by the plagioclase data is displaced to higher $^{40}Ar/^{36}Ar$ than the mixing line defined by the groundmass material (fig. 4.12).

The plagioclase phenocrysts of the Ubatuba dolerites show a number of features that indicate that they are in disequilibrium with the groundmass; many possess melt-sieved cores which may contain fine-grained K feldspar, and most are extensively sericitised.

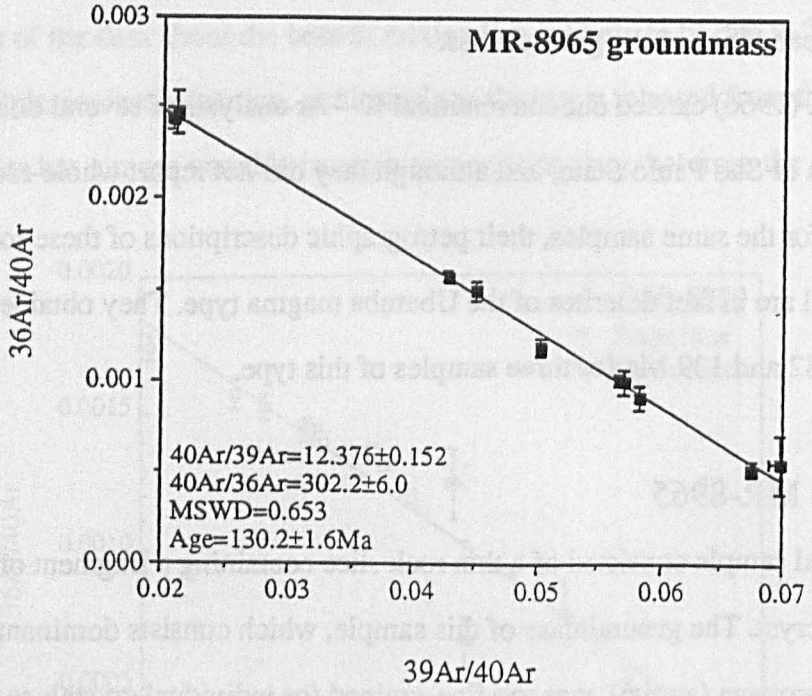

Fig. 4.10
Argon isotope composition and age of sample MR-8965 (Ubatuba magma type). These analyses were obtained from the groundmass material of this sample.

Plagioclase alteration will have a significant effect upon the distribution and isotopic composition of argon, because the fine-grained alteration products will tend to lose radiogenic ^{40}Ar more readily than unaltered plagioclase, even at relatively low temperatures (McDougall and Harrison, 1988), and hence yield anomalously young K—Ar ages. Although the laser was used to try to release argon from unaltered areas of the crystal, the Ca/K ratio of the material analysed (proportional to the $^{37}Ar/^{39}Ar$ ratio; see Kelley et al. (1986), their table 1), is between 0.2 and 1.0. However, microprobe analysis of plagioclase phenocrysts from the Ubatuba dolerites indicates that these have relatively uniform Ca/K values of 4.7—5.7 (see Chapter 3). This may be because although the laser was focussed to a spot on the sample surface approximately 100 μm in diameter, beam scattering from defects within the plagioclase crystal is likely to have resulted in the release of argon from a much larger volume of the crystal than implied by the size of the laser pit (Girard and

Onstott, 1991). Thus it is likely that argon was released from highly sericitised portions of the crystal, and from the grain boundaries. This would explain the low Ca/K values of the material analysed, and the relatively young age obtained from this plagioclase phenocryst. The relatively low K content of plagioclase means that loss of even a small amount of radiogenic ^{40}Ar will have a significant effect upon the calculated age of the sample (Dalrymple et al., 1975). The crystal structure of plagioclase is extremely complex, and the

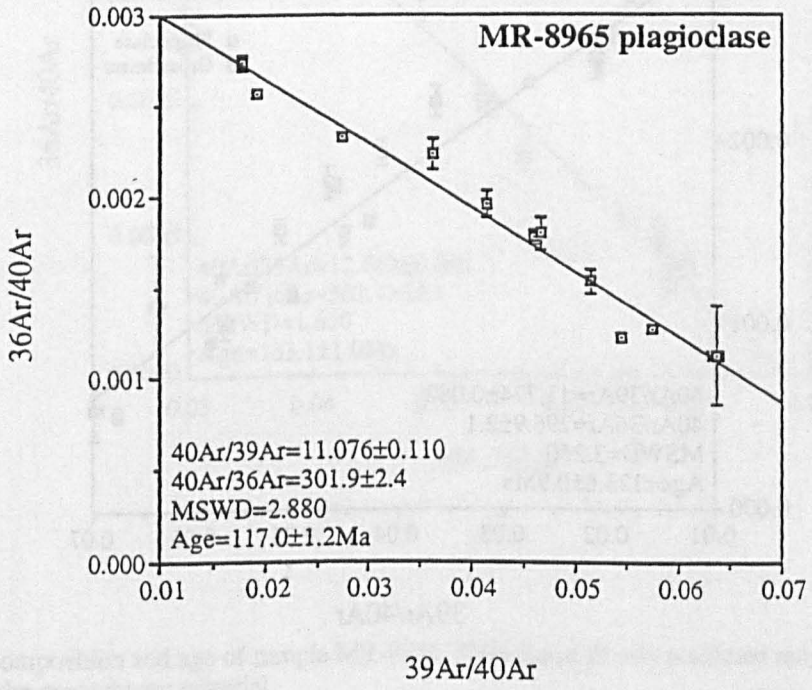

Fig. 4.11
Argon isotope composition and age of sample MR-8965. The analyses were obtained from a plagioclase phenocryst. Note that the calculated age is significantly younger than the age obtained from the groundmass material (fig. 4.10) from the same sample.

development of micropores as a result of interaction of the feldspar with fluids during cooling (Parsons et al., 1988) may also facilitate argon loss from the crystal structure, and lead to anomalously young Ar—Ar ages.

The age calculated from the groundmass material is therefore more likely to approach the true age of this sample, and the age of 123.6 ± 0.9 Ma calculated using the combined phenocryst and groundmass data (fig. 4.12) is unlikely to have any geological significance.

4.5.3.2 Sample MR-8951

5 mm sized phenocrysts of plagioclase (approximate composition An_{45}) are overgrown by small blocky cystals of potassium felspar, which also constitutes much of the

groundmass where it is intergrown with quartz. Small phenocrysts of augite are present; many of these crystals have cores of pigeonite. The sample contains accessory amounts of biotite and amphibole (the latter occurring as overgrowths on clinopyroxene), but most of the potassium in this sample (whole-rock K_2O concentration=3.80%) is likely to be concentrated in the potassium felspar of the groundmass.

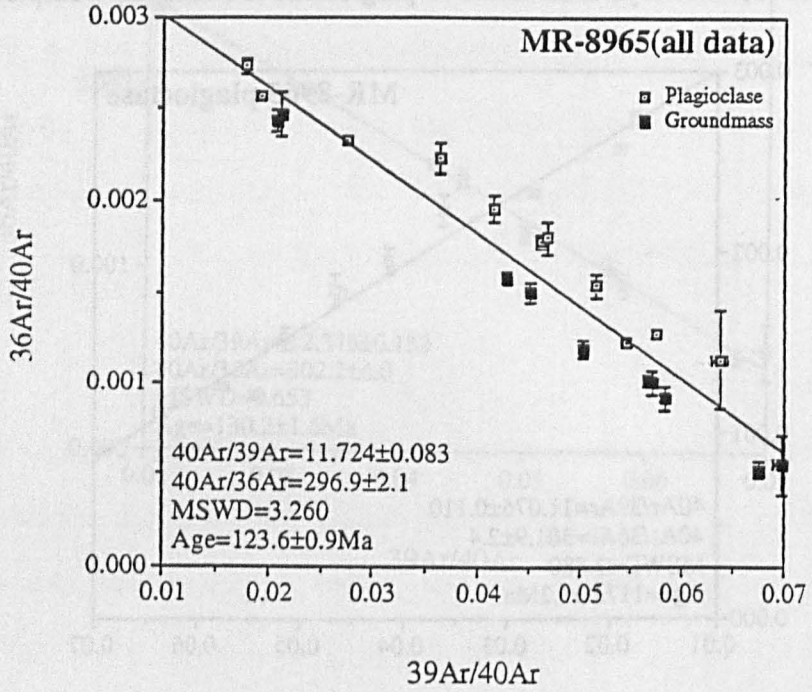

Fig. 4.12
Argon isotope composition and age of sample MR-8965, calculated using both the groundmass and the phenocryst data.

The groundmass material yielded argon with a relatively restricted isotopic composition (fig. 4.13), whereas the argon released from the plagioclase crystals had a more heterogeneous isotopic composition. Microprobe analysis of felspars from the Ubatuba dolerites indicates that these have a relatively restricted compositional range (Chapter 3). Note that unlike the plagioclase phenocrysts of sample MR-8965, these crystals do not appear to have lost radiogenic ^{40}Ar. This may mean that the heterogeneous isotopic composition of argon in these crystals is due to concentration of the trapped component in inclusions and cracks in the crystal structure (Hawkesworth et al., 1992), rather than to sericitisation.

A best-fit line to the data yielded an age of 133.1 ± 1.0 Ma (MSWD=1.619), and the $^{40}Ar/^{36}Ar$ ratio of the trapped component is 303.7 ± 10.1, which is within error of the atmospheric ratio.

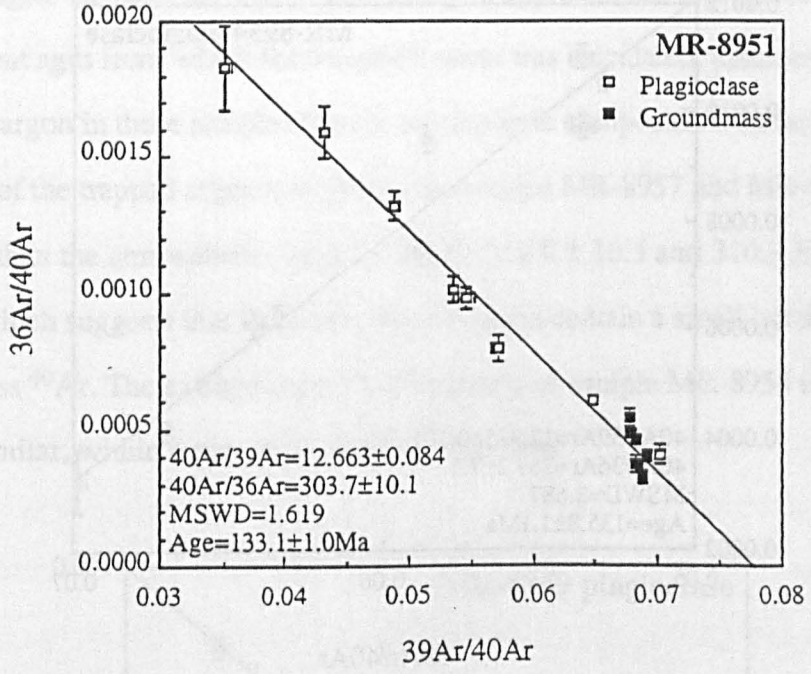

Fig. 4.13
Argon isotope composition and age of sample MR-8951. Note the relatively restricted range in isotope composition of the groundmass material.

4.5.3.3 Plagioclase separates

Crystal fragments of plagioclase were separated from three samples of these dolerites (MR-8954, MR-8957, MR-8959) and dated by the laser fusion technique. The mineral chemistry of one of these samples (MR-8954) was investigated in some detail using electron probe analysis (Chapter 3). Although the plagioclase phenocrysts of this sample often possess thin overgrowths of potassium felspar, no significant compositional variation was observed either within individual phenocrysts, or between different plagioclase phenocrysts within this sample; these have a relatively uniform composition ($Ab_{47.7-48.7}$, $Or_{7.8-8.9}$, $An_{44.5-42.4}$).

Nine individual analyses were obtained from sample MR-8954; these had apparent ages of between 128.8 ± 1.4 and 139.5 ± 1.7 Ma (weighted mean 135.3 ± 0.5 Ma). The isochron age obtained by combining these data (fig. 4.14) was 135.8 ± 1.1 Ma

(MSWD=2.687). Similarly, MR-8957 had an apparent age range of 128.9 ± 2.3 to 140.1 ± 2.0 Ma (weighted mean of 7 analyses; 133.3 ± 0.6 Ma) and an isochron age of 130.7 ± 1.7

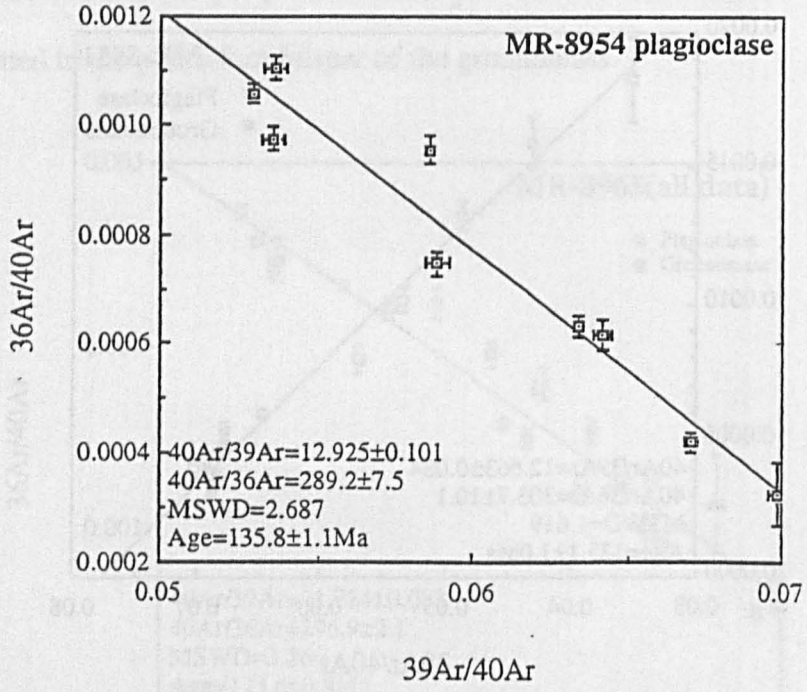

Fig. 4.14
Argon isotope composition and age of plagioclase fragments from sample MR-8954.

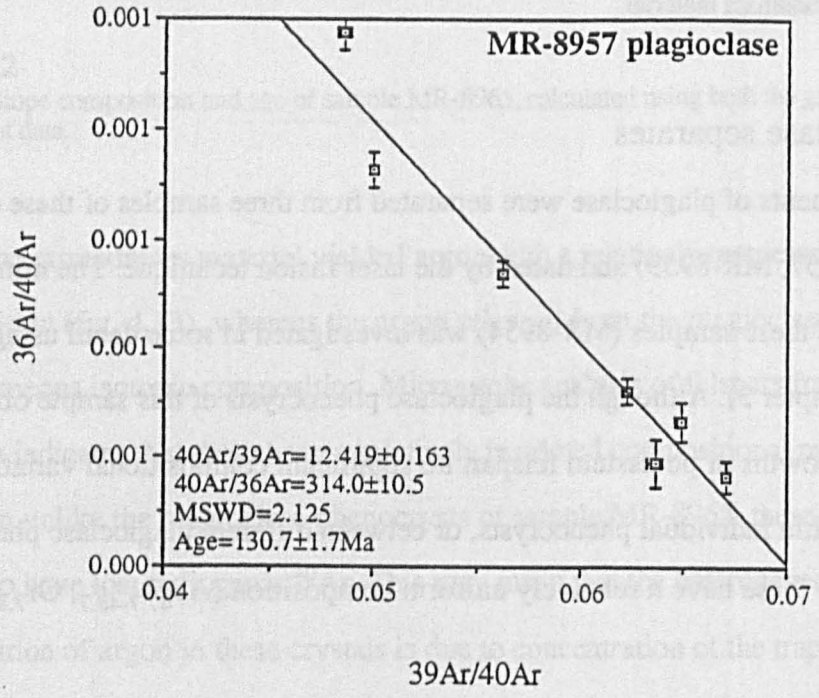

Fig. 4.15
Argon isotope composition, and age of a plagioclase separate from sample MR-8957.

Ma (MSWD=2.125; fig. 4.15). Sample MR-8959 yielded an age range of 126.1 ± 2.3 to 139.5 ± 3.2 (weighted mean of 8 analyses; 131.1 ± 0.3 Ma), and an isochron age of 129.4 ± 0.6 Ma (MSWD=1.502; fig. 4.16).

Of these ages, the isochron age is more likely to approach the true age of each sample, since the apparent ages from which the weighted mean was calculated, assumes that any non-radiogenic argon in these samples has the atmospheric composition. In fact, the $^{40}Ar/^{36}Ar$ ratio of the trapped argon component in samples MR-8957 and MR-8959 are slightly higher than the atmospheric value of 295.5 (314.0 ± 10.5 and 310.9 ± 2.9 respectively), which suggests that these crystals do indeed contain a small but significant amount of excess ^{40}Ar. The extrapolated $^{40}Ar/^{36}Ar$ ratio of sample MR-8954 is 289.2 ± 7.5, which is similar, within error, to the atmospheric ratio.

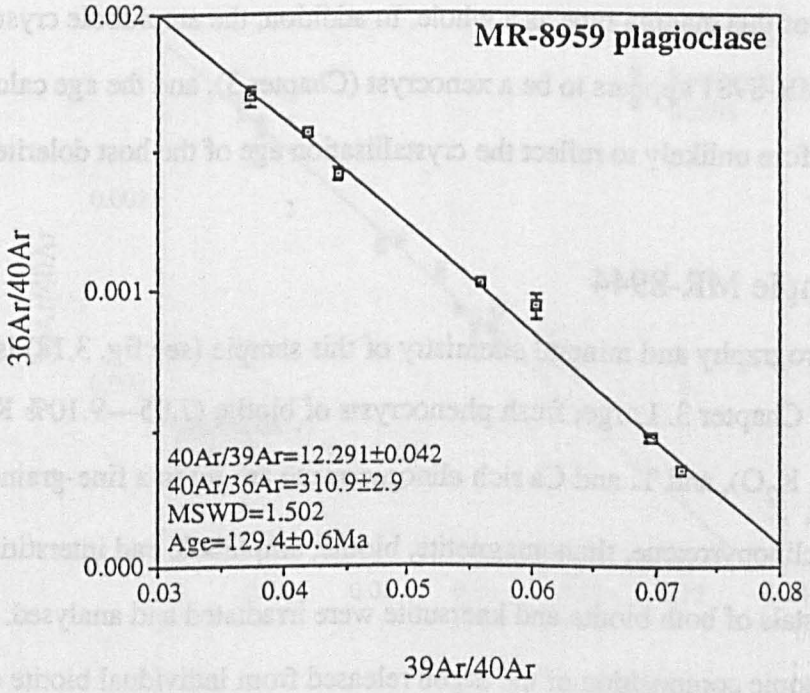

Fig. 4.16
Argon isotope composition, and age of a plagioclase separate from sample MR-8959.

Note that the ages obtained from these felspar separates yield more realistic ages than those obtained from the plagioclase of sample MR-8965. The plagioclase phenocrysts of sample MR-8965 are not obviously any more altered than those of the other samples, although in selecting plagioclase separates for analysis, the least altered crystal fragments

were chosen. The older ages obtained from the latter therefore probably reflect the fact that these contain less sericite.

4.5.4 The dolerites of the Sao Sebastiao magma type

The dolerites of the Sao Sebastiao magma type are typically aphyric and very fine-grained, and are therefore not well suited to dating by the laser ablation technique. Two samples were selected for analysis; an amphibole crystal from sample MR-8981, and biotite and kaersutite separates from sample MR-8944. Because of their high potassium content, these mineral separates yielded a relatively precise age for sample MR-8944, but it should be remembered that samples MR-8944, 45 and 46 were collected from further inland than the main occurences of the Sao Sebastiao magma type, and are the only samples to contain large phenocrysts of biotite and amphibole. The age of these samples may therefore not be representative of this magma type as a whole. In addition, the amphibole crystal separated from sample MR-8981 appears to be a xenocryst (Chapter 3), and the age calculated for this crystal is therefore unlikely to reflect the crystallisation age of the host dolerite.

4.5.4.1 Sample MR-8944

The petrography and mineral chemistry of this sample (see fig. 3.18) is discussed in more detail in Chapter 3. Large, fresh phenocrysts of biotite (7.95—9.10% K_2O), kaersutite (1.78—2.36% K_2O), and Ti and Ca rich clinopyroxene are set in a fine-grained matrix consisting of clinopyroxene, titanomagnetite, biotite, amphibole and interstitial glass. 2—3 mm sized crystals of both biotite and kaersutite were irradiated and analysed.

The isotopic composition of the argon released from individual biotite crystals showed no systematic variation with distance from the crystal margin, which suggests that they have remained more or less closed to argon since cooling through their blocking temperature. The $^{40}Ar/^{36}Ar$ ratio of the trapped argon component (295.5 ± 4.1) is within error of the atmospheric ratio (fig. 4.17). Apparent ages ranged from 77.6 ± 2.6 to 83.3 ± 3.0 Ma (weighted mean of 10 analyses; 80.5 ± 0.5 Ma), and the age calculated from the extrapolated $^{40}Ar/^{39}Ar$ ratio of the radiogenic component is 80.9 ± 0.4 Ma (MSWD=1.414). This is very similar to the ages of the nearby alkalic complexes of Campos do Jordao and Sao Sebastiao,

which have been dated by the conventional K—Ar technique at 81 and 80 Ma respectively (Melcher and Melcher, 1972; Amaral et al., 1967).

A kaersutite crystal from this sample was crushed to 0.5 mm-sized fragments, and after irradiation these yielded apparent ages of between 62.9 ± 1.0 and 74.7 ± 1.7 Ma (weighted mean of 4 analyses; 67.5 ± 0.7 Ma). The isochron age obtained from these data was 49.6 ± 3.9 Ma (MSWD=2.359); significantly younger than the age obtained from the biotite separate from the same sample. The mixing line is controlled largely by a single analysis from an amphibole crystal fragment that appears to have lost radiogenic ^{40}Ar (the extrapolated $^{40}Ar/^{36}Ar$ ratio of the trapped component of the amphibole is 460.4). If this analysis is excluded from the best-fit line routine, the age obtained is 71.5 ± 6.1 Ma, and the $^{40}Ar/^{36}Ar$ ratio of the trapped component is 314.

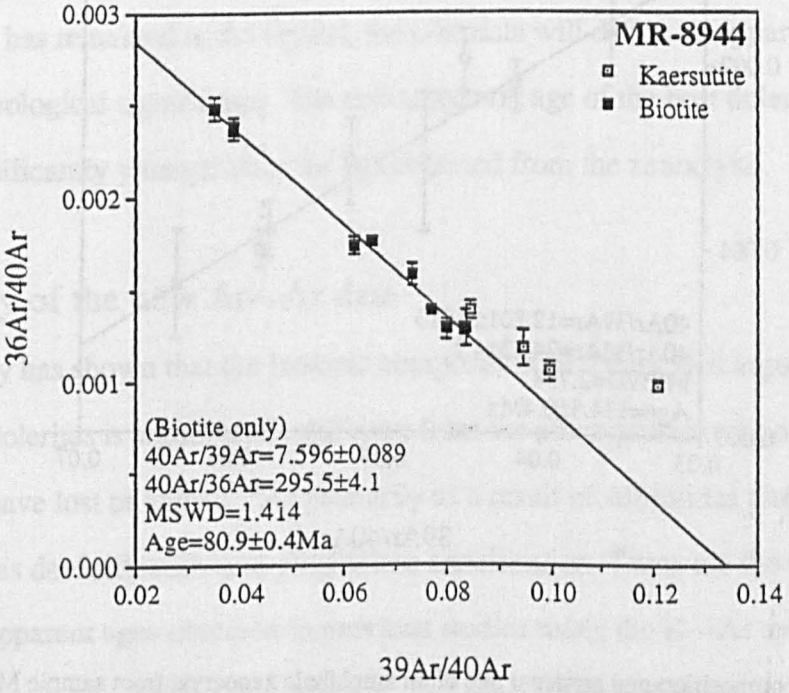

Fig. 4.17
Argon isotope composition and age of sample MR-8944. Note that the kaersutite crystals appear to have lost radiogenic ^{40}Ar, whilst the biotite crystals have not.

The data suggest that the amphibole crystals have lost radiogenic ^{40}Ar, whilst the biotite has not. Although amphibole is generally considered to be more retentive of argon, the kaersutite crystals contain less K than the biotite phenocrysts, and therefore partial loss of radiogenic argon from the former will have a significant effect upon the apparent age. In

any case, too few analyses were obtained from this mineral for an accurate age to be obtained. The preferred age of sample MR-8944 is therefore that calculated from the biotite (80.9 ± 0.4 Ma).

4.5.4.2 Sample MR-8981

The mineral chemistry of this sample was investigated in some detail by means of electron probe analysis (Chapter 3). Phenocrysts of olivine (Fo_{83-86}) and calcic clinopyroxene (En_{40-42}, Wo_{46-48}, Fs_{10-14}) are set in a fine-grained groundmass consisting of clinopyroxene, titanomagnetite and glass. A single large crystal of amphibole was

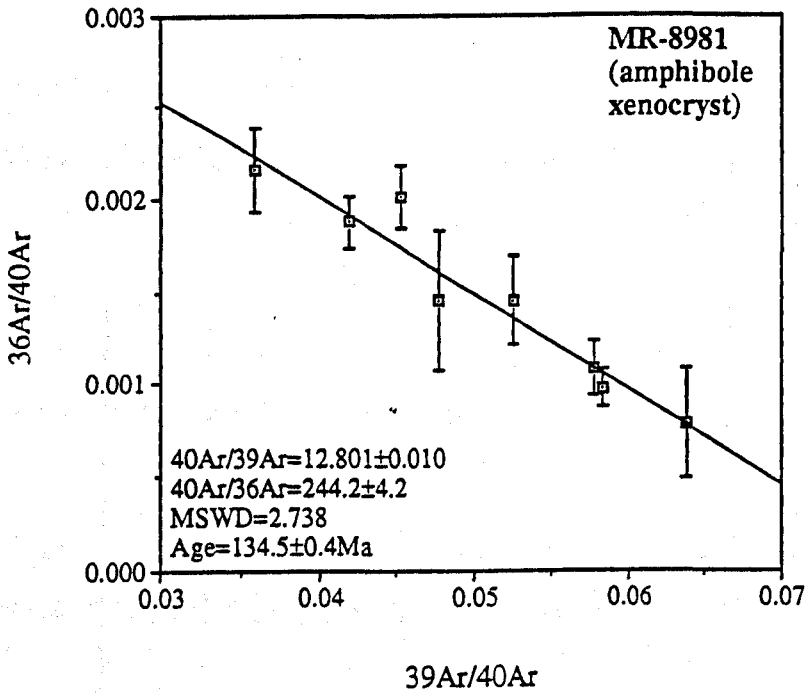

Fig. 4.18
Argon isotope composition and apparent age of an amphibole xenocryst from sample MR-8981. Note the impossibly low $^{40}Ar/^{36}Ar$ value of the trapped component, which suggests that the array of data does not represent a mixing line, and that the age obtained does not therefore reflect the crystallisation age of the dolerite.

separated for analysis. Small clusters of biotite and hornblende occur throughout this rock, and their cumulate textures (fig. 3.17), together with the rounded, partially resorbed margins of some crystals suggest that these are xenocrysts. The dyke from which this sample was collected intrudes a dolerite of the Paraiba magma type (MR-8980; another sample of this magma type has been dated at 133.3 ± 1.7). The basement rocks in this region of Sao Paulo

State are charnockites and granulites which were intruded by calcalkaline, biotite-hornblende granitoids at 650 Ma (Janasi and Ulbrich, 1991), and from which the xenocrysts are likely to have been derived.

The amphibole crystal contained argon of relatively radiogenic composition (fig. 4.18), and yielded an isochron age of 134.5 ± 0.4 Ma (MSWD=2.738). However, in view of the fact that the amphibole crystal is a xenocryst, this age is unlikely to represent the crystallisation age of the dolerite. Note that the apparent $^{40}Ar/^{36}Ar$ ratio of the trapped component (244.2 ± 4.2) is significantly lower than that of air. This suggests that the age of the xenocryst is considerably older than 134 Ma, and that the relatively young age obtained is due to the partial loss of radiogenic ^{40}Ar. If all the radiogenic ^{40}Ar in the xenocrysts had been lost at the time at which the dyke was intruded, the data would lie upon a simple mixing line (fig. 4.3), with a $^{40}Ar/^{36}Ar$ intercept of >295. If however, some of the original radiogenic ^{40}Ar has remained in the crystal, then the data will define an apparent mixing line which has no geological significance. The crystallisation age of the host dolerite is therefore likely to be significantly younger than the age obtained from the xenocryst.

4.6 Summary of the new Ar—Ar data

This study has shown that the isotopic composition of the trapped argon component in many of these dolerites is significantly different from the atmospheric composition, and that some samples have lost or gained ^{40}Ar primarily as a result of subsolidus alteration processes such as devitrification and plagioclase sericitisation. These are the reasons for the wide range of apparent ages obtained in previous studies using the K—Ar technique. Altered samples will in general yield young K—Ar ages, because the fine-grained alteration products often do not retain radiogenic ^{40}Ar, even at relatively low temperatures (Cerling et al., 1985; McDougall and Harrison, 1988). Samples which incorporated foreign ^{40}Ar at the time of crystallisation will yield anomalously old K—Ar ages.

In Chapter 2 it was argued that the dykes of the Ponta Grossa region may have fed the basalt flows of the Pitanga and Paranapanema magma types of the northern Parana. The geochemical stratigraphy of the lava pile (Peate et al., 1992) implies that these were the last

magma types to be erupted (fig. 4.19). The age of these samples can therefore place a lower limit on the age of the Parana magmatism. Samples MR-899, MR-8930, MR-8917 (Paranapanema magma type), and MR-8928 (Pitanga magma type), yielded isochron ages of 131.2 ± 0.5, 133.9 ± 2.5, 130.5 ± 2.9, and 134.1 ± 1.3 Ma respectively. The Paranapanema basalts lie at a higher stratigraphic level than the Pitanga basalts (Peate et al., 1992), and this is consistent with the new Ar—Ar data; the Pitanga dolerite analysed in this study is significantly older than sample MR-899, but has a similar age to that of samples MR-8917 and MR-8930 (Paranapanema type) (fig. 4.20). Interestingly, recent palaeomagnetic data (Ernesto and Pacca, 1988; Raposo and Ernesto, 1989) suggest that the Ponta Grossa dolerites may be younger than the basalts of the southern Parana. There is no evidence to support this in the new Ar—Ar data, which suggest that the Ponta Grossa dolerites are of similar age to the Gramado basalts dated in previous studies (Hawkesworth et al., 1992; Renne et al., 1992b).

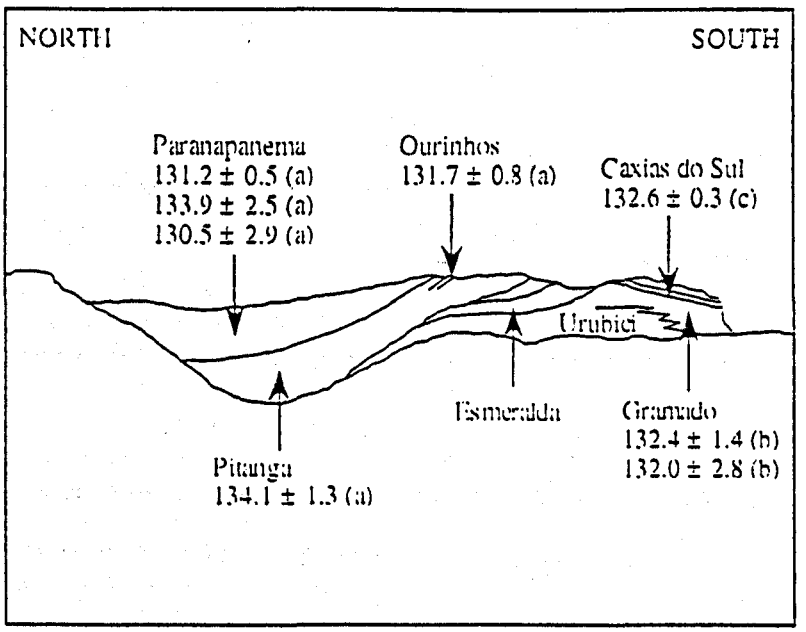

Fig. 4.19
Schematic north—south cross section through the Parana lava field at longitude 52°W, to show the relative stratigraphic positions of the samples that have been dated by the Ar—Ar technique. Data sources; (a), this study; (b), Hawkesworth et al. (1992); (c), Renne et al. (1992b).

A more evolved rock from the Ponta Grossa region, which appears to be an intrusive equivalent of the Ourinhos rhyolite type (Chapter 2) yielded an age of 131.7 ± 0.8 Ma,

slightly younger than the age obtained for the dolerite of the Pitanga magma type. This is consistent with the relative stratigraphic positions of these samples; the Ourinhos rhyolites lie close to the boundary between the Pitanga and Paranapanema basalts (Peate et al., 1992).

Two basalt samples of the Gramado magma type collected from near the base of the lava pile in the southern Parana (fig. 4.19) were dated in an earlier study by Hawkesworth et al. (1992), who obtained isochron ages of 132.4 ± 1.4 and 132.0 ± 2.8 Ma. These ages imply that the entire Parana magmatism occurred within a period of less than about 3 Ma, between 131 and 134 Ma (fig. 4.20), assuming that the geochemical statigraphy of the lava pile as inferred from the borehole data (Peate et al., 1992) is correct.

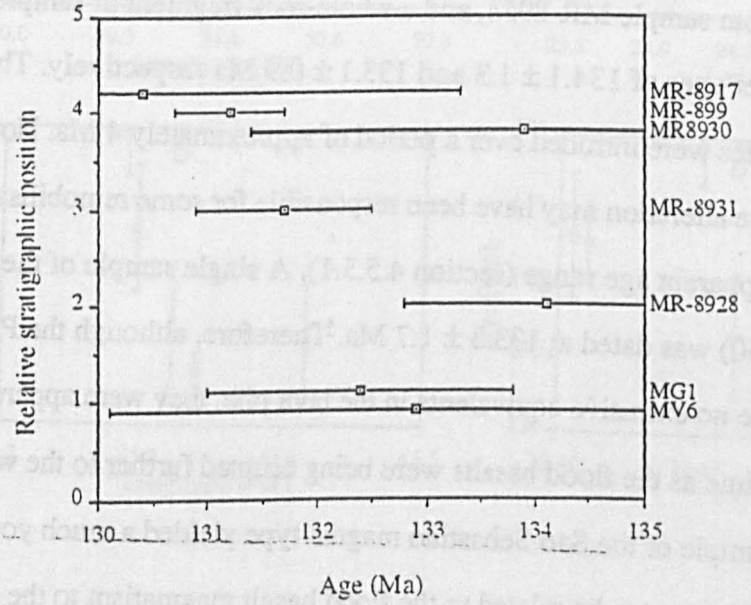

Fig. 4.20
Variation of Ar—Ar ages with relative stratigraphic position of the dolerites from the Ponta Grossa region, and the two Gramado basalt samples from near the base of the lava pile that were dated by Hawkesworth et al. (1992). The data imply that the Parana lavas were erupted within about 3 Ma, at between 134 and 131 Ma (see discussion in section 4.6). Renne et al.'s (1992) data are not included, because of the lack of stratigraphic control on many of their sampling sites.

Simon Turner (pers. comm.) has recently begun a detailed Ar—Ar dating study of the Parana volcanic rocks, using the laser probe equipment at the Open University. Preliminary results for basalt samples of the Urubici and Esmeralda magma types suggest that these too were erupted at approximately 131—132 Ma, consistent with their stratigraphic position relative to the samples dated in this study, as inferred from the borehole data (Peate et al., 1992). However, several basalt samples from the north and west of the lava field (Pitanga

and Paranapanema magma types) have yielded older ages (133—139 Ma), although the geochemical stratigraphy of the lava pile suggests that these are in fact younger than the Gramado basalts of the southern Parana, which yield ages of around 132 ± 1 Ma (Hawkesworth et al., 1992; Renne et al., 1992).

The ages obtained from many of the dolerites from the coastal dyke swarm of Sao Paulo State are similar to those of the Parana flood basalts. The isochron ages obtained from plagioclase separates from MR-8957 and MR-8959, which belong to the Ubatuba magma type, are within error (130.7 ± 1.7 and 129.4 ± 0.6 Ma respectively), and similar to the preferred age of 130.2 ± 1.6 Ma obtained from a whole-rock isochron from MR-8965. A plagioclase separate from sample MR-8954, and a whole-rock fragment of sample MR-8951 yielded somewhat older ages of 134.1 ± 1.3 and 133.1 ± 0.9 Ma respectively. These ages imply that these dolerites were intruded over a period of approximately 4 Ma. However, it appears that plagioclase alteration may have been responsible for some remobilisation of argon, and hence an apparent age range (section 4.5.3.1). A single sample of the Paraiba magma type (MR-8950) was dated at 133.3 ± 1.7 Ma. Therefore, although the Paraiba and Ubatuba dolerites have no extrusive equivalents in the lava pile, they were apparently intruded at the same time as the flood basalts were being erupted further to the west.

In contrast, a sample of the Sao Sebastiao magma type yielded a much younger age, and these dolerites appear not to be related to the flood basalt magmatism to the west. The isochron age of 80.9 ± 0.4 Ma obtained for a biotite separate from sample MR-8944 is similar to the age of the nearby alkalic intrusion of Campos do Jordao. A amphibole xenocryst separated from sample MR-8981 yielded an age of 134.5 ± 0.4 Ma, but the geological significance of this age is uncertain. The nearby alkalic intrusion of Sao Sebastiao has been dated by the conventional K—Ar method at 80 Ma (Ulbrich and Gomes, 1981), and many of the other alkalic intrusive complexes of Sao Paulo and Mato Grosso States have yielded similar ages (Ulbrich and Gomes, 1981).

There is some evidence that the variation in age of the Sao Paulo dolerites may be linked to their geographical position. The dolerites young to the south and west (fig. 4.21), whereas the South Atlantic rift appears to have propagated from south to north (Chapter 5).

This age variation cannot therefore be easily related to the intricacies of the rifting process between Africa and South America. However, note that the samples that were dated were collected from a relatively restricted area of the dyke swarm (fig. 3.1). There is no systematic age variation with geographic position within the Ponta Grossa dykes (fig. 4.23).

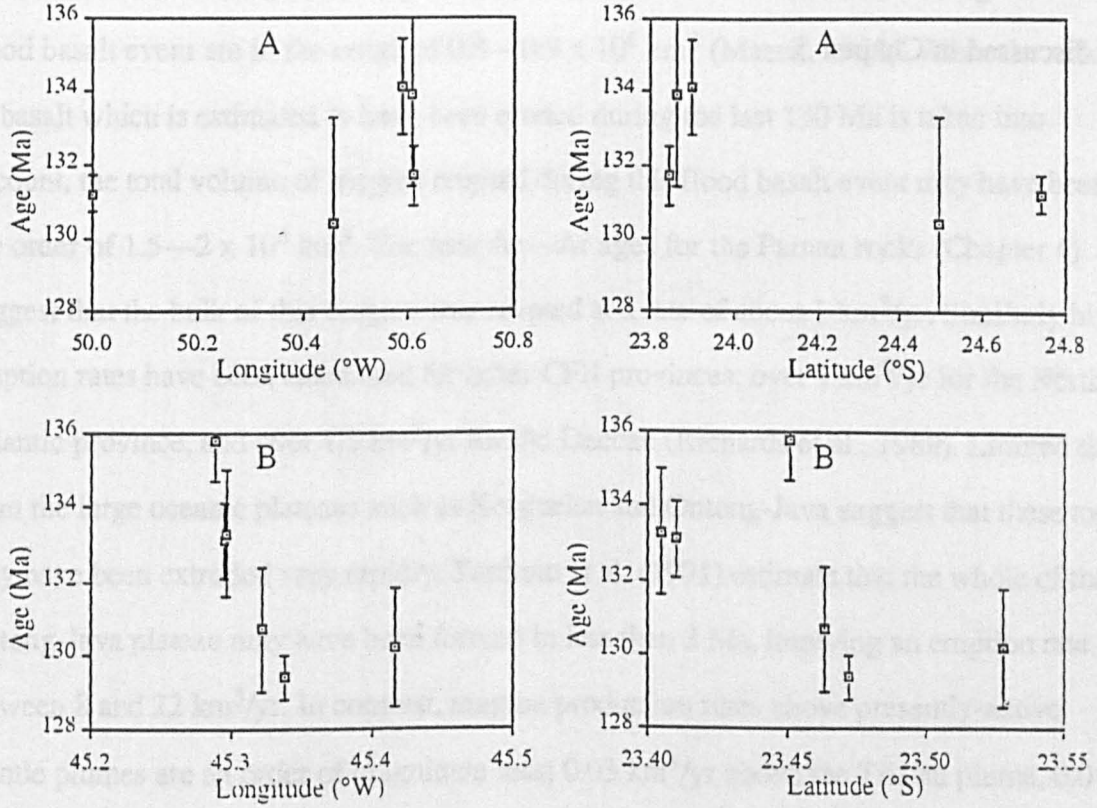

Fig. 4.21
Variation of Ar—Ar age with latitude and longitude for dykes from (a), the Ponta Grossa region; (b), the coastal region of Sao Paulo State. Note that the latter appear to young to the south and west.

In conclusion, the ages obtained from the Ponta Grossa dolerites are consistent with their relative stratigraphic position as inferred from the borehole stratigraphy. The ages obtained from 2 basalt samples of the Gramado magma type from close to the base of the lava pile (Hawkesworth et al., 1992) imply that the Parana lavas were extruded over a period of approximately 3 Ma, between 134 and 131 Ma. However, the fact that an anomalously young age was obtained from a highly sericitised plagioclase crystal, implies that some of the apparent age variation may be due to the loss or gain of radiogenic ^{40}Ar as a

result of subsolidus alteration, and that much of the Parana magmatism took place very rapidly (within about 1 or 2 Ma) at around 132 Ma.

As discussed in section 4.1, the aims of this dating study were not only to determine the absolute age range of the Parana magmatism, but also the relative ages of CFB magmatism and continental rifting in the South Atlantic. The existing age constraints on the age of rifting in the South Atlantic, and the geodynamic implications of the new Ar—Ar data are discussed in Chapter 5.

Chapter 5

Geodynamic modelling of the Parana CFB magmatism

5.1 Introduction

Estimates for the present-day volume of basalt associated with the Parana-Etendeka flood basalt event are in the range of 0.8—0.9 x 10^6 km^3 (Maack, 1962). When the volume of basalt which is estimated to have been eroded during the last 130 Ma is taken into account, the total volume of magma erupted during this flood basalt event may have been of the order of 1.5—2 x 10^6 km^3. The new Ar—Ar ages for the Parana rocks (Chapter 4) suggest that the bulk of this magma was erupted at a rate of about 1 km^3/yr. Similarly high eruption rates have been calculated for other CFB provinces; over 1 km^3/yr for the North Atlantic province, and over 1.5 km^3/yr for the Deccan (Richards et al., 1989). Limited data from the large oceanic plateaus such as Kerguelen and Ontong-Java suggest that these too may have been extruded very rapidly; Tarduno et al. (1991) estimate that the whole of the Ontong-Java plateau may have been formed in less than 3 Ma, implying an eruption rate of between 8 and 22 km^3/yr. In contrast, magma production rates above presently-active mantle plumes are an order of magnitude less; 0.03 km^3/yr above the Tristan plume, 0.04 km^3/yr for the Reunion plume, and 0.16 km^3/yr at Hawaii (Richards et al., 1989; Watson and McKenzie, 1991). For comparison, magma production rates at mid-ocean spreading ridges are in the range 0.7 to 0.07 km^3/yr per kilometer length of ridge.

Despite the recent interest in continental flood basalt provinces worldwide, the geodynamic processes which operate to produce such enormous volumes of magma in such short periods of time are still not well understood. Morgan (1981) drew attention to the fact that most CFB were erupted in extensional continental tectonic settings. Many CFB are located on passive continental margins, and were erupted at the time of continental rifting. For example, the Deccan CFB were erupted at the time of rifting of the Seychelles from the Indian subcontinent; the North Atlantic flood basalts were associated with the rifting of Greenland from northern Europe; and the Parana-Etendeka CFB with the separation of South America and Africa (fig. 5.1).

Morgan (1981) also pointed out that plate reconstructions indicate that a mantle plume existed in the region of each flood basalt province at, or shortly after, the time of magmatism. To use the same examples; the mantle plume presently beneath the Indian Ocean island of Reunion was in the region of the Deccan at the time of eruption at 60 Ma, and the Iceland plume lay beneath the North Atlantic Tertiary igneous province at the time of its eruption. In the case of the Parana-Etendeka, plate reconstructions show that the mantle plume presently beneath the South Atlantic island of Tristan da Cunha lay beneath southern Angola at the time of continental rifting at about 130 Ma (Duncan, 1984).

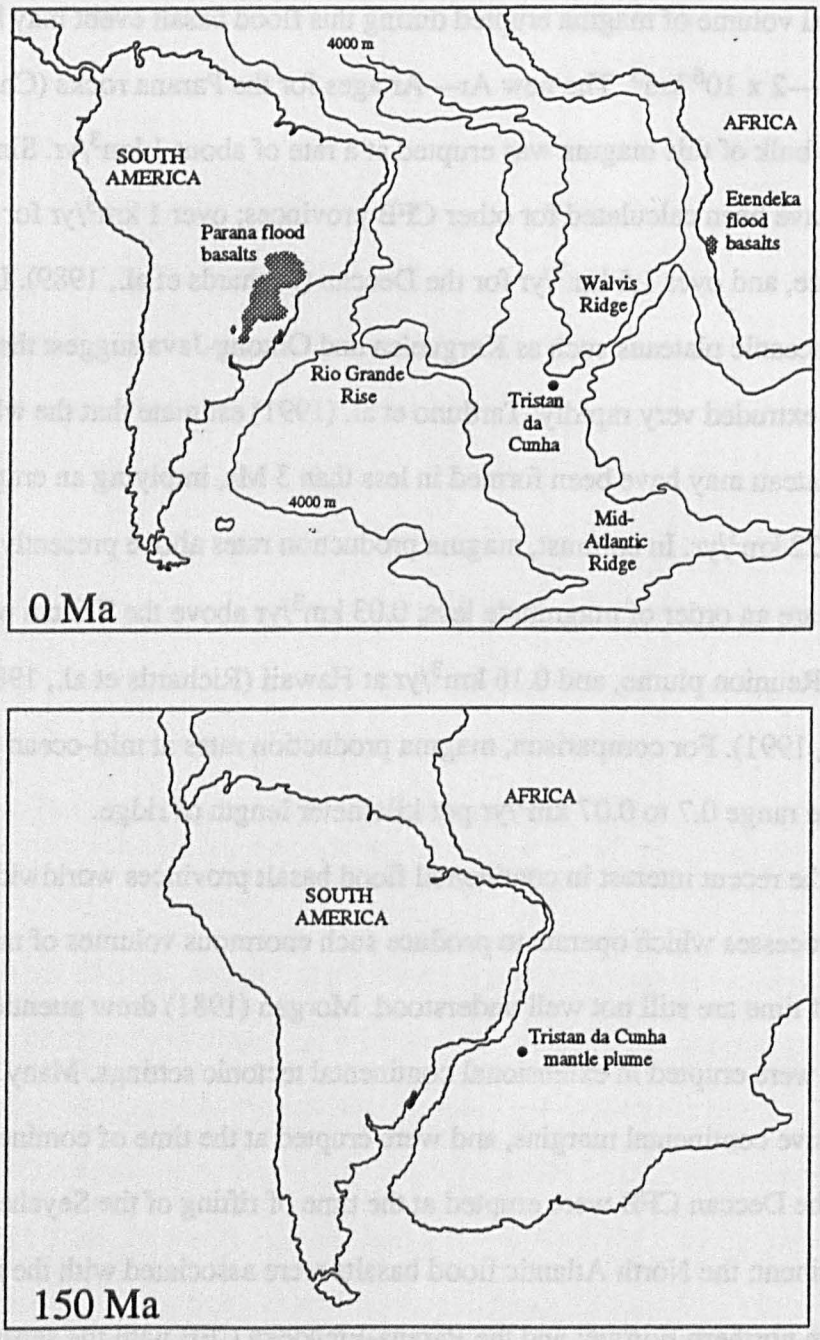

Fig. 5.1
Position of Africa with respect to South America at 150 Ma, and at the present day (after White and McKenzie, 1989).

Recently, two different geodynamic models for CFB have been proposed, which attempt to explain this relationship in space and time between CFB eruption, continental rifting and mantle plumes (Richards et al., 1989; White and McKenzie, 1989). These models are discussed in more detail below. The purpose of this Chapter is to evaluate which of these models can best explain the physical and chemical characteristics of the Parana magmatism.

5.2 The plume initiation model

Morgan (1981) noted that flood basalt provinces appear to represent the earliest surface manifestations of many currently-active hotspots, and proposed that flood basalts are erupted as a result of the initiation of a mantle plume. Recently, scaled fluid dynamic experiments have been carried out (Whitehead and Luther, 1975; Griffiths and Campbell, 1990), which suggest that an initiating plume from the deeper mantle will rise in the form of a spherical vortex followed by a trailing feeder conduit (fig. 5.2). A thermally-driven plume vortex entrains a boundary layer heated by its passage (Griffiths, 1986), and its diameter at a depth z is given by

$$D(z) = Q^{1/5} (\nu/g\alpha\Delta T)^{1/5} \kappa^{2/5} z^{3/5}$$

where Q is the volume flux from the source layer, ν is the kinematic viscosity of the overlying mantle, α is the coefficient of thermal expansion, κ is the thermal conductivity of the mantle, and ΔT the temperature excess of the plume material.

Reasonable estimates of Q, ν, α and κ for the lower mantle suggest that D may reach 800 to 1200 km, if the plume is fed from a boundary layer at the core-mantle boundary. As it nears the base of the lithosphere, the plume head spreads laterally over an area 1500—2500 km in diameter (Griffiths and Campbell, 1991). Richards et al. (1989) pointed out that these are similar to the dimensions of many CFB provinces (1000—2000 km), and proposed that flood basalt magmatism occurs as a consequence of plume initiation beneath the continental lithosphere. Magma is generated within the plume head by adiabatic decompression, and although an accurate calculation of the total melt volume is difficult

because of the complicated thermal structure of the plume vortex, Campbell and Griffiths (1990) estimate that volumes of the order of 10^7 km^3 may be produced in this way.

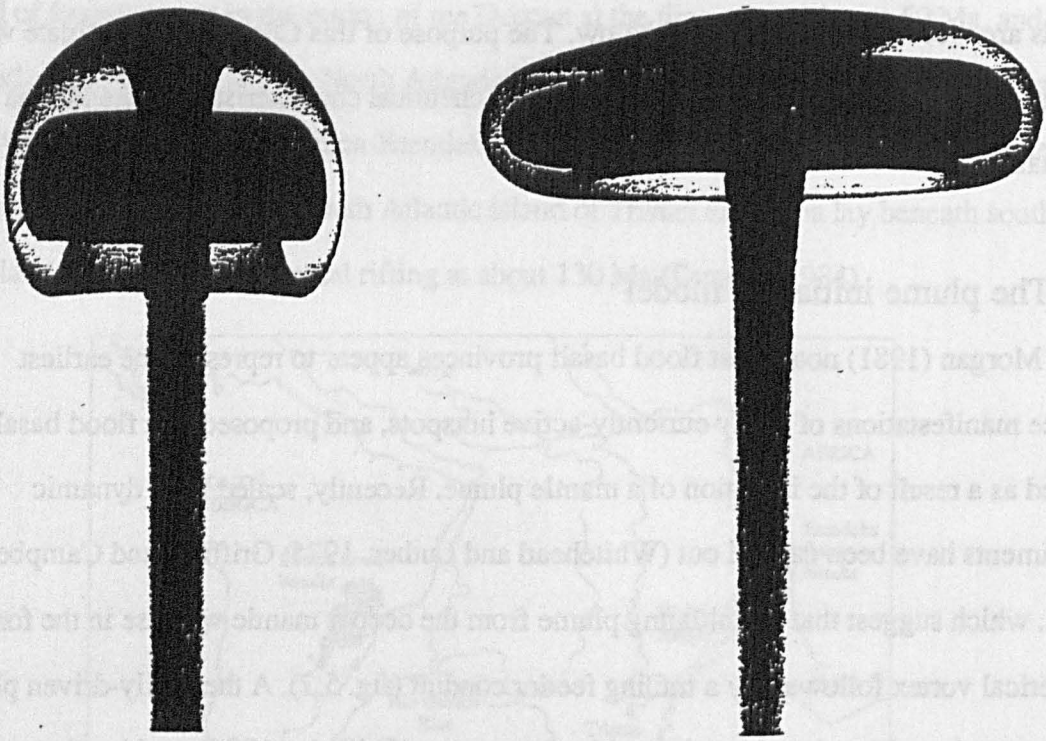

Fig. 5.2
Scaled fluid dynamic experiments illustrating a thermally driven initiating plume in a glucose solution. The plume vortex enlarges during ascent due to entrainment of the surrounding material, and is followed by a narrow feeder conduit. From Griffiths and Campbell (1990).

The density anomaly introduced into the upper mantle results in considerable surface uplift. This uplift begins 10 to 20 Ma before the onset of volcanism, at a rate of 20—40 m/Ma, and is followed by subsidence above the plume axis as the density anomaly disperses. The maximum uplift of between 500 and 1000 m is predicted to occur immediately before eruption of the flood basalts, and this elevation induces stresses within the lithosphere that are sufficient to cause continental rifting and breakup (Houseman and England, 1986; Griffiths and Campbell, 1991). According to the plume initiation model, continental rifting is not primarily responsible for melt generation, although because melt is generated by adiabatic decompression, rifting will substantially increase the total volume of melt that is produced (White, 1992).

Richards et al. (1989) pointed to the fact that not all CFB provinces are associated with continental breakup as evidence for the plume initiation model; for example the Siberian

and Columbia River provinces, although associated with continental extension, were erupted within continental plates. In the Karoo province, the main period of rifting appears to have taken place at around 195 Ma, pre-dating eruption of the flood basalts at 175 Ma (Cox, 1988). In the North Atlantic, the Labrador Sea commenced opening in the south at ~75Ma (Srivasta, 1978), when the Iceland plume appears to have been absent (White and McKenzie, 1989). As rifting extended northwards into Baffin Bay at ~60 Ma, picritic basalts and tholeiitic basalts were erupted in western Greenland as a result of the thermal influence of the Iceland plume, which apparently initiated beneath East Greenland at about 62 Ma. These observations are evidence against models in which CFB magmas represent decompression melts generated as a result of continental rifting (section 5.3). On the other hand, Kent (1991) has used the pattern of uplift in eastern Gondwanaland at 300 Ma, as inferred from sedimentological data and drainage patterns, as evidence that the Kerguelen mantle plume existed beneath the Rajmahal area of eastern India for 150 Ma prior to the start of igneous activity and final continental breakup at 120 Ma. This would suggest that the Rajmahal flood volcanics were not the result of the initiation of the Kerguelen mantle plume, as proposed by Richards et al. (1989).

At present there is considerable debate as to whether or not plume initiation events are responsible for CFB magmatism. The plume initiation model remains the best explanation for the formation of large oceanic plateaus such as Kerguelen and Ontong-Java (Richards et al., 1990), which are clearly not associated with continental rifting events. However, there are difficulties in trying to explain the characteristics of the Parana-Etendeka province in terms of this model (section 5.4).

5.3 Decompression melting during extension of the lithosphere

If extension occurs within a period that is short compared with the thermal conduction constant for the lithosphere (6—12 Ma), mantle material will rise along an adiabatic temperature gradient (fig. 5.3), and may intersect the solidus (Jarvis and McKenzie, 1980). That melt can be generated in this way has been realised for some time, but only recently has a more quantitative approach been adopted, which allows both the volume and the major

element composition of the melts to be calculated (Foucher et al., 1982; McKenzie and Bickle, 1988).

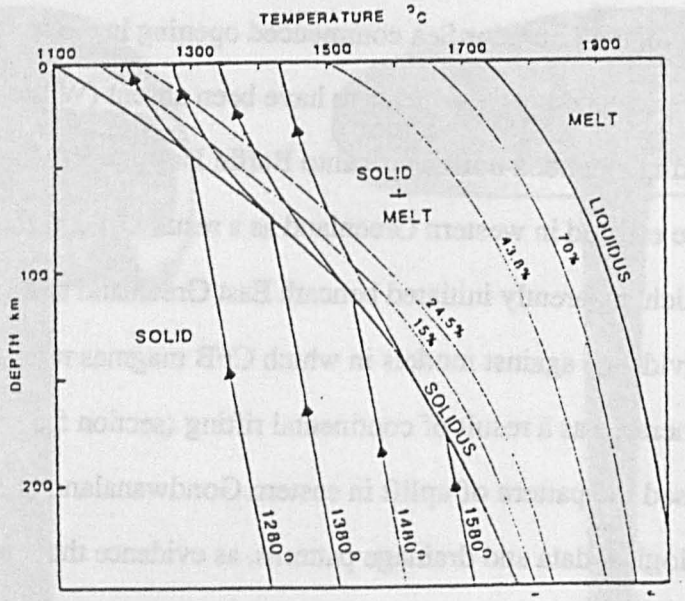

Fig. 5.3
Cooling paths followed by upwelling mantle at various potential temperatures beneath a mid ocean ridge. The initial cooling path is adiabatic, until the mantle reaches the anhydrous peridotite solidus, after which point the cooling rate increases due to the extraction of the latent heat of fusion (assumed here to be 400 J $Kg^{-1}{}^{o}C^{-1}$). From McKenzie and Bickle (1988).

5.3.1 The volume of melt generated during continental extension

Foucher et al. (1982) assumed the lithosphere to behave as a simple mechanical boundary layer (MBL) in which heat is transferred by conduction, overlying a convecting mantle in which the temperature gradient is adiabatic. The temperature variation with depth immediately after extension was calculated, taking into account the temperature decrease due to adiabatic decompression, and the extraction of latent heat of melting. Using an empirical expression for X(T, P) based on the available experimental data (Ahern and Turcotte, 1979), Foucher et al. (1982) were then able to calculate the variation in melt fraction with depth. They found that the region in which partial melting takes place is more or less restricted to the uppermost mantle immediately below the MBL, but the lowermost part of the MBL also melts, and the lithospheric contribution to the total melt volume is greatest at small values of the stretching factor β. Melt will always be produced if the base of the lithosphere rises above a critical depth, the value of which depends upon the potential temperature (T_p) of the

uppermost mantle. The total melt volume for a given T_p is thus a function of the stretching factor β, and the initial thickness of the lithosphere.

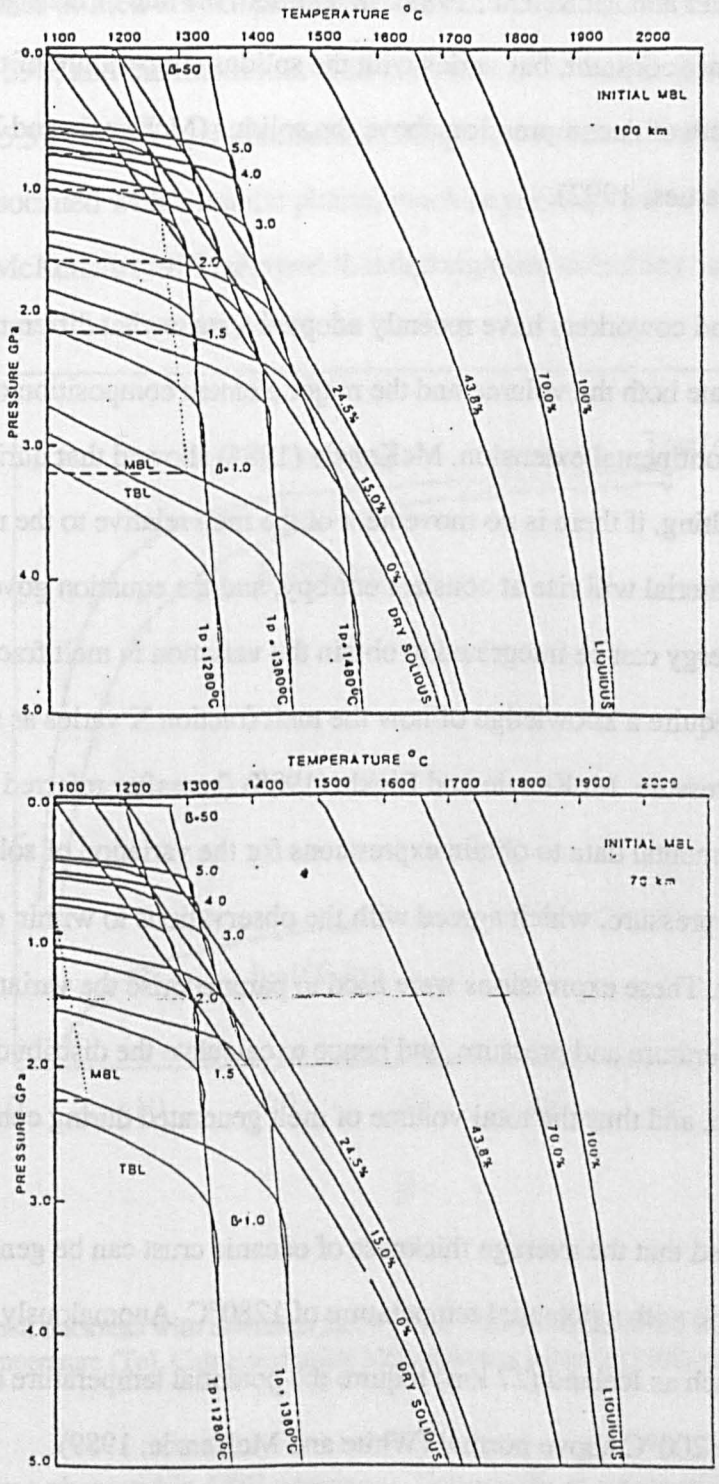

Fig. 5.4
Cooling paths followed by upwelling mantle at various potential temperatures during extension of continental lithosphere assuming a MBL thickness of (a) 100 km, (b) 70 km. Note that for given values of β and Tp, more melt is generated in (b). From Latin et al. (1990).

Foucher et al.'s (1982) model includes a number of simplifying assumptions. They assumed that the lithosphere behaves as a simple mechanical boundary layer, whereas in fact only the uppermost part of the lithosphere is believed to behave in this way (Parsons and Sclater, 1977; Richter and McKenzie, 1981). In addition, the rate of melt generation with pressure release is not constant, but varies with the solidus temperature of the upper mantle, and the specific depth of decompression above the solidus (McKenzie and Bickle, 1988; Kostopoulos and James, 1992).

McKenzie and coworkers have recently adopted a somewhat different approach, and were able to calculate both the volume and the major element composition of the melt generated during continental extension. McKenzie (1984) showed that during decompression melting, if there is no movement of the melt relative to the matrix, then the partially molten material will rise at constant entropy, and the equation governing the conservation of energy can be integrated to obtain the variation in melt fraction with depth. The calculations require a knowledge of how the melt fraction X varies as a function of temperature and pressure. McKenzie and Bickle (1988) (hereafter referred to as M&B) used the existing experimental data to obtain expressions for the variation of solidus and liquidus temperatures with pressure, which agreed with the observations to within estimates of experimental error. These expressions were used to parameterise the variation in melt fraction with temperature and pressure, and hence to calculate the distribution of melt fraction with depth, and thus the total volume of melt generated during continental extension.

M&B showed that the average thickness of oceanic crust can be generated by adiabatic upwelling of mantle with a potential temperature of 1280°C. Anomalously thick oceanic crust in regions such as Iceland (27 km) require the potential temperature of the underlying mantle to be some 200°C above normal (White and McKenzie, 1989).

Of particular interest here however, is the volume of melt that can be generated during extension of the continental lithosphere. In order to calculate the melt distribution associated with finite stretching of the continental lithosphere, an accurate knowledge of the initial geotherm is required. M&B used an elaborate geotherm which was based on the thermal

boundary layer model of Parsons and McKenzie (1978) and Richter and McKenzie (1981), but obtained broadly similar results to Foucher et al. (1982). Assuming the potential temperature of the uppermost mantle to be 1280°C, and a typical MBL thickness of 100 km, significant volumes of melt are not produced until the stretching factor β exceeds a value of about 2.75 (fig. 5.4), and the maximum melt thickness of 6.6 km is predicted at continental separation (fig. 5.5). However, if continental rifting occurs above mantle at the elevated temperatures associated with a mantle plume, much larger volumes of melt can be produced, and White and McKenzie (1989) showed that decompression melting can account for the

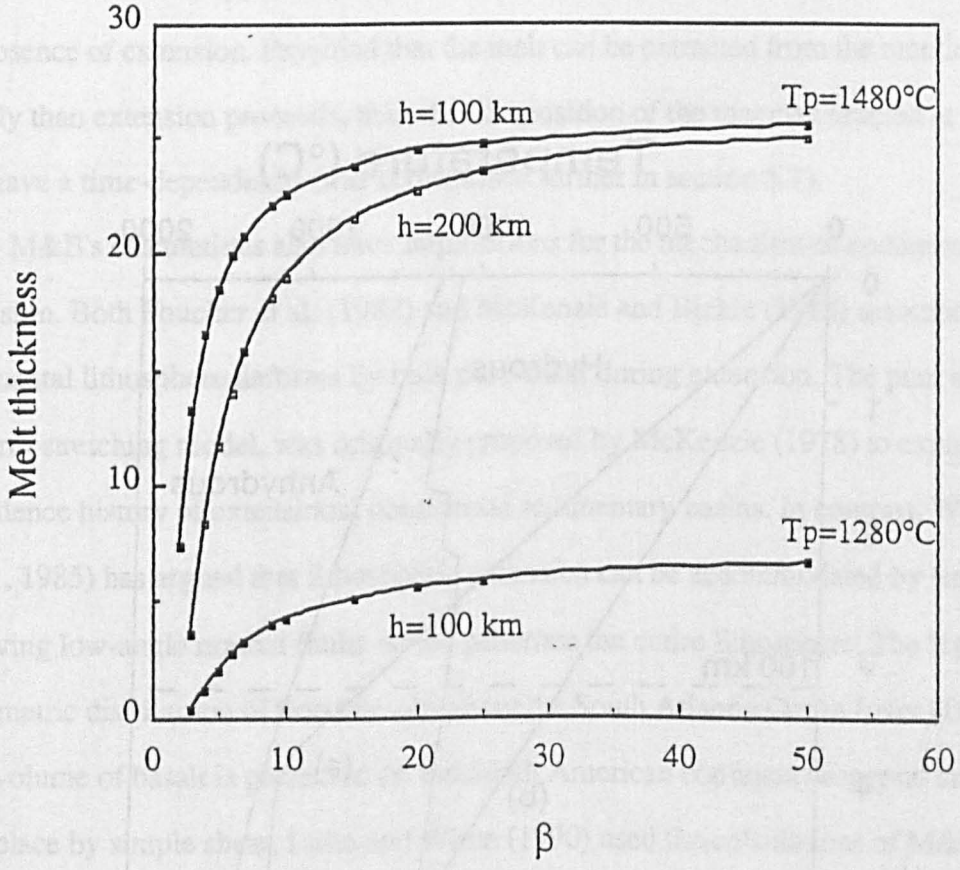

Fig. 5.5
Variation in total melt thickness with extension factor β, for various values of the MBL thickness (h) and the mantle potential temperature (Tp). Calculated using McKenzie and Bickle's (1988) parameterisation.

volumes of magma observed in CFB provinces. For mantle at a potential temperature of 1480°C and an MBL thickness of 100 km, melt is generated when β exceeds a value of 1.21, and a maximum melt thickness of approximately 25.6 km will be produced at continental separation. If the initial thickness of the lithosphere is less than 100 km, then melt will begin to be produced at lower values of β (fig. 5.4).

However, although the calculations show that decompression melting during continental extension above abnormally hot mantle can account for the large volumes of magma erupted in CFB provinces, they also imply that most of the melt generated during continental extension is derived from the sub-lithospheric upper mantle. As discussed in Chapter 1, the major and trace element and radiogenic isotope geochemistry of CFB suggests that they have received a significant contribution from the subcontinental lithospheric mantle (SCLM). Both M&B and Arndt and Christensen (1992) assumed the SCLM to be anhydrous, and showed that less than about 4% of the total melt volume can be produced from it during extension and adiabatic decompression. Gallagher and

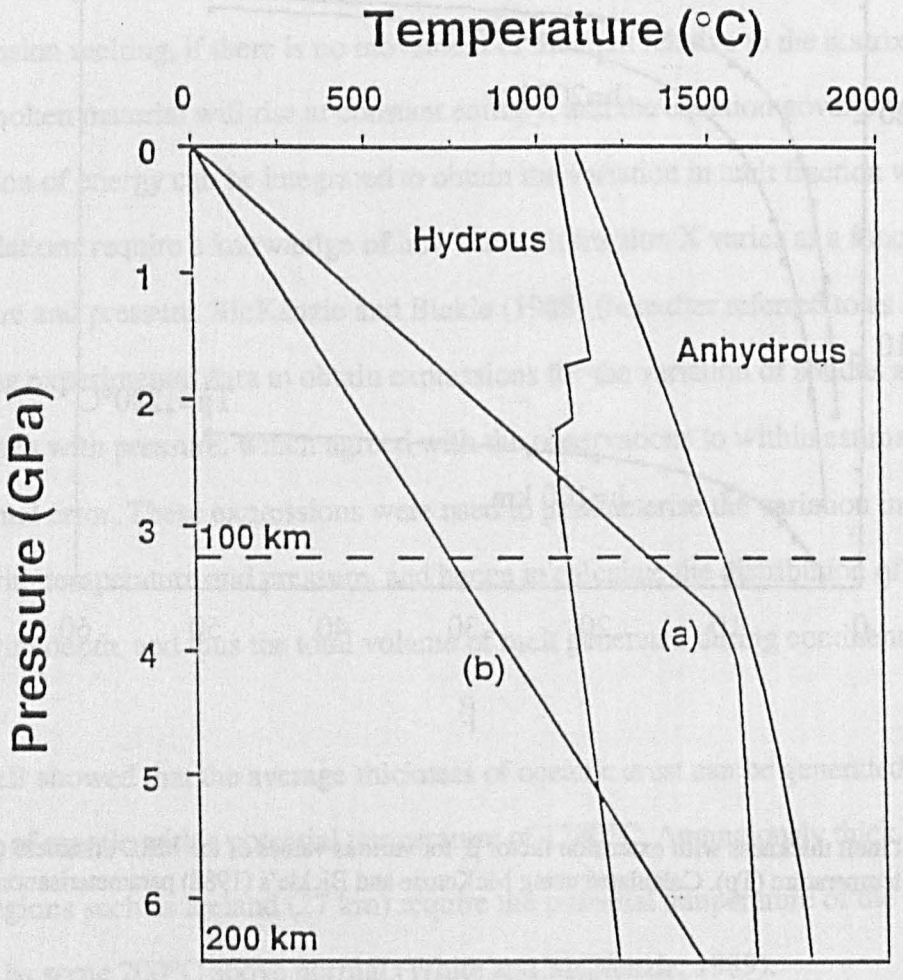

Fig. 5.6
Hydrous and anhydrous solidii, and geothermal gradients assuming a mantle potential temperature of 1480°C and a MBL thickness of (a) 100 km and (b) 200 km. From Gallagher and Hawkesworth (1992).

Hawkesworth (1992) have investigated the consequences of extension when the lowermost lithosphere contains a small amount of water. They used the same approach as McKenzie and Bickle, but assumed the hydrous peridotite solidus of Olafsson and Eggler (1983) to be appropriate for the lowermost part of the MBL. If the lithospheric mantle can accommodate up to 0.4% H_2O in the form of amphibole produced by the hydration of clinopyroxene, then its solidus temperature will be 300—500°C lower than that of dry peridotite (fig. 5.6), and during extension, the lithospheric contribution to the total melt volume is greatly increased. For a mantle potential temperature of 1480°C and a mechanical boundary layer (MBL) thickness of 100 km, approximately 3.2 km of melt is generated entirely from the MBL, in the absence of extension. Provided that the melt can be extracted from the mantle more rapidly than extension proceeds, then the composition of the magmas erupted at the surface will have a time-dependence (this is discussed further in section 5.7).

M&B's calculations also have implications for the mechanism of continental extension. Both Foucher et al. (1982) and McKenzie and Bickle (1988) assumed that the continental lithosphere deforms by bulk pure shear during extension. The pure shear, or uniform stretching model, was originally proposed by McKenzie (1978) to explain the subsidence history of extensional continental sedimentary basins. In contrast, Wernicke (1981, 1985) has argued that lithospheric extension can be accommodated by simple shear involving low-angle normal faults which penetrate the entire lithosphere. The highly asymmetric distribution of flood basalts about the South Atlantic Ocean (over 90% of the total volume of basalt is preserved on the South American continent) suggests that rifting took place by simple shear. Latin and White (1990) used the calculations of M&B to show that very little melt can be generated, even at elevated mantle temperatures and at large values of β, if lithospheric extension takes place by simple shear, rather than by pure shear (fig. 5.7). However, this cannot be taken as conclusive evidence for a plume initiation origin for the Parana-Etendeka CFB, because Harry and Sawyer (1992) have shown that horizontal pressure gradients induced in the lower crust during the early stages of extension as a result of weaknesses in the crust and upper mantle can account for the asymmetric distribution of the lavas about the South Atlantic Ocean.

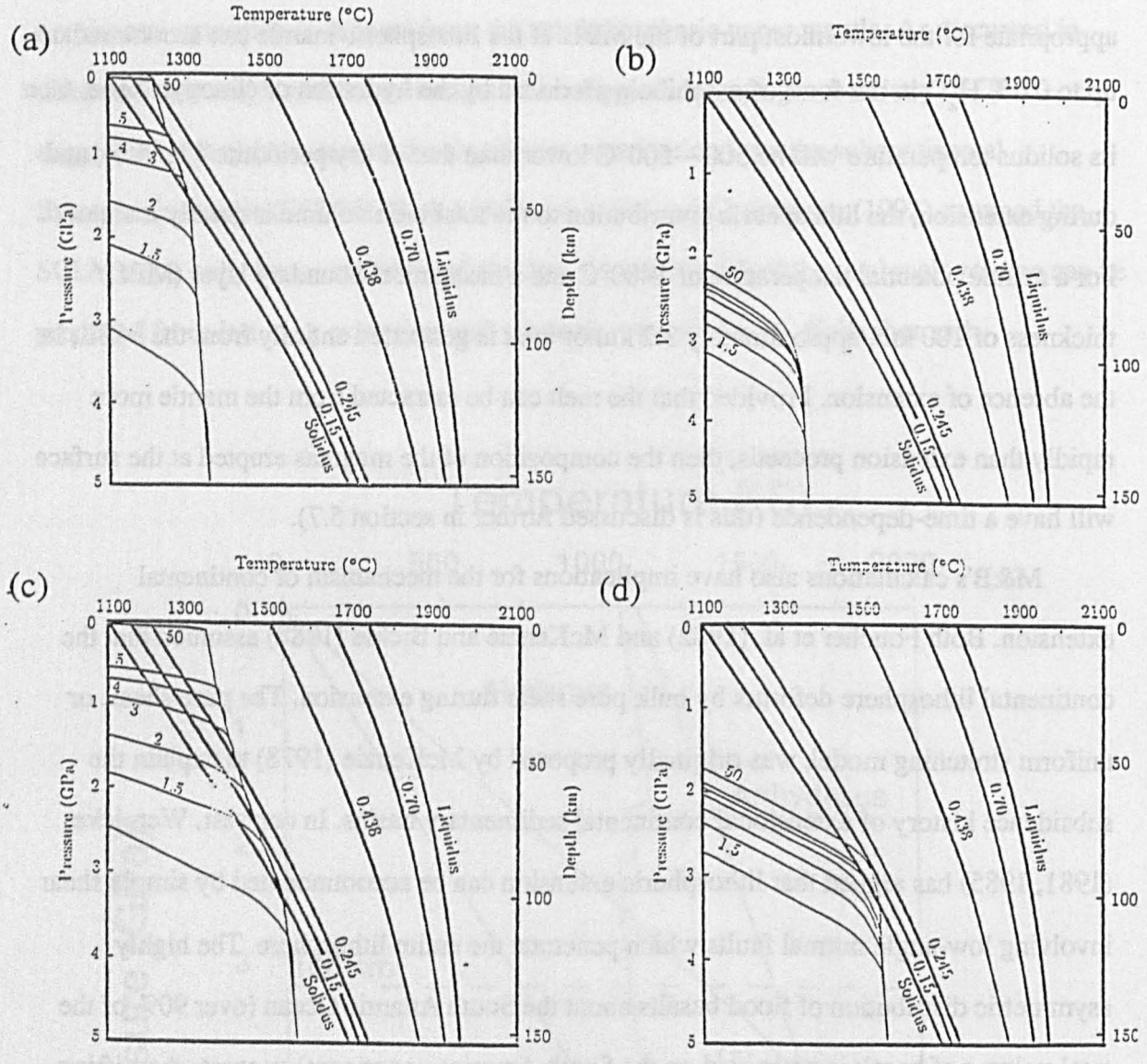

Fig. 5.7
Pressure temperature variation as a result of extension of continental lithosphere (initial MBL thickness=100 km) underlain by mantle at Tp=1280°C ((a) and (b)), and 1480°C ((c) and (d)). In figures (b) and (d), extension is by pure shear, in (a) and (c), extension is by simple shear. Note that for β=50 and Tp=1480°C, a much larger volume of melt is generated by pure shear. From Latin and White (1990).

5.4 The timing of rifting and flood basalt magmatism in the South Atlantic

The new Ar—Ar data for the Parana dolerites presented in Chapter 4 allow us not only to constrain the absolute age and duration of the Parana magmatism, but also the relative ages of magmatism and continental rifting in the South Atlantic. The relative ages of magmatism and rifting can place important constraints upon geodynamic models for the

origin of CFB. The existing age constraints on the rifting of South America from Africa are therefore summarised below.

The age of the oldest oceanic crust in the South Atlantic off the Brazilian coastline obviously places a minimum constraint on the age of the main period of extension. Austin and Uchapi (1982) carried out a geomagnetic survey of the continental margins of Namibia and South Africa. They found the oldest recognisable magnetic anomaly off the Namibian coast to be M4, which corresponds to an age of approximately 126 Ma (Cande et al., 1989) or 130—131 Ma (Harland et al., 1990). The age of the oldest seafloor becomes progressively older towards the south, and off Cape Town in the extreme South Atlantic, the oldest seafloor identified belongs to magnetic anomaly M13 (Rabinowitz and LeBreque, 1979), corresponding to an age of 137—139 Ma (Kent and Gradstein, 1985) (fig. 5.8). Nurnberg and Muller (1991) combined geomagnetic data with Geosat altimetry to construct a plate kinematic model for the South America-Africa rifting event. According to their model, rifting began in the far South Atlantic at approximately 150 Ma, and between 150 (Tithonian) and 130 Ma (Hauterivian), rifting propagated northwards to 38°S. Between 130

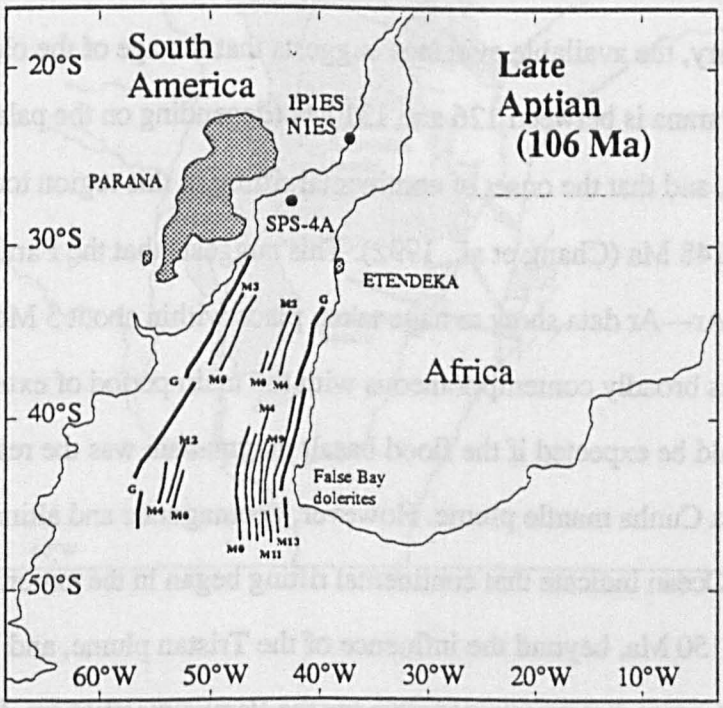

Fig. 5.8
Position of Africa with respect to South America at 106 Ma, showing location of the Parana Etendeka flood basalts, seafloor magnetic anomalies, and the drill sites referred to in the text. Palaeomagnetic data from Rabinowitz and LeBreque (1979).

Ma and about 126.5 Ma, the tip of the South Atlantic rift reached 28°S (the latitude of the Parana), and by approximately 119 Ma (anomaly MO), rifting had propagated northwards into the Benue Trough and Niger Rift.

The age of the oldest oceanic crust can be used to place a lower limit on the age of continental rifting, but cannot constrain the onset of the main period of extension in a particular region. In Namibia, the Etendeka volcanic rocks within 30 km of the Atlantic coast are cut by numerous N—S oriented extensional faults. Rhyolite samples have been recovered in dredge hauls from offshore linear ridges which are believed to represent the edges of tilted fault blocks (Milner, 1988). Erlank et al. (1984) demonstrated that these extensional faults were active before, during and after the flood basalt magmatism. In Brazil, the relationship between extension and magmatism is less clear because of the poor exposure. However, backstripped sediment profiles from boreholes in the Santos and Campos Basins (Chang et al., 1992) suggest that here, continental rifting commenced at ~148 Ma, some 15 Ma before the eruption of the Parana-Etendeka flood basalts. Rift subsidence terminated abruptly during the Aptian (120 Ma).

In summary, the available evidence suggests that the age of the oldest seafloor at the latitude of the Parana is between 126 and 131 Ma (depending on the palaeomagnetic timescale used), and that the onset of continental rifting in this region took place at approximately 148 Ma (Chang et al., 1992). This suggests that the Parana magmatism, which the new Ar—Ar data show to have taken place within about 3 Ma at 134—131 Ma (Chapter 4), was broadly contemporaneous with the main period of extension at this latitude, as would be expected if the flood basalt magmatism was the result of the initiation of the Tristan da Cunha mantle plume. However, geomagnetic and altimetric data from the South Atlantic Ocean indicate that continental rifting began in the extreme south at approximately 150 Ma, beyond the influence of the Tristan plume, and before the proposed plume initiation event that was responsible for the Parana magmatism. It seems rather a coincidence that the northward propagating South Atlantic rift should reach the latitude of the Parana just as the Tristan plume initiated. This suggests that it was the rifting event, rather than plume initiation, that triggered the Parana-Etendeka flood basalt magmatism.

The rate of migration of the flood basalt magmatism, with respect to the developing South Atlantic rift and the inferred position of the Tristan plume, can also place important constraints upon the processes responsible for the magmatism. Peate et al. (1991) used the northward-younging stratigraphy of the lava pile to infer a northward migration of about 750 km in the site of magmatism. The distribution of feeder dykes can give a much more accurate picture of the migration of magmatism, since the lava distribution is likely to have been influenced by differential erosion, and by the topography at the time of eruption. The

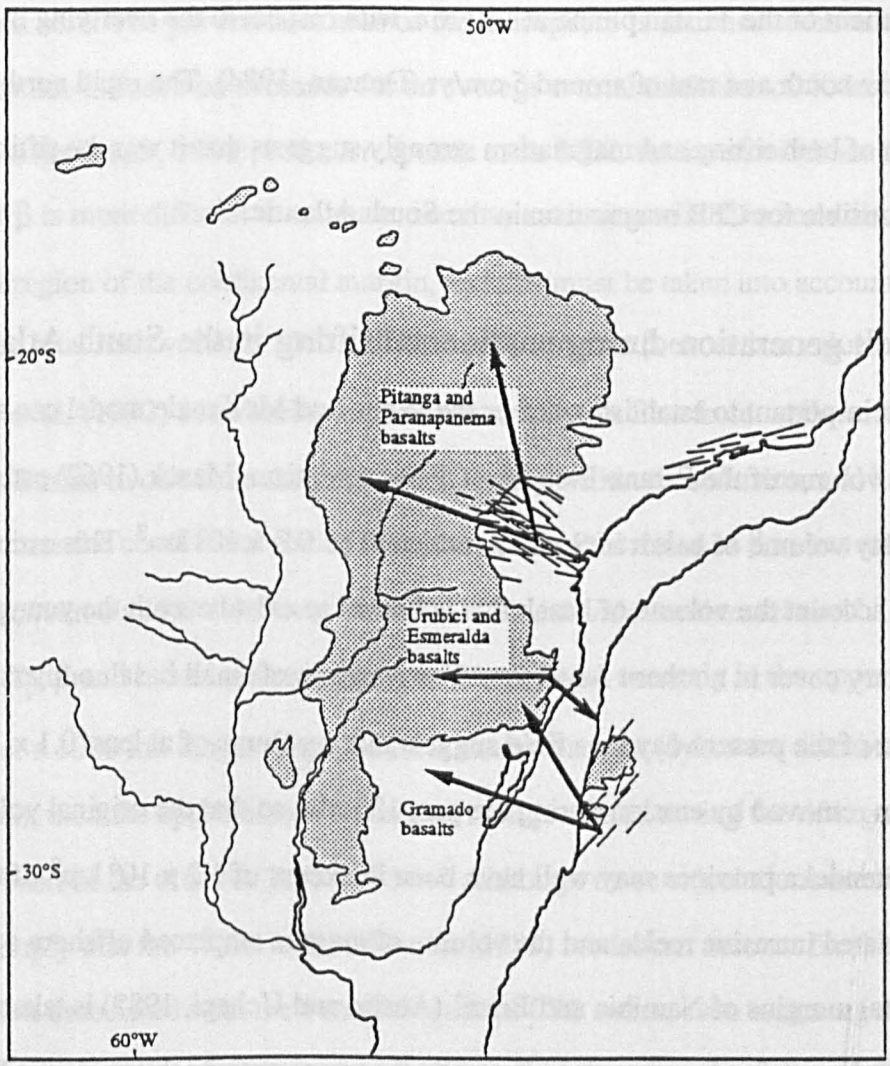

Fig. 5.9
Probable configuration of Africa and South America at 130 Ma, to show location of the flood basalts, associated dyke swarms, and inferred lava flow directions. The oldest basalts are those of the Gramado magma type (see Chapter 4), which were fed from dykes in Namibia. The youngest basalts are those of the Pitanga and Paranapanema magma types (Peate, 1989), which were fed by dykes in the Ponta Grossa region, ~700 km to the north.

relative ages of these dyke swarms can be inferred by correlation with the geochemical stratigraphy of the lava pile. The oldest dykes are those of the Etendeka, which appear to

have fed the Gramado (Tafelberg) basalt lavas of the southern Parana and Etendeka (Erlank et al., 1984). The site of magmatism then shifted northwestwards to the Serra Geral region of southern Brazil (fig. 5.9), where scattered dykes fed lava flows of the Esmeralda magma type (Peate, 1989; Peate et al., 1992). The basalts of the northern Parana were then erupted from feeder dykes in the Ponta Grossa region of Sao Paulo State (Chapter 2). New Ar—Ar data (Hawkesworth et al., 1992; Renne et al., 1992; and this study) indicate that this approximately 700 km northward migration of the magmatism was accomplished in a period of less than about 2 Ma, i.e. at a rate of over 35 cm/y. The available evidence suggests that the movement of the Tristan plume at 130 Ma, with respect to the overlying lithosphere, was towards the south at a rate of around 5 cm/yr (Duncan, 1984). The rapid northward migration of both rifting and magmatism strongly suggests that it was the rifting process that was responsible for CFB magmatism in the South Atlantic.

5.5. Melt generation during continental rifting in the South Atlantic

It is important to establish whether the White and McKenzie model can account for the observed volume of the Parana-Etendeka CFB magmatism. Maack (1962) estimated the present-day volume of basalt in South America to be 0.9×10^6 km^3. This estimate does not take into account the volume of basalt that is known to exist beneath the younger sedimentary cover in northern Argentina. The presence of small basalt outliers to the northwest of the present-day lava field suggest that a volume of at least 0.1×10^6 km^3 may have been removed by erosion during the past 130 Ma, so that the original volume of the Parana-Etendeka province may well have been in excess of 1.2×10^6 km^3. If the volume of the associated intrusive rocks, and the volume of magma emplaced offshore on the continental margins of Namibia and Brazil (Austin and Uchapi, 1982) is taken into account, then the volume of magma emplaced on or in the upper crust in this region is likely to have been greater than about 1.5×10^6 km^3. This estimate does not include the volume of cumulate material that is presumed to exist at depth in the crust, and which may have a similar volume to that of the surface lava field (Cox, 1980). Thus the total amount of melt generated during rifting may have been of the order of $2—3 \times 10^6$ km^3.

In order to be able to predict the volume of melt generated during continental rifting in the South Atlantic, it is necessary to place some constraints on the values of h (the original lithospheric thickness), T_p (the potential temperature of the upper mantle, and β (the stretching factor). The potential temperature of the uppermost mantle at 130 Ma is impossible to estimate directly, but assuming that the Tristan da Cunha plume lay beneath the region at 130 Ma, then the potential temperature of the uppermost mantle over a circular area of about 2000 km diameter is likely to have been between 100 and 200°C above the normal asthenospheric temperature (Courtney and White, 1986). A T_p of 1480°C is therefore used here. The pre-rift thickness of the lithosphere is assumed to have been 125 km. This estimate is based on evidence for an average crustal thickness of 40 km in southern Brazil (Mantovani et al., 1991), and corresponds to an MBL thickness of about 100 km. The value of β is more difficult to estimate, because extension will have been distributed over a broad region of the continental margin, and this must be taken into account when estimating the total melt volume. Melt will be produced when β exceeds a value of about 1.21. Chang et al. (1992) used backstripped sedimentary profiles from wells in the Santos and Campos Basins to calculate the subsidence history within these basins, and hence the value of β across the continental shelf. They showed that the value of β varies more or less uniformly between 0 and 6—6.5 over the 150—200 km wide continental shelf. Using these estimates of T_p, β and h, and assuming that the temperature anomaly in the upper mantle extended over a 1000 km length of the South Atlantic margins (dykes are distributed over about 800 km), then the approximate volume of melt produced during the rifting event would have been of the order of 2.2×10^6 km^3. Although these calculations are necessarily rough, they imply that the White and McKenzie (1989) model can account for the observed volume of melt associated with the Parana-Etendeka CFB event, even assuming that the SCLM is anhydrous. If the SCLM is assumed to be hydrous, then the volume of melt produced would have been significantly larger (Gallagher and Hawkesworth, 1992).

Assuming an initial MBL thickness of 100 km, an upper mantle potential temperature of 1480°C, and that the lowermost 50 km of the MBL contains 0.4% H_2O in the form of amphibole, Gallagher and Hawkesworth (1992) showed that a melt thickness of ~3 km can

be produced from the MBL before the onset of extension, if the geotherm in the MBL is at steady-state. Timescales of the order of 20—40 Ma are required for conductive heating of a 100 km thick MBL in order to achieve 40—50% of the total melt production possible with the steady-state geotherm (Gallagher and Hawkesworth, 1992). This suggests that continental rifting and flood basalt magmatism in the South Atlantic would have been preceded by the eruption of small volumes of magma derived from the MBL, if the region was underlain by the Tristan da Cunha plume at that time.

Recent Ar—Ar dating (Chapter 4) suggests that the Parana CFB magmatism occurred within 3 Ma at about 132 Ma. The numerous alkalic complexes which intrude the continental margins of southern Brazil and Namibia have yielded K—Ar ages of between 65 and 140 Ma (Ulbrich and Gomes, 1981; Marsh, 1973; Erlank et al., 1984). There is therefore no clear evidence for any magmatism in this region prior to the onset of continental rifting at 148 Ma. As discussed above, there is good reason to believe that the Tristan plume did exist prior to 148 Ma, but the absence of any magmatism during this period cannot be taken as conclusive evidence for an anhydrous MBL, because of the relatively small melt volumes involved. Further constraints can be placed upon the nature of the source of these CFB and the role of water during the melting process, by considering the major element compositions of the Parana flood basalts (section 5.6.1).

5.6 The major element composition of decompression melts

M&B used the results of experimental melting studies to parameterise the major element composition of the melts produced during decompression melting, and to calculate the instantaneous melt composition at any particular depth, assuming that the melt remains in equilibrium with the residue until extraction (batch melting). The average composition of the melt erupted at the surface is a complicated function of the instantaneous melt compositions produced at different depths; 'real' magmas are likely to represent mixtures of melts from different levels in the melting column. The instantaneous melt compositions were therefore used to calculate the point average composition (the average composition of all the melt generated from a particular element of solid as the temperature increases at constant depth),

and the point and depth average composition (the weighted average of the point averages over the entire melting region).

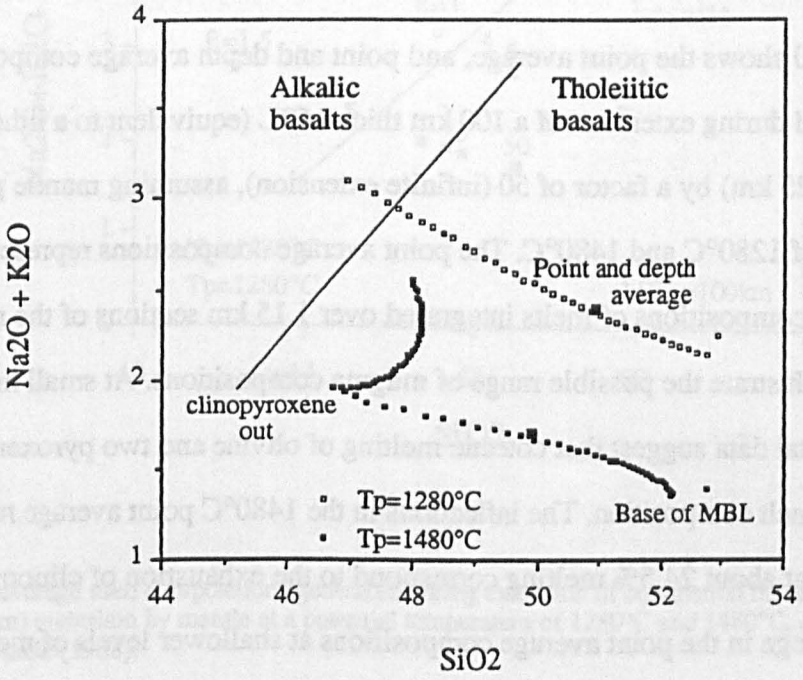

Fig. 5.10
Major element compositions of decompression melts generated during extension of continental lithosphere (MBL thickness=100 km) underlain by mantle at potential temperatures of 1280°C and 1480°C. The point average compositions represent the average compositions of the instantaneous melts integrated over small (1.15 km) sections of the melting column. The point and depth average compositions represent the weighted average of all melt generated during extension. The decompression melt compositions were calculated using McKenzie and Bickle's (1988) parameterisation, and the boundary between tholeiitic and alkalic basalts is taken from Cox et al. (1979).

M&B showed that the point average compositions of the melts produced during decompression melting beneath a ridge axis, assuming a mantle potential temperature of 1280°C, are very similar to the compositions of the least evolved glasses recovered from mid-ocean ridges. In addition, the observed variations in the major element geochemistry of MORB due to variations in the potential temperature of the upper mantle (Klein and Langmuir, 1987) are similar to those predicted by the parameterisation. In the mantle, less than about 3% melt is likely to be in contact with the residue at any time (Ahern and Turcotte, 1979) and during extension, magma generation therefore probably occurs by a fractional melting process. The M&B parameterisation is based upon experimental equilibrium (batch) melt compositions. However, the similarity between the observed and calculated melt compositions suggests that the major element composition of the melts

cannot be very sensitive to the fluid dynamics of the melting process, and that the parameterisation is a useful approach, at least for the case of decompression melting at an ocean ridge.

Fig. 5.10 shows the point average, and point and depth average compositions of melts produced during extension of a 100 km thick MBL (equivalent to a lithosphere thickness of 125 km) by a factor of 50 (infinite extension), assuming mantle potential temperatures of 1280°C and 1480°C. The point average compositions represent the instantaneous compositions of melts integrated over 1.15 km sections of the melting column, and illustrate the possible range of magma compositions. At small melt fractions, the experimental data suggest that cotectic melting of olivine and two pyroxenes will dominate the melt composition. The inflections in the 1480°C point average melt compositions at about 24.5% melting correspond to the exhaustion of clinopyroxene, and the abrupt change in the point average compositions at shallower levels of melting are the result of the variations in the temperature distribution at the base of the lithosphere. Note that at a potential temperature of 1280°C, the clinopyroxene in the source peridotite is not exhausted.

Assuming a 'normal' mantle potential temperature of 1280°C, then for an initial MBL thickness of 100 km, magma is only produced when the stretching factor β exceeds a value of about 2.75. The initial melts are derived from relatively small degrees of melting at depth, and are predicted to have the composition of alkali basalt. If continental rifting takes place above mantle at the elevated temperatures associated with a mantle plume (T_p=1480°C), then for a MBL thickness of 100 km the onset of silicate melting occurs at β=1.21, and the melts have the characteristics of alkali basalt. When β exceeds 2, the point and depth average crosses into the olivine tholeiite field (fig. 5.11), and at still higher values of β, the melts become picritic. Thus the effect of lower values of β, and greater MBL thicknesses is that the point and depth average melt composition becomes more alkalic, for a given value of the mantle potential temperature. At lower T_p, the point and depth average compositions are shifted to higher values of Na_2O+K_2O (fig. 5.11).

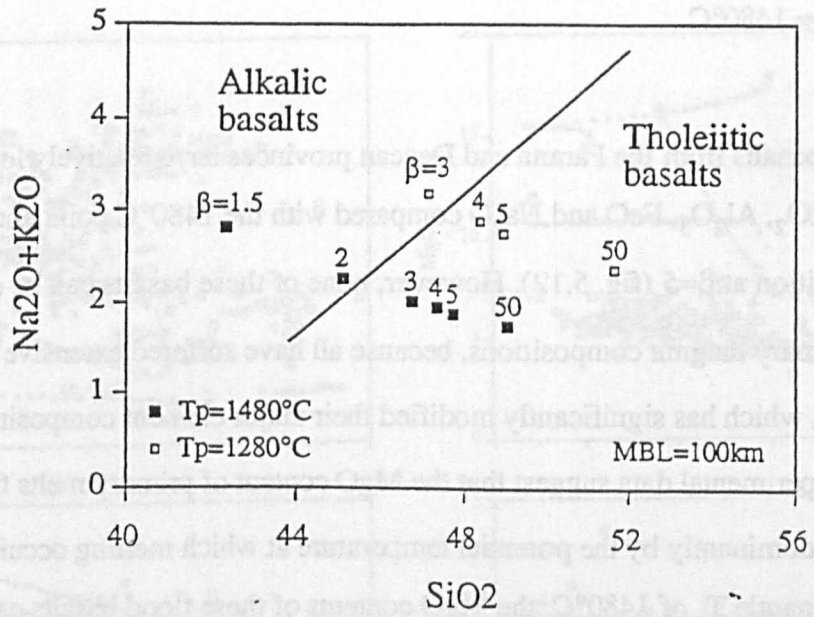

Fig. 5.11
Point and depth average melt compositions generated during extension of continental lithosphere (MBL thickness=100 km) underlain by mantle at a potential temperature of 1280°C and 1480°C. Adapted from McKenzie and Bickle (1988).

5.6.1 Major element geochemistry of the Parana-Etendeka flood basalts

This section will briefly compare the major element geochemistry of flood basalts and related intrusive rocks from the Parana, Deccan and Tasmanian provinces with melt compositions calculated using the M&B parameterisation. The theoretical melt compositions produced by adiabatic decompression melting by extension of a 100 km thick MBL by a factor of 5, assuming a mantle potential temperature of (a) 1280°C, (b) 1480°C were calculated after the method of McKenzie and Bickle (1988), using parameterisation (a) of Watson and McKenzie (1991).

Note that the 1480°C point and depth average melt composition was calculated assuming β=5. Recent backstripped borehole data (Chang et al., 1992) from the Santos and Campos Basins show that although the value of β approaches 6—6.5 at the edge of the Brazilian continental shelf, it is considerably less than 5 over much of the continental margin. At lower values of β, the point and depth average melt composition will have a significantly lower SiO_2 content, because melting is less extensive, and because the melting region is confined to greater depth by the overlying lithosphere. The 1480°C point and depth average composition at β=5 therefore represents an upper limit upon the SiO_2 content (and a

lower limit upon the CaO and Al_2O_3 content) of the magmas generated by decompression melting at T_p= 1480°C.

Flood basalts from the Parana and Deccan provinces have relatively low MgO, and high SiO_2, TiO_2, Al_2O_3, FeO and Na_2O compared with the 1480°C point and depth average melt composition at β=5 (fig. 5.12). However, none of these basalts can be considered to represent primary magma compositions, because all have suffered extensive low pressure fractionation, which has significantly modified their major element compositions.

The experimental data suggest that the MgO content of primary melts from the mantle is controlled dominantly by the potential temperature at which melting occurs (fig. 5.12). Assuming a mantle T_p of 1480°C, the MgO contents of these flood basalts can therefore be used to estimate the amount of fractionation that they have undergone, and this approach suggests that even the least evolved samples have undergone at least 20—30% fractionation.

Shown for reference on fig. 5.12 is a model crystallisation path calculated for the 1480°C point and depth average melt composition, using the program CHAOS of Nielsen (1989). This program attempts to model the major element evolution of a melt during low pressure (1 atmosphere) fractional crystallisation, and uses equilibrium mineral compositions and phase relation constraints from experimental data from the literature. The crystallisation path illustrates the effect of 20% fractionation of olivine, followed by a further 25% fractionation of olivine, clinopyroxene and plagioclase. The latter two minerals dominate the fractionating assemblage in the later stages of fractionation. Whilst most CFB have probably undergone some high pressure fractionation deep within the crust, the 1 atmosphere model fractionation path does illustrate that crystal fractionation cannot account for the relatively high TiO_2 and Na_2O contents of many of these basalts (fig. 5.12), which suggests that the source material was enriched in these elements. Cox (1980) has shown that fractional crystallisation of olivine, clinopyroxene and plagioclase will tend to buffer the concentration of SiO_2 in the residual melt (see fig. 5.12). The high and variable SiO_2 contents of the Parana basalts are therefore difficult to explain in terms of crystal fractionation. Many of these rocks (including the Ponta Grossa dolerites, see Chapter 2) show no evidence of having undergone crustal level contamination (Peate, 1989), which

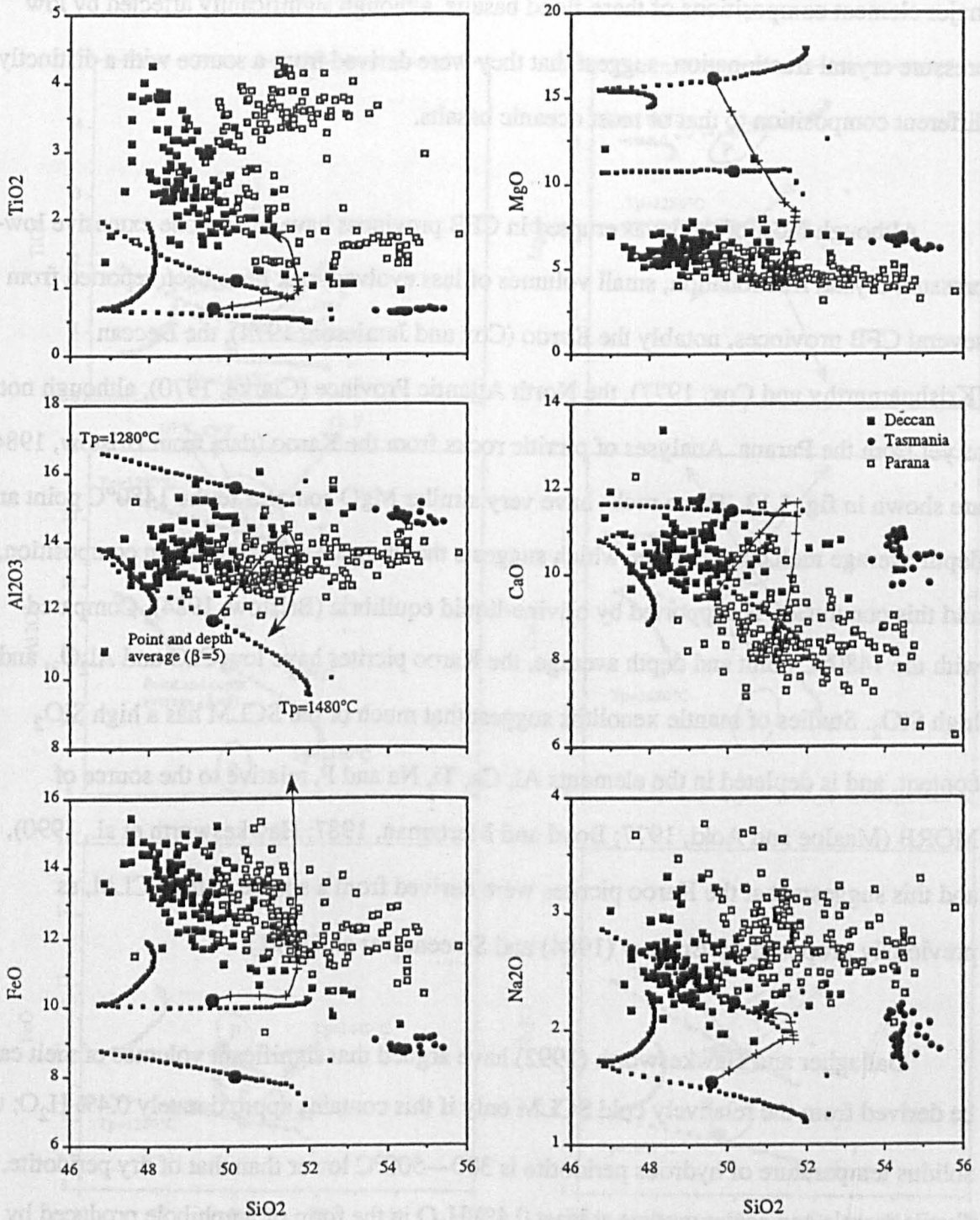

Fig. 5.12
Point average, and point and depth average melt compositions generated during extension of continental lithosphere underlain by mantle at a potential temperature of 1280°C and 1480°C. β=5, the initial MBL thickness is 100 km. Also shown are the major element compositions of flood basalts from the Deccan, Parana and Tasmanian CFB provinces. Data from Hergt et al. (1990), Peate (1989), Lightfoot (1985), and this study. A model 1 atmosphere crystal fractionation path calculated using the program CHAOS of Nielsen (1989) is shown for reference (see text).

implies that the high SiO_2 contents of these rocks were derived from their source. Thus the major element compositions of these flood basalts, although significantly affected by low pressure crystal fractionation, suggest that they were derived from a source with a distinctly different composition to that of most oceanic basalts.

Although most of the lavas erupted in CFB provinces have undergone extensive low-pressure crystal fractionation, small volumes of less evolved rock have been reported from several CFB provinces, notably the Karoo (Cox and Jamieson, 1974), the Deccan (Krishnamurthy and Cox, 1977), the North Atlantic Province (Clarke, 1970), although not as yet from the Parana. Analyses of picritic rocks from the Karoo (data from Bristow, 1984) are shown in fig. 5.13. These rocks have very similar MgO contents to the 1480°C point and depth average melt composition, which suggests that they are near primary in composition, and this conclusion is supported by olivine-liquid equilibria (Bristow, 1984). Compared with the 1480°C point and depth average, the Karoo picrites have low CaO and Al_2O_3, and high SiO_2. Studies of mantle xenoliths suggest that much of the SCLM has a high SiO_2 content, and is depleted in the elements Al, Ca, Ti, Na and P, relative to the source of MORB (Maaloe and Aoki, 1977; Boyd and Mertzman, 1987; Hawkesworth et al., 1990), and this suggests that the Karoo picrites were derived from a source in the SCLM, as previously proposed by Bristow (1984) and Sweeney et al. (1991).

Gallagher and Hawkesworth (1992) have argued that significant volumes of melt can be derived from the relatively cold SCLM only if this contains approximately 0.4% H_2O; the solidus temperature of hydrous peridotite is 300—500°C lower than that of dry peridotite. Fertile mantle can accommodate at least 0.4% H_2O in the form of amphibole produced by the hydration of clinopyroxene (Green, 1973; Olafsson and Eggler, 1983). Phlogopite, pargasite and K—richterite of primary origin have been identified in mantle xenoliths (Downes, 1987; Erlank et al., 1987), although Menzies (1992) concluded from a study of mantle xenoliths that much of the SCLM may be essentially anhydrous. Significant quantites of H_2O may also occur structurally bonded within crystal lattices; clinopyroxene may contain up to 500 ppm H_2O (Smyth et al., 1991). Jambon and Zimmermann (1990) reported

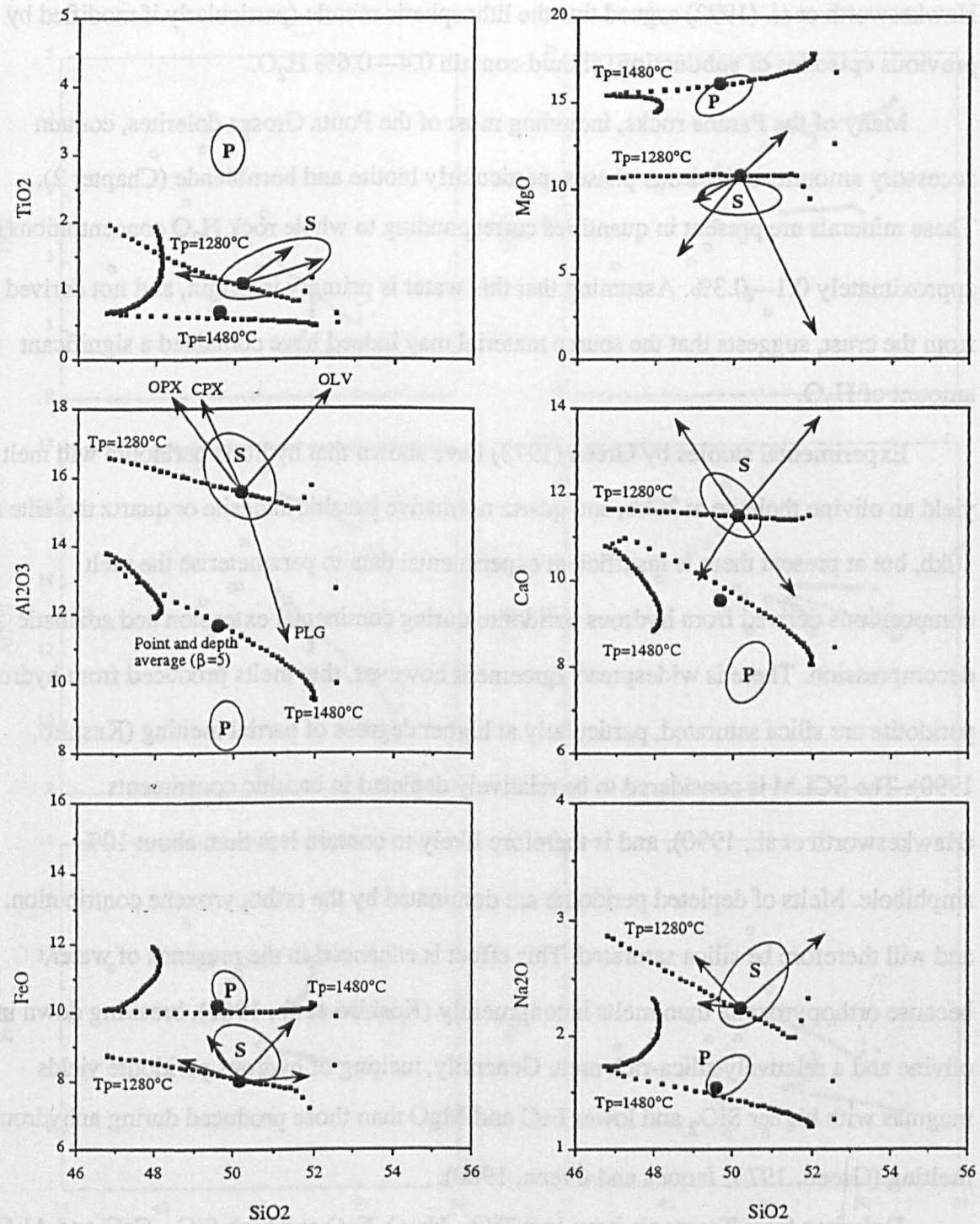

Fig. 5.13
Point average, and point and depth average melt compositions generated during extension of continental lithosphere underlain by mantle at potential temperatures of 1280°C and 1480°C. β=5, the initial MBL thickness is 100 km. Vectors represent the effect on the 1280°C point and depth average composition of 20% fractional crystallisation of olivine, orthopyroxene, clinopyroxene, and plagiolcase. Also shown are the major element compositions of tholeiitic basalts from the Mid Atlantic Ridge between 46 and 32°S ('S', data from Humphris et al., 1985), and picritic rocks from the Karoo CFB province ('P', data from Bristow, 1984). Note the similarity of the MORB data to the 1280°C point and depth average composition.

water contents of 1700—6000 ppm in MORB, and found that H_2O and K_2O contents were coupled due to the incompatible behaviour of H_2O. On the basis of these results, Hawkesworth et al. (1992) argued that the lithospheric mantle (particularly if modified by previous episodes of subduction) should contain 0.4—0.6% H_2O.

Many of the Parana rocks, including most of the Ponta Grossa dolerites, contain accessory amounts of hydrous phases, particularly biotite and hornblende (Chapter 2). These minerals are present in quantities corresponding to whole rock H_2O concentrations of approximately 0.1—0.3%. Assuming that this water is primary in origin, and not derived from the crust, suggests that the source material may indeed have contained a significant amount of H_2O.

Experimental studies by Green (1973) have shown that hydrous peridotite will melt to yield an olivine tholeiite at 20kb, and quartz normative basaltic andesite or quartz tholeiite at 10kb, but at present there is insufficient experimental data to parameterise the melt compositions derived from hydrous peridotite during continental extension and adiabatic decompression. There is widespread agreement however, that melts produced from hydrous peridotite are silica saturated, particularly at higher degrees of partial melting (Kushiro, 1990). The SCLM is considered to be relatively depleted in basaltic constituents (Hawkesworth et al., 1990), and is therefore likely to contain less than about 10% amphibole. Melts of depleted peridotite are dominated by the orthopyroxene contribution, and will therefore be silica saturated. This effect is enhanced in the presence of water, because orthopyroxene then melts incongruently (Kushiro et al., 1968), breaking down into olivine and a relatively silica-rich melt. Generally, melting of hydrous peridotite yields magmas with higher SiO_2 and lower FeO and MgO than those produced during anhydrous melting (Green, 1973; Jaques and Green, 1980).

Dolerites from Tasmania have low TiO_2, Na_2O, FeO and high SiO_2, CaO and Al_2O_3 relative to most other flood basalts (fig. 5.12). Although these rocks have undergone extensive low-pressure, open-system fractionation, Hergt et al. (1991) were able to demonstrate that the high SiO_2 and low FeO contents of these rocks were derived from their source, and argued that the dolerites were derived from a refractory peridotite source, and that melting occurred under hydrous conditions.

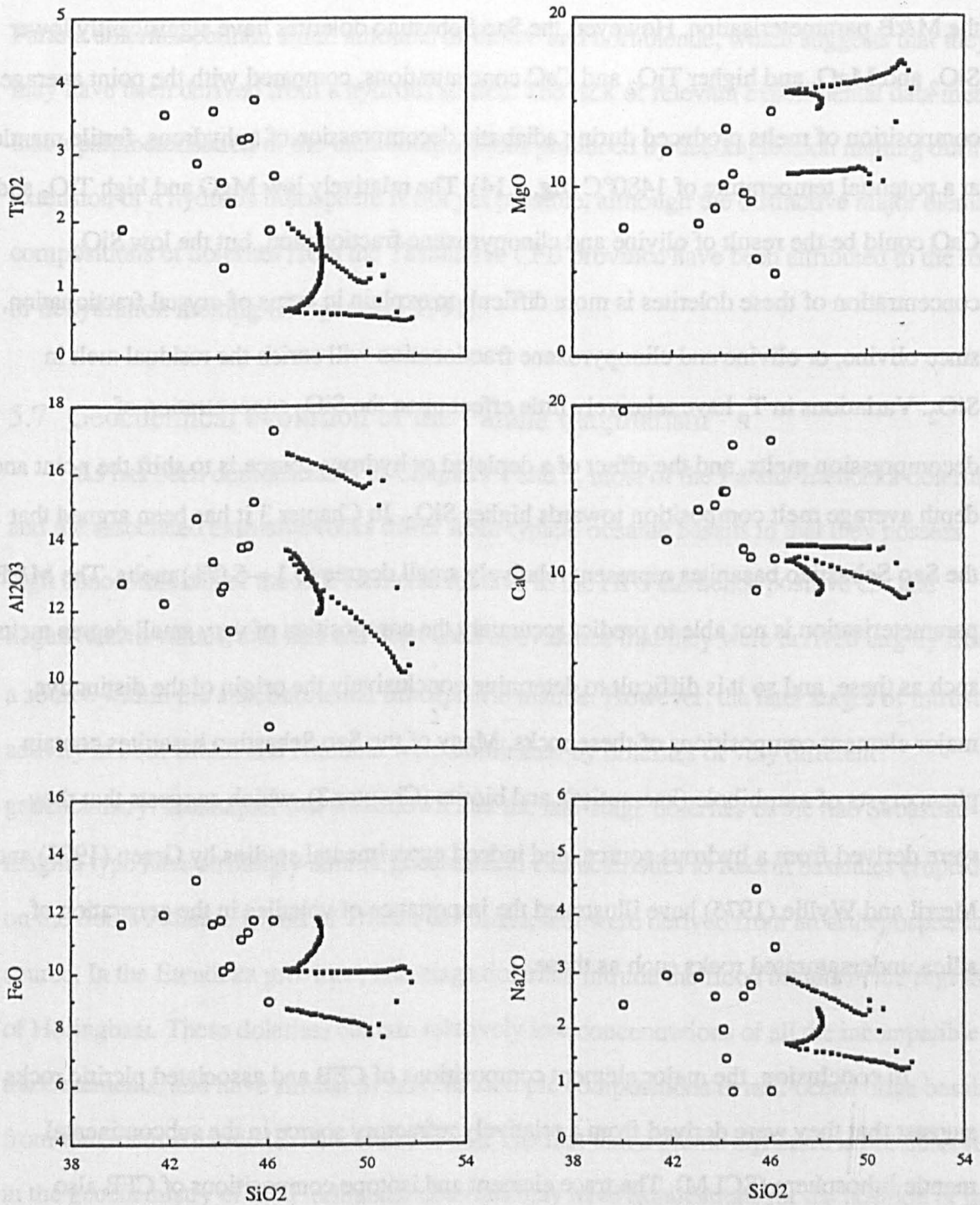

Fig. 5.14 ·
Predicted decompression melt compositions as in fig. 5.13, and the major element compositions of the Sao Sebastiao basanites of Sao Paulo State.

The late-stage dykes of the Sao Sebastiao magma type appear to have undergone very little fractionation, involving olivine and clinopyroxene only (Chapter 3), and so their major element compositions might be expected to be rather similar to that of melts calculated using the M&B parameterisation. However, the Sao Sebastiao dolerites have significantly lower SiO_2 and MgO, and higher TiO_2 and CaO concentrations, compared with the point average composition of melts produced during adiabatic decompression of anhydrous, fertile mantle at a potential temperature of 1480°C (fig. 5.14). The relatively low MgO and high TiO_2 and CaO could be the result of olivine and clinopyroxene fractionation, but the low SiO_2 concentration of these dolerites is more difficult to explain in terms of crystal fractionation, since olivine, or olivine and clinopyroxene fractionation will enrich the residual melt in SiO_2. Variations in T_p have relatively little effect upon the SiO_2 concentration of decompression melts, and the effect of a depleted or hydrous source is to shift the point and depth average melt composition towards higher SiO_2. In Chapter 3 it has been argued that the Sao Sebastiao basanites represent relatively small degree (0.1—5.0%) melts. The M&B parameterisation is not able to predict accurately the composition of very small degree melts such as these, and so it is difficult to determine conclusively the origin of the distinctive major element compositions of these rocks. Many of the Sao Sebastiao basanites contain phenocrysts of amphibole (kaersutite), and biotite (Chapter 3), which suggests that they were derived from a hydrous source, and indeed experimental studies by Green (1973) and Merril and Wyllie (1975) have illustrated the importance of volatiles in the generation of silica undersaturated rocks such as these.

In conclusion, the major element compositions of CFB and associated picritic rocks suggest that they were derived from a relatively refractory source in the subcontinental mantle lithosphere (SCLM). The trace element and isotope compositions of CFB also suggest that the SCLM contributes to flood basalt magmatism. Arndt and Christensen (1992) have proposed that major and trace elements are decoupled during melting, and that trace elements are scavanged from the SCLM by melts derived from the deeper mantle by complex reaction and mixing processes. In contrast, the major element compositions of CFB suggest that much of the melt is derived directly from the SCLM. In order for significant

quantities of melt to be derived from the relatively cold SCLM, the lowermost mantle lithosphere must contain ~0.4% H_2O (Gallagher and Hawkesworth, 1992). The evidence for significant concentrations of water in the SCLM is ambiguous, although many of the Parana dolerites contain small amounts of biotite and hornblende, which suggests that they may have been derived from a hydrous source. The lack of relevant experimental data means that a parameterisation of the melt compositions produced by decompression melting during extension of a hydrous lithosphere is not yet possible, although the distinctive major element compositions of dolerites from the Tasmanian CFB province have been attributed to the role of dehydration melting (Hergt et al., 1991).

5.7 Geochemical evolution of the Parana magmatism

As has been demonstrated in Chapters 2 and 3, most of the Parana-Etendeka dolerites and the associated extrusive rocks differ from typical oceanic basalts in that they possess high concentrations of the LIL elements relative to the HFS elements, positive εSr and negative εNd values, and this has been used as evidence that they were derived largely from a source within the subcontinental lithospheric mantle. However, the later stages of intrusive activity in both Brazil and Namibia were dominated by dolerites of very different geochemistry. In Chapter 3 it was shown that the late-stage dolerites of the Sao Sebastiao magma type have strikingly similar geochemical characteristics to Recent basanites erupted on the South Atlantic island of Tristan da Cunha, and were derived from an asthenospheric source. In the Etendeka province, late-stage dolerites intrude the flood basalts in the region of Horingbaai. These dolerites contain relatively low concentrations of all the incompatible trace elements, and have similar Sr and Nd isotopic compositions to mid-ocean ridge basalts from the South Atlantic (Erlank et al., 1984). The fact that a plume signature is not observed in the geochemistry of the Horingbaai dolerites may have implications for the position of the Tristan plume at that time.

Some of the youngest continental basalts erupted in the region of the Parana as a result of the development of the South Atlantic Ocean were emplaced on the continental shelves of South America and Africa. Basaltic lavas are widespread on the Brazilian continental shelf south of latitude 16°S (Chang et al., 1992). The earliest basalts erupted in the Santos and

Campos Basins are intercalated with terrigenous sediments and were erupted subaerially. Fodor et al. (1983) reported K—Ar ages for 13 samples of basalt drilled from the continental shelf within 200 km of the Brazilian coastline between latitudes 20 and 30°S. A subsequent geochemical study of the same samples by Fodor and Vetter (1983) revealed that many of these samples had undergone considerable alteration, and the accuracy of the ages that these authors obtained must therefore be viewed with caution. Of these samples, the oldest age (138.0 ± 3.5 Ma) was obtained for a rock recovered from drill site SPS-4A, 100 km offshore in the Santos Basin. Sites 1P1ES and N1ES, drilled in the coastline of the Campos Basin (fig. 5.8), penetrated terriginous sediments intercalated with basalts; the latter yielded K—Ar ages of between 130 and 112 Ma. An age of 104.9 ± 2.6 Ma was obtained for a highly spilitised sample, and basalts from drill sites further offshore in the Campos and

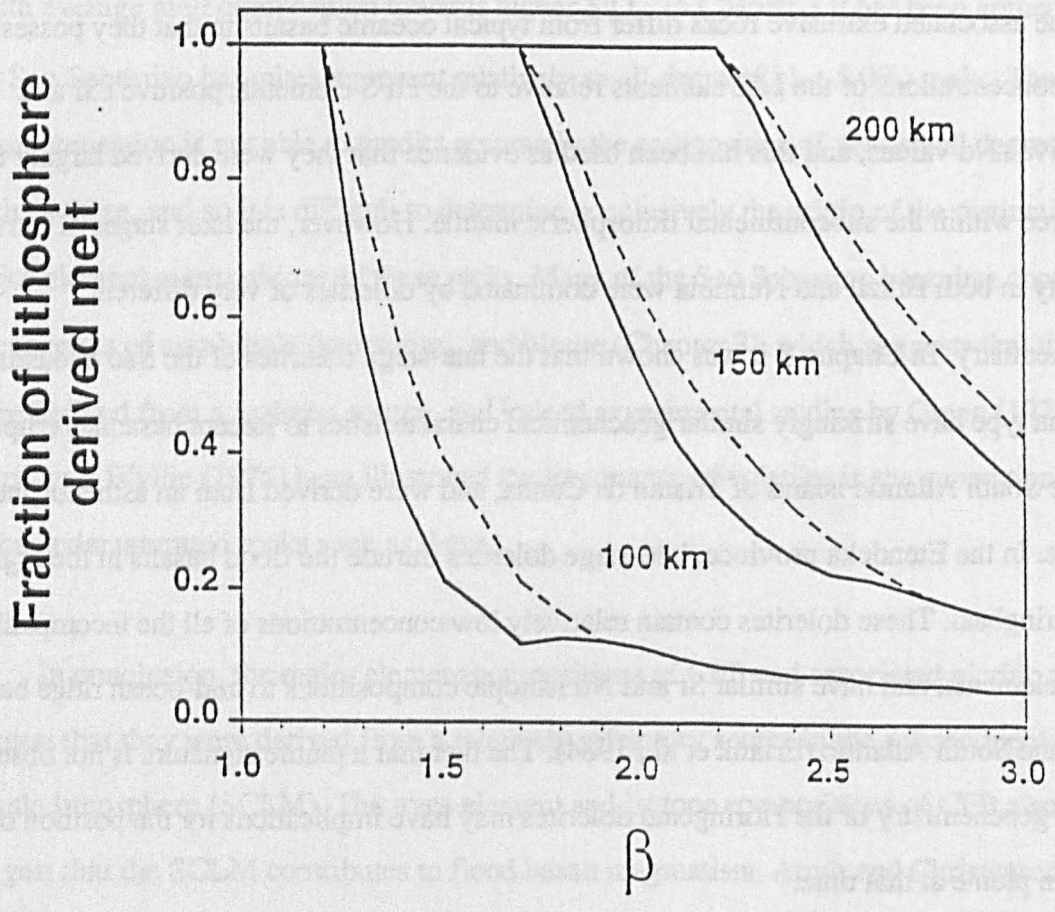

Fig. 5.15

The fraction of the total melt volume derived entirely from the MBL as a function of the stretching factor β, for various values of the MBL thicknesses. The solid lines include the effects of melt freezing, the dashed lines do not. The water content of the lithosphere is assumed to be 0.4%, and the potential temperature of the mantle at the base of the lithosphere is taken to be 1480°C. From Gallagher and Hawkesworth (1992).

Santos Basins yielded somewhat younger K—Ar ages of between 75 and 66 Ma. Fodor and Vetter (1983) showed that many of these samples were derived from a source with a similar trace element and isotope composition to the source of mid-ocean ridge basalts.

Thus there appears to have been a change in the location of the source region to the magmas during continental rifting in the South Atlantic. The earliest magmas were derived from a source in the lowermost lithosphere; later magmas were produced from a source in the convecting mantle immediately below the lithosphere. A similar situation has been recorded from other extension-related volcanic provinces. For example, Bradshaw et al. (1992) have demonstrated a similar change from lithosphere-sourced to asthenosphere-sourced magmatism in the southern Basin and Range, and the later stages of magmatic activity in both the Karoo and North Atlantic CFB provinces were also dominated by basalts and dolerites which were derived from a source in the convecting upper mantle (Erlank et al., 1984; Thompson, 1981).

The geochemical evolution of the Parana magmatism and other CFB provinces can be explained in terms of the extension related decompression melting model discussed earlier. Gallagher and Hawkesworth (1992) showed that much of the melt produced in the early stages of continental extension is derived from the subcontinental lithospheric mantle (provided that this contains sufficient H_2O), particularly if the lithosphere is relatively thick, and is underlain by mantle at an elevated potential temperature of 1480°C. During extension, (provided that melt can be extracted from the mantle more rapidly than extension proceeds), the composition of the magmas erupted at the surface will have a time-dependence. The earliest magmas are dominated by melt from the SCLM, but as the value of β increases, the amount of melt generated across the anhydrous peridotite solidus also increases as more of the sublithospheric upper mantle rises above its solidus (fig. 5.15). Assuming an initial MBL thickness of 100 km, a stretching factor of about 1.3 is sufficient for melts from the asthenosphere to dominate the geochemical signature of the melts erupted at the surface. If the MBL is initially 200 km thick, then the lithosphere must be thinned by over 200% (β=3) before an asthenospheric signature is seen in the magmas that are erupted at the surface.

5.8 Conclusions

The distribution and relative ages of the dolerites emplaced in the continental margins of the South Atlantic record a rapid northward migration of the magmatism. This, together with the fact that the initiation of rifting in the far South Atlantic occurred well away from the influence of the Tristan plume and before the eruption of the flood basalts, suggests that it was the rifting event, rather than plume initiation, that triggered CFB magmatism in this region. Thus the Parana-Etendeka flood basalt magmatism occurred not in response to a mantle plume initiation event, but instead was the result of decompression melting during rifting of South America from Africa above the abnormally hot mantle associated with the mantle plume that at present lies beneath the South Atlantic island of Tristan da Cunha. A decompression melting model can also account for the observed volume of magma associated with this CFB event, although the uncertainties in the estimates for T_p, β and h used in the calculations are large.

The major element composition of basalts and dolerites from the Parana and other CFB provinces have been compared with theoretical decompression melt compositions calculated using McKenzie and Bickle's (1988) parameterisation. The relatively low CaO and Al_2O_3 and high SiO_2 contents of picritic rocks from the Karoo suggests that they were derived fom a source in the SCLM. Although the major element compositions of most lavas from the Parana and Deccan flood basalt provinces have been strongly influenced by low pressure crystal fractionation, it is possible to see through these effects to some extent. The source of these basalts is required to have high TiO_2, SiO_2 and Na_2O, relative to the source of most oceanic basalts. Thus the major element compositions of flood basalts suggest that they were derived from a source in the SCLM. In order for significant volumes of melt to be derived from the relatively cold SCLM, the lowermost lithospheric mantle must contain approximately 0.4% H_2O in the form of amphibole produced by the hydration of clinopyroxene. Although the evidence for significant concentrations of H_2O in the SCLM is ambiguous, many of the Parana dolerites contain small amounts of biotite and amphibole, which suggests that they were indeed derived from a hydrous source. In addition, the distinctive major element compositions of dolerites from Tasmania have been attributed to the role of dehydration melting (Hergt et al., 1991).

The geochemical evolution of the Parana-Etendeka magmatism, from magmas that were derived largely from within the SCLM, to magmas that appear to have had a source in the convecting upper mantle, can also be explained in terms of decompression melting during extension of the lithosphere.

Chapter 6

Summary; flood basalt magmatism in the South Atlantic

The Parana-Etendeka flood basalt magmatism of South America and Africa was accompanied by intense intrusive activity. However, although the Parana flood basalts have been extensively studied, very few geochemical studies of the associated intrusive rocks have been carried out.

This thesis presents new major and trace element and Sr, Nd and Pb isotope data for dolerite samples collected from two regions of southern Brazil. The mineral chemistry of several of these dolerites has been investigated by electron microprobe, and selected samples have been dated using the laser ablation Ar—Ar technique. The aims of this research were;

(1) to constrain the geochemical variation within the dykes associated with the Parana-Etendeka flood basalt magamtism, and thus determine their relationship to the flood basalts,

(2) to investigate the petrogenesis of the Parana dolerites,

(3) to place precise constraints on the age of the Parana magmatism,

(4) to develop a geodynamic model for the origin of the Parana-Etendeka CFB province, which can account for the observed physical and chemical characteristics of the magmatism.

These aspects of the Parana intrusive magmatism are discussed in the following sections.

6.1 The geochemistry of the Parana dolerites

Dolerites from the Ponta Grossa region of Sao Paulo State are tholeiitic, and composed dominantly of augite, plagioclase, titanomagnetite ± olivine, pigeonite, quartz and apatite. Pyroxene geothermometry yields crystallisation temperatures of 1000—1200°C. These dolerites have very similar major and trace element compositions to the Pitanga and Paranapanema basalts which outcrop north of latitude 26°S, and are interpreted as feeders to these surface lava flows. Scarce rhyolite dykes also occur in the Ponta Grossa region, and analysis of a sample collected from one of these intrusions suggests that they fed the Ourinhos rhyolites which outcrop on the northeastern margin of the lava field.

Piccirillo et al. (1990) reported dolerite dykes from the Morro Vermelho region of southern Angola. Plate reconstructions suggest that these may be the African equivalent of the Ponta Grossa dykes (fig. 6.1), and this is supported by geochemical data for rhyolite samples collected from near Namibe (Alberti et al., 1992). These have very similar major and trace element and Sr isotope compositions to the Gurapuava rhyolites of the central Parana, which suggests that the associated dykes of southern Angola are indeed related to the Parana magmatism.

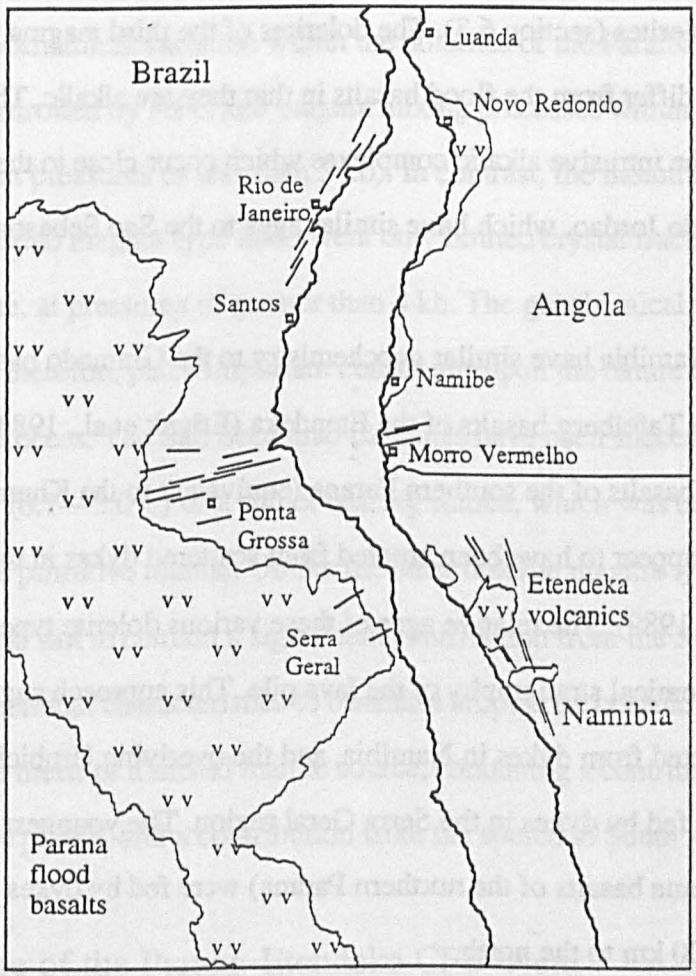

Fig. 6.1
Position of Africa with respect to South America at 150 Ma, showing the present day outcrop of the flood basalts (including the Mesozoic volcanic rocks of Angola), and associated dyke swarms.

The dykes of the coastal region of Sao Paulo State are divisible into three magma types, none of which are related by any simple petrogenetic process. Dolerites of the Paraiba

and Ubatuba magma types, whilst tholeiitic and broadly similar in terms of their geochemistry to many of the flood basalts, do not have extrusive equivalents in the lava pile. However, it is possible that these dykes fed the basaltic lavas which outcrop in northwestern Angola in the region of Novo Redondo; plate reconstructions suggest that these volcanics lay adjacent to Rio de Janiero State prior to continental breakup (fig. 6.1). At present, there are no geochemical data for the Novo Redondo volcanics, which could shed light upon their relationship to the Parana magmatism. Torquato and Amaral (1973) dated 16 basalt samples from flows in the Novo Redondo region using the K—Ar method. 10 of these samples yielded ages of between 124 and 145 Ma, similar to the Ar—Ar ages obtained from the Paraiba and Ubatuba dolerites (section 6.3). The dolerites of the third magma type (the Sao Sebastiao magma type) differ from the flood basalts in that they are alkalic. These rocks appear to be related to the intrusive alkalic complexes which occur close to the towns of Sao Sebastiao and Campos do Jordao, which have similar ages to the Sao Sebastiao samples (section 6.3).

The dolerites of Namibia have similar geochemistry to the Gramado basalts of the southern Parana and the Tafelberg basalts of the Etendeka (Erlank et al., 1984). The Esmeralda and Urubici basalts of the southern Parana (equivalent to the Khumib basalts of the northern Etendeka) appear to have been erupted from scattered dykes in the Serra Geral region of Brazil (Peate, 1989). The relative ages of these various dolerite types can be inferred from the geochemical stratigraphy of the lava pile. This approach suggests that the oldest basalts were erupted from dykes in Namibia, and the overlying Urubici and Esmeralda basalts were fed by dykes in the Serra Geral region. The youngest lava flows (the Pitanga and Paranapanema basalts of the northern Parana) were fed by dykes in the Ponta Grossa region, some 700 km to the north.

6.2 Petrogenesis of the Parana dolerites

The major element variation within the Ponta Grossa dolerites suggests that these have undergone some 70% fractional crystallisation of olivine, clinopyroxene, titanomagnetite and apatite. Least squares modelling of the fractionation process indicates that the dolerites were derived from a source which was enriched in the LRE and LIL elements with respect to

the source of MORB, and which had time integrated high Rb/Sr, U/Pb and low Sm/Nd values relative to the bulk earth. The samples define a $^{207}Pb/^{206}Pb$ array, which if interpreted as a secondary isochron, yields a source age of 2.1 Ga. This is very similar to the age of the lithosphere in this region of southern Brazil. There is no evidence that low pressure crystal fractionation was accompanied by crustal contamination, which suggests that the trace element and isotope signatures of these dolerites were derived largely from the subcontinental mantle. The Ponta Grossa dolerites do not represent parental magmas to the rhyolites which outcrop on the northeastern margin of the lava field, and which were also erupted from dykes in the Ponta Grossa region.

The geochemical variation within the dolerites of the Paraiba and Ubatuba magma types was controlled by AFC and magma mixing processes within magma chambers in the upper crust (at pressures of less than 5 kb). In contrast, the basanites and picritic dolerites of the Sao Sebastiao magma type underwent only limited crystal fractionation of olivine and clinopyroxene, at pressures of greater than 4 kb. The geochemical variation within these dolerites can therefore place important constraints upon the nature of the mantle source and the melting process. The Sao Sebastiao basanites have been successfully modelled as small degree melts (0.1—5.0%) of a spinel bearing source, which was enriched in the LREE relative to the primitive mantle. Unlike the other dolerite magma types, the Sao Sebastiao samples appear not to contain a significant contribution from the SCLM, and have very similar geochemical characteristics to basanites erupted on oceanic islands. They are interpreted as melts of a mixed mantle source, containing a contribution from the Tristan da Cunha mantle plume, and a contribution from the source to South Altantic MORB.

6.3 The age of the Parana-Etendeka CFB event

Selected samples of each of these magma types have been dated using the laser ablation Ar—Ar technique. The relatively coarse crystal size of the dolerites make them more suitable than the overlying basalts for dating by this technique, because argon can be released from individual crystals using the laser.

The dykes of the Ponta Grossa region appear to have fed the basalt flows of the Pitanga and Paranapanema magma types of the northern Parana. The geochemical

stratigraphy of the lava pile (Peate et al., 1992) implies that these were the last magma types to have been erupted, and that the age of the Ponta Grossa dolerites therefore places a lower limit upon the age of the Parana magmatism. Samples MR-899, MR-8930, MR-8917 (Paranapanema magma type), and MR-8928 (Pitanga magma type) yielded isochron ages of 131.2 ± 0.5, 133.9 ± 2.5, 130.4 ± 2.9 and 134.1 ± 1.3 Ma respectively. The Paranapanema basalts lie at a slightly higher stratigraphic level than the Pitanga basalts, and this is consistent with the Ar—Ar data, in that the Pitanga dolerite analysed here is significantly older than sample MR-899, but its age is within error of the ages obtained from samples MR-8917 and MR-8930 (fig. 6.2).

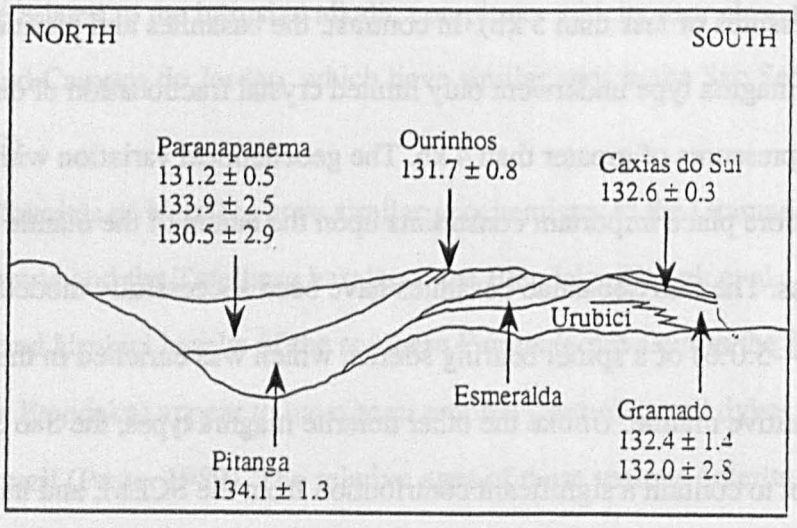

Fig. 6.2
Schematic north—south section through the Parana lava field at 52°W, showing the stratigraphical relationships between the samples which have been dated by the Ar—Ar method (data from Hawkesworth et al., 1992; Renne et al., 1992b, and this study).

An intrusive equivalent of the Ourinhos rhyolites of the Ponta Grossa region yielded an age of 131.7 ± 0.8 Ma. This is consistent with the stratigraphic position of these rhyolites relative to the basalts of the northern Parana as inferred from borehole data, which indicate that the rhyolites lie towards the top of the Pitanga unit.

Two basalt samples of the Gramado magma type collected from near the base of the lava pile in the southern Parana were dated in an earlier study by Hawkesworth et al.

(1992), who obtained Ar—Ar isochron ages of 132.4 ± 1.4 and 132.0 ± 2.8. These ages, together with the new data, imply that the entire Parana magmatism occurred within a period of about 3 Ma, at between 131 and 134 Ma. This is consistent with recent Ar—Ar ages obtained for rocks from the Parana by Renne et al. (1992b). These authors dated whole rock samples and plagioclase separates from the SM, CV, TA and GB sections, using the laser stepped heating technique. The ages obtained from these samples all lay between 131 and 133 Ma. Previous geochemical work by Peate (1989) in this area has shown that the basalts from these sections belong to the Gramado, Urubici and Esmeralda magma types, and thus Renne et al.'s (1992b) data should be regarded as an upper limit upon the age of the Parana magmatism.

The Ar—Ar data contrast with previous dating studies of the Parana basalts carried out using the K—Ar method, which have yielded a wide range of apparent ages of between 120 and 140 Ma. The Ar—Ar data reveal that most of the Parana dolerites contain a significant amount of excess ^{40}Ar, derived from the basement rocks and incorporated into the samples during crystallisation, and this is the reason for the wide range of apparent K—Ar ages.

Many of the dolerites of Sao Paulo State yield similar ages to the flood basalts to the west. The isochron ages obtained from plagioclase separates from samples MR-8957 and MR-8959, which belong to the Ubatuba magma type, are within error (130.7 ± 1.3 and 129.4 ± 0.6 Ma) respectively), and similar to the age of 130.2 ± 1.6 Ma obtained from the groundmass material of sample MR-8965. A plagioclase separate from sample MR-8954, and a whole-rock fragment of sample MR-8951 yielded somewhat older ages of 134.1 ± 1.3 and 133.1 ± 0.9 Ma respectively. However, some of the apparent age range within these samples has been shown to be the result of loss of radiogenic ^{40}Ar during plagioclase sericitisation. A sample of the Paraiba magma type yielded an age of 133.3 ± 1.7 Ma. Therefore, although the Paraiba and Ubatuba dolerites do not have extrusive equivalents in the lava pile, they were intruded at approximately the same time as the flood basalts were being erupted to the west.

In contrast, a much younger age of 80.9 ± 0.4 Ma was obtained for a biotite separate from a sample of the Sao Sebastiao magma type. These samples therefore appear to be unrelated to the flood basalt magmatism, but have very similar ages to the nearby alkalic intrusive complexes of Sao Sebastiao and Campos do Jordao, which have been dated by the K—Ar method at approximately 81 and 80 Ma respectively (Melcher and Melcher, 1972; Amaral et al., 1967).

6.4 Melt generation and flood basalt magmatism in the South Atlantic

The separation of South America from Africa was one stage in the breakup of the Mesozoic supercontinent of Gondwana. Continental rifting initiated in the extreme south at about 145—155 Ma, and backstripped sediment profiles suggest that extension in the Santos and Campos Basins on the continental margins of southern Brazil began at around 148 Ma. Plate reconstructions place the mantle plume that is at present beneath the South Atlantic island of Tristan da Cunha in the region of the Parana at the time of rifting. There was thus a close association in space and time between CFB magmatism, continental rifting, and mantle plume activity in the South Atlantic.

The oldest flood basalts were erupted from dykes in Namibia and the Serra Geral region of southern Brazil at around 134 Ma. Rifting and magmatism migrated rapidly northwards, and the youngest basalts of the lava field were fed by dykes in the Ponta Grossa region of Parana State approximately 3 Ma later. This northward migration of both magmatism and extension, and the fact that rifting initiated in the extreme south, suggests that the Parana-Etendeka CFB represent decompression melts generated during passive rifting above the abnormally hot mantle associated with the Tristan da Cunha plume. Magmatism and extension did not occur in response to a mantle plume initiation event, as has been proposed by Richards et al. (1989). The total volume of magma emplaced in or on the upper crust during the Parana-Etendeka CFB event was of the order of 1.5—2.0 x 10^6 km^6. The intensity of the magmatism in this region of the South Atlantic is attributed to the anomalously high mantle potential temperatures associated with the Tristan plume. Melt was generated during adiabatic decompression as a result of continental rifting, and calculations

show that this process can account for the observed volume of magma erupted in this continental flood basalt event.

The trace element and isotope compositions of many of the Parana dolerites has been shown to be dominated by a contribution from the subcontinental lithospheric mantle (Chapters 2 and 3). It has generally been thought that during lithospheric extension and decompression melting, much of the melt is derived from beneath the mechanical boundary layer, and that the distinctive trace element and isotope signatures of CFB are derived from the SCLM by complex melt reaction and mixing processes (Arndt and Christensen, 1992). However, by comparing the major element compositions of CFB with the predicted compositions of decompression melts at a mantle potential temperature of 1480°C calculated using McKenzie and Bickle's (1988) parameterisation, it has been demonstrated that much of the melt is derived directly from the mantle lithosphere. Gallagher and Hawkesworth (1992) have shown that if the lithosphere contains approximately 0.4% H_2O in the form of amphibole produced by the hydration of clinopyroxene, then its solidus temperature will be 300—500°C lower than for dry peridotite, and significant volumes of melt can thus be derived from the lowermost lithosphere during extension. Although the evidence for such high concentrations of H_2O in the SCLM is ambiguous, many of the Parana dolerites contain significant quantities of biotite and amphibole, which suggests that they may have been derived from a hydrous source. At present, there is insufficient experimental data for a parameterisation of the melt compositions derived from hydrous peridotite during decompression melting to be carried out. However, Hergt et al. (1991) have argued that the distinctive major element compositions of the Mesozoic dolerites of Tasmania probably reflect the role of H_2O in their source.

Gallagher and Hawkesworth (1992) have shown that the melt produced during continental extension is initially dominated by the contribution from the SCLM. With progressive extension, the contribution to the total melt volume by the anhydrous convecting mantle beneath the MBL becomes more important, and such a transition from lithosphere sourced to asthenosphere sourced magmatism is in fact seen in the Parana-Etendeka CFB

province. The later stages of intrusive activity in both Brazil and Namibia were dominated by dolerites which were derived largely from a source beneath the MBL, in the convecting mantle. The Horingbaai dolerites of the southern Etendeka have very similar trace element and radiogenic isotope compositions to basalts erupted at mid ocean ridges, whilst the Sao Sebastiao basanites and picritic dolerites of the northeastern Parana contain a contribution from the mantle plume that is at present beneath the South Atlantic island of Tristan da Cunha.

The oldest oceanic crust off the coast of southern Brazil has been dated at 127—131 Ma. Following the development of the Mid Atlantic Ridge, Africa and South America have rotated into their present positions relative to the Tristan da Cunha mantle plume. The Walvis Ridge and the Rio Grande Rise represent the expression of the Tristan plume beneath the oceanic lithosphere during this period.

References

Ahern J. L., Turcotte D. L. (1979). Magma migration beneath an ocean ridge. *Earth Plan. Sci. Lett.* **45**, 115—122.

Alberti A., Piccirillo E. M., Bellieni G., Civetta L., Comin-Chiaramonti P., Morais E. A. (1992). Mesozoic acid volcanism from southern Angola: Petrology, Sr—Nd isotope characteristics and correlation with the acid stratoid volcanic suites of the Parana basin (southeastern Brazil). *Eur. J. Min.* **4**, 597—604.

Allegre C. J., Treuil M., Minster J-F., Minster J. B., Alberede F. (1977). Systematic use of trace elements in igneous processes. 1: fractional crystallisation processes in volcanic suites. *Contrib. Min. Pet.* **60**, 57—75.

Allsopp H. L., Matton W. I., Bristow J. W., Erlank A. J. (1984). Rb—Sr geochronology of Karoo felsic volcanics. *Spec. Publ. Geol. Soc. S. Afr.* **13**, 273—280.

Almeida F. F. M., Hasui Y. (1984). In: 'O PreCambriano do Brasil' ed. Edgard Blüicher Ltda., Sao Paulo, 187—368.

Amaral G., Cordani U. G., Kawashita K., Reynolds J. H. (1966). Potassium—argon dating of basaltic rocks from southern Brazil. *Geochim. Cosmo. Acta.* **30**, 159—189.

Araujo H. J. T. de, Santos Neto A. de, Trinidade C. A. H., Pinto J. C. de A., Montalvao R. M. G. de, Dourado T. D. de C., Palmeira R. C. de B., Tassinari C. C. G (1982). Geologia. In: Projeto RADAMBRASIL, Folha SF 21, Campo Grande. Lev. Rec. Nat. **28**, 23—124.

Arndt N. T., Christensen U. (1992). The role of lithospheric mantle in continental flood volcanism: thermal and geochemical constraints. *J. Geophys. Res.* **97**, 10967—10981.

Arndt N. T., Goldstein S. L. (1987). Use and abuse of crust-formation ages. *Geology* **15**, 893—895.

Austin J. A., Uchapi E. (1982). Continental-oceanic transition off southwest Africa. *Am. Ass. Pet. Geol. Bull.* **66**, 1328—1347.

Baksi A. K., Farrar E. (1991). $^{40}Ar/^{39}Ar$ dating of the Siberian Traps, USSR: evaluation of the ages of the two major extinction events relative to episodes of flood basalt volcanism in the USSR and the Deccan Traps, India. *Geology* **19**, 461—464.

Baksi A. K., Fodor R. V., Farrar E. (1991). Preliminary results of $^{40}Ar/^{39}Ar$ dating studies on rocks from the Serra Geral flood basalt province and the Brazilian continental margin. Abstract, *EOS* **72**, 300.

Basei M. A. S. (1985). O Cinturao Dom Feliciano em Santa Catarina. PhD thesis, IG/USP, Sao Paulo, 185pp.

Basei M. A. S., Siga O., de Vasconcellos J. P. B. C. (1987). Geometria e cronologia dos dobramentos superpostos no Grupo Brusque, SC. In: Simp. Sul-Bras. Geol. **3**, Curitiba (1987): SBG Nucleo Rio Grande do Sul **2**, 707—724.

Beane J. E., Turner C. A., Hooper P. R., Subbarao K. V., Walsh J. N. (1986). Stratigraphy, composition and form of the Deccan basalts, Western Ghats, India. *Bull. Volcanol.* **48**, 61—83.

Bellieni G., Brotzu P., Comin-Chiaramonti P., Ernesto M., Melfi A. J., Pacca I. G., Piccirillo E. M. (1984). Flood basalt to rhyolite suites in the southern Parana plateau (Brazil): palaeomagnetism, petrogenesis and geodynamic implication. *J. Pet.* **25**, 579—618.

Bellieni G., Brotzu P., Comin-Chiaramonti P., Ernesto M., Melfi A. J., Pacca I. G., Piccirillo E. M., Stolfa D. (1983). Petrological and palaeomagnetic data on the plateau basalt to rhyolite sequences of the southern Parana basin (Brazil). *An. Acad. Bras. Cienc.* **55**, 355—383.

Bellieni G., Comin-Chiaramonti P., Marques L. S., Martinez L. A., Melfi A. J., Nardy A. J. R., Piccirillo E. M., Stolfa D. (1986). Continental flood basalts from the central-western regions of the Parana plateau (Paraguay and Argentina): petrology and petrogenetic aspects. *N. Jb. Miner. Abh.* **154**, 111—139.

Bellieni G., Comin-Chiaramonti P., Marques L. S., Melfi A. J., Nardy A. J. R., Papatrechas C., Piccirillo E. M., Roisenberg A., Stolfa D. (1986). Petrogenetic aspects of acid and basaltic lavas from the Parana plateau (Brazil): mineralogical and petrochemical relationships. *J. Pet.* **27**, 915—944.

Bellieni G., Comin-Chiaramonti P., Marques L. S., Melfi A. J., Piccirillo E. M., Nardy A. J. R., Roisenberg A., (1984). High- and low-Ti flood basalts from the Parana plateau (Brazil): petrology and geochemical aspects bearing on their mantle origin. *N. Jb. Miner. Abh.* **150**, 273—306.

Bellieni G., Comin-Chiaramonti P., Marques L. S., Melfi A. J., Piccirillo E. M., Stolfa D. (1984). Low pressure evolution of basalt sills from boreholes in the Parana basin. *Tsch. Min. Pet. Mit.* **33**, 25—47.

Berger G. W., York D. (1981). Geothermometry from $^{40}Ar/^{39}Ar$ dating experiments. *Geochim. Cosmo. Acta.* **45**, 795—811.

Betton P. J., Cox K. G. (1979). Production of rhyolites at continental margins: an example from the Lebombo Monocline. *Abstr. Geocongress 1979, Geol. Soc. S. Africa*, 29—32.

Biondi J. C. (1983). Mapa geologico da area do embasamento do Estado do Parana, escala 1:250,000. *Mineropar, Secretaria da Industria e Comercio do Parana.*

Bitschene P. R., (1987). Mesozoischer und Kanozoischer anorogener magmatismus in Ostparaguay: arbeiten zur geologie und petrologie zweier alkali provinzen. PhD thesis, Univ. Heidelberg, 318pp.

Bowen N. L. (1928). The evolution of the igneous rocks. Princeton Univ. Press, 322pp.

Boyd F. R., Mertzman S. A. (1987). Composition and structure of the Kaapvaal lithosphere, South Africa. In 'Magmatic processes: physiochemical principles' ed. B. O. Mysen. *Geochem. Soc. Spec. Publ.* **1**, 13—24.

Bradshaw T. K., Hawkesworth C. J., Gallagher K. (1993). Basaltic volcanism in the southern Basin and Range: no role for a mantle plume? *Earth Plan. Sci. Lett.* (in press).

Bristow J. W. (1984). Picritic rocks of the north Lebombo and southeast Zimbabwe. *Spec. Publ. Geol. Soc. S. Afr.* **13**, 105—123.

Cadogan P. H. (1977). Palaeoatmospheric argon in Rhynie chert. *Nature* **268**, 38—40.

Campbell I. H., Griffiths R. W. (1990). Implications of mantle plume structure for the evolution of flood basalts. *Earth Plan. Sci. Lett.* **99**, 79—93.

Cande S. C., LaBreque J. L., Haxby W. B. (1989). Plate kinematics of the South Atlantic: Chron 34 to present. *J. Geophys. Res.* **93**, 13479—13492.

Cantanzaro E. J., Murphy T. J., Shields W. R., Garner E. L. (1968). Absolute isotope abundance ratios of common, equal atom, and radiogenic lead isotopic standards. *J. Res. Nat. Bur. Stand. (US).* **72A**, 261—267.

Carter S. R., Evensen N. M., Hamilton P. J., O'Nions R. K. (1978). Nd and Sr isotopic evidence for crustal contamination of continental volcanics. *Science* **202**, 743—747.

Cerling T. E., Brown F. H., Bowman J. R. (1985). Low-temperature alteration of volcanic glass: hydration, Na, K, ^{18}O and Ar mobility. *Chem. Geol.* **52**, 281—293.

Chang H. K., Kowsmann R. O., Figueiredo A. M. F., Bender A. A. (1992). *Tectonophys.* **213**, 97—138.

Clarke D. B. (1970). Tertiary basalts of Baffin Bay: possible primary magmas from the mantle. *Rev. Geophys.* **2**, 35—88.

Class C., Goldstein S. L., Galer S. J. G. (1992). Plume tracks, evolving hotspot sources and continental flood basalts. *Abstract, Am. Geophys. Un.* 1992.

Class C., Goldstein S. L., Galer S. J. G., Weis D. (1991). Plume tracks, evolving hotspot sources and their young formation ages. *Abstract, Am. Geophys. Un.* 1991.

Cleverly R. W., Betton P. J., Bristow J. W. (1984). Geochemistry and petrogenesis of the Lebombo rhyolites. *Spec. Publ. Geol. Soc. S. Afr.* **13**, 171—194.

Cliff R. A., Baker P. E., Mateer N. J. (1991). Geochemistry of Inaccessible Island volcanics. *Chem. Geol.* **92**, 251—260.

Comin-Chiaramonti P., Gomes C. B., Piccirillo E. M., Rivalenti G. (1983). High TiO2 basaltic dikes in the coastline of Sao Paulo and Rio de Janeiro states (Brazil). *N. Jb. Miner. Abh.* **146**, 133—150.

Cordani U. G., Civetta L., Mantovani M. S. M., Petrini R., Kawashita K., Hawkesworth C. J., Taylor P., Longinelli A., Cavazzini G., Piccirillo E. M. (1988). Isotope geochemistry of flood volcanics from the Parana basin (Brazil). In: 'The Mesozoic flood volcanism of the Parana basin: petrogenetic and geophysical aspects' ed. E. M. Piccirillo, A. J. Melfi. *IAG-USP Press, Sao Paulo,* 157—178.

Cordani U. G., Sartori P. L., Kawashita K. (1980). Geoquimica dos isotopos de estroncio e a evolucao da atividade vulcanica na Bacia do Parana (Sul do Brasil) durante o Cretaceo. *An. Acad. Brasil. Cienc.* **52**, 811—818.

Courtillot V., Feraud G., Malaski H., Vandamme D., Moreau M. G., Besse J. (1988). Deccan flood basalts and the Cretaceous/Tertiary boundary. *Nature* **333**, 843—846.

Courtney R. C., White R. S. (1986). Anomalous heat flow and geoid across the Cape Verde Rise: evidence for dynamic support from a thermal plume in the mantle. *Geophys. J. Roy. Soc.* **87**, 815—867.

Cox K. G. (1980). A model for flood basalt vulcanism. *J. Pet.* **21**, 629—650.

Cox K. G. (1988). The Karoo Province. In 'Continental flood basalts' ed. J. D. McDougall, 239—271. Kluwer Academic Press.

Cox K. G., Bell J. D., Pankhurst R. J. (1979). The interpretation of igneous rocks. London, Allen and Unwin, 450pp.

Cox K. G., Hawkesworth C. J. (1985). Geochemical stratigraphy of the Deccan traps at Mahabaleshwar, Western Ghats, India, with implications for open system magmatic processes. *J. Pet.* **26**, 355—377.

Cox K. G., Jamieson B. G. (1974). The olivine-rich lavas of Nuanetsi: study of polybaric magmatic evolution. *J. Pet.* **15**, 269—301.

Creer K. M. (1962). Palaeomagnetism of the Serra Geral formation. *Geophys. J. R. Astron. Soc.* **7**, 1—22.

Creer K. M., Miller J. A., Smith A. G. (1965). Radiometric age of the Serra Geral formation. *Nature* **207**, 282—283.

Dalrymple G. B., Gromme C. S., White R. R. (1975). Potassium argon age and palaeomagnetism of diabase dykes in Liberia: initiation of central Atlantic rifting. *Geol. Soc. Am. Bull.* **86**, 399—411.

Damasceno E. C. (1966). Estudo preliminar dos diques de rochas basicas e ultrabasicas da regiao de Ubatuba, Estado de Sao Paulo. *An. Acad. bras. Cienc.* **38**, 293—304.

Deer W. A., Howie R. A., Zussman J. (1966). An introduction to the rock forming minerals. Longman.

DePaolo D. J. (1981)a. Nd isotopic studies: some new perspectives on Earth structure and evolution. *EOS* **62**, 137—140.

DePaolo D. J. (1981)b. Trace element and isotopic effects of combined wallrock assimilation and fractional crystallisation. *Earth Plan. Sci. Lett.* **53**, 189—202.

DePaolo D. J., Wasserburg G. H. (1976). Nd isotopic variations and petrogenetic models. *Geophys. Res. Lett.* **3**, 249—252.

Devey C. W., Lightfoot P. C. (1986). Volcanological and tectonic control of stratigraphy and structure in the western Deccan Traps. *Bull. Volcanol.* **48**, 195—207.

Devey C. W., Stephens W. E. (1991). Tholeiitic dykes in the Seychelles and the original spatial extent of the Deccan. *J. Geol. Soc. Lond.* **148**, 979—983.

Dickin A. P. (1981). Isotope geochemistry of Tertiary igneous rocks from the Isle of Skye, NW Scotland. *J. Pet.* **22**, 155—189.

Downes H. (1987). Relationship between geochemistry and texture type in spinel lherzolites, Massif Central and Languedoc, France. In : 'Mantle Xenoliths' ed. P. N. Nixon. JHohn Wiley and Sons, 125—134.

Duncan R. A. (1984). Age progressive volcanism in the New England Seamounts and the opening of the central Atlantic Ocean. *J. Geophys. Res.* **89**, 9980—9990.

Duncan R. A., Marsh J. S., Milner S. C., Erlank A. J. (1988). Distribution and petrogenesis of the basic rocks of the Etendeka formation of northwestern Namibia. *Ext. Abstr., Int. Conf.* 'Geochemical evolution of the continental crust' Pocos de Caldas (Brazil), 10—19.

Duncan R. A., Pyle D. G. (1988). Rapid eruption of the Deccan flood basalts at the Cretaceous/Tertiary boundary. *Nature* **333**, 841—843.

Dupre B., Allegre C. J. (1983). Pb—Sr isotope variation in Indian Ocean basalts and mixing phenomena. *Nature* **303**, 142—146.

Emery K. O., Uchapi E. (1984). The geology of the Atlantic Ocean. Springer-Verlag, New York, 1050pp.

Erlank A. J., Marsh J. S., Duncan A. R., Miller R. McG., Hawkesworth C. J., Betton P. J., Rex D. C. (1984). Geochemistry and petrogenesis of the Etendeka volcanic rocks from South West Africa/Namibia. *Spec. Publ. Geol. Soc. S. Afr.* **13**, 195—246.

Erlank A. J., Waters F. G., Hawkesworth C. J., Haggerty H. L., Allsopp R. S., Rickard R. S., Menzies M. A. (1987). Evidence for mantle metasomatism in peridotite nodules from

the Kimberly pipes, South Africa. In: 'Mantle metasomatism' ed. M. A. Menzies, C. J. Hawkesworth, Academic Press, London, 221—311.

Ernesto M., Hiodo F. Y., Pacca I. G. (1979). Estudo paleomagnetico de sequencia de derrames basalticos da formacao Serra Geral em Santa Catarina. *An. Acad. bras. Cienc.* **51**, 327—332.

Ernesto M., Pacca I. G. (1988). Palaeomagnetism of the Parana basin flood volcanics, southern Brazil. In: 'The Mesozoic flood volcanism of the Parana basin: petrogenetic and geophysical aspects' ed. E. M. Piccirillo, A. J. Melfi, IAG-USP Press, 229—255.

Fairchild T. R. (1984). Caution: an 'Ediacaran' or Early Cambrian age for the Corumba and Jacadigo Groups (SW Brazil) still requires definitive proof. In: *Abstracts, Intern. Geol. Congr. 27, Moscow IVGS* **1**, 38—39.

Feffeira F. J. F., Algarte J. P., Theodorovicz A., Momma R., Martins F. A. G., Tassinari C. G. C., Silva R. B., Rodriquez E. P., Coutinho J. M. V. (1987). A alcalina de Pariquera-Acu. *Atas do 6 Simp. Reg. Geol. Soc. Bras. Geol., Sao Paulo, Rio Claro* **1**, 159—171.

Feigenson M. D., Hofmann A. W., Spera F. J. (1983). Case studies on the origin of basalt II. The transition from tholeiitic to alkalic volcanism on Kohala volcano, Hawaii. *Contrib. Min. Pet.* **84**, 390—405.

Fisk M. R., Upton B. G. J., Ford C. E. (1988). Geochemical and experimental study of the genesis of magmas of Reunion Island, Indian Ocean. *J. Geophys. Res.* **93** 4933—4950.

Fodor R. V. (1987). Low- and high-TiO2 flood basalts of southern Brazil: origin from picritic parentage and a common mantle source. *Earth Plan. Sci. Lett.* **84**, 423—430.

Fodor R. V., Corwin C., Roisenberg A. (1985). Petrology of Serra Geral (Parana) continental flood basalts, southern Brazil: crustal contamination, source material, and South Atlantic magmatism. *Contrib. Min. Pet.* **91**, 54—65.

Fodor R. V., Corwin C., Sial A. N. (1985). Crustal signatures in the Serra Geral flood basalt province, southern Brazil: O and Sr isotope evidence. *Geology* **13**, 763—765.

Fodor R. V., McKee E. H., Asmus H. E. (1983). K—Ar ages and the opening of the South Atlantic Ocean: basaltic rock from the Brazilian margin. *Marine Geol.* **54**, M1—M8.

Fodor R. V., Vetter S. K. (1984). Rift-zone magmatism: petrology of basaltic rocks transitional from CFB to MORB, southeastern Brazil. *Contrib. Min. Pet.* **88**, 307—321.

Foucher J. P., lePichon X., Sibuet J. C. (1982). The ocean-continent transition in the uniform lithospheric stretching model: role of partial melting in the mantle. *Phil. Trans. Roy. Soc. Lond.* **A305**, 27—43.

Frey F. A., Green D. H., Roy S. D. (1978). Integrated models of basalt petrogenesis: a study of quartz thoeliites to olivine melilitites from southeastern Australia utilising geochemical and experimental petrological data. *J. Pet.* **19**, 463—513.

Gallagher K., Hawkesworth C. J. (1992). Dehydration melting and the generation of continental flood basalts. *Nature* **358**, 57—59.

Gasparini R., Mantovani M. S. M. (1979). Geochemistry of charnockites from Sao Paulo State, Brazil. *Earth Plan. Sci. Lett.* **42**, 311—320.

Gidskehaug A., Creer K. M., Mitchell J. G. (1975). Palaeomagnetism and K—Ar ages of the South West African basalts and their bearing on the timing of initial rifting of the South Atlantic Ocean. Geophys. *J. R. Astron. Soc.* **42**, 1—20.

Girardi V. A. V. (1976). Geologia e petrologia do complexo basico-ultrabasico de Pien, PR. *Rev. Bras. Geoc.* **6**, 109—124.

Girardi V. A. V., Cordani U. G., Candido A., Melfi A. J., Kawashita K. (1974). Geocronologia do complexo basico-ultrabasico Pre-Brasiliano de Pien, PR. *In: Congr. Bras. Geol. 28, Poto Alegre 1974, SBG* **2**, 532—533.

Giraud J. P., Onstott T. C. (1991). Application of $^{40}Ar/^{39}Ar$ laser probe and step heating techniques to the dating of diagenetic K feldspar overgrowths. *Geochim. Cosmo. Acta.* **55**, 3777—3793.

Green D. H. (1973). Experimental melting studies in a model of upper mantle compositions at high pressures under water saturated and water undersaturated conditions. *Earth Plan. Sci. Lett.* **9**, 37—53.

Griffiths R. W. (1986). The differing effects of compositional and thermal buoyancies on the evolution of mantle diapirs. *Phys. Earth Plan. Inter.* **43**, 261—273.

Griffiths R. W., Campbell I. H. (1990). Stirring and structure in mantle starting plumes. *Earth Plan. Sci. Lett.* **99**, 66—78.

Griffiths R. W., Campbell I. H. (1991). Interaction of plume heads with the Earth's surface and onset of small-scale convection. *J. Geophys. Res.* **96**, 18295—18310.

Guimaraes D. (1960). *Reports, Dept. Nac. Prod. Min.* **107**, 1—410.

Gurney J. J., Harte B. (1980). Chemical variations in upper mantle nodules from southern African kimberlites. *Phil. Trans. Roy. Soc. Lond.* **A297**, 273—293.

Harland W. B., Cox A. V., Llewellyn P. G., Pickton C. A. G., Smith A. G., Walters R. (1982). A geologic time scale. 131pp, Cambridge University Press.

Hart S. R. (1984). A large-scale isotope anomaly in the southern hemispere mantle. *Nature* **309**, 753—757.

Harte B. (1983). Mantle peridotites and processes-the kimberlite sample. In 'Continental basalts and mantle xenoliths' ed. C. J. Hawkesworth, M. J. Norry. Shiva Press, 46—91.

Hasui Y. (1982). The Mantiqueira province: Archean structure and Proterozoic evolution. *Rev. Bras. Geoc.* **12**, 167—171.

Hawkesworth C. J., Gallagher K., Kelley S., Mantovani M. S. M., Peate D. W., Regelous M., Rogers N. W. (1992). Parana magmatism and the opening of the South Atlantic. In 'Magmatism and the causes of continental breakup' ed. B. C. Storey, T. Alabaster, R. J. Pankhurst. *Geol. Soc. Lond. Spec. Publ.* **68**, 221—240.

Hawkesworth C. J., Kempton P. D., Rogers N. W., Ellam R. M., van Calsteren P. W. (1990). Continental mantle lithosphere, and shallow level enrichment processes in the Earth's mantle. *Earth Plan. Sci. Lett.* **96**, 256—268.

Hawkesworth C. J., Kramers J. D., Miller R. McG. (1981). Old model Nd ages in Namibian Pan-African rocks. *Nature* **289**, 278—282.

Hawkesworth C. J., Mantovani M. S. M., Peate D. W. (1988). Lithosphere remobilisation during Parana magmatism. In 'Oceanic and continental lithosphere: similarities and differences' *J. Pet. Spec. Vol.* 205—223.

Hawkesworth C. J., Mantovani M. S. M., Taylor P. N., Palacz Z. (1986). Evidence from the Parana of South Brazil for a continental contribution to Dupal basalts. *Nature* **322**, 356—359.

Heizler M. T., Harrison T. M. (1988). Multiple trapped argon isotope components revealed by $^{40}Ar/^{39}Ar$ isochron analysis. *Geochim. Cosmo. Acta.* **52**, 1295—1303.

Hergt J., Peate D. W., Hawkesworth C. J. (1991). The petrogenesis of Mesozoic Gondwana low Ti flood basalts. *Earth Plan. Sci. Lett.* **105**, 134—148.

Hoel P. G. (1976). Elementary Statistics (4th edition). Wiley, New York.

Hofmann A. W., Feigenson M. D. (1983). Case studies on the origin of basalts I. Theory and reassessment of Grenada basalts. *Contrib. Min. Pet.* **84**, 382—389.

Hooper P. R. (1982). The Columbia River basalts. *Science* **215**, 1463—1468.

Houseman G., England P. (1986). A dynamical model of lithosphere extension and sedimentary basin formation. *J. Geophys. Res.* **91**, 719—729.

Huene F von (1933). Zur stratigraphie Brasiliens. *Zentralbl. fur Min. Geol. Palaeont. Abt.* **7**, 418—423.

Humphris S. E., Thompson G. (1983). Geochemistry of rare earth elements in basalts from the Walvis Ridge: implications for its origin and evolution. *Earth Plan. Sci. Lett.* **66**, 223—242.

Humphris S. E., Thompson G., Schilling J. G., Kingsley R. H. (1985). Petrological and geochemical variations along the mid Atlantic Ridge between 46°S and 32°S: influence of the Tristan da Cunha mantle plume. *Geochim. Cosmo. Acta.* **49**, 1445—1464.

Irving A. J., Frey F. A. (1984). Trace element abundancies in megacrysts and their host basalts: constraints on partition coefficients and megacryst genesis. *Geochim. Cosm. Acta.* **48**, 1201—1221.

Jacobsen S. B., Wasserburg G. H. (1979). The mean age of mantle and crustal reservoirs. *J. Geophys. Res.* **84**, 7411—7426.

Jambon A., Zimmermann J. L. (1990). Water in oceanic basalts: evidence for dehydration of recycled crust. *Earth Plan. Sci. Lett.* **101**, 323—331.

Janasi V. de. A., Ulbrich H. H. G. J. (1991). Late Proterozoic granitoid magmatism in the state of Sao Paulo, southeastern Brazil. *Precamb. Res.* **51**, 351—374.

Jaques A. L., Green D. H. (1980). Anhydrous melting of peridotite at 0—15kb pressure and the genesis of tholeiitic basalts. *Contrib. Min. Pet.* **73**, 287—310.

Jarvis G. T., McKenzie D. P. (1980). Convection in a compressible fluid with infinite Prandtl number. *J. Fluid Mech.* **96**, 515—583.

Kaul P. F. T. (1979). PreCambriano e EoPaleozoico do Nordesto de Santa Catarina e Leste do Parana: reavaliacao de dados e correlacaes com e Africa. In: *Simp. Reg. Geol. 3, Rio Claro (1979), SBG Nucleo Sao Paulo* **1** 1—15.

Kaul P. F. T., Teixeira W. (1982). Archean and Early Proterozoic complexes of Santa Catarina, Parana and Sao Paulo States, south-southeastern Brazil: an outline of their geological evolution. *Rev. Bras. Geoc.* **12**, 172—182.

Kent D. V., Gradstein F. M. (1985). A Cretaceous and Jurassic geochronology. *Bull. Geol. Soc. Am.* **96**, 1419—1427.

Kent D. V., Gradstein F. M. (1986). A Jurassic to Recent chronology. In 'The western North Atlantic region' ed. P. R. Vogt, B. E. Tucholke. *Geol. Soc. Am. DNAG Ser. M*, 45—50.

Kent R. (1991). Lithospheric uplift in eastern Gondwana: evidence for a long lived mantle plume system? *Geology* **19**, 19—23.

Keuhner S. M., Edgar A. D., Arima M. (1981). Petrogenesis of the ultrapotassic rocks from the Leucite Hills, Wyoming. *Am. Min.* **66**, 663—677.

Klein E. M., Langmuir C. H. (1987). Global correlations of oceanic ridge basalt chemistry with axial depth and crustal thickness. *J. Geophys. Res.* **92** 8089—8115.

Kostopoulos D. K., James S. D. (1992). Parameterisation of the metling regime of the shallow upper mantle and the effects of variable lithospheric stretching on mantle modal stratification and trace element concentrations in magmas. *J. Pet.* **33**, 665—691.

Kretz R. (1982). Transfer and exchange equilibria in a protion of the pyroxene quadrilateral as deduced from natural and experimental data. *Geochim. Cosmo. Acta.* **46**, 411—421.

Krishnamurthy P., Cox K. G. (1977). Picrite basalts and related lavas from the Deccan Traps of Western India. *Contrib. Min. Pet.* **62**, 53—75.

Kushiro I. (1990). Partial melting of mantle wedge and evolution of island arc crust. *J. Geophys. Res.* **95**, 15929—15939.

Kushiro I., Yoder H. S., Nishikawa M. (1968). *Bull. Geol. Soc. Am.* **79**, 1685—1692.

Langmuir C. H., Plank T. (1988). Quantitative reevaluation of magma chamber processes and melting regime shape. *Chem. Geol.* **70**, 153—162.

Latin D. M., Dixon J. E., Fitton J. G., White N. (1990). Mesozoic magmatic activity in the North Sea Basin: implications for stretching history. In 'Tectonic events responsible for Britain's oil and gas reserves' ed. R. F. P. Hardman, J. Brookes. *Geol. Soc. Lond. Spec. Publ.* **55**, 207—227.

Latin D., White N. (1990). Generating melt during lithospheric extension: pure shear vs simple shear. *Geology* **18**, 327—331.

le Roex A. P., Cliff R. A., Adair B. J. I. (1990). Tristan da Cunha, South Atlantic: geochemistry and petrogenesis of a basanite-phonolite lava series. *J. Pet.* **31**, 779-812.

Leinz V., Bartorelli A., Isotta C. A. L. (1968). Contribuicao ao estudo do magmatismo basaltico Mesozoic da bacia do Parana. *An. Acad. Bras. Cienc.* **40**, 167—181.

Leinz V., Bartorelli A., Sadowiski G. R., Isotta C. A. L. (1966). Sobre o compartamento especial do trapp basaltico da Bacia do Parana. *Bol. Soc. Bras. Geol.* **15**, 79—91.

Lightfoot P. C. (1985). Isotope and trace element geochemistry of the South Deccan lavas, India. PhD thesis, Open University, 589pp.

Lindsley D. H. (1976). The crystal chemistry and structure of oxide minerals as exemplified by the Fe—Ti oxides. *Rev. Min.* **3**, L1—L52.

Lindsley D. H., Dixon S. A. (1976). Diopside—enstatite equilibria at 850°-1400°C, 5—35 kbar. *Am. J. Sci.* **276**, 1285—1301.

Long P. E., Duncan R. A. (1983). *Trans. Am. Geophys. Un.* **64**, 90.

Lopes O. F. (1981). Compartimentacao paleogeografica, faciologica e estratigrafica em terranos do Grupo Acungui da regiao Tigre Colonia Marques de Abrantes muncipios de Cerro Azul e Bocaiuva do Sul, PR. In: *Simp. Reg. Geol. 3, Curitiba 1981.* SBG 1 155—169.

Maack R. (1952). Die Entwicklung der Gondwana-Schichten Suedbrasiliens und ihre Beziehungen zur Karru-Formation Suedafrikas. *Int. Geol. Congr. Algiers* **19**, 339—372.

Maaloe S., Aoki K. (1977). The major element composition of the upper mantle estimated from the composition of lherzolites. *Contrib. Min. Pet.* **63**, 161—173.

Macedo M. H. de F., Basei M. A. S., Bonhome M. G., Kawashita K (1984). Dados geocronologicos referentes as rochas metassedimentares do Grupo Itajai, SC. *Rev. Bras. Geoc.* **14**, 30—34.

Mahood G., Hildreth W. (1983). Large partition coefficients for trace elements in high silica rhyolites. *Geochim. Cosmo. Acta.* **47**, 11—30.

Mangan M. T., Wright T. L., Swanson D. A., Byerly G. R. (1986). Regional correlation of Grande Ronde flows, Columbia River basalt group, Washington, Oregon and Idaho. *Bull. Geol. Soc. Am.* **97**, 1300—1318.

Manhes G., Minster J. F., Allegre C. J. (1978). Comparative uranium-thorium-lead and rubidium-strontium study of the Saint Severin amphoterite: consequences for early solar system chronology. *Earth Plan. Sci. Lett.* **39**, 14—24.

Mantovani M. S. M., Cordani U. G., Roisenberg A. (1985). Geochimica isotopica em vulcanicas acidas da Bacia do Parana e implicacoes geneticas associadas. *Rev. Bras. Geoc.* **15**, 61—65.

Mantovani M. S. M., Hawkesworth C. J. (1990). An inversion approach to assimilation and fractional crystallisation processes. *Contrib. Min. Pet.* **105**, 289—302.

Mantovani M. S. M., Hawkesworth C. J., Basei M. A. S. (1987). Nd and Sr isotope studies bearing on the crustal evolution of southeastern Brazil. *Rev. Bras. Geoc.* **17**, 263—268.

Mantovani M. S. M., Hawkesworth C. J., Taylor P. N., Palacz Z. (1986). Abstr. vol. IAVCEI, New Zealand, 181.

Mantovani M. S. M., Marques L. S., De Souza M. A., Civetta L., Atalla L., Innocenti f. (1985). Trace element and strontium isotope constraints on the origin and evolution of Parana continental flood basalts of Santa Catarina State (southern Brazil). *J. Pet.* **26**, 187—209.

Mantovani M. S. M., Vasconcellos A. C. B. C., Shukowski W., Milani E. J., Basei M. A. S., Hurter S. J., de Frietas S. R. C. (1991). The Brusque transect (SA20) from the Dom Feliciano belt to the Amazon Craton: explanatory pamphlet. Global Geosciences Transect Project.

Marimon M. P. C., Moreira M. L. D., Ayala L. (1983). Formacao Serra Geral no Sul do Brasil: novos dados de razoes isotopicas $^{87}Sr/^{86}Sr$ e implicacoes com geese das rochas desta formacao. *Atas do 1 Simposio Sul-Brasileiro do Geologia, Porto Allegre, RS*, 69—81.

Marsh J. S. (1973). Relationships between transform directions and alkaline igneous rock lineaments in Africa and South America. *Earth Plan. Sci. Lett.* **18**, 317—323.
Marsh J. S., Eales H. V. (1984). The chemistry and petrogenesis of igneous rocks of the Karoo central area, southern Africa. *Spec. Publ. Geol. Soc. S. Afr.* **13**, 27—68.

McCulloch M. T., Gregory R. T., Wasserburg G. J., Taylor H. P. (1980). A Nd, Sr and O isotopic study of the Cretaceous Samail Ophiolite and implications for the petrogenesis and seawater hydrothermal alteration of oceanic crust. *Earth Plan. Sci. Lett.* **46**, 201—211.

McCulloch M. T., Wasserburg G. J. (1978). Sm—Nd and Rb—Sr chronology of continental crust formation. *Science* **200**, 1003—1011.

McDougall I., Harrison T. M. (1988). Geochronology and thermochronology by the $^{40}Ar/^{39}Ar$ method. Oxford University Press, 212pp.

McDougall I., Ruegg N. R. (1966). Potassium—argon dates on the Serra Geral formation of South America. *Geochim. Cosmo. Acta.* **30**, 191—195.

McKenzie D. P. (1978). Some remarks on the development of sedimentary basins. *Earth Plan. Sci. Lett.* **40**, 25—32.

McKenzie D. P. (1984). The generation and compaction of partially molten rock. *J. Pet.* **25**, 713—765.

McKenzie D. P., Bickle M. J. (1988). The volume and composition of melt generated by extension of the lithosphere. *J. Pet.* **29**, 625—679.

McKenzie D. P., O'Nions R. K. (1991). Partial melt distributions from inversion of rare earth element concentrations. *J. Pet.* **32**, 1021—1091.

Melcher G. C., Melcher B. A. (1972). *Abstract, 26 Congr. Bras. Geol.* **1**, 216—217.

Melfi A. J. (1967). Potassium—argon ages for core samples of basaltic rocks from southern Brazil. *Geochim. Cosmo. Acta.* **31**, 1079—1089.

Menzies M. A. (1992). The lower lithosphere as a major source for continental flood basalts: a reappraisal. In 'Magmatism and the causes of continental breakup' ed. B. C. Storey, T. Alabaster, R. J. Pankhurst. *Geol. Soc. Spec. Publ.* **68**, 31—39.

Menzies M. A., Murthy V. R. (1980). Enriched mantle: Nd and Sr isotopes in diopsides from kimberlite nodules. *Nature* **283**, 634—636.

Merril R. B., Wyllie P. J. (1975). Kaersutite and kaersutite eclogite from Kakanui, New Zealand—water excess and water deficient melting to 30kb. *Geol. Soc. Am. Bull.* **86**, 555—570.

Milner S. C. (1986). The geological and volcanological features of the quartz latites of the Etendeka Formation. *Commun. Geol. Surv. S.W. Africa/Namibia* **2**, 109—116.

Milner S. C., Duncan A. R. (1987). Geochemical characterisation of quartz latite units in the Etendeka Formation. *Commun. Geol. Surv. S.W.Africa/Namibia* **3**, 83—90.

Milner S. C., Ewart A (1989). The geology of the Goboboseb Mountain volcanics and their relationship to the Messum Complex, Namibia. *Commun. Geol. Surv. Namibia* **5**, 31—40.

Minioli B., Poncano W. L., Oliviera S. M. B. (1971). Extensao geografica do vulcanismo basaltico do Brasil meridional. *An. Acad. brasil. Cienc.* **43**, 433—437.

Morgan W. J. (1981). Hotspot tracks and the opening of the Atlantic and Indian Oceans. In 'The Sea: Vol. 7; the oceanic lithosphere' ed. C. Emiliani. Wiley, New York, 443—487.

Nakamura N. (1974). Determination of REE, Ba, Fe, Mg, Na and K in carbonaceous and ordinary chondrites. *Geochim. Cosmo. Acta.* **38**, 757—775.

Nakamura Y., Kushiro I. (1970). Equilibrium relations of hypersthene, pigeonite and augite in crystallising magmas: microprobe study of a pigeonite andesite from Wieselberg, Germany. *Am. Min.* **55**, 1999—2015.

Nielsen R. L. (1989). A model for the simulation of combined major and trace element liquid lines of descent. *Geochim. Cosmo. Acta.* **52**, 27—38.

Nier A. O. (1950). A redetermination of the relative abundancies of the isotopes of carbon, nitrogen, oxygen, argon and potassium. *Phys. Rev.* **77**, 789—793.

Nurnberg D., Muller R. D. (1991). The tectonic evolution of the South Atlantic from late Jurassic to present. *Tectonophys.* **191**, 27—53.

Officer C. B., Drake C. L. (1985). Terminal Cretaceous environmental events. *Science* **227**, 1161—1167.

Olafsson M., Eggler D. H. (1983). Phase relations of amphibole, amphibole-carbonate, and phlogopite-carbonate peridotite: petrologic constraints on the asthenosphere. *Earth Plan. Sci. Lett.* **64**, 305—315.

Oliveira de M. A. F. (1982). Bulk geochemistry of the Paraiba do Sul granulitic belt. *Rev. Bras. Geoc.* **12**, 369—374.

Pacca I. G., Hiodo F. Y. (1976). Palaeomagnetic analysis of Mesozoic Serra Geral lava flows in southern Brazil. *An. Acad. brasil. Cienc.* **48**, 207—214.

Parsons B., McKenzie D. P. (1978). Mantle convection and the thermal structure of plates. *J. Geophys. Res.* **83**, 4485—4496.

Parsons B., Sclater J. G. (1977). An analysis of the variation of ocean floor bathymetry and heat flow with age. *J. Geophys. Res.* **82**, 803—827.

Patchett P. J. (1980). Thermal effects of basalt on continental crust, and crustal contamination of magmas. *Nature* **283**, 559—561.

Patterson C., Tatsumoto S. (1964). The significance of lead isotopes in detrital felspar with respect to chemical differentiation within the Earth's mantle. *Geochim. Cosmo. Acta.* **28**, 1—22.

Peate D. W. (1989). Stratigraphy and petrogenesis of the Parana continental flood basalts, southern Brazil. PhD thesis, Open University, 359pp.

Peate D. W., Hawkesworth C. J., Mantovani M. S. M. (1992). Chemical stratigraphy of the Parana lavas, South America: classification of magma types and their spatial distribution. *Bull. Volcanol.* **55**, 119—139.

Peate D. W., Hawkesworth C. J., Mantovani M. S. M., Shukowsky W. (1990). Mantle plumes and flood basalt stratigraphy in the Parana, South America. *Geology* **18**, 1223—1226.

Petrini R., Civetta L., Piccirillo E. M., Bellieni G., Comin-Chiaramonti P., Marques L S., Melfi A. J. (1987). Mantle heterogeneity and crustal contamination in the genesis of low-Ti continental flood basalts from the Parana plateau (Brazil): Sr and Nd isotope and geochemical evidence. *J. Pet.* **28**, 701—726.

Piccirillo E. M., Bellieni G., Cavazzini G, Comin-Chiaramonti P., Petrini R., Melfi A. J., Pinese J. P. P., Zantadeschi P., De Min A. (1990). Lower Cretaceous tholeiitic dyke swarms from the Ponta Grossa Arch (southeast Brazil): petrology, Sr—Nd isotopes and genetic relationships with the Parana flood volcanics. *Chem. Geol.* **89**, 19—48.

Piccirillo E. M., Melfi A. J. (1988). The Mesozoic flood volcanism of the Parana basin: petrogenetic and geophysical aspects. IAG—USP Press, Sao Paulo, 660pp.

Piccirillo E. M., Melfi A. J., Comin-Chiaramonti P., Bellieni G., Ernesto M., Marques L. S., Nardy A. J. R., Pacca I. G., Roisenberg A., Stolfa D. (1988). Continental flood volcanism from the Parana basin (Brazil). In 'Continental flood basalts' ed. J. D. McDougall. Kluwer academic publishers, 195—238.

Piccirillo E. M., Raposo M. I. B., Melfi A. J., Comin-Chiaramonti P., Bellieni G., Cordani U. G., Kawashita K. (1987). Bimodal fissural volcanic suites from the Parana basin (Brazil): K—Ar age, Sr isotopes and geochemistry. *Geochim. Bras.* **1**, 53—69.

Potts P. J., Williams Thorpe O., Isaacs M. C., Wright D. W. (1985). High precision instrumental neutron activation analysis of geological samples employing simulataneous counting with both planar and coaxial detectors. *Chem. Geol.* **48**, 145—155.

Rabinowitz P. D., LaBreque J. (1979). The Mesozoic South Atlantic Ocean and evolution of its continental margins. *J. Geophys. Res.* **84**, 5973—6002.

Rampino M. R., Stothers R. B. (1988). Flood basalt volcanism during the past 250 million years. *Science* **241**, 663—668.

Raposo M. I. B., Ernesto M. (1989). Rochas intrusivas basicas do Arco de Ponta Grossa: resultados paleomagneticos preliminares. Rev. *Bras. Geoc.* **19**, 393—400.

Renne P. R., Ernesto M., Pacca I. G., Coe R. S., Glen J. M., Prevot M., Perrin M. (1992)a. The age of Parana flood volcanism, rifting of Gondwanaland, and the Jurassic-Cretaceous boundary. *Science* **258**, 975—979.

Renne P. R., Ernesto M., Pacca I. G., Coe R. S., Glen J. M., Prevot M., Perrin M. (1992)b. Age and duration of Parana flood volcanism in Brazil. Abstracts, *EOS*, 531.

Richards M. A., Duncan R. A., Courtillot V. E. (1989). Flood basalts and hotspot tracks: plume heads and tails. *Science* **246**, 103—107.

Richards M. A., Jones D. L., Duncan R. A., DePaolo D. J. (1991). A mantle plume initiation model for the Wrangellia flood basalts and other oceanic plateaus. *Science* **254**, 263—267.

Richardson S. H., Erlank A. J., Duncan A. R., Reid D. L. (1982). Correlated Nd. Sr and Pb isotopic variation in Wlavis Ridge basalts and implications for the evolution of their mantle source. *Earth Plan. Sci. Lett.* **59**, 327—342.

Richardson S. H., Gurney A. J., Erlank A. J., Harris K. W., (1984). Origin of diamonds in old enriched mantle. *Nature* **310**, 198—202.

Richter F. M., McKenzie D. P. (1981). Parameterisations for the horizontally averaged temperature of infinite Prandtl number convection. *J. Geophys. Res.* **86**, 1738—1744.

Roeder P. L., Emslie R. F. (1970). Olivine—liquid equilibrium. *Contrib. Min. Pet.* **29**, 275—289.

Sanford R. M., Lange F. W. (1960). Basin study approach to oil evaluation of the Parana miogeosyncline, south Brazil. *Am. Ass. Pet. Geol.* **44**, 1316—1370.

Sartori P. L., Maciel F. G. L., Menegotto E. (1975). Contribuicao ao estudo das rochas vulcanicas da Bacia do Parana na regiao de Santa Maria, RS. *Rev. Bras. Geoc.* **5**, 141—159.

Schobbenhaus C., Almeida Campos D. de, Derze G. R., Asmus H. E. (1984). Geologia do Brasil: texto explicativo do mapa geologico do Brasil e da area oceanica adjacente incluindo depositos minerais, DNPM, Brasilia.

Scoll W. V., Lopes O. F., Silva A. C. G. A., Prozzi C. R. (1980). Geologio do PreCambriano da regiao articlinal Setuva, municipios de Bocaiuva da Sul e Rio Branco do Sul, PR. In: Congr. Bras. Geol. 31, Camboria SBG **5**, 3003—3012.

Shaw D. M. (1970). Trace element fractionation during anatexis. *Geochim. Cosmo. Acta* **34**, 237—243.

Siedner G., Miller J. A. (1968). K—Ar age determinations on basaltic rocks from South West Africa, and their bearing on continental drift. *Earth Plan. Sci. Lett.* **4**, 451—458.

Siedner G., Mitchell J. G. (1976). Episodic Mesozoic volcanism in Namibia and Brazil: a K—Ar isochron study bearing on the opening of the South Atlantic. *Earth Plan. Sci. Lett.* **30**, 292—302.

Smyth J. R., Bell D. R., Rossman G. R. (1991). Incorporation of hydroxyl in upper mantle clinopyroxenes. *Nature* **351**, 732—735.

Srivastava S. P. (1978). Evolution of the Labrador Sea and its bearing on the early evolution of the North Atlantic. *J. Roy. Astron. Soc.* **52**, 313—357.

Stacey J. S., Kramers J. D. (1975). Approximation of terrestrial lead isotope evolution by a two stage model. *Earth Plan. Sci. Lett.* **26**, 207—221.

Stolper E., Walker D., Hager B. H., Hays J. F. (1981). Melt segregation from partially molten source regions: the importance of melt density and source region size. *J. Geophys. Res.* **86**, 6261—6271.

Sun S. S., McDonough W. F. (1989). Chemical and isotopic systematics of oceanic basalts: implications for mantle composition and processes. In 'Magmatism in the Ocean Basins' ed. A. D. Saunders, M. J. Norry. *Geol. Soc. Lond. Spec. Publ.* **42**, 313—345.

Swanson D. A., Wright T. L., Helz R. T. (1975). Linear vent systems and estimated rates of magma production and eruption for the Yakima basalt on the Columbia Plateau. *Am. J. Sci.* **275**, 877—905.

Swanson D. A., Wright T. L., Hooper P. R., Bentley R. D. (1979). Revisions in stratigraphic nomenclature of the Columbia River Basalt Group. *U.S. Geol. Surv. Bull.* **1457G**, G1—G59.

Sweeney R. J., Falloon T. J., Green D. H., Tatsumi Y. (1991). The mantle origins of Karoo picrites. *Earth Plan. Sci. Lett.* **107**, 256—271.

Tarduno J. A., Sliter W. V., Kroenke L., Leckie M., Mayer H., Mahoney J. J., Musgrave R., Storey M., Winterer E. L. (1991). Rapid formation of the Ontong Java Plateau by Aptian mantle plume volcanism. *Science* **254**, 399—403.

Taylor H. P. (1980). The effects of assimilation of country rocks by magmas on $^{18}O/^{16}O$ and $^{87}Sr/^{86}Sr$ systematics in igneous rocks. *Earth Plan. Sci. Lett.* **47**, 243—254.

Taylor S. R., McLennan S. M. (1985). The continental crust: its composition and evolution. Oxford, Blackwell Scientific.

Thompson R. N. (1977). Columbia/Snake River-Yellowstone magmatism in the context of western U.S. Cenozoic geodynamics. *Tectonophys.* **39**, 621—636.

Thompson R. N. (1981). Magmatism of the British Tertiary Volcanic Province. *Scot. J. Geol.* **18**, 49—107.

Thompson R. N. (1984). Primary basalts and magma genesis. *Contrib. Min. Pet.* **45**, 317—341.

Thompson R. N., Morrison M. A., Dickin A. P., Hendry G. L. (1983). Continental flood basalts.....arachnids rule OK? In 'Continental basalts and mantle xenoliths' ed. C. J. Hawkesworth, M. J. Norry, 158—185. Nantwich, Shiva.

Toquato J. R., Amaral G. (1973). Algumas idades K/Ar do magmatismo Mesozoico de Angola e sua correlacao com o corrispondente do sul do Brasil. *Inst. Invest. Cient. Angola* **10**, 1—10.

Ulbrich H. H. G. J., Gomes C. B. (1981). Alkaline rocks from continental Brazil. *Earth Sci. Rev.* **17**, 135—154.

Vandoros P., Ruegg N. R., Cordani U. G. (1966). On potassium—argon age measurements of basaltic rocks from southern Brazil. *Earth Plan. Sci. Lett.* **1**, 449—452.

Watson E. B. (1979). Zircon saturation in felsic liquids: experimental results and applications to the trace element geochemistry. *Contrib. Min. Pet.* **70**, 407—419.

Watson E. B. (1982). Basalt contamination by continental crust: some experiments and results. *Contrib. Min. Pet.* **80**, 73—87.

Watson S., McKenzie D. P. (1991). Melt generation by plumes: a study of Hawaiian volcanism. *J. Pet.* **32**, 501—537.

Weaver B. L., Tarney J. (1984). Empirical approach to estimating the composition of the continental crust. *Nature* **310**, 575—577.

Wernicke B. (1981). Low angle normal faults in the Basin and Range province: nappe tectonics in an extending orogen. *Nature* **291**, 645—648.

Wernicke B. (1985). Uniform sense normal simple shear of the continental lithosphere. *Can. J. Earth Sci.* **22**, 108—125.

White R. S. (1992). Magmatism during and after continental breakup. In 'Magmatism and the causes of continental breakup' ed. B. C. Storey, T. Alabaster, R. J. Pankhurst. *Geol. Soc. Spec. Publ.* **68**, 1—16.

White R. S., McKenzie D. P. (1989). Magmatism at rift zones: the generation of volcanic continental margins and flood basalts. *J. Geophys. Res.* **94**, 7685—7730.

Whitehead J. A., Luther D. S. (1975). Dynamics of laboratory diapir and plume models. *J. Geophys. Res.* **80**, 705—717.

Wilkinson J. F. G., Binns R. A. (1977). Relatively iron-rich lherzolite xenoliths of the Cr—diopside suite: a guide to the primary nature of anorogenic tholeiitic magmas. *Contrib. Min. Pet.* **65**, 199—212.

Wood D. A., Gibson I. L., Thompson R. N. (1976). Element mobility during zeolite facies metamorphism of the Tertiary basalts of eastern Iceland. *Contrib. Min. Pet.* **55**, 241—255.

Wright T. L., Doherty P. C. (1970). A linear programming and least-squares computer method for solving petrologic mixing problems. *Bull. Geol. Soc. Am.* **81**, 1995—2008.

York D. (1969). Least squares fitting of a straight line with correlated errors. *Earth Plan. Sci. Lett.* **5**, 320—324.

Zalan P. V., Wolff S., Conceicao J. C. J., Astolfi M. A. M., Vieira I. S., Appi V. T., Zanotto O. A., Marques A. (1987). Tectonics and sedimentation of the Parana basin. Anais do 7 symposio de Gondwana, 35pp.

Zanbrano J. J., Urien C. M. (1974). PreCretaceous basins in the Argentine continental shelf. In: 'The geology of continental margins' ed. C. A. Burke, C. L. Drake. New York, Springer-Verlag, 463—470.

Appendix

A.1 Sample powder and mineral separate preparation

Dolerite samples of between 3 and 5kg were collected from each locality. These were split into ~5cm sized fragments using a hydraulic splitter, and any weathered material removed. Approximately 1kg of the sample was then crushed in a hardened steel jaw crusher, and a representative 100g portion of the crushate taken by cone and quartering. This was powdered in an agate-lined tema swing mill for ~15 minutes to a powder of less than 200 mesh grain size.

Plagioclase, amphibole and biotite separates used in Ar—Ar analysis were obtained by sieving a portion of the crushate from the jaw crusher. Individual crystals were handpicked from the 100μm—1mm fraction under a binocular microscope. These were rinsed twice with distilled water in an ultrasonic bath. Plagioclase separates used in Pb isotope analysis were cleaned in a similar manner before being crushed to a fine powder in an agate pestle and mortar.

A.2 XRF sample preparation and analysis

Major and trace element analysis of the samples collected during the 1989 field season (prefixed MR-89; table A.1) was carried out at Oxford University, using a Philips PW1400 x-ray fluoresence spectrometer, and the data processed using on a PDP11 minicomputer. The x-rays were generated using a Rh tube, and the analysing crystals used were LiF 220, LiF 200, PE and PX1. Mass absorption was corrected for using De Jongh's formula (major element analyses), and the Rh Compton scatter peak (trace elements). The concentrations of the elements Co, Cr, V and Ba were corrected for the Fe, Mn and Ti absorption edges and line overlaps.

Major element analyses were performed on glass discs prepared by fusing a mixture of 1.0000g rock powder and 5.0000g lithium metaborate-tetraborate mixture (Spectroflux 100B) in a zirconia grained Pt—5%Au alloy crucible in a muffle furnace at 1175°C for 5 minutes. The melt was poured into a Pt—Au alloy casting mould, and quenched over a jet of air. The flux had been pre-dried at 600°C for at least 12 hours, and the sample powder pre-

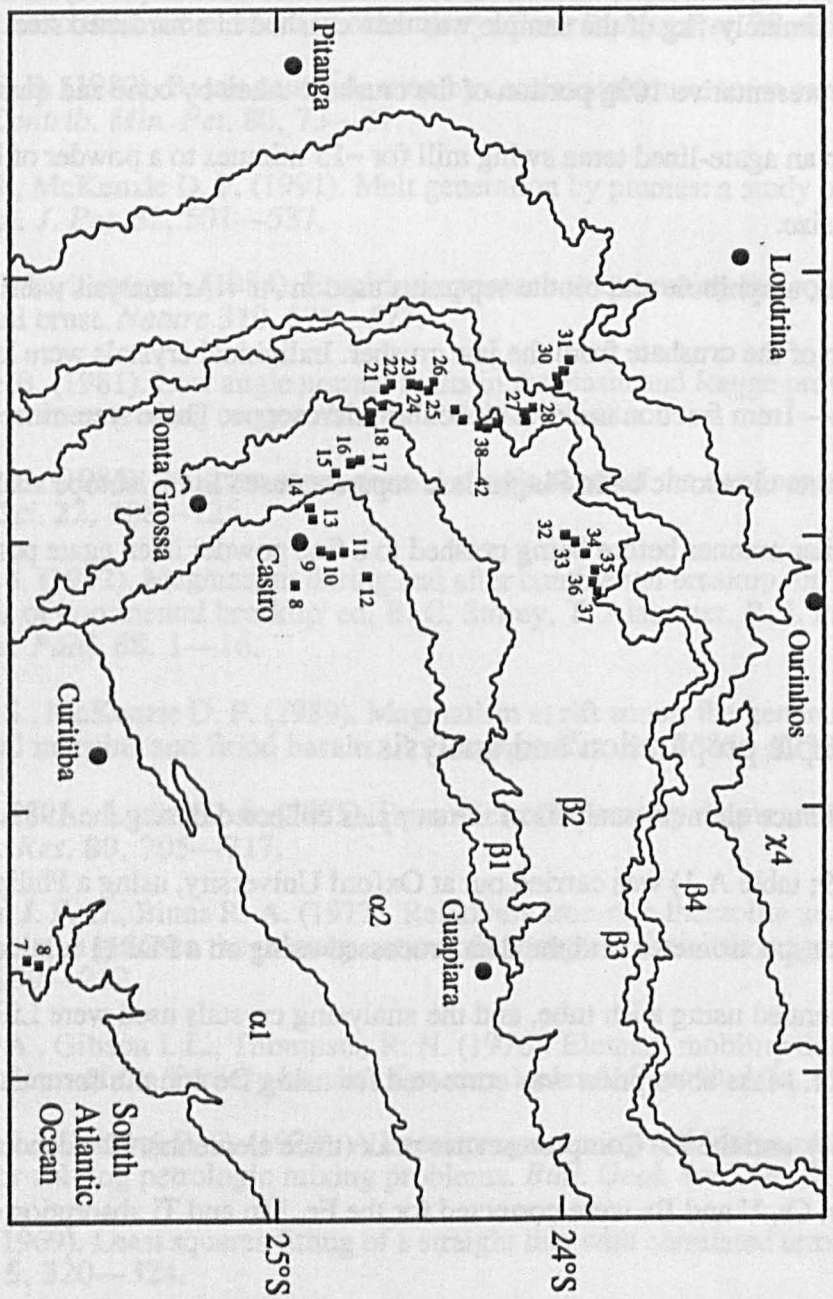

Fig. A.1

Location of the samples collected in the Ponta Grossa region. Key; α1, Archean high-grade metamorphic rocks of the Curitiba Massif; α2, late Proterozoic metasediments and Cambrian granitoids; β1—β4, Devonian—Jurassic sediments of the Parana Basin; χ4, Parana flood basalts and rhyolites.

ignited at 1000°C for a minimum of 20 hours. Crucibles were cleaned in hot 6M HCl, and rinsed in distilled water. Loss on ignition values were calculated at the Open University by heating approximately 7g of the sample in a pre-dried silica crucible in a muffle furnace at 1000°C for 20 minutes, and measuring the percentage loss of weight.

Trace element analyses were carried out on pressed powder pellets prepared by mixing thoroughly ~10g rock powder and ~1ml Moviol binder in an agate pestle and mortar. The mixture was pressed into a 3 cm diameter pellet in a hydraulic press at a pressure of 105 Pa for 30s. The pellets were dried for 12hr at 80°C before analysis.

The borehole samples (table A.5) donated by M.S.M. Mantovani, and those samples collected by A.C. Vasconcellos during 1990 (table A.4), were analysed by XRF at the Open University. The sample preparation techniques used were similar to those described above, except that a correction for flux volatilisation during fusion was applied to each set of discs. Analyses were carried out on an ARL 8420+ dual goniometer, wavelength dispersive XRF spectrometer at the Open University. X-rays are generated using a 3kW Rh anode end-window X-ray tube, and the diffracting crystals used are AX06, PET, Ge111, LiF200 and LiF220. Elemental intensities are corrected for background and known peak overlap interferences. Instrumental intensity drift is taken into account using a drift monitor. Count times for most trace elements are selected to achieve 2s precision better than 2ppm. Major element matrix corrections employ the empirical Traill-Lachance procedure; trace element matrix corrections usually involve ratioing with the Compton scattered tube lines.

A.3 Instrumental neutron activation analysis

INAA was carried out on 36 samples (table A.3) to determine the concentrations of the rare earth elements La, Ce, Nd, Sm, Eu, Tb, Yb and Lu; also Th, U, Co, Ta and Hf.

0.3g pre-dried rock powder was weighed into a polythene capsule and sealed. Nine samples and two standards were stacked into a cylinder, with weighed lacquered iron foil between each capsule to monitor the neutron flux variation along the length of the cylinder. The standards used included the irradiation standard AC (OURS).

Samples were irradiated in the core tube at the Imperial College reactor centre, Ascot, in a thermal flux of 5×10^{12} n cm^2 sec^{-1} for 24—30 hours. The samples were left for a week

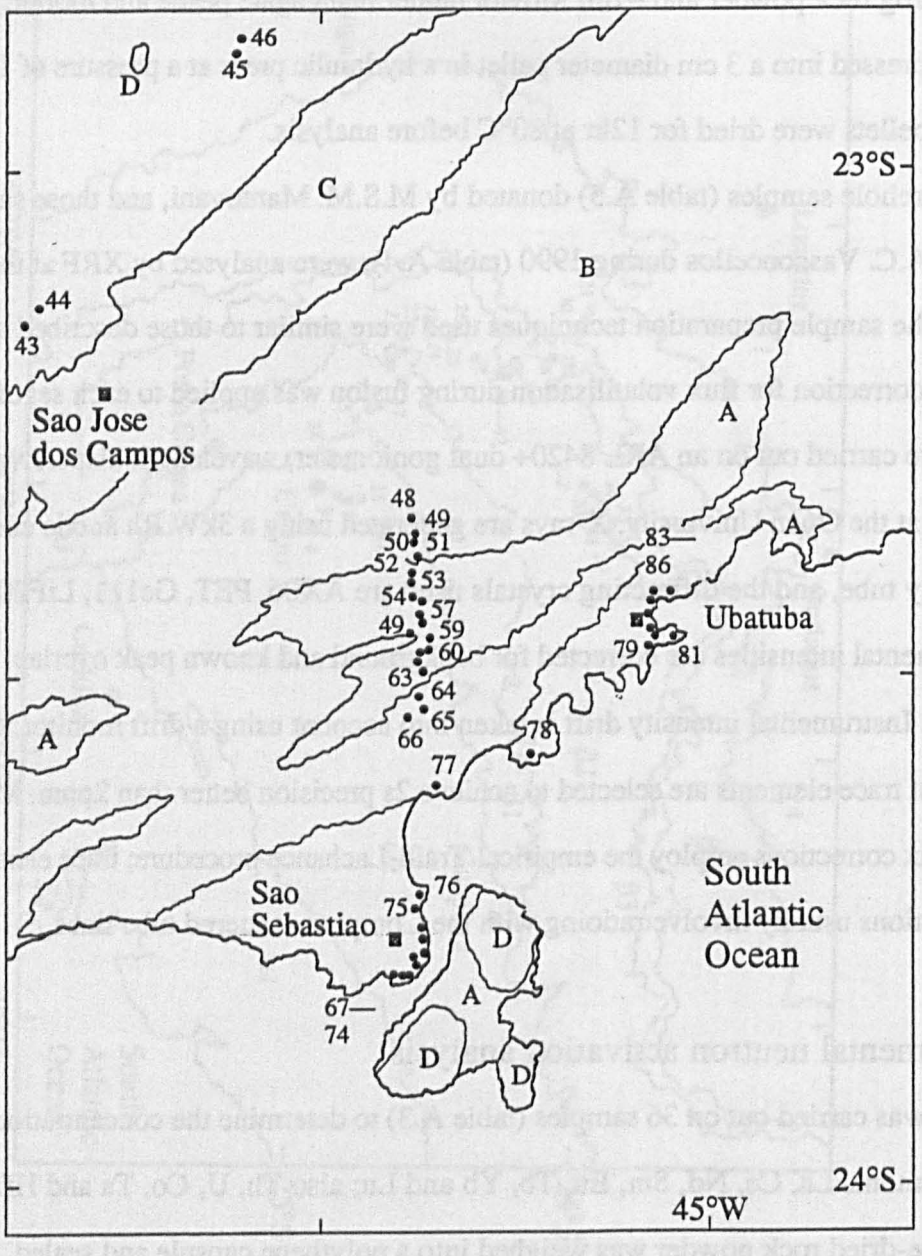

Fig. A.2
Location of the samples collected from Sao Paulo State. Key; A and B, basement rocks of Archean and Proterozoic age respectively; C, Cenozoic sediments of the Taubate Group; D, alkalic intrusive rocks of Cretaceous age.

before analysis to allow short lived radioactive isotopes to decay; details of counting conditions, peak fitting, calibration and corrections are decribed in Potts et al. (1985).

A.4 Wavelength dispersive microprobe analysis

Electron microprobe analyses (table A.2) were carried out on a wavelength dispersive Cambridge microscan Mk9 instrument, using a ZAF-matrix correction, an accelerating potential of 20kV, a beam current of 3.05nA and a typical spot size of 10—15μm. The instrument was calibrated daily using mineral standards, and drift was monitored by analysing an internal standard (a basaltic glass).

A.5 Radiogenic isotope analysis

A.5.1 Sample dissolution and separation techniques

All isotopic analyses and preparations were carried out in a clean-air laboratory in which a positive air pressure was maintained. All solutions used in the dissolutions were made up with either quartz distilled or Milli-Q reverse osmosis purified water (ROW). Sample dissolutions were carried out in teflon beakers which were normally opened only in laminar flow cupboards. Prior to use, beakers were rinsed in ROW, soaked in ~15M HNO3 (aq) at ~80°C for at least 24hr, then rinsed and soaked in ROW overnight. Total procedural blanks for Sr and Nd over the period of analysis did not exceed 1ng.

Between 100 and 150mg of rock powder was subjected to a HNO3+HF digestion, and repeatedly treated with hot 15M HNO3 and 6M HCl. When the sample was completely dissolved, the solution was evaporated to dryness and the residue redissolved in 1ml 2.5M HCl. Rb and Sr were separated using carefully calibrated ion-exchange columns of 10ml preconditioned Bio-rad AG50W X8 200—400 mesh resin. If Sm and Nd was required, the MREE fraction was collected in 3M HNO3 and evaporated to dryness. This residue was dissolved in 1ml 0.25M HCl, and Sm and Nd separated using preconditioned reverse ion-excange columns composed of 1g teflon powder (Voltalef 300LD PL micro) and 100g DEP (di(2-ethylhexyl)phosphate). Samples for Rb and Sr or Sm and Nd isotope dilution were treated in a similar manner, except that 1 drop of a combined ^{87}Rb—^{84}Sr or ^{150}Nd—^{149}Sm spike was added to the sample before dissolution.

All reagents used in Pb isotope analysis were made up with water that had been twice distilled in teflon distillation flasks. The smallest possible reagent volumes were used, in order to keep blanks to a minimum. Total procedural blanks carried out over the period of analysis were between 0.54 and 1.02ng. Following HNO3+HF digestion and HNO3+HCl dissolution, the solution was evaporated to dryness, and the Pb extracted in 1ml HBr. Ion-exchange columns consisted of 2ml polythene pipette tips loaded with 3—4 drops of Dowex 200—400 mesh anion exchange resin, and the sample was passed twice through these columns in order to concentrate the Pb. The Pb was dissolved in 1µl phosphoric acid before loading.

Whole rock powders of selected samples of the Sao Sebastiao magma type were leached prior to dissolution for isotope analysis. The samples were soaked in warm 6M HCl for 24hr, before being thoroughly washed in distilled water in an ultrasonic bath. The powder was then dried, and the dissolution carried out as for the other samples.

A.5.2 Mass spectrometry

Spiked samples for Rb, Sr, Sm, Nd isotope dilution analysis were analysed on a Vacuum Generators Isomass 54E solid source mass spectrometer. All other analyses were carried out on a Finnegan M80 261 solid source, multi-collector mass spectrometer, interfaced with a HP 9836 computer using software designed by D.W. Wright and P.W.C van Calsteren. Filaments for both mass spectrometers were outgassed before loading for 5 minutes at 4.5A in a vacuum better than 10^{-6} torr. Sr was loaded in phosphoric acid on single Ta filaments, and the measured $^{87}Sr/^{86}Sr$ ratios were exponentially fractionation corrected within run to $^{86}Sr/^{88}Sr=0.1194$. The mean value of $^{87}Sr/^{86}Sr$ for the standard NBS981 during the period of analysis was 0.71024±0.00002 (2σ standard deviation on 12 measurements). Nd was loaded on Ta filaments (a Re ionisation filament was used) and run as metal ions. $^{143}Nd/^{144}Nd$ ratios were exponentially fractionation corrected to $^{146}Nd/^{144}Nd=0.72190$. Eight analyses of a J&M Nd standard over the period of analysis had a mean value of 0.511820±0.000028 (2σ standard deviation). Pb was run on single Ta filaments, using a silica gel technique adapted from Manhes et al. (1978) and collected statically. Pb isotope fractionation corrections were made using mass discrimination

coefficients calculated from the mean value of the NBS981 standard for each run, and assuming this standard to have $^{206}Pb/^{204}Pb=16.937$, $^{207}Pb/^{204}Pb=15.491$, $^{208}Pb/^{204}Pb=36.700$. (Note that the $^{208}Pb/^{204}Pb$ ratio used differs from the value of 36.721 quoted by Catanzaro et al., 1968). Runs with low (less than about 1.5pA) and variable beam intensity were discarded from the data set, because of the error associated with measuring the small ^{204}Pb peak.

A.5.3 Age correction of the radiogenic isotope data

Age correction of the measured $^{87}Sr/^{86}Sr$ and $^{143}Nd/^{144}Nd$ ratios were carried out assuming an age of 130 Ma for all samples other than those of the Sao Sebastiao magma type (Chapter 4), which were assumed to have an age of 80 Ma. The natural abundancies of ^{87}Rb, ^{86}Sr, ^{147}Sm and ^{144}Nd were used to caculate $^{87}Rb/^{86}Sr$ and $^{147}Sm/^{144}Nd$ for each sample from the elemental ratios measured by XRF (Rb, Sr) or INAA and isotope dilution (Sm, Nd);

$$^{87}Rb/^{86}Sr=2.891Rb/Sr$$
$$^{147}Sm/^{144}Nd=0.602Sm/Nd$$

$$(^{87}Sr/^{86}Sr)_{measured}=(^{87}Sr/^{86}Sr)_{initial}+^{87}Rb/^{86}Sr(e^{\lambda 1t}-1)$$
$$(^{143}Nd/^{144}Nd)_{measured}=(^{143}Nd/^{144}Nd)_{initial}+^{147}Sm/^{144}Nd(e^{\lambda 2t}-1)$$

where $\lambda 1=1.42 \times 10^{-11}\ y^{-1}$ and $\lambda 2=6.54 \times 10^{-12}\ y^{-1}$.

Pb isotope data were corrected for U and Th decay using

$$(^{206}Pb/^{204}Pb)_{measured}=(^{206}Pb/^{204}Pb)_{initial}+^{238}U/^{204}Pb(e^{\lambda 3t}-1)$$
$$(^{207}Pb/^{204}Pb)_{measured}=(^{207}Pb/^{204}Pb)_{initial}+^{235}U/^{204}Pb(e^{\lambda 4t}-1)$$
$$(^{208}Pb/^{204}Pb)_{measured}=(^{208}Pb/^{204}Pb)_{initial}+^{232}Th/^{204}Pb(e^{\lambda 5t}-1)$$

where $\lambda 3$, $\lambda 4$ and $\lambda 5$ are 1.55125×10^{-10}, 9.8485×10^{-10} and $4.9475 \times 10^{-11}\ y^{-1}$ respectively.

$^{238}U/^{204}Pb$, $^{235}U/^{204}Pb$ and $^{232}Th/^{204}Pb$ were calculated from;

$$^{238}U/^{204}Pb=U/Pb \times (\text{atomic weight Pb}/238.08) \times (99.27/\%^{204}Pb)$$

where 238.03 is the atomic weight of U and 99.27 is the percentage of ^{238}U;

$$^{235}U/^{204}Pb=(^{238}U/^{204}Pb)/137.88$$

$$^{232}Th/^{204}Pb=Th/Pb \times (\text{atomic weight Pb}/232.038) \times (100/\%^{204}Pb)$$

where 232.038 is the atomic weight of Th and 100 is the percentage of ^{232}Th. The atomic weight of Pb, and the concentration of ^{204}Pb was calculated separately for each sample.

A.6 Ar—Ar mass spectrometry

Samples selected for analysis were cut into approximately 500mm thick slices and polished on one side. These, together with plagioclase, biotite and amphibole mineral separates, were irradiated at the Ford reactor, Michigan, where they received approximately 10^{18} fast neutrons cm^{-1}. J values for the irradiation were calculated using the flux monitors mmHbl and Hb3gr, and were;

MR-8930	0.00598±0.00002
MR-8950	0.00599±0.00002
MR-8917	0.00600±0.00002
MR-8931	0.00601±0.00002
MR-8965	0.00602±0.00002
MR-8928	0.00603±0.00002
MR-899	0.00604±0.00002
MR-8951	0.00604±0.00002

Argon was extracted from individual mineral grains by firing short pulses of a continuous Nd YAG laser beam (TEMoo, wavelength 1064nm) through a modified petrological microscope, and focussed to a spot size of about 20mm on the sample surface. Typical powers of 10—17W were used, and pulse lengths of between 50 and 200ms, depending upon the reflectivity of the sample. The argon was purified using a SAES GP10 getter at 400°C for 5 minutes, and isotope analysis was carried out using a Mass Analyser Products 215 mass spectrometer with an electron multiplier detector. Seven masses were analysed; 25, 36, 37, 38, 39, 40 and 41. Measurement of mass 41 was made in order to assess the levels of hydrocarbon, and 35 in order to monitor the presence of Cl background

in the mass spectrometer. At the end of each run, peaks were regressed to the inlet time. A blank run was made after every sample run; average blank levels during the period of analysis were approximately 2, 0.06, 0.03, 0.06 and 0.04 x 10^{-12} cm^3 STP for ^{40}Ar, ^{39}Ar, ^{38}Ar, ^{37}Ar and ^{36}Ar respectively. The data (table AT.9) were corrected for interfering nuclear reactions involving Ca and K; the correction factors used were $(^{39}Ar/^{37}Ar)_{Ca}$=0.000781±0.000053, $(^{36}Ar/^{37}Ar)_{Ca}$=0.000205±0.000022 and $(^{40}Ar/^{39}Ar)_{K}$=0.031±0.008. Corrections were also applied for mass spectrometer fractionation, ^{37}Ar decay since the time of irradiation, and background levels of Ar (monitored from analysis of blanks).

A.7 List of constants used in this thesis

Where Sr and Nd data are reported using the ε notation of DePaolo and Wasserberg (1976), the constants used in the conversions were;

$^{143}Nd/^{144}Nd_{CHUR}$=0.51264
$^{147}Sm/^{144}Nd_{CHUR}$=0.1967
$^{87}Sr/^{86}Sr_{Bulk\ earth}$=0.7047
$^{87}Rb/^{86}Sr_{Bulk\ earth}$=0.0847

Model Sr and Nd ages are reported relative to depleted mantle (DePaolo, 1981; Jacobsen and Wasserburg, 1979);

$^{87}Sr/^{86}Sr_{DM}$=0.70306
$^{87}Rb/^{86}Sr_{DM}$=0.0487
$^{143}Nd/^{144}Nd_{DM}$=0.51310
$^{147}Sm/^{144}Nd_{DM}$=0.2238

Normalising values used in this thesis

	(a)	(b)	(c)
Rb	43	0.56	31.0
Ba	722	6.3	350
Th	6.86	0.12	4.00
U	1.22	0.05	1.02
K	1.95	0.07	1.45
Ta	4.54	0.13	2.7
Nb	62	2.33	48.0
La	55.3	2.5	37.0
Ce	121	7.5	80.0
Sr	1076	90	660
Nd	55	7.3	38.5
P	0.7	0.117	0.62
Hf	6.6	2.05	7.80
Zr	280	74	280
Eu	3.31	1.02	3.00
Ti	2.85	1.268	2.87
Tb	0.93	0.67	1.05
Y	26.3	28	29

	(d)	(e)
SiO2	66.0	58.0
TiO2	0.6	0.8
Al2O3	16.0	18.0
FeO	4.5	7.5
MgO	2.3	0.14
CaO	3.5	3.5
Na2O	3.8	7.5
K2O	3.3	3.5
P2O5	0.17	1.5
Cr	35	55
Ni	20	30
Rb	110	42
Sr	350	400
Ba	700	350
Th	10.5	4.8
U	2.5	1.25
Pb	15	10
Zr	240	100
Nb	25	11
La	30	19
Ce	64	38
Nd	26	16
Sm	4.5	3.7
Eu	0.88	1.1
Yb	2.2	2.2
Y	22	22

	(f)
La	0.328
Ce	0.805
Nd	0.630
Sm	0.203
Eu	0.077
Gd	0.276
Tb	0.052
Ho	0.780
Tm	0.043
Yb	0.220
Lu	0.034

(a), average Tristan da Cunha basanite composition (data from le Roex et al., 1990); (b), average N-type MORB; (c), average oceanic island basalt ((b) and (c) from Sun and McDonough, 1989). (d) average upper crust, and (e), average continental crust (from Taylor and McLennan, 1981), used in the AFC calculations in Chapter 3. (f) is the chondritic rare earth element composition of Nakamura (1974).

Partition coefficients used in the trace element modelling in Chapters 2 and 3, were taken from Henderson (1982) and Erlank et al. (1984). Partition coefficients for the rare earth elements were taken from McKenzie and O'Nions (1992)

	Olivine	O.pyroxene	C.pyroxene	Plagioclase	T.magnetite	Apatite
Zr	0.01	0.03	0.100	0.01	0.10	0.01
Nb	0.001	0.15	0.100	0.01	0.80	0.01
Y	0.01	0.20	0.500	0.01	0.20	15.0
Rb	0.0001	0.001	0.05	0.01	0.01	0.01
Sr	0.001	0.01	0.100	2.0	0.01	0.01
Ba	0.0001	0.001	0.05	0.15	0.01	0.01
Ni	4.48	1.12	0.78	0.01	0.01	0.01
Cr	2.1	10.0	8.40	0.20	11.0	0.01
La	0.0004	0.002	0.054	0.27	0.01	
Ce	0.0005	0.003	0.098	0.20	0.01	
Nd	0.0010	0.0068	0.21	0.14	0.01	
Sm	0.0013	0.010	0.26	0.11	0.01	
Eu	0.0016	0.013	0.31	0.73	0.01	
Gd	0.0015	0.016	0.30	0.066	0.01	
Tb	0.0015	0.019	0.31	0.06	0.01	
Yb	0.0015	0.049	0.28	0.031	0.01	
Lu	0.0015	0.060	0.28	0.025	0.01	

A.9 Discriminant functions

The discriminant functions used in classification of the dolerite magma types in Chapters 2 and 3 were calculated using the statistical programme SPSSX on the Open University VAX. The discriminant functions have the form

$$Xa.A + Xb.B + Xc.C \ldots\ldots\ldots\ldots Xn.N + \text{constant}$$

where Xa is the concentration of element a, and A, B, C etc are the discriminant factors calculated by the program and listed below

Chapter 2

	Function 1	Function 2
SiO2	-0.01723161	0.1591835
TiO2	2.942523	2.607987
Al2O3	-0.1733708	0.03356253
Fe2O3	-1.229843	-0.08873302
K2O	0.4927523	-1.071174
P2O5	-3.044805	6.104037
Rb	-0.007510658	0.02386565
Sr	0.00539181	-0.007283205
Y	-0.001320992	-0.006857603
Zr	0.00006303477	-0.009978715
Ba	0.001539753	0.001798541
Constant	7.091665	-11.91341

	Function 1	Function 2
SiO2	0.9580039	0.1071938
TiO2	4.252995	-0.06839953
Fe2O3	-0.01152031	-0.136052
K2O	0.5598957	-0.1780675
P2O5	5.902192	-2.434293
Ba	-0.0009455685	-0.00001310996
Rb	0.002185035	0.03448961
Sr	-0.00001789572	0.001972352
Zr	-0.03854529	-0.0007226138
Constant	-52.63988	-6.287436

A.9 Data tables

Sample	MR891	MR892	MR895	MR896	MR897	MR898	MR899
Magma type	Esmeralda	Esmeralda	Ponta Grossa	Ponta Grossa	Ponta Grossa	Ponta Grossa	Ponta Grossa
Latitude (°S)	25.753	25.753	25.161	24.741	24.741	24.580	24.741
Longitude (°W)	48.514	48.514	49.351	50.000	50.000	49.912	50.000
SiO2	52.02	51.79	51.18	50.84	49.90	50.20	51.21
TiO2	1.42	1.75	3.71	2.85	2.81	3.81	1.83
Al2O3	14.01	13.89	13.16	13.25	13.25	14.40	14.11
Cr2O3	0.02					0.00	0.03
Fe2O3	13.88	13.84	14.93	15.42	15.27	14.33	13.88
MnO	0.21	0.20	0.21	0.22	0.21	0.19	0.26
MgO	5.83	5.50	4.04	4.54	5.31	4.23	6.51
CaO	9.82	9.52	7.76	8.39	9.49	8.33	10.29
Na2O	2.57	2.55	2.67	2.73	2.53	2.93	2.33
K2O	0.75	0.92	1.96	1.72	1.19	1.57	0.84
P2O5	0.15	0.20	1.07	0.58	0.41	0.62	0.21
TOTAL	100.65	100.14	100.69	100.52	100.37	100.60	101.48
MgO/(MgO+FeO)	49.47	48.08	38.68	40.70	44.77	40.76	52.22
Loss on ignition		0.26	1.06	0.88	0.21		
Zn			136.9	117.9	113.0	119.8	93.6
Cu			64.1	244.3	267.9	125.7	205.9
Ni			20.3	47.6	54.5	31.5	78.6
Co			43.6	41.3	44.8	39.6	49.8
Cr			24.6	58.8	95.7	11.0	145.6
V			306.3	356.0	408.9	367.7	406.8
Ba			554.5	631.6	459.0	613.9	318.9
Ga			25.6	21.4	22.4	26.8	19.3
Rb			47.6	49.2	30.7	37.5	20.6
Sr			620.3	382.5	398.3	721.6	309.4
Y			51.2	46.7	36.7	74.1	38.5
Zr			313.7	214.0	176.8	238.6	130.5
Nb			30.3	19.3	17.0	22.1	11.5
Pb			7.1	6.8	5.0	5.0	3.0
Th			4.7	5.2	2.2	2.9	3.0
U			0.5	1.2	0.5	0.3	
Quartz	2.89	3.44	5.49	2.52	1.74	2.66	1.77
Corundum							
Orthoclase	4.43	5.44	11.58	10.16	7.03	9.28	4.96
Albite	21.75	21.58	22.59	23.10	21.41	24.79	19.72
Anorthite	24.48	23.74	18.13	18.82	21.28	21.50	25.56
Leucite							
Nepheline							
Diopside	19.29	18.41	11.16	15.89	19.21	13.11	19.89
Hypersthene	20.38	19.39	17.48	18.40	18.59	16.07	21.15
Olivine							
2CaO.SiO2							
Magnetite	3.02	3.01	3.25	3.35	3.32	3.12	3.02
Ilmenite	2.70	3.32	7.05	5.41	5.34	7.24	3.48
H2O apatite	0.35	0.47	2.52	1.37	0.97	1.46	0.50
H2O+	-0.01	-0.01	-0.05	-0.02	-0.02	-0.03	-0.01
Total	99.27	98.78	99.21	99.01	98.86	99.20	100.03
87Sr/86Sr (measured)	0.707480	0.706599				0.705958	0.706284
87Sr/86Sr (initial)	0.706138	0.705265				0.705680	0.705928
εSr	25.39	12.99				18.89	22.41
143Nd/144Nd (measured)	0.512513						0.512394
143Nd/144Nd (initial)	0.512366						0.512273
εNd	-2.05						-3.86
206Pb/204Pb	18.8565		18.0742	17.9427	17.9129	18.0212	17.9536
207Pb/204Pb	15.7028		15.5054	15.5063	15.4768	15.4846	15.5306
208Pb/204Pb	38.9004		38.3602	38.3104	38.1852	38.2343	38.3772

Sample	MR8910	MR8911	MR8912	MR8913	MR8914	MR8915	MR8916
Magma type	Ponta Grossa	Ponta Grossa	Ponta Grossa	Ponta Grossa	Ponta Grossa	Ponta Grossa	Ponta Grossa
Latitude (°S)	24.741	24.741	24.741	24.741	24.778	24.741	24.593
Longitude (°W)	50.000	50.000	50.000	50.000	50.041	50.135	50.270
SiO2	51.19	51.20	50.92	51.15	52.10	50.12	51.29
TiO2	1.85	3.23	1.93	1.84	3.22	3.11	3.05
Al2O3	13.99	13.25	13.96	13.93	12.98	13.08	12.70
Cr2O3	0.02	0.02		0.02	0.01		0.01
Fe2O3	13.78	15.06	14.02	13.77	15.26	16.55	15.74
MnO	0.31	0.19	0.19	0.21	0.21	0.29	0.22
MgO	6.33	4.80	5.95	6.28	4.40	4.74	5.12
CaO	10.31	8.38	10.13	10.47	7.05	7.87	8.42
Na2O	2.28	2.58	2.37	2.36	2.93	2.57	2.57
K2O	0.82	1.39	0.94	0.79	1.91	1.46	1.44
P2O5	0.21	0.40	0.22	0.21	0.42	0.48	0.38
TOTAL	101.09	100.49	100.63	101.04	100.51	100.26	100.93
MgO/(MgO+FeO)	51.71	42.62	49.73	51.53	40.19	40.03	43.12
Loss on ignition			0.51			1.20	
Zn	91.5	108.2	92.7	100.1	124.7	104.9	113.0
Cu	207.6	226.1	228.9	200.7	262.2	139.0	207.5
Ni	77.3	59.6	64.7	89.8	39.8	39.6	63.2
Co	46.1	49.3	42.4	50.3	47.5	43.9	46.1
Cr	135.8	144.5	128.9	138.6	35.6	26.9	46.1
V	404.6	409.4	400.0	396.5	436.2	453.6	528.2
Ba	308.5	509.6	388.7	295.9	685.9	489.6	539.5
Ga	20.0	25.0	21.2	18.1	23.1	23.5	22.5
Rb	20.5	38.4	23.4	18.5	52.6	35.5	39.6
Sr	311.8	540.3	335.0	305.2	452.1	415.2	355.6
Y	29.7	43.9	31.1	30.8	43.9	42.9	43.8
Zr	131.8	237.5	137.4	131.2	274.0	231.4	213.1
Nb	11.3	19.6	11.8	11.5	24.6	20.9	19.3
Pb	3.7	8.2	2.6	3.7	6.9	6.2	7.7
Th	2.8	3.6	3.0	2.3	2.5	3.6	6.5
U	0.4	0.9	1.8		0.2	2.0	2.0
Quartz	2.45	4.53	2.07	2.05	4.16	3.16	3.75
Corundum							
Orthoclase	4.85	8.21	5.56	4.67	11.29	8.63	8.51
Albite	19.29	21.83	20.05	19.97	24.79	21.75	21.75
Anorthite	25.52	20.47	24.68	25.08	16.62	19.84	18.86
Leucite							
Nepheline							
Diopside	20.02	15.38	19.97	21.04	13.03	13.43	17.00
Hypersthene	20.47	18.25	19.69	19.84	18.67	21.14	19.40
Olivine							
2CaO.SiO2							
Magnetite	3.00	3.28	3.05	2.99	3.32	3.60	3.42
Ilmenite	3.51	6.13	3.67	3.49	6.12	5.91	5.79
H2O apatite	0.50	0.94	0.52	0.50	0.99	1.13	0.90
H2O+	-0.01	-0.02	-0.01	-0.01	-0.02	-0.02	-0.02
Total	99.59	99.01	99.25	99.63	98.97	98.57	99.37
87Sr/86Sr (measured)					0.707116	0.706186	
87Sr/86Sr (initial)					0.706495	0.705729	
εSr					30.45	19.58	
143Nd/144Nd (measured)						0.512399	
143Nd/144Nd (initial)						0.512278	
εNd						-3.76	
206Pb/204Pb		17.5788	17.9255		16.9510		
207Pb/204Pb		15.5100	15.5136		15.4066		
208Pb/204Pb		38.0369	38.3318		37.5514		

Sample	MR8917	MR8918	MR8919	MR8920	MR8921	MR8922	MR8924
Magma type	Ponta Grossa	Ponta Grossa	Ponta Grossa	Ponta Grossa	Ponta Grossa	Ponta Grossa	Ponta Grossa
Latitude (°S)	24.494	24.463	24.438	24.321	24.161	24.148	24.056
Longitude (°W)	50.455	50.507	50.560	50.627	50.560	50.560	50.507
SiO2	51.85	50.28	51.71	49.85	52.74	52.13	51.72
TiO2	2.60	3.00	2.83	3.53	3.31	2.05	2.61
Al2O3	12.70	13.23	13.38	12.70	13.69	13.65	12.84
Cr2O3	0.01	0.01	0.01		0.00	0.02	0.01
Fe2O3	15.57	15.15	14.58	16.05	13.64	14.13	15.72
MnO	0.20	0.21	0.21	0.21	0.20	0.20	0.22
MgO	4.60	4.61	4.55	4.44	3.70	5.62	4.54
CaO	8.60	8.50	8.48	8.32	7.78	9.86	8.57
Na2O	2.36	2.66	2.61	2.66	2.84	2.34	2.51
K2O	1.20	1.45	1.55	1.39	2.03	0.93	1.23
P2O5	0.32	0.39	0.40	0.47	0.78	0.24	0.34
TOTAL	100.01	99.48	100.32	99.63	100.72	101.18	100.30
MgO/(MgO+FeO)	40.78	41.49	42.11	39.20	38.73	48.11	40.23
Loss on ignition				0.27			
Zn	112.0	108.8	109.7	116.6	121.8	98.0	121.9
Cu	322.9	255.7	246.8	247.8	58.9	234.1	289.2
Ni	39.0	39.5	48.1	32.6	14.2	50.5	37.1
Co	40.2	45.7	43.7	40.8	28.9	47.2	39.9
Cr	54.9	45.3	42.4	32.9	9.0	85.2	47.9
V	403.3	474.5	423.6	489.2	269.9	385.2	464.8
Ba	426.0	532.4	574.8	517.8	675.2	379.1	427.8
Ga	22.6	23.9	23.6	23.9	27.1	20.6	21.8
Rb	31.9	37.4	37.6	38.4	39.0	21.9	31.7
Sr	250.8	473.4	448.1	405.7	915.8	271.2	282.9
Y	53.0	36.7	39.3	42.4	50.1	37.6	46.3
Zr	220.1	223.6	244.1	229.0	326.0	163.4	221.2
Nb	18.2	20.7	22.6	19.9	30.4	13.4	18.7
Pb	7.3	5.6	5.0	5.5	5.9	5.5	5.8
Th	2.6	2.3	4.6	4.4	4.0	1.2	3.1
U	0.4	1.3	1.5	0.6	1.6	1.7	
Quartz	6.35	2.96	4.55	3.46	6.22	4.47	5.39
Corundum							
Orthoclase	7.09	8.57	9.16	8.21	12.00	5.50	7.27
Albite	19.97	22.51	22.09	22.51	24.03	19.80	21.24
Anorthite	20.51	19.88	20.21	18.61	18.61	23.99	20.14
Leucite							
Nepheline							
Diopside	16.77	16.46	16.03	16.37	12.43	19.35	16.87
Hypersthene	18.71	17.71	17.33	17.59	15.00	19.10	18.68
Olivine							
2CaO.SiO2							
Magnetite	3.39	3.29	3.17	3.49	2.97	3.07	3.42
Ilmenite	4.94	5.70	5.37	6.70	6.29	3.89	4.96
H2O apatite	0.75	0.92	0.94	1.11	1.84	0.57	0.80
H2O+	-0.01	-0.02	-0.02	-0.02	-0.03	-0.01	-0.01
Total	98.47	97.98	98.85	98.04	99.35	99.75	98.74
87Sr/86Sr (measured)		0.707023	0.706206		0.708336	0.706563	
87Sr/86Sr (initial)		0.706601	0.705758		0.708109	0.706132	
εSr		31.96	19.99		53.36	25.29	
143Nd/144Nd (measured)			0.512382		0.512413		
143Nd/144Nd (initial)			0.512261		0.512292		
εNd			-4.09		-3.49		
206Pb/204Pb	17.6915		17.8687	17.9693	18.1169	17.9225	
207Pb/204Pb	15.5069		15.5184	15.5468	15.5406	15.5300	
208Pb/204Pb	38.3534		38.3714	38.4746	38.4596	38.3897	

Sample	MR8925	MR8926	MR8927	MR8928	MR8929	MR8930	MR8931
Magma type	Ponta Grossa	Ponta Grossa	Ponta Grossa	Ponta Grossa	Ponta Grossa	Ponta Grossa	Ponta Grossa
Latitude (°S)	24.016	23.926	23.926	23.901	23.877	23.862	23.774
Longitude (°W)	50.493	50.573	50.575	50.587	50.607	50.608	50.000
SiO2	50.34	51.02	51.52	54.37	53.85	50.23	65.68
TiO2	2.61	3.04	3.08	3.46	3.41	3.23	1.43
Al2O3	14.18	13.27	13.02	13.08	13.18	13.57	13.96
Cr2O3	0.01		0.01	0.00		0.00	0.00
Fe2O3	15.49	15.40	15.68	13.51	13.42	16.62	7.47
MnO	0.20	0.22	0.20	0.17	0.16	0.22	0.11
MgO	4.84	4.52	4.47	3.28	3.18	3.79	0.37
CaO	9.42	8.33	8.49	6.64	6.48	8.78	1.99
Na2O	2.59	2.47	2.69	2.95	3.10	2.69	3.65
K2O	1.08	1.52	1.24	2.48	2.47	1.31	4.14
P2O5	0.35	0.47	0.35	0.80	0.80	0.41	0.41
TOTAL	101.11	100.24	100.76	100.75	100.04	100.85	99.72
MgO/(MgO+FeO)	42.14	40.62	39.92	36.14	35.58	34.70	10.35
Loss on ignition		1.08			0.16		
Zn	100.6	102.0	117.8	124.1	124.3	122.7	259.5
Cu	234.2	176.8	219.2	133.5	141.2	281.6	-
Ni	45.2	34.9	34.7	25.3	23.9	23.3	21.2
Co	43.4	52.7	42.3	28.6	28.0	38.8	16.8
Cr	66.4	29.1	32.6	18.8	23.7	18.3	-
V	502.3	423.9	500.1	292.5	297.7	536.4	18.1
Ba	433.6	776.7	433.1	942.0	911.3	485.3	1625.5
Ga	22.5	23.1	23.5	29.8	30.3	23.9	24.9
Rb	30.6	52.9	31.8	77.3	77.6	36.8	277.0
Sr	372.7	729.0	423.6	595.7	586.9	387.1	424.3
Y	36.8	41.8	42.6	47.4	46.5	42.6	45.0
Zr	164.4	219.9	234.6	476.4	473.2	198.3	579.7
Nb	14.8	18.2	18.8	28.2	28.6	17.9	45.4
Pb	5.2	8.7	5.1	13.5	10.2	6.3	14.7
Th	2.3	4.7	3.7	11.3	10.3	3.2	11.9
U	1.0	0.4		2.6	3.0	0.8	2.5
Quartz	2.10	4.68	4.76	8.30	7.36	3.27	21.66
Corundum							
Orthoclase	6.38	8.98	7.33	14.66	14.60	7.74	24.47
Albite	21.92	20.90	22.76	24.96	26.23	22.76	30.89
Anorthite	23.88	20.63	19.79	15.12	14.75	21.08	7.19
Leucite							
Nepheline							
Diopside	17.17	14.71	16.75	10.54	10.20	16.67	0.00
Hypersthene	19.00	18.60	17.74	14.47	14.36	16.98	8.13
Olivine							
2CaO.SiO2							
Magnetite	3.37	3.35	3.41	2.94	2.92	3.61	1.62
Ilmenite	4.96	5.77	5.85	6.57	6.48	6.13	2.72
H2O apatite	0.83	1.11	0.83	1.89	1.89	0.97	0.97
H2O+	-0.01	-0.02	-0.01	-0.03	-0.03	-0.02	-0.02
Total	99.58	98.73	99.20	99.42	98.75	99.21	98.46
87Sr/86Sr (measured)	0.706259	0.706816		0.706402			0.707547
87Sr/86Sr (initial)	0.705820	0.706428		0.705709			0.704060
εSr	20.88	29.51		19.29			-4.12
143Nd/144Nd (measured)	0.512381	0.512413			0.512435		0.512819
143Nd/144Nd (initial)	0.512260	0.512292			0.512314		0.512698
εNd	-4.11	-3.49			-3.06		4.44
206Pb/204Pb							18.3246
207Pb/204Pb							15.5845
208Pb/204Pb							38.6354

Sample	MR8932	MR8933	MR8935	MR8936	MR8937	MR8938	MR8939
Magma type	Ponta Grossa	Ponta Grossa	Ponta Grossa	Ponta Grossa	Ponta Grossa	Ponta Grossa	Ponta Grossa
Latitude (°S)	23.778	23.774	23.774	23.774	23.774	23.774	23.716
Longitude (°W)	50.040	50.000	50.000	49.987	49.977	49.971	49.907
SiO2	60.65	50.76	50.72	51.61	51.43	50.75	50.55
TiO2	1.46	2.63	2.57	2.67	2.61	2.63	3.28
Al2O3	12.65	13.18	13.23	13.10	13.24	13.27	12.78
Cr2O3	0.00	0.01	0.01	0.01	0.02	0.01	0.01
Fe2O3	12.99	15.53	15.29	14.53	14.58	15.62	16.65
MnO	0.21	0.22	0.21	0.20	0.21	0.22	0.22
MgO	0.91	5.08	5.06	5.27	5.35	4.91	4.61
CaO	4.75	9.35	9.13	9.30	8.88	9.35	8.59
Na2O	3.39	2.52	2.36	2.54	2.70	2.59	2.55
K2O	3.10	1.14	1.10	1.19	1.30	1.22	1.30
P2O5	0.49	0.38	0.39	0.30	0.30	0.38	0.33
TOTAL	100.60	100.81	100.09	100.72	100.62	100.94	100.87
MgO/(MgO+FeO)	14.04	43.26	43.54	45.81	46.10	42.28	39.22
Loss on ignition							
Zn	141.9	112.2	125.3	97.0	106.6	105.1	116.0
Cu	48.6	235.8	222.4	211.4	210.2	250.9	342.8
Ni	1.3	46.8	48.4	52.6	58.7	49.6	40.6
Co	16.1	40.7	43.7	42.0	42.6	47.0	45.1
Cr		67.6	67.5	75.5	78.1	73.4	37.1
V	0.5	436.5	446.1	442.9	445.6	431.3	622.3
Ba	1027.3	431.0	439.2	446.5	430.8	446.4	461.9
Ga	26.9	22.2	21.7	22.2	22.7	21.4	23.9
Rb	84.7	32.0	32.8	28.7	33.2	32.9	33.6
Sr	329.2	525.1	363.6	395.6	426.2	357.8	410.6
Y	83.0	39.2	40.0	40.2	40.4	40.6	40.6
Zr	451.3	165.9	179.5	204.2	202.2	188.2	223.4
Nb	34.2	15.0	16.2	16.3	15.1	16.2	19.0
Pb	14.0	4.9	6.8	5.2	1.9	8.7	6.0
Th	7.7	1.7	3.8	4.7	3.1	4.2	3.6
U	0.8		1.7	0.5	1.3	1.5	0.9
Quartz	14.64	3.01	4.22	3.92	2.79	2.55	3.66
Corundum							
Orthoclase	18.32	6.74	6.50	7.03	7.68	7.21	7.68
Albite	28.69	21.32	19.97	21.49	22.85	21.92	21.58
Anorthite	10.14	21.28	22.26	20.83	20.17	20.98	19.59
Leucite							
Nepheline							
Diopside	8.91	18.85	17.07	19.37	18.19	19.13	17.46
Hypersthene	11.84	18.80	19.43	17.70	18.65	18.33	18.64
Olivine							
2CaO.SiO2							
Magnetite	2.83	3.38	3.33	3.16	3.17	3.40	3.62
Ilmenite	2.77	4.99	4.88	5.07	4.96	4.99	6.23
H2O apatite	1.16	0.90	0.92	0.71	0.71	0.90	0.78
H2O+	-0.02	-0.02	-0.02	-0.01	-0.01	-0.02	-0.01
Total	99.28	99.25	98.55	99.27	99.15	99.39	99.22
87Sr/86Sr (measured)	0.707686						
87Sr/86Sr (initial)	0.706312						
εSr	27.85						
143Nd/144Nd (measured)							
143Nd/144Nd (initial)							
εNd							
206Pb/204Pb	18.0826						
207Pb/204Pb	15.5415						
208Pb/204Pb	38.4347						

Sample	MR8940	MR8941	MR8942	MR8987	MR8988	MR8989	MR8990
Magma type	Ponta Grossa	Ponta Grossa	Ponta Grossa	Ponta Grossa	Ponta Grossa	Ponta Grossa	Ponta Grossa
Latitude (°S)	23.679	23.678	23.654	22.795	22.700	22.329	22.447
Longitude (°W)	49.840	49.838	49.853	47.022	46.977	46.869	46.720
SiO2	51.67	51.28	51.25	50.33	50.21	49.10	49.64
TiO2	2.59	2.60	3.58	2.89	2.37	3.19	3.31
Al2O3	13.04	12.99	12.97	13.61	13.80	13.48	12.91
Cr2O3	0.02	0.02	0.00	0.01	0.02	0.01	0.01
Fe2O3	14.79	14.86	14.87	15.72	14.58	16.01	16.15
MnO	0.22	0.22	0.19	0.21	0.21	0.21	0.22
MgO	5.32	5.20	4.19	4.90	6.20	5.38	4.85
CaO	9.60	9.44	8.08	9.44	10.35	9.76	9.55
Na2O	2.50	2.50	2.71	2.63	2.43	2.48	2.64
K2O	0.93	0.88	1.50	1.19	0.96	1.13	0.92
P2O5	0.30	0.30	0.50	0.35	0.28	0.34	0.39
TOTAL	100.98	100.29	99.85	101.28	101.40	101.08	100.58
MgO/(MgO+FeO)	45.60	44.92	39.64	42.08	49.78	43.92	41.17
Loss on ignition							
Zn	105.2	119.0	127.5	107.3	95.1	107.3	129.9
Cu	274.1	266.7	50.5	252.9	198.6	182.4	208.7
Ni	46.0	46.5	25.0	44.8	65.9	49.1	46.6
Co	44.2	42.3	43.2	42.8	47.5	47.7	48.5
Cr	93.4	89.1	22.7	74.7	122.8	58.9	57.6
V	399.2	400.7	388.2	569.6	446.2	602.2	499.2
Ba	288.4	371.1	511.6	488.6	380.3	414.9	412.2
Ga	21.9	21.5	24.5	22.5	21.6	23.4	22.3
Rb	21.3	15.7	36.1	30.8	25.5	27.8	77.0
Sr	259.1	284.0	503.0	392.3	384.2	429.7	451.4
Y	49.7	46.4	43.5	36.8	30.9	31.2	36.2
Zr	204.3	203.9	274.5	184.5	148.9	178.7	205.4
Nb	16.5	16.6	22.7	16.9	13.9	15.8	20.9
Pb	3.7	3.8	9.0	6.8	2.4	5.9	2.0
Th	2.2	4.6	3.9	1.8	2.5	2.8	3.5
U			0.8		1.4	0.9	0.9
Quartz	4.43	4.55	5.51	1.85	0.58	0.60	2.46
Corundum							
Orthoclase	5.50	5.20	8.86	7.03	5.67	6.68	5.44
Albite	21.15	21.15	22.93	22.25	20.56	20.99	22.34
Anorthite	21.61	21.62	18.79	21.82	23.91	22.31	20.66
Leucite							
Nepheline							
Diopside	19.97	19.32	15.03	18.95	21.15	19.85	20.16
Hypersthene	17.99	18.08	16.06	18.10	19.74	18.76	17.23
Olivine							
2CaO.SiO2							
Magnetite	3.22	3.23	3.23	3.42	3.17	3.48	3.51
Ilmenite	4.92	4.94	6.80	5.49	4.50	6.06	6.29
H2O apatite	0.71	0.71	1.18	0.83	0.66	0.80	0.92
H2O+	-0.01	-0.01	-0.02	-0.01	-0.01	-0.01	-0.02
Total	99.48	98.78	98.38	99.72	99.94	99.51	98.98
87Sr/86Sr (measured)			0.706294				0.708009
87Sr/86Sr (initial)			0.705911				0.707098
εSr			22.16				39.01
143Nd/144Nd (measured)							0.512382
143Nd/144Nd (initial)							0.512261
εNd							-4.09
206Pb/204Pb			17.9743	18.0171			
207Pb/204Pb			15.5393	15.5602			
208Pb/204Pb			38.4182	38.4308			

Sample	MR8991	MR8992	MR8944	MR8945	MR8946	MR8967	MR8968
Magma type	Ponta Grossa	Ponta Grossa	Sao Sebastiao	Sao Sebastiao	Sao Sebastiao	Sao Sebastiao	Sao Sebastiao
Latitude (°S)	22.358	22.032	23.102	22.783	22.768	23.822	23.823
Longitude (°W)	46.392	46.903	45.973	45.613	45.615	45.264	45.441
SiO2	49.86	51.93	44.4	44.39	43.07	45.53	42.24
TiO2	3.33	2.38	3.71	3.18	3.58	1.85	2.8
Al2O3	12.92	12.74	14.84	13.64	13.26	8.59	14.41
Cr2O3	0.01	0.01	0	0.06	0.03	0.15	
Fe2O3	16.33	15.94	12.85	12.46	12.83	9.89	14.45
MnO	0.23	0.24	0.22	0.19	0.24	0.15	0.18
MgO	5.01	4.91	5.58	8.9	8.53	14.22	7.6
CaO	9.23	9.02	8.89	10.78	13.86	17.62	13.55
Na2O	2.50	2.56	4.34	2.71	2.54	0.91	2.86
K2O	1.26	1.10	2.98	2.57	1.2	0.88	0.69
P2O5	0.39	0.29	1.41	0.84	0.82	0.31	0.86
TOTAL	101.09	101.12	99.22	99.7	99.97	100.11	99.64
MgO/(MgO+FeO)	41.69	41.79	50.3	62.5	60.8	77	
Loss on ignition			3.142	5.584	3.765	6.215	1.267
Zn	123.0	124.5	129.6	101.6	86.8	57.8	95.5
Cu	209.6	247.4	13	27.7	54.2	80.5	48.3
Ni	43.5	43.2	28.5	138.8	82.2	290.6	82.2
Co	49.3	45.7	36	51.6	52.4	55.5	63.5
Cr	52.5	70.9	36.5	362.4	169.9	794.8	118.1
V	516.0	449.0	219.6	228	307.2	265	382.1
Ba	419.2	367.6	3789.5	1011.5	1483.3	414.6	778.9
Ga	23.6	20.9	22.7	19.6	18.4	11.7	19.4
Rb	30.7	27.7	129.5	63.9	90.4	26	32.6
Sr	431.1	281.9	1892.9	1093.6	1583.2	469.8	1219.7
Y	36.5	40.9	39.3	30.1	31.2	17.9	29.4
Zr	212.1	185.4	434.4	282.6	276.4	130.3	192.4
Nb	20.4	16.4	103.3	75.3	82.8	32.1	49.9
Pb	7.2	9.2	11.3	4.1	6.6	3.6	0.1
Th	3.6	4.2	12.8	6.3	7.2	1.8	5.8
U	0.2		1.6	1.9		1.5	1.7
Quartz	2.28	4.42					
Corundum							
Orthoclase	7.45	6.50	17.61	15.19	7.09		4.08
Albite	21.15	21.66	11.89	6.10	4.29		5.74
Anorthite	20.31	20.02	12.21	17.43	21.24	16.76	24.44
Leucite						4.08	
Nepheline			13.46	9.12	9.32	4.17	10.00
Diopside	19.11	19.08	18.59	24.69	34.13	52.03	30.43
Hypersthene	18.36	19.16					
Olivine			11.05	15.15	11.04	14.49	13.08
2CaO.SiO2						1.06	
Magnetite	3.55	3.47	2.79	2.71	2.79	2.15	3.14
Ilmenite	6.32	4.52	7.05	6.04	6.80	3.51	5.32
H2O apatite	0.92	0.68	3.33	1.98	1.94	0.73	2.03
H2O+	-0.02	-0.01	-0.06	-0.04	-0.04	-0.01	-0.04
Total	99.44	99.51	97.91	98.41	98.60	98.96	98.23
87Sr/86Sr (measured)	0.706024	0.706406	0.706054	0.705610	0.706354	0.705484	0.704747
87Sr/86Sr (initial)	0.705644	0.705881	0.705829	0.705418	0.706166	0.705302	0.704659
εSr	18.37	21.74	21.00	15.16	25.79	13.52	4.39
143Nd/144Nd (measured)			0.512530	0.512238	0.512503	0.512660	
143Nd/144Nd (initial)			0.512474	0.512179	0.512442	0.512595	
εNd			0.06	-5.69	-0.56	2.41	
206Pb/204Pb	18.7860	18.6231			18.6280	19.0047	18.9530
207Pb/204Pb	15.6625	15.6196			15.4948	15.5633	15.5438
208Pb/204Pb	38.7420	38.6167			38.7953	39.1191	39.0112

Sample	MR8969	MR8970	MR8971	MR8972	MR8973	MR8974	MR8976
Magma type	Sao Sebastiao	Sao Sebastiao	Sao Sebastiao	Sao Sebastiao	Sao Sebastiao	Sao Sebastiao	Sao Sebastiao
Latitude (°S)	23.823	23.821	23.824	23.824	23.824	23.821	23.787
Longitude (°W)	45.441	45.441	45.424	45.424	45.417	45.417	45.397
SiO2	66.8	43.6	43.98	38.47	59.11	43.65	45.22
TiO2	0.52	2.54	2.24	1.82	1.63	1.3	2.62
Al2O3	15.92	12.44	11.34	12.3	17.72	12.57	16.92
Cr2O3	0	0.04	0.07	0	0	0.14	0
Fe2O3	5.59	13.03	11.25	12.47	9.74	11.07	12.91
MnO	0.2	0.19	0.17	0.34	0.11	0.19	0.21
MgO	0.19	9.93	10.59	7.25	1.19	13.15	4.7
CaO	0.2	14.68	17.4	18.89	0.97	14.66	10.66
Na2O	5.43	1.97	0.9	2.33	5.87	1.48	3.34
K2O	5.83	1.63	1.95	1.64	2.79	1.25	2.29
P2O5	0.06	0.39	0.36	2.09	0.86	0.67	0.52
TOTAL	100.75	100.43	100.23	97.62	99.99	100.13	99.37
MgO/(MgO+FeO)	7.3	64	68.7	57.5	22.2	73.5	45.9
Loss on ignition	2.829	4.166	5.155	14.185	3.364	5.024	1.757
Zn	101.6	81.2	71.8	96.1	157	64.3	93
Cu	-	107	131.6	52.4	-	60.1	131.4
Ni	1.2	162.6	200.3	83	18.3	376.2	46.4
Co	5.1	60.9	58.5	51.4	12.7	57.5	45.5
Cr	-	212.9	344.6	23.9	3.1	811.7	20.3
V	0.2	336.5	326.1	318.2	38	209.3	310.4
Ba	503	808.6	951.8	1856.3	1009.7	712.5	977.4
Ga	24	16	15.2	13.2	22.5	12.2	21.3
Rb	119.7	44.3	53	38.3	64.6	45.8	56.2
Sr	27.7	589.4	524.7	3144.1	395.2	874	971.8
Y	54	22.4	22.2	38.8	69.8	27.8	32.9
Zr	519	182.6	176.3	209	546.7	177.3	271.4
Nb	107	51.8	49.8	88.4	90.1	49.2	77.5
Pb	15.9	7	3.9	19.7	97.7	3.1	7.8
Th	12.8	5	3.1	25.6	13.9	4.8	7.4
U	2.4	1.7		8.6	3	0.9	3
Quartz	9.49				8.41		
Corundum	0.46				5.34		
Orthoclase	34.45	1.93			16.49	1.48	13.53
Albite	45.95				49.67		10.97
Anorthite	0.60	20.29	21.14	18.26	-0.81	23.96	24.41
Leucite		6.04	9.04	7.60		4.63	
Nepheline		9.03	4.13	10.68		6.78	9.37
Diopside		40.49	41.05	25.97		35.65	20.78
Hypersthene	6.77				12.75		
Olivine		12.76	12.50	13.37		19.92	10.03
2CaO.SiO2			3.67	9.31			
Magnetite	1.22	2.83	2.45	2.71	2.12	2.41	2.81
Ilmenite	0.99	4.82	4.25	3.46	3.10	2.47	4.98
H2O apatite	0.14	0.92	0.85	4.93	2.03	1.58	1.23
H2O+	-0.00	-0.02	-0.02	-0.09	-0.04	-0.03	-0.02
Total	100.06	99.10	99.05	96.20	99.05	98.86	98.08
87Sr/86Sr (measured)		0.706122			0.705919	0.705437	0.705129
87Sr/86Sr (initial)		0.705875			0.705382	0.705265	0.704939
εSr		21.65			14.65	12.99	8.36
143Nd/144Nd (measured)	0.512512	0.512667	0.512693		0.512508	0.512709	0.512653
143Nd/144Nd (initial)	0.512442	0.512667	0.512693		0.512446	0.512649	0.512592
εNd	-0.57	3.82	4.33		-0.48	3.47	2.36
206Pb/204Pb	18.3289	18.9147	18.8151	18.3370	19.0724	18.8392	
207Pb/204Pb	15.4597	15.5371	15.5401	15.6260	15.6182	15.5416	
208Pb/204Pb	38.4773	38.9345	38.8217	38.7381	39.1538	39.0018	

Sample	MR8979	MR8981	MR8943	MR8948	MR8949	MR8950	MR8955
Magma type	Sao Sebastiao	Sao Sebastiao	Paraiba	Paraiba	Paraiba	Paraiba	Paraiba
Latitude (°S)	23.478	23.465	23.098	23.391	23.392	23.405	23.450
Longitude (°W)	45.07	45.064	45.975	45.296	45.296	45.296	45.282
SiO2	44.1	41.31	52.44	52.4	52.4	51.7	51.88
TiO2	3.14	3.54	3.57	3.45	3.66	4.12	3.65
Al2O3	13.62	12.11	13.08	13.81	14	13.14	13.79
Cr2O3	0.06	0.04	0.02	0.01	0.01	0.01	0.01
Fe2O3	12.22	13.25	13.1	12.39	12.56	13.88	13.04
MnO	0.22	0.19	0.17	0.16	0.18	0.18	0.19
MgO	9.35	11.88	4.9	4.77	4.65	4.54	4.31
CaO	11.29	11.93	8.03	8.08	7.95	8.06	7.23
Na2O	2.54	2.91	2.8	2.73	2.92	2.73	2.93
K2O	2.25	2.24	1.88	2.06	2.06	1.98	2.35
P2O5	0.85	0.97	0.49	0.52	0.55	0.58	0.94
TOTAL	99.64	100.37	100.48	100.39	100.94	100.93	100.31
MgO/(MgO+FeO)	64.1	67.6	46.6	47.3	46.3	43.3	43.5
Loss on ignition	3.129	4.423	0.751	0.965	1.282	0.388	1.355
Zn	104.7	109.1	102.5	85.3	108.8	100	85.9
Cu	26.7	18.2	160.3	142.8	134.3	186.8	58.2
Ni	185.2	206.5	64.4	66	66.9	57.9	47.1
Co	52.2	57.6	42.4	40.6	43.9	43.2	44.9
Cr	412.6	265.6	91.2	72.2	55.2	59.2	25
V	207.7	237.8	297.9	267.6	273.8	327.2	276.2
Ba	2058.9	1407.1	685.1	785	777.4	761.9	922.6
Ga	19.8	18.6	25.9	24.9	24.8	26.7	25.5
Rb	68.5	61.5	50.4	52.7	46.8	46.8	53.7
Sr	1603.8	1041	726.8	807.4	843.8	862.1	925.3
Y	32.3	33.4	41.1	38	39.9	41.4	69
Zr	342	323.8	282.6	308	315.1	315.4	335.3
Nb	83.9	74.9	24.6	26.7	29.9	28.6	40
Pb	7.3	7.9	6.6	11.5	8.7	10.2	10
Th	9.3	8.9	4.6	5.5	4.4	5.4	6.9
U	2.7	1.6	0.5	2	0.7	0.2	1.5
Quartz			4.99	4.79	4.18	4.83	4.35
Corundum							
Orthoclase	13.30	0.01	11.11	12.17	12.17	11.70	13.89
Albite	6.11		23.69	23.10	24.71	23.10	24.79
Anorthite	19.12	13.37	17.57	19.34	19.01	17.75	17.53
Leucite		10.38					
Nepheline	8.33	13.34					
Diopside	25.30	31.73	15.72	14.28	13.87	15.25	10.09
Hypersthene			15.33	15.02	14.79	14.74	16.41
Olivine	15.57	18.35					
2CaO.SiO2							
Magnetite	2.66	2.88	2.85	2.70	2.73	3.02	2.84
Ilmenite	5.96	6.72	6.78	6.55	6.95	7.83	6.93
H2O apatite	2.01	2.29	1.16	1.23	1.30	1.37	2.22
H2O+	-0.04	-0.04	-0.02	-0.02	-0.02	-0.02	-0.04
Total	98.32	99.01	99.17	99.16	99.68	99.55	99.01
87Sr/86Sr (measured)	0.705689	0.705252	0.706106	0.706886	0.707160	0.705664	0.707817
87Sr/86Sr (initial)	0.705549	0.705058	0.705736	0.706537	0.706864	0.705374	0.707507
εSr	17.02	10.05	19.67	31.05	35.69	14.54	44.82
143Nd/144Nd (measured)	0.512647	0.512658	0.512427		0.512328	0.512465	0.512284
143Nd/144Nd (initial)	0.512586	0.512598	0.512325		0.512221	0.512363	0.512180
εNd	2.24	2.48	-2.86		-4.88	-2.12	-5.67
206Pb/204Pb					17.6276		17.8615
207Pb/204Pb					15.5319		15.5336
208Pb/204Pb					38.2972		38.4900

Sample	MR8962	MR8963	MR8975	MR8977	MR8978	MR8980	MR8982
Magma type	Paraiba	Paraiba	Paraiba	Paraiba	Paraiba	Paraiba	Paraiba
Latitude (°S)	23.485	23.480	23.811	23.565	23.493	23.465	23.042
Longitude (°W)	45.369	45.380	45.408	45.279	45.148	45.064	44.983
SiO2	52.42	51.83	51.93	52.95	50.4	50.52	52.84
TiO2	3.43	3.67	4.08	3.19	3.97	3.91	3.38
Al2O3	13.66	13.5	13.75	13.62	14.19	13.44	13.76
Cr2O3	0.01	0.01	0	0.01	0.01	0	0.01
Fe2O3	12.71	12.72	14.44	12.4	13.11	14.61	12.68
MnO	0.18	0.17	0.15	0.18	0.16	0.17	0.18
MgO	4.04	4.63	4.24	4.66	4.85	4.52	4.19
CaO	6.41	6.88	6.91	7.18	7.96	7.56	6.7
Na2O	3.23	3.08	2.81	2.85	2.55	2.99	3.04
K2O	2.88	2.58	1.48	2.75	2.63	2.07	2.7
P2O5	0.87	0.55	0.64	0.73	0.52	0.63	0.88
TOTAL	99.83	99.62	100.43	100.53	100.36	100.45	100.36
MgO/(MgO+FeO)	42.6	45.9	40.6	46.7	46.3	41.9	43.5
Loss on ignition	1.16	1.211	2.055	1.159	7.011	1.955	1.199
Zn	107.1	131.1	125.2	85.6	108.8	118.5	105.7
Cu	54.8	143.9	154.5	95	10.9	84.5	53.7
Ni	34.8	72.8	65	65.6	28.2	39.8	53.7
Co	40.9	48.6	40.1	40.1	40.2	40	48.3
Cr	23.9	51.8	27	71.3	45.6	22.1	22.6
V	248.6	281.4	422.8	241	309.5	405.2	243.5
Ba	1110	864.6	1694.1	914.5	1463.7	641.9	1064.3
Ga	24.6	23.3	25.1	23.5	21.9	24.2	25.1
Rb	87.2	79.3	30.8	83.5	97	68.2	70.2
Sr	893.3	867.7	715.2	936.4	1124.7	630.4	911.4
Y	40.3	42.7	42.6	43.8	28.3	40.7	41.7
Zr	334.5	319	302.2	325.1	306.6	276	349.6
Nb	37.4	30.2	29.4	31.9	36.9	26.7	37.1
Pb	11.4	8	3.9	11.4	8.2	4.7	9.5
Th	8.1	4.2	5.1	6.4	6.6	3.9	9.5
U	2.1	0.5	2.6	0.9	1.2	1.7	1.2
Quartz	3.03	2.56	7.31	3.90	1.60	1.98	4.35
Corundum							
Orthoclase	17.02	15.25	8.75	16.25	15.54	12.23	15.96
Albite	27.33	26.06	23.78	24.12	21.58	25.30	25.72
Anorthite	14.27	15.39	20.53	16.25	19.50	17.14	15.93
Leucite							
Nepheline							
Diopside	9.82	12.48	7.94	12.05	13.65	13.49	9.58
Hypersthene	15.80	15.60	18.37	16.30	15.59	16.81	16.35
Olivine							
2CaO.SiO2							
Magnetite	2.76	2.77	3.14	2.70	2.85	3.18	2.76
Ilmenite	6.51	6.97	7.75	6.06	7.54	7.43	6.42
H2O apatite	2.05	1.30	1.51	1.72	1.23	1.49	2.08
H2O+	-0.04	-0.02	-0.03	-0.03	-0.02	-0.03	-0.04
Total	98.57	98.36	99.05	99.27	99.06	99.01	99.09
87Sr/86Sr (measured)	0.708533	0.707860	0.707749	0.707458	0.710089	0.707286	0.708491
87Sr/86Sr (initial)	0.708012	0.707372	0.707519	0.706982	0.709628	0.706708	0.708080
εSr	51.99	42.90	44.99	37.36	74.94	33.48	52.95
143Nd/144Nd (measured)	0.512282	0.512357		0.512320		0.512409	0.512233
143Nd/144Nd (initial)	0.512180	0.512249		0.512218		0.512307	0.512131
εNd	-5.69	-4.33		-4.94		-3.21	-6.64
206Pb/204Pb	17.7123	17.6178		17.7803	17.9333	18.3033	17.7083
207Pb/204Pb	15.5333	15.5301		15.5307	15.5654	15.5776	15.5253
208Pb/204Pb	38.4194	38.2727		38.4270	38.5542	38.5832	38.3997

Sample	MR8951	MR8952	MR8953	MR8954	MR8956	MR8957	MR8958
Magma type	Ubatuba	Ubatuba	Ubatuba	Ubatuba	Ubatuba	Ubatuba	Ubatuba
Latitude (°S)	23.410	23.411	23.420	23.451	23.467	23.463	23.458
Longitude (°W)	45.295	45.291	45.287	45.287	45.315	45.322	45.324
SiO2	56.62	54.44	57.66	57.25	57.29	57.46	56.57
TiO2	2.53	2.5	2.47	2.53	2.47	2.22	2.5
Al2O3	13.68	13.33	14.41	13.83	13.8	15.11	13.63
Cr2O3	0.02	0.03	0.01	0.01	0.01		0.02
Fe2O3	9.89	9.61	9.58	10.13	9.79	8.64	9.8
MnO	0.14	0.16	0.15	0.19	0.15	0.14	0.16
MgO	4.33	4.64	3.1	3.46	3.29	2.68	4.27
CaO	5.83	5.73	4.67	4.91	4.94	4.95	5.68
Na2O	3.12	2.92	3.35	3.16	3.32	3.62	3.2
K2O	3.8	3.39	4.54	4.36	4.29	4.32	3.86
P2O5	0.48	0.45	0.62	0.63	0.61	0.59	0.47
TOTAL	100.44	97.21	100.57	100.46	99.95	99.74	100.17
MgO/(MgO+FeO)	50.5	52.9	43	44.3	43.9		50.4
Loss on ignition						0.62	
Zn	92.7	106.6	96	95.4	95.1	89.2	89.2
Cu	36.8	34	20.1	25.9	27.8	16.5	32.7
Ni	64	78.6	22.4	37.8	23.4	18.4	51.3
Co	36.6	36.8	28	31	25.9	23.8	36.6
Cr	134.6	145.9	28.7	63.2	49.8	21.1	124.7
V	176.8	192.3	171.6	178.6	159.1	146.9	170.1
Ba	1373.9	1248.4	1421.7	1408.5	1407.9	1435.9	1348.4
Ga	22.2	21.6	23.7	22.9	23.9	24.8	22.4
Rb	109.5	99.4	131.4	131.2	130.4	128	114.9
Sr	859.5	851.8	829.6	768.1	795	1076	867.9
Y	38.2	43.3	39.1	41.5	37.8	38.1	34.5
Zr	398.1	401.1	503.6	467	466.3	468.8	400
Nb	51.7	54.4	63.8	62.6	61.4	56.3	50.9
Pb	16.1	14.6	16.2	18.3	18	18.9	14.7
Th	11.1	11.7	14	14.7	15.5	14.5	11.8
U	2.7	2.5	3.2	3.6	3.3	3.1	3.1
Quartz	5.43	5.47	5.97	6.34	6.19	5.40	5.09
Corundum							
Orthoclase	22.46	20.03	26.83	25.77	25.35	25.53	22.81
Albite	26.40	24.71	28.35	26.74	28.09	30.63	27.08
Anorthite	12.10	13.25	10.87	10.67	10.08	12.22	11.43
Leucite							
Nepheline							
Diopside	11.24	10.01	6.84	7.92	8.65	7.04	11.23
Hypersthene	13.75	14.84	12.52	13.49	12.36	10.57	13.54
Olivine							
2CaO.SiO2							
Magnetite	2.15	2.09	2.08	2.20	2.13	1.88	2.13
Ilmenite	4.81	4.75	4.69	4.81	4.69	4.22	4.75
H2O apatite	1.13	1.06	1.46	1.49	1.44	1.39	1.11
H2O+	-0.02	-0.02	-0.03	-0.03	-0.03	-0.03	-0.02
Total	99.44	96.19	99.58	99.40	98.97	98.85	99.15
87Sr/86Sr (measured)	0.708345	0.708139	0.708353			0.708089	0.708356
87Sr/86Sr (initial)	0.707664	0.707516	0.707507			0.707454	0.707649
εSr	47.06	44.94	44.82			44.06	46.83
143Nd/144Nd (measured)		0.512211				0.512244	0.512213
143Nd/144Nd (initial)		0.512123				0.512156	0.512125
εNd		-6.78				-6.14	-6.74
206Pb/204Pb						18.2054	
207Pb/204Pb						15.5896	
208Pb/204Pb						38.7449	

Sample	MR8959	MR8960	MR8961	MR8964	MR8965	MR8966	MR8983
Magma type	Ubatuba	Ubatuba	Ubatuba	Ubatuba	Ubatuba	Ubatuba	Ubatuba
Latitude (°S)	23.472	23.473	23.483	23.519	23.528	23.577	23.130
Longitude (°W)	45.339	45.342	45.362	45.391	45.417	45.463	44.980
SiO2	56.42	57.96	56.8	56.79	57.8	57.55	57.79
TiO2	2.5	2.27	2.47	2.5	2.25	2.51	2.4
Al2O3	13.55	15.03	13.67	13.71	15.03	13.77	14.38
Cr2O3	0.02	0.01	0.02	0.02	0	0.01	0.01
Fe2O3	9.82	8.75	9.65	9.74	8.78	9.96	9.38
MnO	0.16	0.14	0.15	0.15	0.12	0.15	0.14
MgO	4.31	2.82	4.15	4.24	2.71	3.33	2.91
CaO	5.86	4.87	5.78	5.83	4.66	4.94	4.95
Na2O	3.14	3.49	3.22	3.19	3.57	3.3	3.37
K2O	3.76	4.42	3.79	3.78	4.49	4.35	4.53
P2O5	0.48	0.58	0.47	0.47	0.57	0.62	0.62
TOTAL	100.02	100.34	100.18	100.41	99.99	100.5	100.48
MgO/(MgO+FeO)	50.6	42.9	50.1	50.4	41.8	43.8	42
Loss on ignition							
Zn	96.2		94.9	95.8	92.6	95.5	91
Cu	36.2		31.4	32.2	18.4	25.7	20.1
Ni	61.7		53.1	51.1	17.4	25.1	17.1
Co	57.3		36.9	36.5	26.6	32.7	24.3
Cr	122.4		118.7	126.8	24.9	51.1	27.2
V	164.5		164.2	171	149.7	163.3	168.4
Ba	1362.8		1323.7	1301.4	1474	1443.5	1480.1
Ga	23.3		22.3	23	24.5	23.1	23.7
Rb	112.4		110.2	111.1	132.7	131.3	134
Sr	876.8		875.3	871.2	1093.7	765.8	822
Y	45.6		35.2	37.9	45.2	39.1	38.3
Zr	400.5		408.8	404.3	468	466	504.3
Nb	49.3		52.6	52.8	57.7	59.3	63.3
Pb	17.8		15.7	14.4	16.3	18.9	18.4
Th	12.9		14.6	12	13.5	15	15.4
U	3.1		3.1	2.9	4.1	2.1	1.9
Quartz	5.35	6.09	5.56	5.49	5.66	6.26	6.10
Corundum							
Orthoclase	22.22	26.12	22.40	22.34	26.54	25.71	26.77
Albite	26.57	29.53	27.25	26.99	30.21	27.92	28.52
Anorthite	11.77	12.29	11.65	11.93	11.72	9.91	10.73
Leucite							
Nepheline							
Diopside	11.63	6.70	11.46	11.43	6.37	8.74	8.12
Hypersthene	13.47	11.16	12.98	13.29	11.11	12.57	11.26
Olivine							
2CaO.SiO2							
Magnetite	2.14	1.90	2.10	2.12	1.91	2.17	2.04
Ilmenite	4.75	4.31	4.69	4.75	4.27	4.77	4.56
H2O apatite	1.13	1.37	1.11	1.11	1.35	1.46	1.46
H2O+	-0.02	-0.03	-0.02	-0.02	-0.02	-0.03	-0.03
Total	99.00	99.45	99.18	99.42	99.11	99.48	99.53
87Sr/86Sr (measured)	0.708139	0.708236	0.708390	0.708375	0.708005	0.708482	0.708583
87Sr/86Sr (initial)	0.707454	0.708236	0.707717	0.707694	0.707357	0.707566	0.707712
εSr	44.07	55.17	47.81	47.47	42.69	45.66	47.73
143Nd/144Nd (measured)				0.512165		0.512488	0.512240
143Nd/144Nd (initial)				0.512077		0.512400	0.512153
εNd				-7.69		-1.38	-6.21
206Pb/204Pb		18.1829	18.1783		18.1942		18.1883
207Pb/204Pb		15.5548	15.5756		15.5783		15.5570
208Pb/204Pb		38.6342	38.6523		38.7073		38.6498

Sample	MR8984	MR8985	MR8986
Magma type	Ubatuba	Ubatuba	Ubatuba
Latitude (°S)			
Longitude (°W)			
SiO2	56.84	56.89	59.03
TiO2	2.57	2.52	2.23
Al2O3	13.49	13.66	14.27
Cr2O3	0.02	0.02	0.01
Fe2O3	10.08	9.77	8.84
MnO	0.17	0.14	0.15
MgO	4.42	4.2	3.07
CaO	5.9	5.9	4.73
Na2O	3.06	3.15	3.49
K2O	3.78	3.84	4.15
P2O5	0.48	0.48	0.47
TOTAL	100.82	100.59	100.44
MgO/(MgO+FeO)	50.5	50.1	44.7
Loss on ignition			
Zn	99.2	91.4	103.1
Cu	32.8	34	19.1
Ni	39.4	37.3	24.4
Co	29.1	30.6	26.5
Cr	131.9	128.4	34.1
V	182.6	172.2	138.1
Ba	1352.3	1400	1523.4
Ga	22.2	23.2	24
Rb	111.4	115.8	125.4
Sr	845.2	857.7	857.9
Y	35.1	33.3	41.4
Zr	412.3	411.6	424.2
Nb	52	51.5	52.3
Pb	16.8	15.2	18.4
Th	12.5	12.4	14.3
U	3.5	2.8	2.4
Quartz	5.82	5.62	8.01
Corundum			
Orthoclase	22.34	22.69	24.53
Albite	25.89	26.66	29.53
Anorthite	11.91	11.79	11.01
Leucite			
Nepheline			
Diopside	11.68	11.78	7.76
Hypersthene	13.94	13.02	11.44
Olivine			
2CaO.SiO2			
Magnetite	2.19	2.13	1.92
Ilmenite	4.88	4.79	4.24
H2O apatite	1.13	1.13	1.11
H2O+	-0.02	-0.02	-0.02
Total	99.76	99.58	99.53
87Sr/86Sr (measured)		0.708277	0.708933
87Sr/86Sr (initial)		0.707556	0.708152
εSr		45.51	53.98
143Nd/144Nd (measured)		0.512217	0.512190
143Nd/144Nd (initial)		0.512129	0.512101
εNd		-6.66	-7.23
206Pb/204Pb		18.1640	
207Pb/204Pb		15.5558	
208Pb/204Pb		38.5836	

Table A.1
Whole rock geochemistry of the samples collected during the 1989 field season. Major and trace element compositions by XRF at Oxford University. CIPW normative compositions were calculated using the program CIPWNORM written by D.W. Wright. Radiogenic isotope measurements were carried out at the Open University.

Analysis	ZZA	ZZL	ZZP	ZZF	ZZV	ZZC	ZZD	ZZO	ZZQ
Sample	MR8952	MR8952	MR8952	MR8952	MR8952	MR8952	MR8952	MR8952	MR8952
Mineral	P	I	I	P	P	C	C	C	C
SiO2	56.95	0.05	0.07	55.61	57.37	51.41	51.18	51.61	51.07
TiO2		45.95	46.12			0.94	0.95	0.85	1.19
Al2O3	26.33	0.57	0.53	27.02	25.91	2.29	1.91	1.87	2.91
Cr2O3		0.30	0.37			0.07	0.02	0.02	0.07
FeO	0.66	46.72	47.24	0.59	0.56	12.18	12.04	12.46	11.28
MnO		0.37	0.41			0.33	0.34	0.37	0.30
MgO		3.81	4.25			17.57	14.45	14.46	14.61
CaO	9.00	0.02	0.02	10.17	8.75	17.57	18.48	17.96	18.23
Na2O	5.42			4.90	5.39	0.43	0.36	0.34	0.40
K2O	1.30			0.98	1.40				
BaO	0.16			0.09	0.15				
SrO	0.43			0.43	0.47				
Total	100.25	97.79	99.01	99.79	100.00	99.90	99.73	99.94	100.06

Analysis	XYI	XYJ	XYK	XYA	XYE	XYU	XYC	XYF
Sample	MR8954	MR8954	MR8954	MR8954	MR8954	MR8954	MR8954	MR8954
Mineral	C	C	C	P	P	P	I	I
SiO2	50.93	51.73	50.47	57.32	57.63	56.95	0.69	2.18
TiO2	1.46	0.93	1.22				46.79	45.69
Al2O3	2.04	2.08	3.10	26.03	25.66	26.03	0.43	0.78
Cr2O3	0.00	0.03	0.02				0.06	0.03
FeO	12.35	12.15	12.04	0.59	0.53	0.55	47.89	45.76
MnO	0.37	0.31	0.33				0.51	0.59
MgO	14.32	14.38	13.84				2.04	2.99
CaO	18.01	18.22	18.19	8.82	8.40	8.80	0.04	0.02
Na2O	0.34	0.37	0.39	5.33	5.33	5.21		
K2O				1.32	1.49	1.30		
BaO				0.15	0.15	0.17		
SrO				0.45	0.44	0.43		
Total	99.82	100.20	99.60	100.01	99.63	99.44	98.45	98.04

Analysis	YYA	YYB	YYC	YYE	YYL	YYN	YYJ	YYD	YYG
Sample	MR8984	MR8984	MR8984	MR8984	MR8984	MR8984	MR8984	MR8984	MR8984
Mineral	P	P	P	I	I	M	G	C	C
SiO2	57.08	55.96	56.04	0.05	0.07	0.80	53.05	51.37	51.49
TiO2				48.60	48.63	20.01	0.48	0.95	0.91
Al2O3	26.30	26.94	27.08	0.17	0.17	2.08	0.96	1.99	1.85
Cr2O3				0.03	0.08	0.91	0.02	0.03	0.03
FeO	0.56	0.59	0.60	47.09	46.69	67.33	19.97	11.85	11.79
MnO				0.60	0.53	1.67	0.55	0.31	0.33
MgO				1.84	2.06	0.69	22.30	14.37	14.67
CaO	9.06	10.03	9.91	0.02	0.02	0.05	2.13	18.04	18.27
Na2O	5.37	5.04	5.09				0.04	0.36	0.34
K2O	1.14	0.91	0.86						
BaO	0.13	0.11	0.08						
SrO	0.44	0.43	0.47						
Total	100.08	100.01	100.13	98.40	98.25	93.54	99.50	99.27	99.68

Analysis	XXC	XXI	XXE	XXR	XXL	XXP	XXB	XXG	XXK
Sample	MR8932	MR8932	MR8932	MR8932	MR8932	MR8932	MR8932	MR8932	MR8932
Mineral	P	P	M	M	O	O	C	C	C
SiO2	57.61	58.76	0.31	0.31	30.39	30.45	49.13	49.37	49.01
TiO2			21.53	22.50	0.06	0.10	0.74	0.80	0.78
Al2O3	25.97	25.40	0.50	0.47	0.05		0.91	0.97	0.91
Cr2O3									
FeO	0.51	0.49	72.70	71.24	65.80	65.11	24.26	23.10	24.11
MnO			0.54	0.64	1.30	1.35	0.58	0.57	0.60
MgO			0.02	0.05	2.26	2.86	5.44	6.55	5.65
CaO	8.65	7.99	0.02	0.01	0.24	0.39	18.73	18.65	18.91
Na2O	6.09	6.47			0.03	0.03	0.21	0.17	0.17
K2O	0.58	0.60							
BaO	0.05	0.09							
SrO	0.14	0.13							
Total	99.60	99.93	95.62	95.22	100.13	100.29	100.00	100.18	100.14

Analysis	XYI	XYJ	XYQ	XYA	XYE	XYU	XYC	XYF	XYH
Sample	MR8954	MR8954	MR8954	MR8954	MR8954	MR8954	MR8954	MR8954	MR8954
Mineral	C	C	C	P	P	P	I	I	M
SiO2	50.93	51.73	51.49	57.32	57.63	56.95	0.69	2.18	2.29
TiO2	1.46	0.93	0.89				46.79	45.69	20.19
Al2O3	2.04	2.08	1.95	26.03	25.66	26.03	0.43	0.78	3.33
Cr2O3		0.03	0.02				0.06	0.03	0.25
FeO	12.35	12.15	11.77	0.59	0.53	0.55	47.89	45.76	63.62
MnO	0.37	0.31	0.36				0.51	0.59	2.01
MgO	14.32	14.38	14.55				2.04	2.99	0.05
CaO	18.01	18.22	18.36	8.82	8.40	8.80	0.04	0.02	1.43
Na2O	0.34	0.37	0.36	5.33	5.33	5.21			
K2O				1.32	1.49	1.30			
BaO				0.15	0.15	0.17			
SrO				0.45	0.44	0.43			
Total	99.82	100.20	99.75	100.01	99.63	99.44	98.45	98.04	93.17

Analysis	LLB	JJE	JJL	JJM	JJC	JJH	JJJ	JJB	JJK
Sample	MR8944	MR8944	MR8944	MR8944	MR8944	MR8944	MR8944	MR8944	MR8944
Mineral	C	A	A	A	B	B	B	C	C
SiO2	45.65	40.11	39.26	38.83	35.75	38.84	35.45	47.57	47.98
TiO2	2.97	4.84	5.34	5.41	8.19	3.13	8.85	2.17	2.03
Al2O3	7.90	12.40	13.73	13.74	16.21	12.78	16.42	8.18	7.84
Cr2O3		14.35	15.56	15.49	9.60	12.68	10.67	7.41	6.80
FeO	8.40	0.25	0.34	0.31	0.05	0.11	0.06	0.14	0.11
MnO	0.16				0.24		0.02	0.09	0.03
MgO	11.41	10.31	8.84	8.79	15.24	17.99	14.34	12.64	12.93
CaO	20.98	10.49	10.62	10.53	0.04	0.01	0.06	20.30	20.51
Na2O	0.98	2.90	2.69	2.70	0.52	0.67	0.57	1.03	0.96
K2O		1.97	1.83	1.78	9.10	9.22	9.07		
BaO		0.02	0.04	0.04	0.01	0.01	0.01		
F		0.04	0.09	0.13	0.22	0.41	0.18		
Cl					2.11	1.16	1.72		
Total	98.45	97.68	98.34	97.75	97.28	97.01	97.42	99.53	99.19

Analysis	KKA	KKD	KKS	KKE	KKH	KKJ	KKY	KKW	KKZ
Sample	MR8967	MR8967	MR8967	MR8967	MR8967	MR8967	MR8967	MR8967	MR8967
Mineral	O	O	O	C	C	C	A	A	A
SiO2	40.75	40.60	40.82	51.26	52.93	52.82	43.40	42.75	36.94
TiO2	0.04	0.04	0.04	1.15	0.53	0.47	1.17	1.68	3.73
Al2O3	0.02	0.02	0.02	3.85	2.82	2.93	18.73	16.84	15.72
FeO	13.49	13.48	11.38	5.06	3.20	3.14	10.43	14.70	15.66
MnO	0.20	0.22	0.19	0.09	0.05	0.09	0.06	0.40	0.31
Cr2O3				0.26	0.59	0.94			
MgO	45.62	45.99	47.47	15.21	16.76	16.70	10.11	3.18	8.51
CaO	0.50	0.51	0.47	23.41	22.77	22.18	1.62	10.29	11.77
Na2O				0.21	0.30	0.30	0.11	4.98	2.01
K2O							7.90	1.51	2.02
Cl							0.02	0.07	0.04
F							0.09	0.30	0.35
Total	100.62	100.86	100.39	100.50	99.95	99.57	93.64	96.70	97.06

Analysis	HHK	HHL	HHM	HHD	HHF	HHA	HHJ
Sample	MR898	MR898	MR898	MR898	MR898	MR898	MR898
Mineral	C	C	C	P	P	C	C
SiO2	50.15	50.46	50.19	53.95	54.42	50.58	50.51
TiO2	1.00	0.98	1.22	0.13	0.09	1.06	1.15
Al2O3	2.06	2.14	2.50	28.30	27.86	2.23	2.31
FeO	12.27	11.98	11.47	0.76	0.66	11.64	11.43
MnO	0.31	0.30	0.30			0.30	0.31
MgO	13.92	14.64	14.60			14.71	14.73
CaO	18.26	17.82	17.65	11.61	11.01	17.64	18.05
Na2O	0.26	0.26	0.25	4.54	4.94	0.25	0.27
K2O				0.43	0.42		
Total	98.23	98.58	98.18	99.72	99.40	98.41	98.76

Analysis	RRA	RRN	RRR	RRF	RRH	RRI	RRK	RRU	RRW	RRY
Sample	MR8982	MR8982	MR8982	MR8982	MR8982	MR8982	MR8982	MR8982	MR8982	MR8982
Mineral	G	G	C	K	P	P	K	C	P	C
SiO2	52.41	52.57	51.29	69.52	55.25	56.18	67.35	50.98	52.20	51.66
TiO2	0.41	0.36	0.97					1.00	0.56	0.87
Al2O3	0.76	0.58	1.97	18.88	26.22	26.64	18.72	2.10	1.08	1.76
Cr2O3										
FeO	21.55	21.44	10.20	0.20	0.60	0.65	0.24	11.12	18.86	10.67
MnO	0.66	0.66	0.30					0.33	0.56	0.30
MgO	19.32	20.17	15.12					14.74	20.30	15.35
CaO	4.92	3.60	18.69	0.49	10.23	10.32	0.65	18.19	5.56	17.97
Na2O	0.07	0.04	0.30	5.23	5.06	3.22	4.59	0.29	0.09	0.25
K2O				8.81	0.60	0.60	9.49			
BaO				0.01	0.07	0.03	0.17			
SrO										
Total	100.10	99.42	98.84	103.14	98.03	97.64	101.21	98.75	99.21	98.83

Analysis	RSH	RSP	RSC	RSE	RSJ	RSL	RSN	RSR	RSV	RSX
Sample	MR8943	MR8943	MR8943	MR8943	MR8943	MR8943	MR8943	MR8943	MR8943	MR8943
Mineral	C	C	P	P	P	M	M	C	C	P
SiO2	50.26	50.40	56.29	54.76	56.85	0.47	1.99	51.43	50.55	54.37
TiO2	1.30	1.11				14.15	14.89	0.83	1.11	
Al2O3	2.50	2.24	25.75	26.99	26.57	1.24	1.52	1.63	2.23	27.13
Cr2O3	0.02					0.04	0.01	0.02		
FeO	11.98	13.08	0.68	0.75	0.68	76.18	70.73	13.66	12.31	0.80
MnO	0.30	0.30				0.55	0.60	0.33	0.30	
MgO	14.72	14.65				0.05	0.07	15.26	14.09	
CaO	17.52	16.87	9.73	11.16	10.01	0.32	1.54	15.78	18.13	10.87
Na2O	0.26	0.26	5.42	4.46	5.17			0.22	0.29	4.93
K2O			0.62	0.48	0.59					0.50
BaO			0.04	0.03	0.04					0.01
SrO										
Total	98.86	98.91	98.53	98.63	99.91	93.00	91.35	99.16	99.01	98.61

Analysis	WWA	WWF	WWB	WWD	WWH
Sample	MR8981	MR8981	MR8981	MR8981	MR8981
Mineral	C	C	O	O	O
SiO2	47.56	48.70	40.11	40.58	40.47
TiO2	2.38	1.80	0.04	0.02	0.04
Al2O3	9.39	8.17	0.05	0.05	0.05
Cr2O3	0.22	0.43		0.02	0.02
FeO	6.34	6.70	15.44	13.03	13.37
MnO	0.09	0.11	0.22	0.16	0.16
MgO	12.95	12.62	44.04	46.04	45.96
CaO	20.17	20.55	0.26	0.23	0.24
Na2O	1.06	1.36	0.02	0.02	0.03
K2O					
BaO					
SrO					
Total	100.16	100.44	100.18	100.15	100.34

Analysis	VVE	VVF	VVJ	VVK	VVD	VVG	VVH	VVN	VVC	VVM
Sample	MR8988	MR8988	MR8988	MR8988	MR8988	MR8988	MR8988	MR8988	MR8988	MR8988
Mineral	C	P	P	P	M	M	O	O	C	C
SiO2	51.47	52.52	52.64	50.77	0.54	0.16	34.02	34.06	50.75	52.49
TiO2	0.78				22.02	21.01	0.07	0.07	1.13	0.48
Al2O3	2.17	29.38	29.24	30.33	1.77	2.10	0.05	0.05	3.20	0.71
Cr2O3	0.24				0.07	0.08			0.24	
FeO	9.15	0.73	0.76	0.87	69.88	71.48	47.67	47.19	11.15	21.75
MnO	0.23				0.66	0.43	0.71	0.73	0.27	0.51
MgO	15.28				0.94	0.96	17.76	17.96	14.35	19.14
CaO	19.85	13.02	13.22	14.28	0.11	0.01	0.38	0.30	18.42	4.35
Na2O	0.25	3.85	3.83	3.18			0.02	0.02	0.25	0.05
K2O		0.30	0.26	0.19						
BaO		0.01	0.01	0.01						
SrO		0.11	0.10	0.09						
Total	99.42	99.92	100.06	99.72	95.99	96.23	100.68	100.38	99.76	99.48

Analysis	IID	IIH	IIB	IIR	IIF	III	IIO	IIP	IIQ
Sample	MR8950	MR8950	MR8950	MR8950	MR8950	MR8950	MR8950	MR8950	MR8950
Mineral	C	C	C	G	B	B	A	A	A
SiO2	50.84	50.79	51.05	51.24	44.06	42.04	44.74	44.02	44.46
TiO2	1.19	1.13	0.83	0.43	1.42	1.55	0.07	0.12	0.12
Al2O3	2.14	2.19	1.88	0.98	5.60	6.62	3.20	4.24	4.18
FeO	12.16	12.14	12.79	23.54	25.29	24.53	33.11	32.58	32.01
MnO	0.27	0.25	0.25	0.48	0.34	0.26	0.26	0.23	0.23
Cr2O3		0.02							
MgO	14.18	14.77	14.81	17.50	6.91	6.63	3.99	4.43	4.49
CaO	18.31	17.44	16.79	4.71	8.97	10.91	0.66	1.05	0.73
Na2O	0.29	0.26	0.26	0.06	1.74	2.12	0.23	0.17	0.14
K2O					0.87	0.96	0.31	0.30	0.31
Cl					0.42	0.50	0.01	0.01	0.01
F					1.01	1.26			
Total	99.38	98.99	98.66	98.94	96.63	97.38	86.58	87.15	86.68

Analysis	RRF	RRS	RRW	RRR	RRY	RRK	RRW	MMD	MMM
Sample	MR8943	MR8943	MR8943	MR8943	MR8943	MR8943	MR8943	MR8982	MR8982
Mineral	C	C	C	A	B	P	P	C	C
SiO2	50.48	50.73	50.46	46.12	32.19	54.39	55.68	51.40	51.52
TiO2	1.26	0.83	1.22	1.33	3.37	0.11	0.11	0.72	0.87
Al2O3	2.50	1.88	2.45	5.36	12.92	27.73	26.78	1.64	3.04
FeO	11.81	15.17	12.00	21.53	28.62	0.75	0.67	13.05	10.35
MnO	0.27	0.39	0.27	0.34	0.17			0.44	0.28
Cr2O3		0.02							0.02
MgO	14.43	13.34	14.19	9.41	8.62			13.90	13.80
CaO	18.33	16.88	18.37	11.36	1.18	11.07	10.07	17.80	17.96
Na2O	0.29	0.26	0.31	1.65	0.24	4.64	5.31	0.28	0.64
K2O				0.68	3.52	0.47	0.61		
BaO					0.07				
Total	99.37	99.50	99.27	86.03	90.90	99.16	99.23	99.23	98.48

Table A.2

Representative mineral analyses of the Parana dolerites. All analyses were carried out on a Cambridge microscan Mk9 electron probe (operating conditions are described in section A.4). Abbreviations; P=plagioclase, I=ilmenite, C=clinopyroxene, M=magnetite, G=pigeonite, O=olivine, K=potassium felspar, A=amphibole, B=biotite.

	MR8948	MR8950	MR8982	MR8932	MR8933	MR8942	MR8928	MR898
La	44.9	45.3	64.3	63.7	25.4	33.9	62.3	37.1
Ce	94.5	97.6	130	131	56.4	75.2	130	78.7
Nd	52.4	56.2	70.3	71	30.4	46.8	73.6	49.3
Sm	10.8	11.1	13.3	14.4	6.64	9.86	14.1	10.4
Eu	3.36	3.63	4.2	4.21	2.24	3.18	4.29	3.7
Tb	1.29	1.44	1.57	2.23	1.11	1.39	1.8	1.6
Yb	2.57	2.84	2.77	7.63	3.56	3.32	3.14	4.66
Lu	0.37	0.39	0.39	1.12	0.51	0.48	0.42	0.74
Th	5.23	4.8	7.2	8.91	2.97	3.52	8.2	3.18
U	1.22	1.27	1.82	1.92	0.57	0.69	1.87	0.79
Ta	1.87	2.06	2.62	2.42	1.06	1.52	2	1.74
Hf	7.75	8.08	8.53	12.1	4.62	7.14	11.3	6.41

	MR8965	MR8974	MR8967	MR8944	MR8979	MR8969	MR892	MR8960	MR891
La	98.7	45.4	25	96.2	68.8	80.8	15.2	97.1	10.9
Ce	185	81.8	46.8	189	125	164	31.3	189	24.4
Nd	86.9	38.8	26.5	100	63.4	76.8	20.7	88.8	15.5
Sm	13.9	6.94	5.12	16.5	11.2	14.1	4.83	14	4.03
Eu	3.72	2.23	1.67	4.94	3.62	2.68	1.6	3.73	1.32
Tb	1.47	0.84	0.63	1.57	1.25	1.78	0.96	1.44	0.82
Yb	3.31	2.16	1.15	2.3	1.87	4.33	3.07	2.65	3.14
Lu	0.46	0.32	0.15	0.33	0.28	0.6	0.45	0.39	0.46
Th	14.1	4.24	2.43	10.2	8.07	13.6	2.85	14.2	2.59
U	3.25	1.58	0.87	2.77	2.16	2.62	0.8	3.03	1.02
Ta	3.93	2.75	1.89	7.41	5.05	6.13	0.85	3.98	0.66
Hf	11.3	3.64	3.38	9.3	6.85	11.8	3.52	11.5	3.02

	MR8955	MR8992	MR8972	MR8971	MR8929	MR8962	MR8954	MR8952	MR8980
La	68.3	24.1	169	35.1	63.4	63	96.6	80.3	40.8
Ce	142	48.4	273	72.1	141	136	198	166	89.6
Nd	70.5	25.7	98.3	36.6	74.9	72.9	77.3	72.9	50.2
Sm	14.8	6.16	14.8	6.93	14.4	13.2	13.9	12	10.2
Eu	4.13	1.87	4.22	2.22	4.42	4.25	3.42	3.3	3.31
Tb	1.91	1.06	1.46	0.87	1.79	1.51	1.43	1.33	1.39
Yb	3.69	3.2	2.74	1.52	3.05	2.64	2.73	2.68	2.8
Lu	0.61	0.55	0.41	0.23	0.44	0.41	0.42	0.42	0.45
Th	6.21	2.63	24.8	3.88	8.78	7.09	14.1	11.6	4.82
U	1.38	0.64	9.14	1.38	1.95	1.66	3.63	2.79	0.97
Ta	2.14	0.88	4.31	3.08	2.06	2.63	3.07	3.45	1.76
Hf	8.13	4.74	4.14	4.65	12.9	8.76	11.4	9.64	7.06

	MR8986	MR8981	MR8976	MR8970	MR8991	MR899	MR8941	MR8931	MR8943
La	90.2	82.1	48.6	34.4	28.7	18.2	22.1	142	39.7
Ce	182	157	99.5	73.2	61.8	37.5	48.5	289	85.3
Nd	78.9	69.4	49.2	37.2	35.5	22.4	29.1	342	48.1
Sm	12.8	13.1	9.03	7.24	7.25	4.75	6.78	85.9	10.03
Eu	3.44	4.05	2.89	2.34	2.45	1.62	2.16	29.2	3.2
Tb	1.36	1.44	1.09	0.89	1.12	0.89	1.26	22.4	1.38
Yb	2.78	1.93	2.58	1.72	2.59	2.63	3.64	79.1	2.59
Lu	0.42	0.29	0.39	0.24	0.46	0.4	0.6	13.1	0.39
Th	13.8	9.15	6.19	3.84	3.05	2.11	2.54	10.1	4.62
U	3.05	2.26	1.71	1.23	0.73	0.57	0.5	2.49	1.01
Ta	3.55	4.05	4.67	3.24	1.29	0.68	1.01	2.97	1.71
Hf	10.3	7.1	5.94	4.67	5.47	3.62	5.23	14.2	7.3

Table A.3
Trace element data obtained by instrumental neutron activation analysis (section A.3).

	CJ1710B	CJ1710C	MM9007	MM9011	MM9012A	MM9014	MM9016	MM9017	MM9018	MM9019
SiO2	51.75	51.75		49.79	49.66	51.51	53.30	48.82	49.40	55.22
TiO2	3.475	3.461		2.936	2.853	2.344	3.446	2.318	3.272	2.382
Al2O3	13.26	13.31		13.12	13.04	12.71	12.49	12.85	12.71	13.03
Fe2O3	12.47	12.07		15.08	15.96	16.02	14.42	15.15	17.03	13.29
MnO	0.149	0.142		0.186	0.209	0.215	0.195	0.199	0.212	0.198
MgO	5.38	5.27		4.45	4.88	4.98	3.71	5.94	4.61	2.48
CaO	8.57	8.22		9.22	9.08	9.14	7.15	9.51	8.78	6.19
Na2O	2.55	2.50		2.43	2.61	2.46	3.09	2.43	2.53	3.08
K2O	1.73	1.84		1.24	0.98	0.84	2.08	1.01	1.15	2.35
P2O5	0.484	0.485		0.412	0.399	0.265	0.601	0.322	0.312	0.821
LOI	0.74	1.37		0.98	0.35	0.20	0.07	0.73	0.76	1.63
Total	100.56	100.42		99.84	100.02	100.69	100.55	99.34	100.77	100.67
Rb	37	39	44	48	31	18	49	32	25	50
Sr	752	739	974	393	397	242	488	397	457	574
Y	36	38	37	51	39	48	51	33	41	59
Zr	302	307	270	218	216	196	386	164	227	439
Nb	23	25	24	20	20	14	31	14	17	34
Ba	574	540	637	601	436	222	621	355	420	863
Pb	9	8	10	8	8	6	10	8	9	10
Th	3	2	6	6	6	4	5	5	4	6
U	0	0	0	0	0	2	0	0	0	0
Sc	23	26	20	32	31	39	23	32	32	17
V	314	310	325	482	459	438	359	430	609	156
Cr	97	111	22	70	73	85	40	128	41	14
Co	46	51	47	55	53	53	44	57	56	36
Ni	76	88	30	52	44	40	24	68	43	3
Cu	168	174	173	238	233	241	64	191	345	35
Zn	103	109	95	126	120	104	122	112	116	134
Ga	24	23	29	23	23	22	25	21	24	25

	MM9020A	MM9020B	MM9021	MM9022B	MM9032	MM9032A	MM9067	MM9088	PP1654
SiO2	50.36	49.88	50.89	63.10	50.28	50.96	51.43	46.47	42.00
TiO2	2.935	2.924	2.913	0.675	2.963	2.990	2.213	1.195	4.242
Al2O3	12.77	12.84	13.76	16.05	12.42	12.48	12.99	14.21	14.53
Fe2O3	15.38	15.34	16.09	6.43	16.44	16.46	15.42	9.47	14.10
MnO	0.210	0.209	0.206	0.107	0.210	0.212	0.212	0.169	0.192
MgO	4.40	4.57	3.41	2.59	4.31	4.30	4.74	11.43	5.37
CaO	8.38	8.08	8.45	0.45	8.94	8.84	9.16	9.18	10.05
Na2O	2.70	3.15	2.76	2.04	2.33	2.37	2.37	2.38	3.43
K2O	1.17	1.00	1.35	5.99	1.11	1.09	1.05	1.59	2.72
P2O5	0.347	0.347	0.467	0.133	0.403	0.398	0.286	0.427	0.937
LOI	1.42	1.57	0.70	2.04	0.56	0.99	0.61	3.04	2.72
Total	100.07	99.91	101.00	99.60	99.96	101.09	100.48	99.57	100.35
Rb	28	29	35	229		27	22	67	
Sr	386	358	382	111		264	298	455	
Y	44	42	47	26		57	44	21	
Zr	247	251	253	146		282	212	125	
Nb	20	20	20	15		21	15	19	
Ba	433	428	443	742		404	321	647	
Pb	5	9	9	24		7	11	5	
Th	1	3	6	12		5	4	4	
U	1	0	0	4		1	1	1	
Sc	31	27	31	14		35	30	28	
V	480	462	429	101		425	442	226	
Cr	54	59	24	90		66	71	758	
Co	53	55	51	21		50	49	45	
Ni	36	37	22	28		34	36	246	
Cu	202	197	246	29		362	230	43	
Zn	133	137	122	99		125	105	87	
Ga	24	22	24	24		21	21	14	

Table A.4
Major and trace element compositions of the dolerite samples collected by A. C. Vasconcellos (data by XRF at the Open University).

Sample	AN2718	AN2880	RS1740	RO4266	AN3207	SE3039	SE3060	AN3615
SiO2	49.76	49.56	51.6	49.35	53.51	50.85	48.33	49.86
TiO2	2.959	3.416	2.267	3.127	2.987	1.227	1.239	2.72
Al2O3	12.24	12.99	12.68	12.78	14.25	13.89	14.36	13.2
Fe2O3	17.91	15.35	15.62	15.29	12.11	13.12	12.63	15.09
MnO	0.228	0.196	0.215	0.195	0.159	0.193	0.187	0.196
MgO	4.67	5.13	4.37	5.52	3.54	6.12	5.71	5.09
CaO	8.96	8.05	8.86	9.61	7.23	10.71	11.12	9.43
Na2O	2.54	3.39	2.56	2.43	3.46	2.47	2.37	2.56
K2O	1	1.67	1.2	1.14	2.28	0.7	0.73	1.14
P2O5	0.274	0.368	0.305	0.331	0.639	0.156	0.148	0.347
LOI	0.19	0.72	0.57	0.28	0.88	0.6	3.25	0.51
Total	100.73	100.12	100.25	100.05	101.05	100.04	100.07	100.14
Zn	119.9	119.1	113.5	117.2	103.7	83.6	444.3	118.5
Cu	255.7	138.7	247.2	309.2	78.5	148.1	168.8	169.9
Ni	40.7	50.4	28.1	61.8	18.5	57.7	62.9	58.2
Co	51.2	42.7	39.2	49.8	28.6	46.7	45	47.5
Cr	32.1	75	25.9	98.6	86.1	86.9	114.3	126.1
V	721.2	461.8	439.4	504.6	290	346	366.6	507.5
Ba	402.9	479.3	455.5	456.7	773.6	234.6	220.2	440.4
Ga	21.9	23.1	21.2	21.8	25.6	19.6	19	21.8
Rb	30.1	69.8	32.8	28.9	66.6	24.4	27.4	34.4
Sr	311.7	524.7	365.8	431.4	707.5	190.3	191.3	419.3
Y	39.4	35.2	39.3	33.2	43.7	31.8	30.2	35.1
Zr	169.4	204	186.3	184.3	295.8	7.1	104.3	191.8
Nb	14.1	16.8	14.7	16.3	24	4.3	6.9	15.8
Pb	4.7	5.5	5.7	3.5	10.5	1.8	7.3	5.4
Th	2.4	2.3	4.1	2.8	5.6	1.5	1.5	3.2
U		1.4	1.3	1.2	0.7			1.2

Sample	RO4269	TI2880	TI3084	CS2532	SE1674	RS2061	SE3048	SE1806
SiO2	49.72	50.32	50.12	46.83	51.74	52.25	47.92	50.64
TiO2	3.118	3.051	3.641	3.01	2.163	3.088	1.258	1.801
Al2O3	13.06	13.65	13.03	12.9	13.63	14.06	14.73	13.49
Fe2O3	15.21	13.69	15.1	17.25	14.2	11.24	12.34	13.7
MnO	0.193	0.19	0.193	0.19	0.196	0.138	0.191	0.202
MgO	5.32	5.44	4.64	5.95	4.95	4.78	5.62	6.36
CaO	9.55	8.91	8.43	10.69	9.24	8.66	11.84	10.18
Na2O	2.54	2.69	2.89	2.31	2.7	2.99	2.38	2.52
K2O	1.23	1.06	1.49	0.73	1.24	1.69	0.65	0.85
P2O5	0.347	0.357	0.477	0.2	0.279	0.448	0.146	0.202
LOI	0.29	0.91	0.49	0.41	0.26	0.65	3.38	0.41
Total	100.58	100.08	100.5	100.47	100.6	99.99	100.46	100.35
Zn	107.9	109	124.4	99.6	96.9	99.2	73.7	94.1
Cu	297	204.3	202.8	502.9	221.6	137.3	159.8	175.2
Ni	56.6	67.2	41.1	86.7	46.2	70.4	66.1	68.8
Co	45.7	45.2	38.5	54.7	42.8	36.2	42.5	47
Cr	77.6	121.2	49.6	49.5	69.9	90.8	116.8	119.3
V	487.5	447	424.8	746.2	414.3	295.2	360.1	409.2
Ba	488.4	321.5	525.3	279.6	437.2	576	205.5	326.8
Ga	22.9	24.3	24.6	22.4	21.6	25.2	18	20.1
Rb	29.7	23.7	38.2	20.3	36.1	41.8	23.3	24.4
Sr	446.7	491.7	527	417.7	398.3	814.8	195.5	386.1
Y	33.2	33.2	39.1	25.3	35.3	36.4	29.8	29.2
Zr	186.9	208	241.7	120	172.8	252.3	100.8	132.7
Nb	15.8	16.7	21.2	10	14.3	20.4	7	12.3
Pb	5.2	2.4	7.2	3.6	5.9	7.1	6.2	3.6
Th	3.3	0.3	2.4	3	1.8	4.5	2.9	1.7
U	0.9				1.5	1	0.9	0.8

Table A.5
Major and trace element compositions of the borehole samples (sills) provided by M. S. M. Mantovani and D. W. Peate. Data by XRF at the Open University.

Sample	Sm	Nd	Sample	Rb	Sr
MR8981	13.15±0.009	69.39±0.047	MR8976	53.03±0.03	969.3±0.43
MR8986	13.44±0.057	77.06±0.020	MR8974	43.13±0.02	887.6±0.67
MR8967	5.436±0.003	26.21±0.009	MR8967	24.03±0.02	470.7±0.22
MR8963	11.82±0.008	56.02±0.017	MR8969	121.2±0.05	26.08±0.13
MR8964	11.68±0.007	67.71±0.020	MR8981	57.31±0.02	1026±1.20
MR8946	11.45±0.009	59.51±0.042	MR8979	62.70±0.03	1571±0.72
MR8955	15.55±0.012	76.72±0.040	Leached samples		
MR8983	15.23±0.086	89.83±0.034	MR8976	26.54±0.02	923.2±0.41
MR8949	11.08±0.013	53.05±0.061	MR8974	25.26±0.01	669.8±0.37
MR8985	12.77±0.009	74.68±0.046	MR8967	9.754±0.01	228.1±0.09
MR8945	11.07±0.008	59.48±0.054	MR8969	127.6±0.05	27.41±0.01
MR8944	17.22±0.012	96.68±0.035	MR8981	36.06±0.02	513.4±0.26
MR891	4.127±0.003	14.38±0.005	MR8979	34.96±0.02	1148±0.53
MR899	4.884±0.003	20.73±0.006			
MR8969	13.79±0.012	73.61±0.030			
MR8979	11.96±0.010	61.73±0.028			
MR8976	9.225±0.006	47.45±0.014			
MR8973	17.17±0.013	87.82±0.036			
MR8974	8.215±0.006	43.08±0.014			
MR8971	6.932±0.007				
MR8970	7.808±0.005				
MR8943	10.35±0.009				
MR8950	11.51±0.008				
MR8982	13.99±0.010				

Table A.6

Sm, Nd, Rb and Sr concentrations of selected samples measured by isotope dilution (see section A.5).

Sample	87Sr/86Sr (measured)	87Sr/86Sr (initial)	143Nd/144Nd (measured)	143Nd/144Nd (initial)
MR8967	0.704583	0.704443	0.512597	0.512532
MR8969	0.723697	0.708399	0.512542	0.512472
MR8974	0.704496	0.704372	0.512743	0.512683
MR8976	0.704701	0.704607		
MR8979	0.704351	0.704251	0.512568	0.512507
MR8981	0.704436	0.704205	0.512658	0.512598

Table A.7

Isotope composition of Sr and Nd of the Sao Sebastiao dolerites after leaching in 6M HCl for 24 hours (see section A.7).

Time	87Sr/86Sr (measured)
5 hours	0.704683±11
10 hours	0.704643±10
24 hours	0.704597±11
48 hours	0.704548±10
96 hours	0.704561±11

Table A.8

Isotope composition of Sr after leaching sample MR-8967 in 6M HCl for various lengths of time (see section A.5).

MR-8954	Mineral	Mass 41	±	40Ar	±	39Ar	±	38Ar	±	37Ar	±
w27	Plagioclase	0.000160	0.000142	7.000996	0.007623	0.411873	0.002690	0.008399	0.000085	0.003924	0.000365
w29	Plagioclase	0.000110	0.000085	4.223856	0.013933	0.271201	0.000694	0.004721	0.000089	0.002881	0.000190
w35	Plagioclase	0.001000	0.000078	3.889781	0.019886	0.208329	0.000730	0.005653	0.000146	0.003990	0.000618
w37	Plagioclase	0.000580	0.000085	3.303962	0.002846	0.177274	0.001153	0.003796	0.000057	0.002950	0.000321
w39	Plagioclase	0.000920	0.000071	5.908391	0.010869	0.346125	0.000121	0.007652	0.000103	0.001927	0.000319
w41	Plagioclase	0.000430	0.000063	3.559910	0.001332	0.225794	0.000393	0.004078	0.000064	0.003583	0.000386
w45	Plagioclase	0.000610	0.000081	5.579592	0.006619	0.295441	0.000790	0.007975	0.000078	0.001500	0.000113
w47	Plagioclase	0.000180	0.000050	4.340176	0.001875	0.291080	0.000773	0.006360	0.000101	0.003001	0.000505
MR-8957											
w10	Plagioclase	0.000220	0.000058	2.951093	0.002580	0.147386	0.000318	0.004230	0.000141	0.001599	0.000320
w12	Plagioclase	0.000330	0.000100	3.529302	0.002129	0.198107	0.000632	0.003523	0.000114	0.001326	0.000809
w17	Plagioclase	0.000310	0.000067	1.458501	0.001643	0.094524	0.000238	0.001716	0.000067	0.001978	0.000141
w19	Plagioclase	0.000260	0.000078	1.595681	0.001711	0.101441	0.000511	0.001746	0.000077	0.002065	0.000618
w21	Plagioclase	0.000140	0.000095	3.815869	0.005747	0.247275	0.000551	0.001835	0.000092	0.003192	0.000591
w23	Plagioclase	0.000250	0.000092	3.058111	0.017841	0.148177	0.000446	0.003382	0.000089	0.001640	0.000107
w25	Plagioclase	0.000270	0.000072	3.093731	0.006760	0.207437	0.000481	0.004290	0.000054	0.003347	0.000474
MR-8959											
v93	Plagioclase	0.000470	0.000058	6.691370	0.004942	0.250237	0.000322	0.007642	0.000083	0.002818	0.000296
v97	Plagioclase	0.000960	0.000058	13.080320	0.016147	0.730510	0.001620	0.017030	0.000124	0.006289	0.000376
v99	Plagioclase	0.000310	0.000067	7.449958	0.006140	0.517524	0.001352	0.010196	0.000124	0.004740	0.000523
w1	Plagioclase	0.000580	0.000050	8.623119	0.007494	0.360544	0.000700	0.012417	0.000083	0.003106	0.000324
w3	Plagioclase	0.000120	0.000050	6.901194	0.006185	0.480394	0.000941	0.010711	0.000051	0.004199	0.000814
w5	Plagioclase	0.000360	0.000103	7.618286	0.009376	0.337896	0.000716	0.009418	0.000155	0.001244	0.000297
w7	Plagioclase	0.000220	0.000112	6.785691	0.004745	0.490021	0.000700	0.009217	0.000165	0.002417	0.000533
MR-8951											
aac38	Plagioclase	0.000110	0.000064	0.468826	0.000504	0.015793	0.000199	0.000787	0.000045	-0.001340	0.001107
aac40	Plagioclase	0.000570	0.000112	1.281774	0.006746	0.073082	0.000410	0.002039	0.000067	0.003521	0.001388
aac42	Groundmass	0.000130	0.000099	2.807973	0.016482	0.191983	0.000602	0.014506	0.000112	-0.000211	0.001051
aac44	Plagioclase	0.004810	0.002960	4.284163	0.023745	0.290129	0.000997	0.008571	0.000354	0.005985	0.001181
aac46	Plagioclase	0.000000	0.000094	1.368390	0.007944	0.074575	0.000933	0.002827	0.000041	0.001690	0.001731
aac48	Groundmass	0.000240	0.000139	1.755068	0.003534	0.118917	0.000159	0.006764	0.000099	0.001338	0.000946
aac50	Groundmass	0.000390	0.000078	3.082448	0.016916	0.212134	0.000561	0.008974	0.000083	0.001831	0.002214
aac52	Plagioclase	0.000440	0.000076	1.839916	0.003272	0.089718	0.000598	0.004028	0.000051	0.000000	0.001191
aac54	Plagioclase	0.000400	0.000142	2.478567	0.006235	0.132315	0.000462	0.005007	0.000072	0.001267	0.001486
aac57	Plagioclase	0.000220	0.000126	4.139887	0.004261	0.268097	0.001142	0.010034	0.000122	0.003380	0.001633
aac59	Groundmass	0.000220	0.000128	5.463027	0.005234	0.377806	0.000973	0.026085	0.000143	0.003591	0.001240
aac61	Plagioclase	0.000260	0.000112	3.052281	0.009522	0.214305	0.000871	0.006117	0.000076	0.000352	0.001339
aac63	Plagioclase	0.000110	0.000092	1.234460	0.003023	0.053136	0.000301	0.002170	0.000050	-0.001060	0.001037
aac65	Groundmass	0.000130	0.000099	6.391551	0.008511	0.436238	0.001010	0.027630	0.000243	0.000122	0.001822
aac67	Groundmass	0.000350	0.000120	7.156892	0.013722	0.485019	0.001080	0.017181	0.000179	0.003806	0.001172

MR-8954	36Ar	±	Mass 35	±	40Ar*/39Ar	±	Age (Ma)	±	36Ar/40Ar	±	39Ar/40Ar	±
w27	0.005219	0.000148	0.000840	0.000620	13.253400	0.138051	138.907700	1.461277	0.000745	0.000021	0.058831	0.000390
w29	0.002589	0.000122	0.000570	0.000440	12.753200	0.146263	133.854900	1.540010	0.000613	0.000029	0.064207	0.000268
w35	0.003779	0.000085	0.001390	0.000259	13.310850	0.161171	139.487200	1.684979	0.000972	0.000023	0.053558	0.000332
w37	0.003649	0.000071	0.001050	0.000275	12.554390	0.144276	131.842500	1.520551	0.001105	0.000021	0.053655	0.000352
w39	0.005629	0.000148	0.000360	0.000336	12.253820	0.130645	128.796000	1.387750	0.000953	0.000025	0.058633	0.000129
w41	0.002239	0.000071	0.000870	0.000533	12.835630	0.097116	134.688400	1.071891	0.000629	0.000020	0.063427	0.000135
w45	0.005899	0.000108	0.000800	0.000328	12.985190	0.115399	136.200100	1.244150	0.001057	0.000019	0.052950	0.000155
w47	0.001819	0.000071	0.000370	0.000481	13.063580	0.081471	136.991900	0.931518	0.000419	0.000016	0.067066	0.000193
MR-8957												
w10	0.003330	0.000094	-0.000490	0.000242	13.347110	0.192122	140.053300	1.990207	0.001128	0.000032	0.049943	0.000116
w12	0.003310	0.000081	0.000050	0.000353	12.878260	0.127535	135.313400	1.361068	0.000938	0.000023	0.056132	0.000182
w17	0.000970	0.000050	0.000930	0.000205	12.398800	0.166784	130.453400	1.743252	0.000665	0.000034	0.064809	0.000263
w19	0.000940	0.000072	0.000360	0.000326	12.993140	0.226052	136.476000	2.327707	0.000589	0.000045	0.063572	0.000388
w21	0.002749	0.000092	0.000530	0.000506	12.654750	0.120975	133.049500	1.297414	0.000721	0.000024	0.062194	0.000172
w23	0.004210	0.000095	0.001670	0.000532	12.243180	0.227254	128.873200	2.344988	0.001377	0.000032	0.048454	0.000318
w25	0.001749	0.000086	-0.000390	0.000298	12.422150	0.130026	130.690500	1.383869	0.000565	0.000028	0.067051	0.000214
MR-8959												
v93	0.011369	0.000265	0.000570	0.000628	13.314190	0.313747	139.520800	3.194925	0.001699	0.000040	0.037397	0.000056
v97	0.013319	0.000089	0.000010	0.000452	12.518160	0.050683	131.475600	0.663242	0.001018	0.000007	0.055848	0.000142
v99	0.003509	0.000108	-0.000510	0.000398	12.391760	0.070507	130.194900	0.826928	0.000471	0.000015	0.069467	0.000190
w1	0.013519	0.000146	0.000140	0.000374	12.836560	0.123671	134.697900	1.322255	0.001568	0.000017	0.041811	0.000089
w3	0.003259	0.000099	0.000150	0.000481	12.360930	0.066787	129.882300	0.794159	0.000472	0.000014	0.069610	0.000150
w5	0.010749	0.000187	-0.000690	0.000187	13.145830	0.168038	137.822200	1.752101	0.001411	0.000025	0.044353	0.000109
w7	0.002380	0.000058	0.000020	0.000560	12.412840	0.040557	130.408500	0.585279	0.000351	0.000009	0.072214	0.000115
MR-8951												
aac38	0.000710	0.000073	0.000000	0.000326	16.396350	1.378139	170.579300	13.690930	0.001515	0.000155	0.033685	0.000426
aac40	0.001019	0.000063	0.000160	0.000524	13.417440	0.281939	140.763300	2.880374	0.000795	0.000050	0.057016	0.000439
aac42	0.001030	0.000092	-0.000780	0.000478	13.040740	0.170828	136.957400	1.781849	0.000367	0.000033	0.068371	0.000455
aac44	0.002049	0.000064	0.000490	0.000286	12.666630	0.113205	133.169900	1.223317	0.000478	0.000015	0.067791	0.000442
aac46	0.001340	0.000058	-0.000280	0.000515	13.040940	0.302217	136.959500	3.087399	0.000979	0.000043	0.054498	0.000752
aac48	0.000950	0.000057	-0.000080	0.000323	12.398800	0.151509	130.453400	1.593119	0.000541	0.000032	0.067756	0.000295
aac50	0.001000	0.000076	0.000430	0.000192	13.138220	0.137234	137.943100	1.455002	0.000324	0.000025	0.068820	0.000419
aac52	0.002430	0.000094	0.000130	0.000341	12.504150	0.323640	131.522500	3.309662	0.001321	0.000051	0.048762	0.000336
aac54	0.002510	0.000120	-0.000080	0.000380	13.127330	0.275942	137.833000	2.823663	0.001013	0.000049	0.053384	0.000230
aac57	0.002499	0.000076	0.000630	0.000630	12.686970	0.101130	133.376000	1.109487	0.000604	0.000018	0.064760	0.000284
aac59	0.002169	0.000114	0.001110	0.000284	12.763190	0.096035	134.148300	1.062555	0.000397	0.000021	0.069157	0.000190
aac61	0.001230	0.000106	0.000640	0.000324	12.546760	0.161051	131.954700	1.686626	0.000403	0.000035	0.070212	0.000360
aac63	0.001960	0.000120	-0.000100	0.000361	12.330920	0.673397	129.764300	6.850074	0.001588	0.000097	0.043044	0.000266
aac65	0.002920	0.000117	0.000200	0.000197	12.673630	0.087033	133.240900	0.978951	0.000457	0.000018	0.068252	0.000186
aac67	0.003449	0.000081	0.000200	0.000481	12.654440	0.063291	133.046400	0.769016	0.000482	0.000011	0.067770	0.000199

MR-8965	Mineral	Mass 41	±	40Ar	±	39Ar	±	38Ar	±	37Ar	±
j84	Plagioclase	0.000360	0.000058	5.818794	0.002974	0.111702	0.000390	0.006541	0.000151	0.057723	0.000946
j86	Plagioclase	0.000120	0.000071	0.265071	0.000871	0.016861	0.000211	0.000293	0.000045	0.007356	0.000643
j88	Plagioclase	0.000280	0.000067	4.708188	0.003514	0.269970	0.000170	0.004815	0.000083	0.047551	0.000892
j90	Plagioclase	0.000320	0.000036	6.737768	0.004563	0.367104	0.000722	0.006087	0.000102	0.031820	0.000702
j92	Plagioclase	0.000010	0.000067	1.619292	0.001052	0.074533	0.000420	0.001555	0.000063	0.015948	0.000363
j94	Plagioclase	0.000120	0.000064	1.152455	0.001952	0.059323	0.000261	0.001121	0.000054	0.011529	0.000938
j96	Plagioclase	0.000140	0.000064	1.113902	0.002582	0.051960	0.000272	0.001151	0.000058	0.011363	0.000616
j98	Plagioclase	0.000070	0.000072	1.088618	0.001614	0.045175	0.000245	0.001181	0.000032	0.011610	0.000438
j100	Plagioclase	0.000120	0.000071	1.040703	0.002143	0.037715	0.000263	0.001080	0.000081	0.005464	0.000486
k4	Pyroxene	0.000160	0.000050	0.834781	0.001539	0.017644	0.000092	0.000858	0.000050	0.004151	0.000445
k6	Pyroxene	0.000110	0.000081	1.292177	0.000844	0.026740	0.000190	0.001464	0.000054	0.006806	0.000565
k8	K-felspar	0.000060	0.000057	1.037572	0.001951	0.060472	0.000371	0.002221	0.000099	0.020951	0.000800
k10	K-felspar	0.000040	0.000072	1.803044	0.002957	0.121790	0.000381	0.003574	0.000057	0.023826	0.000522
k12	K-felspar	0.000200	0.000064	0.871236	0.001221	0.049641	0.000380	0.001383	0.000054	0.007275	0.000576
k14	K-felspar	0.000050	0.000036	0.804653	0.001064	0.036278	0.000233	0.001171	0.000078	0.013753	0.000718
k18	Plagioclase	0.000110	0.000078	1.883082	0.003627	0.033415	0.000140	0.001524	0.000054	0.004274	0.000702
k20	Plagioclase	0.000250	0.000120	4.557731	0.004004	0.124566	0.000621	0.003937	0.000081	0.014860	0.000545
l18	K-felspar	0.000150	0.000050	2.874256	0.006456	0.122976	0.000311	0.006451	0.000095	0.037684	0.000894
l20	K-felspar	0.000260	0.000064	2.572837	0.004275	0.129187	0.000711	0.006915	0.000085	0.044696	0.000755
l22	K-felspar	0.000130	0.000041	1.995594	0.002287	0.113041	0.000272	0.005835	0.000078	0.032211	0.001281
MR-8950											
aae41	Plagioclase	0.000340	0.000148	2.207098	0.003080	0.112151	0.000385	0.004684	0.000094	0.001851	0.001779
aae43	Plagioclase	0.000200	0.000136	2.173574	0.005513	0.082245	0.000418	0.003523	0.000054	-0.001450	0.001623
aae45	Plagioclase	0.000090	0.000164	3.053607	0.004602	0.126158	0.000296	0.003483	0.000124	0.001209	0.001027
aae47	Plagioclase	0.000270	0.000095	3.871727	0.004783	0.155987	0.000643	0.004361	0.000095	0.001290	0.001914
aae49	Plagioclase	0.000290	0.000162	5.382286	0.029376	0.245599	0.001184	0.005714	0.000078	0.007017	0.001777
aae80	Plagioclase	0.000530	0.000120	2.246469	0.002052	0.080972	0.000560	0.002806	0.000095	0.004352	0.001162
aae82	Groundmass	0.000030	0.000108	0.793537	0.004515	0.040205	0.000282	0.003059	0.000041	-0.001640	0.001725
aae84	Groundmass	0.000250	0.000136	0.746012	0.001583	0.037252	0.000367	0.001999	0.000104	0.000329	0.001794
aae86	Plagioclase	0.000400	0.000164	6.821885	0.060320	0.305927	0.000633	0.007773	0.000151	0.004934	0.001192
aae88	Groundmass	0.000030	0.000212	1.452488	0.002972	0.085671	0.000395	0.002362	0.000092	0.000082	0.001395
aaf16	Plagioclase	0.000180	0.000094	2.920918	0.009080	0.118593	0.000535	0.003614	0.000083	0.000670	0.001734
aaf18	Groundmass	0.000200	0.000086	0.568735	0.002635	0.032546	0.000257	0.002887	0.000100	0.000168	0.002201
aaf20	Plagioclase	0.000040	0.000193	2.800181	0.003770	0.149799	0.000566	0.007299	0.000124	0.002598	0.002238
aaf24	Plagioclase	0.000320	0.000149	2.381007	0.011087	0.072952	0.000539	0.002594	0.000117	0.000839	0.001390
aaf50	Plagioclase	0.000100	0.000072	3.332435	0.007134	0.157763	0.000872	0.004099	0.000085	-0.000430	0.000887
aaf52	Plagioclase	0.000080	0.000157	3.496966	0.002262	0.219274	0.000761	0.003725	0.000126	0.002049	0.002361
aaf54	Plagioclase	0.000280	0.000130	2.382527	0.010748	0.099202	0.000562	0.002958	0.000126	-0.000510	0.001911
MR-899											
k90	Plagioclase	0.000110	0.000071	0.182604	0.000758	0.009690	0.000151	0.000525	0.000054	0.084952	0.000986
k92	Plagioclase	0.000190	0.000042	0.389224	0.000691	0.015136	0.000134	0.000586	0.000041	0.086250	0.001162
k94	Groundmass	0.000300	0.000050	0.493987	0.001117	0.023262	0.000271	0.001090	0.000054	0.238854	0.001763
k96	Groundmass	0.000200	0.000064	0.671004	0.001081	0.033032	0.000222	0.001585	0.000081	0.234843	0.001255
k100	Plagioclase	0.000350	0.000076	0.805368	0.001522	0.043124	0.000281	0.001928	0.000081	0.325580	0.001951
l1	Groundmass	0.000130	0.000050	0.327283	0.000500	0.012453	0.000125	0.000848	0.000063	0.040901	0.000846
l3	Plagioclase	0.000060	0.000072	0.452441	0.001468	0.027599	0.000085	0.001221	0.000036	0.140930	0.001099
l5	Plagioclase	0.000360	0.000057	0.687953	0.001222	0.007612	0.000108	0.000848	0.000054	0.032562	0.000894
l8	Groundmass	0.000210	0.000085	0.805739	0.000804	0.039032	0.000171	0.002080	0.000095	0.123656	0.000784
l10	Groundmass	0.000330	0.000086	0.587374	0.001073	0.006535	0.000151	0.000636	0.000064	0.021126	0.001186
l12	Groundmass	0.000190	0.000081	0.454033	0.000651	0.020297	0.000177	0.000939	0.000050	0.049081	0.000837
l14	Plagioclase	0.000170	0.000058	0.494013	0.000702	0.017816	0.000304	0.001050	0.000057	0.134894	0.001241
l16	Groundmass	0.000280	0.000050	0.685124	0.001381	0.023284	0.000196	0.001292	0.000054	0.081571	0.000615
l24	Groundmass	0.000360	0.000072	1.707209	0.002054	0.062024	0.000316	0.003654	0.000067	0.215771	0.001469

MR-8965	36Ar	±	Mass 35	±	40Ar*/39Ar	±	Age (Ma)	±	36Ar/40Ar	±	39Ar/40Ar	±
j84	0.014918	0.000117	-0.000010	0.000385	12.627120	0.313895	132.705900	4.962746	0.002564	0.000020	0.019197	0.000068
j86	0.000298	0.000071	0.000090	0.000369	10.489790	1.247267	110.918700	13.186150	0.001126	0.000267	0.063609	0.000823
j88	0.005950	0.000117	0.000070	0.000278	10.926740	0.128494	115.394300	3.578597	0.001264	0.000025	0.057340	0.000056
j90	0.008173	0.000130	0.000480	0.000290	11.774610	0.107892	124.047200	3.734731	0.001213	0.000019	0.054485	0.000113
j92	0.002867	0.000058	0.000250	0.000361	10.360140	0.238858	109.588600	4.004109	0.001770	0.000036	0.046028	0.000261
j94	0.001758	0.000072	-0.000420	0.000252	10.671620	0.363741	112.782500	4.948149	0.001525	0.000063	0.051475	0.000242
j96	0.001998	0.000100	0.000140	0.000367	10.076800	0.573300	106.678300	6.651589	0.001793	0.000090	0.046647	0.000267
j98	0.002128	0.000081	-0.000200	0.000336	10.180630	0.531463	107.745300	6.285696	0.001954	0.000074	0.041497	0.000233
j100	0.002319	0.000085	0.000140	0.000304	9.425329	0.675050	99.968980	7.542991	0.002228	0.000082	0.036240	0.000264
k4	0.002059	0.000099	0.000120	0.000192	12.825820	1.653115	134.718100	17.171780	0.002467	0.000118	0.021136	0.000117
k6	0.003149	0.000078	-0.000460	0.000300	13.529080	0.869032	141.821800	9.656402	0.002437	0.000061	0.020694	0.000148
k8	0.000946	0.000071	-0.000230	0.000368	12.536660	0.355435	131.789100	5.225300	0.000911	0.000068	0.058282	0.000374
k10	0.000945	0.000067	0.000020	0.000510	12.511420	0.169158	131.533300	4.148340	0.000524	0.000037	0.067547	0.000239
k12	0.000869	0.000058	-0.000310	0.000318	12.380820	0.360659	130.208700	5.232813	0.000997	0.000067	0.056977	0.000444
k14	0.001197	0.000042	0.000350	0.000369	12.428570	0.355925	130.693000	5.208325	0.001488	0.000053	0.045086	0.000296
k18	0.005139	0.000083	-0.000210	0.000184	10.907300	0.738689	115.195400	8.255815	0.002729	0.000044	0.017745	0.000082
k20	0.010597	0.000121	-0.000030	0.000264	11.450450	0.294036	120.743900	4.592202	0.002325	0.000027	0.027331	0.000138
l18	0.004512	0.000094	0.000520	0.000304	12.529950	0.234832	131.721100	4.469252	0.001570	0.000033	0.042785	0.000145
l20	0.003051	0.000125	0.000480	0.000298	12.937130	0.297170	135.844400	4.921039	0.001186	0.000049	0.050212	0.000289
l22	0.002013	0.000064	0.000500	0.000190	12.390560	0.171212	130.307400	4.126670	0.001009	0.000032	0.056645	0.000151
MR-8950												
aae41	0.002170	0.000089	-0.000310	0.000341	13.963040	0.242047	146.261100	2.479247	0.000983	0.000041	0.050814	0.000188
aae43	0.003320	0.000106	-0.000460	0.000314	14.498530	0.394704	151.641000	3.988550	0.001528	0.000049	0.037838	0.000215
aae45	0.004350	0.000122	0.001010	0.000336	14.016150	0.289156	146.795500	2.945574	0.001424	0.000040	0.041315	0.000115
aae47	0.005560	0.000155	0.000620	0.000262	14.288560	0.301489	149.533400	3.064861	0.001436	0.000040	0.040289	0.000173
aae49	0.007019	0.000104	0.000640	0.000464	13.470330	0.185215	141.297000	1.921942	0.001304	0.000021	0.045631	0.000332
aae80	0.003529	0.000112	0.000030	0.000394	14.864570	0.421546	155.309200	4.248710	0.001571	0.000050	0.036044	0.000252
aae82	0.000520	0.000072	0.000030	0.000286	15.912820	0.553117	165.773000	5.530121	0.000656	0.000091	0.050666	0.000157
aae84	0.000920	0.000099	0.000690	0.000353	12.728690	0.792378	133.798800	8.039010	0.001233	0.000132	0.049935	0.000503
aae86	0.009279	0.000206	-0.000250	0.000472	13.336340	0.281585	139.944600	2.877730	0.001360	0.000033	0.044845	0.000407
aae88	0.001000	0.000114	0.000750	0.000306	13.505000	0.399669	141.646700	4.056614	0.000688	0.000079	0.058983	0.000297
aaf16	0.004220	0.000126	0.000140	0.000441	14.115100	0.330530	147.790500	3.355743	0.001445	0.000044	0.040601	0.000222
aaf18	0.000430	0.000064	-0.000100	0.000316	13.570830	0.596682	142.310600	6.033605	0.000756	0.000113	0.057226	0.000524
aaf20	0.002559	0.000051	-0.000340	0.000411	13.644020	0.115782	143.018400	1.252482	0.000914	0.000018	0.053496	0.000214
aaf24	0.004140	0.000112	0.000830	0.000294	15.869070	0.491884	165.337500	4.924768	0.001739	0.000048	0.030639	0.000268
aaf50	0.003940	0.000102	-0.000630	0.000222	13.743030	0.210482	144.046100	2.169208	0.001182	0.000031	0.047342	0.000281
aaf52	0.002430	0.000108	-0.000310	0.000228	12.673780	0.152014	133.242400	1.598027	0.000695	0.000031	0.062704	0.000221
aaf54	0.003330	0.000083	0.000290	0.000292	14.097350	0.280108	147.612000	2.854899	0.001398	0.000035	0.041637	0.000302
MR-899												
k90	0.000243	0.000028	0.000200	0.000171	11.446290	0.884292	120.701400	9.666452	0.001328	0.000155	0.053068	0.000858
k92	0.000662	0.000067	0.000300	0.000300	12.784790	1.315341	134.302800	13.862040	0.001702	0.000172	0.038887	0.000352
k94	0.000621	0.000089	-0.000100	0.000446	13.346510	1.147760	139.980400	12.257260	0.001257	0.000181	0.047091	0.000558
k96	0.000882	0.000064	0.000400	0.000570	12.424620	0.579788	130.653000	6.976588	0.001314	0.000095	0.049228	0.000340
k100	0.000933	0.000064	0.000400	0.000364	12.280630	0.447379	129.191700	5.865949	0.001159	0.000080	0.053546	0.000363
l1	0.000682	0.000063	0.000100	0.000381	10.107110	1.504727	106.989800	15.771430	0.002083	0.000193	0.038050	0.000387
l3	0.000161	0.000078	-0.000500	0.000314	14.668660	0.839170	153.273900	9.476817	0.000356	0.000173	0.060999	0.000274
l5	0.002003	0.000104	0.000800	0.000219	12.608320	4.060229	132.515500	41.319080	0.002912	0.000152	0.011064	0.000158
l8	0.001115	0.000078	-0.000300	0.000344	12.204290	0.594063	128.416600	7.072890	0.001383	0.000097	0.048443	0.000218
l10	0.001706	0.000089	-0.000300	0.000361	12.753400	4.058277	133.985000	41.269810	0.002904	0.000152	0.011126	0.000258
l12	0.000600	0.000089	-0.000100	0.000320	13.635180	1.308011	142.891200	13.798750	0.001321	0.000197	0.044703	0.000396
l14	0.000912	0.000076	0.000400	0.000228	12.596230	1.281946	132.393000	13.535880	0.001847	0.000154	0.036064	0.000618
l16	0.001263	0.000014	0.000600	0.000419	13.392390	0.220226	140.443300	4.595990	0.001844	0.000021	0.033985	0.000295
l24	0.002936	0.000050	0.000470	0.000275	13.538200	0.250214	141.913800	4.782899	0.001720	0.000029	0.036330	0.000190

MR-8917	Mineral	Mass 41	±	40Ar	±	39Ar	±	38Ar	±	37Ar	±
k25	Plagioclase	0.000710	0.000054	2.997649	0.002002	0.014611	0.000211	0.002574	0.000090	0.017863	0.000619
k28	Plagioclase	0.000980	0.000064	1.208613	0.002871	0.001729	0.000081	0.001201	0.000045	0.006626	0.000704
k30	Plagioclase	0.000560	0.000064	1.386373	0.001629	0.006286	0.000173	0.001121	0.000058	0.029189	0.000709
k33	Plagioclase	0.000360	0.000085	1.516421	0.001613	0.052380	0.000192	0.001888	0.000036	0.096839	0.001011
k35	Plagioclase	0.000520	0.000078	0.719762	0.000969	0.012313	0.000146	0.003251	0.000073	0.337678	0.001855
k37	Plagioclase	0.002170	0.000092	1.154587	0.001477	0.023770	0.000190	0.001958	0.000064	0.198835	0.001312
k39	Plagioclase	0.000260	0.000081	0.401163	0.001191	0.004060	0.000117	0.000444	0.000064	0.008792	0.000656
k41	Plagioclase	0.000610	0.000120	2.411842	0.003382	0.074877	0.000391	0.003705	0.000122	0.276237	0.001630
k44	Pyroxene	0.000150	0.000089	0.107184	0.000453	0.001340	0.000045	0.000212	0.000073	0.076791	0.000775
k46	Plagioclase	0.000650	0.000081	4.503373	0.003524	0.102427	0.000252	0.005017	0.000073	0.323398	0.000999
k48	Pyroxene	0.000140	0.000050	1.064376	0.001621	0.041557	0.000233	0.001343	0.000072	0.033551	0.000793
k50	Pyroxene	0.000130	0.000064	0.017934	0.000244	0.000910	0.000076	0.000111	0.000036	0.003488	0.000565
k52		0.000150	0.000086	0.171994	0.000404	0.002859	0.000072	0.000172	0.000067	0.014759	0.001279
k54		0.000360	0.000076	1.989473	0.001390	0.059024	0.000391	0.001968	0.000108	0.031495	0.000833
k56		0.000100	0.000022	0.035370	0.000446	0.000281	0.000054	0.000091	0.000041	0.056291	0.000687
k58		0.002860	0.000664	-0.007400	0.000191	0.001155	0.000190	0.001070	0.000301	0.002075	0.001134
MR-8928											
k61	Plagioclase	0.000290	0.000057	1.126153	0.001455	0.016281	0.000191	0.002029	0.000057	0.114006	0.001219
k65	Plagioclase	0.000240	0.000089	1.453812	0.002586	0.083733	0.000352	0.001797	0.000064	0.118410	0.001120
k67	Plagioclase	0.000230	0.000036	1.379254	0.002097	0.089329	0.000126	0.001645	0.000045	0.109053	0.000826
k69	Groundmass	0.000460	0.000085	4.776731	0.004196	0.301614	0.000494	0.005512	0.000054	0.085180	0.000885
k71	Groundmass	0.000070	0.000092	1.219416	0.001988	0.061813	0.000260	0.001757	0.000092	0.070060	0.000768
k73	Plagioclase	0.000340	0.000072	1.676546	0.003379	0.100554	0.000275	0.002029	0.000072	0.073391	0.000633
k75	Pyroxene	0.000350	0.000076	2.012535	0.003584	0.142117	0.000502	0.003765	0.000076	0.137201	0.000931
k77	Groundmass	0.000190	0.000064	2.948362	0.003113	0.187835	0.000614	0.003341	0.000143	0.077096	0.001017
k79	Plagioclase	0.000120	0.000089	2.235652	0.002326	0.126851	0.000672	0.002423	0.000102	0.087987	0.001802
k81	Plagioclase	0.000250	0.000108	0.998186	0.001536	0.049061	0.000326	0.001292	0.000073	0.061602	0.001121
k83	Groundmass	0.000210	0.000067	1.789568	0.002322	0.096662	0.000373	0.001938	0.000063	0.030090	0.000582
k86	Plagioclase	0.000250	0.000067	1.985174	0.002030	0.111263	0.000303	0.002312	0.000050	0.061086	0.000748
k88	Pyroxene	0.000220	0.000042	1.517457	0.001577	0.091604	0.000331	0.003473	0.000036	0.131127	0.001353
MR-8930											
aaf57	Groundmass	0.000060	0.000122	2.648996	0.012418	0.135035	0.000498	0.004169	0.000106	-0.001030	0.001209
aaf61	Groundmass	0.000070	0.000202	0.490613	0.001842	0.001266	0.000094	0.000616	0.000086	0.001968	0.001680
aaf68	Groundmass	0.000100	0.000086	0.308066	0.000679	0.011096	0.000127	0.000878	0.000050	-0.000790	0.001472
aaf70	Plagioclase	0.000160	0.000086	0.859083	0.004515	0.027503	0.000177	0.001121	0.000067	0.003000	0.000946
aaf72	Plagioclase	0.000170	0.000136	1.158801	0.006104	0.028183	0.000168	0.003907	0.000114	0.003355	0.001125
aaf74	Groundmass	0.000250	0.000144	2.719503	0.006749	0.101379	0.000608	0.006430	0.000072	0.003003	0.001616
aaf76	Plagioclase	0.000110	0.000156	2.369561	0.014361	0.087501	0.000684	0.003513	0.000081	0.008042	0.001308
aaf78	Plagioclase	0.000370	0.000078	3.755009	0.003955	0.154852	0.000677	0.004361	0.000072	0.000177	0.002958
aaf80	Groundmass	0.000310	0.000143	0.730042	0.003409	0.017272	0.000180	0.003907	0.000089	0.000354	0.001538
aaf83	Plagioclase	0.000370	0.000171	3.716056	0.003186	0.110403	0.000463	0.004139	0.000100	0.006373	0.001252
aaf86	Plagioclase	0.000090	0.000125	1.162875	0.002452	0.055174	0.000345	0.001373	0.000072	-0.000089	0.002066
aaf88	Plagioclase	0.000380	0.000089	3.153753	0.015992	0.103083	0.000623	0.003907	0.000106	0.003722	0.001150
aaf92	Plagioclase	0.000210	0.000095	0.390712	0.001977	0.009195	0.000177	0.000606	0.000050	0.005500	0.002251
aaf94	Plagioclase	0.000670	0.000121	8.343885	0.013034	0.299305	0.000655	0.009489	0.000078	0.003550	0.001999
aaf98	Plagioclase	0.000230	0.000152	1.962205	0.008257	0.038681	0.000404	0.002766	0.000064	0.001777	0.002546

MR-8917	36Ar	±	Mass 35	±	40Ar*/39Ar	±	Age (Ma)	±	36Ar/40Ar	±	39Ar/40Ar	±
k25	0.009636	0.000076	-0.000060	0.000347	10.273750	1.553417	108.701700	16.256780	0.003215	0.000026	0.004874	0.000070
k28	0.004139	0.000078	-0.000380	0.000374	-8.302300	-13.455700	-92.894200	154.522700	0.003424	0.000065	0.001431	0.000067
k30	0.004484	0.000092	-0.000210	0.000386	9.759622	4.350269	103.414900	44.899320	0.003234	0.000067	0.001534	0.000125
k33	0.003040	0.000073	0.000210	0.000453	11.799480	0.426487	124.300400	5.624956	0.002005	0.000048	0.034542	0.000326
k35	0.001991	0.000085	-0.000270	0.000240	10.679070	2.041872	112.858800	21.169740	0.002766	0.000118	0.017107	0.000201
k37	0.003309	0.000086	0.000080	0.000438	7.433933	1.072845	79.304040	11.432750	0.002866	0.000075	0.020588	0.000166
k39	0.001138	0.000071	-0.000820	0.000335	15.966260	5.175042	166.226000	51.686290	0.002837	0.000176	0.010121	0.000292
k41	0.004953	0.000091	-0.000580	0.000489	12.662310	0.366213	133.062500	5.324618	0.002054	0.000038	0.031046	0.000168
k44	0.000254	0.000041	0.000050	0.000276	23.924830	9.135978	243.693500	87.309070	0.002372	0.000385	0.012499	0.000421
k46	0.011134	0.000215	0.000590	0.000264	11.846080	0.623074	124.774700	7.286563	0.002472	0.000048	0.022745	0.000059
k48	0.001853	0.000100	0.000340	0.000171	12.435430	0.715559	130.762600	8.172246	0.001741	0.000094	0.039044	0.000227
k50	0.000009	0.000086	0.000330	0.000175	49.655970	28.240220	473.567800	237.199500	0.000194	0.001795	0.018986	0.001592
k52	0.000437	0.000112	0.000440	0.000390	14.995590	11.563910	156.546000	115.716400	0.002541	0.000650	0.016621	0.000421
k54	0.004324	0.000139	-0.000010	0.000304	12.060720	0.700480	126.957800	8.001310	0.002173	0.000070	0.029668	0.000197
k56	0.000108	0.000054	-0.000430	0.000326	11.831390	56.781220	124.625200	577.914900	0.003066	0.001523	0.007933	0.001526
k58	0.000150	0.000058	0.000460	0.000168	-44.692900	-16.642600	########	249.478900	-0.020200	-0.007890	-0.155960	-0.026020
MR-8928												
k61	0.001807	0.000057	-0.000200	0.000188	12.797690	0.366378	134.433400	5.351075	0.001604	0.000050	0.041097	0.000178
k65	0.001186	0.000057	-0.000300	0.000276	13.177930	0.209454	138.278400	4.492899	0.000816	0.000039	0.057596	0.000263
k67	0.000938	0.000063	0.000000	0.000276	12.338460	0.218589	129.778700	4.338645	0.000680	0.000046	0.064766	0.000324
k69	0.003163	0.000061	0.000100	0.000266	12.738780	0.064651	133.837000	3.896329	0.000662	0.000013	0.063142	0.000117
k71	0.001486	0.000072	-0.000100	0.000605	12.625350	0.350283	132.688000	5.206385	0.001218	0.000059	0.050691	0.000229
k73	0.001365	0.000076	-0.000500	0.000368	12.661900	0.228942	133.058400	4.468419	0.000814	0.000046	0.059977	0.000204
k75	0.000582	0.000089	-0.000100	0.000386	12.951190	0.193163	135.986600	4.362252	0.000289	0.000044	0.070616	0.000279
k77	0.001584	0.000112	-0.000100	0.000318	13.204320	0.181863	138.544900	4.375141	0.000537	0.000038	0.063708	0.000219
k79	0.001792	0.000117	-0.000300	0.000354	13.449820	0.281447	141.022600	4.936869	0.000802	0.000052	0.056740	0.000306
k81	0.001287	0.000078	0.000000	0.000227	12.591930	0.478812	132.349400	6.163135	0.001290	0.000078	0.049150	0.000335
k83	0.001794	0.000100	0.000000	0.000391	13.029770	0.310748	136.781200	5.025242	0.001002	0.000056	0.054014	0.000220
k86	0.001807	0.000092	0.000200	0.000164	13.041710	0.248086	136.901800	4.658279	0.000910	0.000047	0.056047	0.000163
k88	0.001113	0.000072	0.000300	0.000550	12.974690	0.237909	136.224200	4.588244	0.000734	0.000048	0.060367	0.000227
MR-8930												
aaf57	0.002890	0.000114	-0.000130	0.000264	13.292440	0.270401	139.501200	2.766665	0.001091	0.000043	0.050976	0.000304
aaf61	0.001660	0.000099	0.000180	0.000256	0.159734	23.030020	1.742049	251.039400	0.003383	0.000201	0.002581	0.000193
aaf68	0.000450	0.000071	0.000750	0.000434	15.775010	1.892737	164.400900	18.860200	0.001461	0.000230	0.036019	0.000421
aaf70	0.001719	0.000095	0.000110	0.000297	12.762220	1.035684	134.138500	10.499380	0.002001	0.000111	0.032015	0.000266
aaf72	0.002689	0.000057	0.000450	0.000228	12.919610	0.636101	135.732000	6.452029	0.002321	0.000050	0.024321	0.000193
aaf74	0.004819	0.000089	0.000330	0.000414	12.777480	0.279781	134.293000	2.865855	0.001772	0.000033	0.037279	0.000242
aaf76	0.004378	0.000085	0.000150	0.000408	12.294250	0.343914	129.391900	3.517084	0.001848	0.000038	0.036927	0.000365
aaf78	0.006360	0.000081	0.000050	0.000268	12.112500	0.164712	127.545200	1.723312	0.001694	0.000022	0.041239	0.000186
aaf80	0.001810	0.000054	0.000460	0.000143	11.302070	0.949592	119.287100	9.705652	0.002479	0.000075	0.023659	0.000271
aaf83	0.008119	0.000136	0.001850	0.000236	11.928810	0.368598	125.676800	3.772584	0.002185	0.000037	0.029710	0.000127
aaf86	0.001610	0.000072	0.000770	0.000198	12.453630	0.396501	131.010000	4.044860	0.001385	0.000062	0.047446	0.000313
aaf88	0.006199	0.000100	0.000530	0.000326	12.823460	0.335034	134.758700	3.419539	0.001966	0.000033	0.032686	0.000258
aaf92	0.000969	0.000081	-0.000630	0.000430	11.355500	2.609121	119.832700	26.641540	0.002480	0.000207	0.023533	0.000468
aaf94	0.015489	0.000161	-0.000290	0.000316	12.585180	0.167326	132.344200	1.748254	0.001856	0.000020	0.035871	0.000096
aaf98	0.004920	0.000114	0.000060	0.000394	13.144720	0.907269	138.008700	9.180753	0.002507	0.000059	0.019713	0.000222

MR-8931	Mineral	Mass 41	±	40Ar	±	39Ar	±	38Ar	±	37Ar	±
aac70	Plagioclase	0.000220	0.000136	1.365564	0.003459	0.039857	0.000209	0.001151	0.000086	0.002349	0.000865
aac72	Plagioclase	0.000020	0.000122	0.910716	0.004565	0.024140	0.000233	0.000717	0.000050	-0.002140	0.001262
aac74	Plagioclase	0.000120	0.000166	1.862858	0.009771	0.109278	0.000381	0.001908	0.000064	0.005772	0.001556
aac78	Amygdale	0.000260	0.000112	0.454801	0.002244	0.030355	0.000177	0.000464	0.000036	0.000357	0.001265
aad8	Groundmass	0.000580	0.000071	5.954588	0.005811	0.361306	0.001400	0.006864	0.000083	0.001532	0.001732
aad10	Groundmass	0.000410	0.000130	4.833469	0.026590	0.313707	0.001075	0.004583	0.000072	0.003211	0.001171
aad12	Groundmass	0.000670	0.000150	6.057457	0.018835	0.393059	0.001251	0.006218	0.000146	0.005183	0.001271
aad14	Plagioclase	0.000270	0.000205	0.383334	0.002059	0.023701	0.000141	0.000454	0.000058	0.001972	0.001546
aad18	Groundmass	0.001280	0.000126	8.917655	0.012239	0.581290	0.001427	0.009237	0.000130	0.002779	0.001075
aad20	Plagioclase	0.001660	0.000150	1.673582	0.002538	0.063030	0.000260	0.002372	0.000142	0.004975	0.001575
aad22	Groundmass	0.001140	0.000092	5.269150	0.015382	0.324154	0.002852	0.005037	0.000143	0.002562	0.002086
aad24	Plagioclase	0.002300	0.000177	5.199962	0.005837	0.291651	0.001093	0.006097	0.000114	-0.000510	0.001683
aad26	Groundmass	0.000710	0.000150	4.775962	0.006142	0.345493	0.001813	0.012619	0.000143	0.003517	0.001242
aae4	Groundmass	0.001040	0.000156	3.861346	0.005465	0.272916	0.000772	0.003695	0.000064	0.001421	0.001091
aae6	Plagioclase	0.001100	0.000135	1.103060	0.001314	0.063804	0.000410	0.001777	0.000114	0.001421	0.002115
aae8	Groundmass	0.000680	0.000220	4.317125	0.004684	0.251041	0.000615	0.004119	0.000078	-0.000240	0.001309
aae10	Plagioclase	0.001130	0.000144	2.068361	0.002105	0.099494	0.000844	0.003109	0.000117	0.002134	0.001669
MR-8944											
v25	Biotite	0.000340	0.000086	3.696914	0.006375	0.143148	0.000257	0.004119	0.000063	-0.000680	0.000325
v27	Biotite	0.000390	0.000064	3.756083	0.005477	0.145846	0.000226	0.004260	0.000058	-0.000460	0.000360
v30	Biotite	0.000450	0.000081	2.122176	0.007148	0.131241	0.000682	0.002897	0.000103	-0.000120	0.000472
v32	Biotite	0.000440	0.000050	1.137163	0.002238	0.095408	0.000335	0.001787	0.000041	0.000080	0.000494
v34	Biotite	0.000250	0.000092	1.377217	0.001716	0.101138	0.000455	0.002191	0.000089	0.000201	0.000326
v36	Biotite	0.000390	0.000057	1.624466	0.002053	0.129830	0.000457	0.002615	0.000067	0.000725	0.000289
v38	Biotite	0.000530	0.000063	3.991736	0.004441	0.307340	0.000579	0.006027	0.000108	0.000060	0.000317
v40	Biotite	0.000190	0.000099	3.648967	0.004109	0.304023	0.000714	0.005734	0.000108	0.000484	0.000345
v42	Biotite	0.000500	0.000092	3.734414	0.006499	0.244661	0.000585	0.005239	0.000104	0.000988	0.000497
v65	Kaersutite	0.001020	0.000095	0.753427	0.001122	0.071187	0.000392	0.006309	0.000117	0.002176	0.000333
v67	Kaersutite	0.003100	0.000108	1.665262	0.002072	0.140770	0.000296	0.013063	0.000108	0.004970	0.000256
v70	Kaersutite	0.003140	0.000128	1.677086	0.001741	0.167282	0.000750	0.009237	0.000152	0.004809	0.000479
v91	Kaersutite	0.000880	0.000106	2.219990	0.003450	0.268197	0.001182	0.025742	0.000251	0.005799	0.000324
MR-8981											
v47	Hornblende	0.000350	0.000100	2.957312	0.004363	0.155165	0.000671	0.003281	0.000054	0.001226	0.000293
v49	Hornblende	0.000070	0.000076	0.702251	0.001051	0.033520	0.000260	0.000929	0.000050	0.000572	0.000695
v51	Hornblende	0.000290	0.000058	1.536092	0.000804	0.055183	0.000355	0.001716	0.000081	0.001023	0.000538
v54	Hornblende	0.000680	0.000042	6.036457	0.003496	0.352574	0.000582	0.008147	0.000120	0.000696	0.000297
v56	Hornblende	0.000180	0.000092	0.681864	0.001597	0.030812	0.000089	0.000787	0.000042	0.000430	0.000249
v58	Hornblende	0.000400	0.000125	5.559054	0.008386	0.354804	0.001581	0.006178	0.000114	0.002500	0.000520
v60	Hornblende	0.000820	0.000117	9.177475	0.012322	0.384945	0.001171	0.009812	0.000067	0.004961	0.000447
v63	Hornblende	0.000140	0.000058	1.772062	0.002770	0.102567	0.000212	0.001989	0.000050	0.001293	0.000385

Table A.9
Argon isotope data for the Parana dolerite samples dated by the Ar—Ar method.

MR-8931	36Ar	±	Mass 35	±	40Ar*/39Ar	±	Age (Ma)	±	36Ar/40Ar	±	39Ar/40Ar	±
aac70	0.003030	0.000113	-0.000590	0.000347	11.800670	0.845537	124.372200	8.620291	0.002219	0.000083	0.029187	0.000170
aac72	0.002010	0.000122	-0.000500	0.000301	13.116370	1.511416	137.722200	15.285380	0.002208	0.000134	0.026507	0.000288
aac74	0.001729	0.000057	0.000100	0.000172	12.372030	0.182352	130.181700	1.897160	0.000928	0.000031	0.058662	0.000369
aac78	0.000280	0.000092	-0.000540	0.000322	12.257540	0.903369	129.019100	9.185664	0.000615	0.000203	0.066744	0.000510
aad8	0.001700	0.000163	0.000470	0.000516	12.637020	0.142769	132.869800	1.507872	0.000789	0.000027	0.060677	0.000242
aad10	0.002849	0.000092	0.000540	0.000122	12.723610	0.128942	133.747300	1.374157	0.000590	0.000019	0.064903	0.000121
aad12	0.001049	0.000104	0.000690	0.000171	12.367100	0.100031	130.131700	1.097077	0.000668	0.000017	0.064888	0.000289
aad14	0.000370	0.000081	0.000710	0.000361	11.565740	1.011297	121.978000	10.320300	0.000964	0.000210	0.061828	0.000496
aad18	0.005859	0.000072	-0.000570	0.000428	12.362490	0.052040	130.084900	0.671834	0.000657	0.000008	0.065184	0.000183
aad20	0.003249	0.000095	0.000010	0.000436	11.320110	0.449011	119.471400	4.601169	0.001941	0.000057	0.037662	0.000165
aad22	0.001399	0.000045	-0.000680	0.000275	12.244500	0.124570	128.886600	1.330645	0.000835	0.000009	0.061519	0.000570
aad24	0.005600	0.000104	0.000610	0.000392	12.155400	0.116898	127.981200	1.256413	0.001077	0.000020	0.056087	0.000219
aad26	0.001549	0.000064	0.000160	0.000484	12.498530	0.087285	131.465400	0.979687	0.000324	0.000013	0.072340	0.000391
aae4	0.001560	0.000081	0.000380	0.000322	12.459680	0.096241	131.071300	1.062228	0.000404	0.000021	0.070679	0.000223
aae6	0.001180	0.000067	-0.000200	0.000430	11.824630	0.320502	124.616200	3.287820	0.001069	0.000061	0.057843	0.000378
aae8	0.003860	0.000041	-0.000730	0.000342	12.653240	0.060541	133.034200	0.745900	0.000894	0.000010	0.058150	0.000156
aae10	0.002950	0.000136	0.000140	0.000301	12.028550	0.417187	126.691400	4.262501	0.001426	0.000066	0.048103	0.000411
MR-8944												
v25	0.008840	0.000146	0.000670	0.000469	7.577134	0.304152	80.837190	3.183953	0.002391	0.000040	0.038721	0.000096
v27	0.008850	0.000141	0.000200	0.000718	7.822510	0.289239	83.395400	3.025366	0.002356	0.000038	0.038829	0.000083
v30	0.003690	0.000104	0.000800	0.000456	7.861693	0.244732	83.803570	2.563428	0.001739	0.000050	0.061843	0.000383
v32	0.001470	0.000108	-0.000570	0.000411	7.366078	0.336833	78.633870	3.527649	0.001293	0.000095	0.083900	0.000338
v34	0.002170	0.000085	0.000420	0.000344	7.277104	0.252346	77.704230	2.649258	0.001576	0.000062	0.073437	0.000343
v36	0.002090	0.000086	0.000630	0.000420	7.755622	0.198319	82.698410	2.084134	0.001286	0.000053	0.079922	0.000299
v38	0.005550	0.000036	0.001330	0.000366	7.651827	0.040226	81.616300	0.495586	0.001390	0.000009	0.076994	0.000168
v40	0.004690	0.000099	0.000310	0.000460	7.443838	0.098247	79.445970	1.057502	0.001285	0.000027	0.083318	0.000217
v42	0.006580	0.000085	0.000130	0.000373	7.316601	0.107310	78.116980	1.149397	0.001762	0.000023	0.065515	0.000194
v65	0.000890	0.000072	0.000770	0.000502	6.891236	0.302145	73.559500	3.169296	0.001181	0.000096	0.094484	0.000539
v67	0.002299	0.000078	0.000090	0.000577	7.003695	0.165267	74.735410	1.744424	0.001381	0.000047	0.084533	0.000207
v70	0.001769	0.000092	0.000140	0.000394	6.900559	0.166097	73.657020	1.753574	0.001055	0.000055	0.099746	0.000459
v91	0.002179	0.000076	0.000500	0.000336	5.876845	0.088751	62.917990	0.955980	0.000981	0.000034	0.120810	0.000564
MR-8981												
v47	0.004300	0.000063	0.000640	0.000239	10.870590	0.132309	114.709300	1.401868	0.001454	0.000022	0.052468	0.000240
v49	0.001020	0.000078	-0.000490	0.000309	11.959420	0.695439	125.807100	7.077788	0.001452	0.000111	0.047732	0.000377
v51	0.003310	0.000076	0.000780	0.000234	10.112670	0.413233	106.943800	4.256893	0.002155	0.000050	0.035924	0.000232
v54	0.005910	0.000086	0.000370	0.000530	12.167920	0.075499	127.924500	0.868561	0.000979	0.000014	0.058407	0.000102
v56	0.001370	0.000078	0.000400	0.000244	8.991845	0.751286	95.398460	7.769654	0.002009	0.000115	0.045188	0.000169
v58	0.004379	0.000100	-0.000230	0.000466	12.020480	0.101795	126.427400	1.110238	0.000788	0.000018	0.063825	0.000300
v60	0.017219	0.000218	0.000000	0.000282	10.622990	0.173714	112.176100	1.814600	0.001876	0.000024	0.041945	0.000139
v63	0.001930	0.000050	0.000290	0.000244	11.717410	0.148551	123.346400	1.562203	0.001089	0.000028	0.057880	0.000150